CHARACTERISATION AND EVALUATION OF THERMALLY TREATED RECYCLED GLASS FOR MASS FINISHING AND SUPERFINISHING PROCESSES

MIKDAM JAMAL

A thesis submitted in partial fulfilment of the requirements of Liverpool John Moores University for the degree of Doctor of Philosophy

August 2015

ABSTRACT

This thesis presents the work on the characterisation and evaluation of an entirely new mass finishing product based wholly on thermally treated recycled glass, which acts as both a bond and abrasive for mass finishing and superfinishing processes. The recycling of glass is excellent in respect of sustainability and environmental efficiency. The aim of the study was to establish requirements for the high volume manufacture of thermally treated recycled glass preforms to satisfy stated performance criteria.

Several powder characterization techniques were employed to assess morphology and flowability of various grades of soda lime glass powder. The results obtained have demonstrated that flowability and packing properties improve with an increase of particle size. Thermal analyses were successfully employed for various types of mould material to determine the optimal glass powder size in terms of crystallinity and mechanical properties. It was found that by controlling the time transformation temperature TTT relationship, it is possible to consistently produce abrasive media possessing particular mechanical and physical properties that deliver target mass finishing performance. The residual stresses developed during different thermal cycles were investigated numerically and experimentally. Compressive stress was observed near the media edge and tensile stress in the mid-plane at the end of the solidification process. The results showed that the numerical FEA code is a suitable tool for the prediction of residual stresses of thermally treated recycled glass. A study concerned with the tip geometry of the Vickers and Berkovich indenters was completed to ensure an accurate contact area determination. A new method is proposed for the determination of contact area based on residual imprint measurements using 3-D optical profilometry. The outcomes show that by measuring contact area with the new method the overall relative error in the obtained mechanical properties is improved.

A combined Finite Element Analysis FEA and optimization algorithm has been developed using various indentation processes to determine the mechanical properties of a wide range of materials, using target FE indentation curves which were then extended to actual glass media taking into account the predicted residual stress in the material. The results obtained from the proposed methods of dual indenters and optimization algorithm have demonstrated that excellent convergence can be achieved with the target FE indentation curve of complex material systems; and also accurate results have been obtained for the actual glass. The material characterization tests were extended to investigate the fracture toughness based on the stress fields mapped at the unloading stage of the Vickers

Abstract

indentation. The median and Palmqvist crack systems were analysed separately using FEA. Dimensionless analyses were then carried out, and the critical SIF (fracture toughness) derived for the measured crack length and material properties. The developed numerical models were validated with the experimental data proposed by many researchers over a wide range of material properties as well as Vickers indentation induced cracking of thermally treated glass.

The performance programme was designed as a comparative study with a range of conventional media that included an industrial benchmark media. Performance indicators included surface roughness and brightness. The results of the laboratory based research studies provided promising evidence that the thermally treated glass media has a process capability and performance comparable to that of conventional media. The glass media was trailed on a production machine annexed for this purpose. Turbine blades were employed as the component for these trails. The results though very promising did identify that a heavy workpiece may crush some media thereby generating small shards that may scratch or impair a fine surface finish (contribute against Ra). However, a novel jig arrangement was designed to hold the part in a horizontal position and allowed free rotation of the workpiece with the media flow in the trough. The new system was successfully used to deliver better performance results with the conventional and thermally treated recycled glass media.

The kinematics of the mass finishing process were investigated with a two-dimensional discrete element model (DEM) developed to perform single-cell circulation in a vibratory bed. The sensitivity of the predicted model corresponding to the contact parameters was considered and the parameters were optimized with respect to the experimental results of media velocity vectors using particle image velocimetry (PIVLab). The results suggested that the bulk circulation increases with increasing bed depth resulting in an increase in pressure and shear forces between particle layers.

The optimization of the advanced mass finishing (Drag and Stream finishing process) process has been studied using the design and analysis of experiment (DOE) approach. Regression analyses, analysis of variance (ANOVA), Taguchi methodology and Response Surface Methodology (RSM) have been chosen to aid this study. The effects of various finishing parameters were evaluated and the optimal parameters and conditions determined. The interaction of finishing parameters was established to illustrate the essential relationship between process parameters and surface roughness. The predicted models were confirmed by experimental validation and confirmation finishing trials.

Acknowledgments

List of Contents

List of Contents

List of Contents

List of Figures

List of Figures

List of Figures

List of Figures

List of Figures

List of Figures

List of Figures

List of Tables

NOMENCLATURE

Symbol	Meaning
H_v	Vickers hardness
d	Imprint diagonal
F	Load
A_{proj}	Projected area
h_c	Contact depth
H_b	Berkovich hardness
A_C	Contact area
$A_{(proj)k}$	Knoob projected area
l	Long diagonal
w	Short diagonal
H_k	Knoop hardness
H_R	Rockwell hardness
H_B	Brinell hardness
a_c	Contact radius
S	Contact stiffness
E_r	Reduced modulus
A	Contact area
h	Indenter depth
α and m	constants relative to the indenter tip shape
h_f	Final depth
ϵ	indenter geometry constant
F_{max}	Maximum indentation load
C	Curvature constant
v	Poisson's ratio
σ_u	Ultimate tensile stress
σ_y	Yield stress
E	Elastic modulus
$hmax$	Maximum indentation depth
W_p	Plastic work
W_t	Total work
W_e	Elastic work
P_{avr}	Contact pressure
K	Yield strength
n	strain hardening exponent
ε	Equivalent yield strain
θ	Indenter angle
π	Buckingham theorem
$\mathrm{d}f/\mathrm{d}h$	Initial unloading slop
$d\sigma/d\varepsilon$	Work hardening
HR	Hausner Ratio
CI	Carr's Index
ρ_t	Tap density
ρ_a	Apparent density
D_{10}	10% smaller than the target particle
D_{50}	50% smaller than the target particle

Nomenclature

D_{90}	90% smaller than the target particle
$d\varepsilon/dt$	Strain rate
η	Viscosity
$\sigma(t)$	Stress relaxation with time
$G(t)$	Relaxation shear modulus
K_e	Deferred bulk modulus
K_g	Instantaneous bulk modulus
G_g	Instantaneous shear modulus
M_v	Structural relaxation volume function
$(\varepsilon_{th})_g$	Gas thermal expansion coefficient
$(\varepsilon_{th})_l$	Liquid thermal expansion coefficient
T_f	Fictitious temperature
ξ	Reduced time
τ_{ref}	Relaxation time
R	Universal gas constant
H	Activation energies
H_g	Activation energies with temperature
H_S	Activation energies with structure
T_g	Glass transition temperature
$\bar{Q}$	Hole drilling constant
$\partial g/\partial t$	Deflection of current thickness
d	Inter-planer spacing
λ	Wave length
θ	Diffraction intensity position
d_0	Un stressed inter-planer spacing
$d_{\varphi\psi}$	Inter-planer spacing at rotation angle
σ_φ	Biaxial residual stress
λ	Thermal conductivity
Q	heat quantity
C_p	Specific heat
$C_{p.l}$	Specific heat of liquid glass
$C_{p.g}$	Specific heat of solid glass
D	Thermal diffusivity
E_l	Elastic modulus of liquid glass
E_g	Elastic modulus of solid glass
β_g	Thermal expansion of solid glass
β_l	Thermal expansion of liquid glass
ϵ_{th}	Thermal expansion
h_{rad}	Radiation heat resistance
σ	Boltzmann constant
$T_{sm}(t)$	Surrounded medium temperature
$T(P,t)$	Surface temperature at point P
T_{ref}	Reference temperature
δ	Indenter correction factor
E_i	Indenter elastic modulus
ν_i	Indenter Poisson's ratio
$A(h_c)$	Area function of contact depth
S_s	Specimen stiffness

Nomenclature

C_F	Frame structure compliance
C_T	Total compliance
C_S	Specimen compliance
S_T	Total stiffness
h_d	Distance between the blunted edge and the cone-end
A_{PS}	Projected area of the spherical part
h_e	Recover indentation depth
α'	Effective half-angle
Re	Relative error
q	Von Mises equivalent stress
σ_m	Hydrostatic pressure stress
S_{ij}	Stress deviator
σ_{yc}	Compressive stress
β	Friction coefficient
hw	Workpiece Height
rw	Workpiece width
$min\ F(x)$	Minimum objective function
F_{exp-l}^i	Experimental force at loading stage
F_{exp-ul}^i	Experimental force at unloading stage
F_{num-l}^i	Numerical force at loading stage
F_{num-ul}^i	Numerical force at unloading stage
H_{IT}	Indentation hardness
σ_e	Von Mises equivalent stress
σ_S	Shear stress
μ	Hydrostatic stress sensitivity parameter
ψ	Dilatation angle
K	Flow stress ratio
μ^*	Flow parameter
v^p	Plastic component of Poisson's ratio
σ_{res}	Residual Stress
E_p	Plastic hardening modulus
ε_e^p	Equivalent plastic strain
σ_m	Equivalent stress
σ_f	Fracture stress
σ_{ni}	Normal stress
u_0	Maximum crack opening displacement
u_i	Crack opining displacement
u_t	Total damage magnitude
ε_{ij}	Total strain
ε_{ij}^e	Strains due to elastic
ε_{ij}^p	Strains due to plastic
ε_{ij}^c	Strains due to crack
K_I	Stress intensity factor
J	Energy release
I_n	Mass inertia
σ_o	Effective yield stress
ε_o	Effective strain

Nomenclature

K_{IC}	Fracture toughness
Ra	Average surface roughness
$\ddot{x}_i$	Particle velocity at central node
ω_1	Angular velocities
g_i	Acceleration due to gravity
kn	normal stiffness
F_n	Normal force
δ_n	Normal overlap
R_i	Radius of particles i
r_i	Position vectors of mass i
R^*	Equivalent radius
e_r	Coefficient of restitution
m^*	Equivalent mass
v_n^r	Normal component of relative velocity
F_t	Tangential force
k_t	Tangential force
F_t^d	Tangential damping force
v_t^r	Tangential component of relative velocity
F_{ij}	Resultant contact force
μ_r	Coefficient of rolling friction
d_n	Relative displacement along the normal directions
d_t	Relative displacement along the tangential directions
c_n	Normal damping coefficient
c_t	Tangential damping coefficient
ρ_d	Density of the disk elements
ρ_p	Density of the actual particle
A_r	Area ratio
A_{unc}	Uncovered area
A_t	Total area
c_{cr}	Critical damping coefficient
T_m	Milting Temperature
T_x	Crystallization Temperature
T_n	Nucleation Temperature
T_o	Oxidation Temperature
M_{res}	Residual Mass

ABBREVIATIONS

FEA	Finite Element Analysis
FEM	Finite Element Modelling
KPVs	key Process Variables
VG+06	Vibraglaz Particle Size = 106μm
VG+150	Vibraglaz Particle Size = 250μm
VG+350	Vibraglaz Particle Size = 450μm
VG+450	Vibraglaz Particle Size = 550μm
MTC	Manufacturing Technology Centre
SEM	Scanning Electron Microscopy
LSM	London and Scandinavian Metallurgy Co.)
CERAM	Ceram Research Limited
XRF	X-Ray Fluorescence
LOI	Loss On Ignition
ADH	Apparent Density
HR	Hausner Ratio
CI	Carr's Index
SLSG	Soda Lime Silica Glass
BFE	Basic Flow Energy
SI	Stability Index
FRI	Flow Rate Index
SE	Specific Energy
TTT	Time-Temperature-Transformation
DTA	Differential Thermal Analysis
TGA	Thermo-Gravimetric Analysis
DSC	Differential Scanning calorimeter
GTS	Glass Technology Services Ltd
VT	Vibraglaz Temperature = 800°C
VT-10	Vibraglaz Temperature = 790°C
VT-70	Vibraglaz Temperature = 730°C
VT+60	Vibraglaz Temperature = 860°C
VT-90	Vibraglaz Temperature = 710°C
VT-50	Vibraglaz Temperature = 750°C
VT-200	Vibraglaz Temperature = 600°C
VT+100	Vibraglaz Temperature = 900°C
HTC	Heat Transfer Coefficient
CAE	Computer Added Engineering
RMSE	Root Mean Square Error
odp.	Output Data Base
inp.	Input Data File
LSQNONLIN	Non-linear Least-squares Objective Function
SIF	Stress Intensity Factor
K_{IC}	Fracture Toughness
VP	Holding Time = 60 min.
VP+10	Holding Time = 70 min.
VP-20	Holding Time = 40 min.
VP+20	Holding Time = 80 min.
RT	Cooling Rate

Nomenclature

RT50	Cooling Rate = 50 min.
RT40	Cooling Rate =40 min
ORC	Overlapping Rigid Clusters
DEM	Discrete Element Modelling
PIV	Particle Image Velocimetry
GUI	Graphical Use Interface
FFT	Fast-Fourier-Transform
MF	Mass Finishing Process
DOE	Design of Experiment
ANOVA	Analysis of variance
SS	Sum of Square
MS	Mean Square
DF	Degree of Freedom
RSM	Response Surface Methodology
DSS	Drag Spindle Speed
DHS	Drag Head Speed
DID	Drag Immersion Depth
SHS	Stream head speed
SBS	Stream Bowl Speed
SID	Stream Immersion Depth

CHAPTER ONE
INTRODUCTION

1.1   Introduction

1.1.1   Background

Mass finishing processes continue to gain widespread acceptance in manufacturing industries, primarily as a relatively low cost technology for producing edge and surface finishes. Mass finishing refers to the finishing, polishing and / or refining of surfaces using the fluidized motion of a volume of moving abrasive tools (preform media), which can include plastics and ceramics, or metals. While at first, vibratory finishing may be judged a somewhat niche operation, it is increasingly a necessary operation and mass finishing machines are frequently found adjacent to, for example: laser cut, water jet cut and CNC milling operations. Globally, there are in excess of 50,000 vibratory finishing machine tools operational in over 120 different countries and this number is increasing annually as the demand for the process rises, (Gillespie 2006). In general, mass finishing operations include edge breaking, edge contouring, surface smoothing and improvement, tool mark blending, burnishing, polishing, super finishing, and micro finishing (Davidson 2003, Davidson 2005). It is also commonly used to deburr large numbers of parts simultaneously; it can produce hundreds of parts per hour (Davidson 2003). As the term suggests, this is the advantage that defines mass finishing compared with other processes -which do not allow deburring or surface finishing on as large a scale. Parts finished with this process are varied and diverse, examples include domestic items such as musical instruments, coinage and cutlery to higher precision engineered parts such as medical implants and aerospace turbine blades to ultra-high precision engineering components with surface roughness values measured in the nanometre scale.

Vibratory deburring is a member of the family of operations within the *Mass finishing* processes, (also known as '*loose' abrasive finishing*). Other operations include: barrel finishing, shaker tumbling, roll-flow finishing, centrifugal barrel finishing and screw rotor deburring. Vibratory systems have become the predominant method due to advantages inherent to the method in terms of ease of use, automation, and material handling. When first developed in the 1950's, these systems were typically modest in size, and were used for deburring and finish processing of smaller components. Being able to process larger batches of modestly sized parts was important to competitiveness.

The majority of finishing applications employ preform media of aluminium oxide or silicon carbide abrasive in either a ceramic bond (45% to 55% abrasive by weight) or resin bond (40% to 70% abrasive by weight). Ceramic bonds (most common) are of vitreous materials that includes glass frit. Resin bonds are principally of polyester or urea-formaldehyde. A liquid compound may also be used to aid lubrication and to remove dust and debris from the container.

Energy is introduced to the abrasive media mass by a variety of means to impart motion to it and to cause it to rub or wear away at part surfaces. Most manufacturing companies that employ mass finishing techniques do so because of the potential economic advantages, especially when compared with manual deburring and surface finishing techniques which are often labour intensive and require extensive part handling. This is especially important in meeting increasingly stringent quality control standards, as most mass finishing processes generate surface effects with part-to-part and lot-to-lot uniformity that cannot be replicated with processes in which parts are individually handled.

1.1.2   The Need for the Research

It has been identified from preliminary studies that use of mass finishing technology has been rapidly increasing over the past four decades. It has been introduced into a range of well-known manufacturing industries and companies are using the technique to achieve their goal in respect of part quality and appearance. However, the number of researches in this field remains limited and only a few technical papers have been released since 1970.

Mass finishing processes have become increasingly popular as a finishing method. However, there is an environmental impact associated with media production and a limitation in the efficiency of its production. The major benchmark media in common use in industry employs a small percentage of recognized abrasives (Aluminium Oxide, Silicon Carbide or Quartz) and large volumes of bond material such as the feldspars and glass frits, plastics or low-density ceramics. The raw materials used for production of these media are finite, require extraction, processing and transportation and when exhausted are sent to landfill. Plastic based media is also very unpleasant to work with and leaves significant residues that require compex flushing and disposal.

Landfill deposition is also a common method for the disposal of large volumes of glass and is a relatively expensive disposal solution. It also has a deleterious environmental impact. Furthermore, it contravenes the fundamental principle that natural resources should be recycled or reused rather than disposed of wastefully. Recycling therefore, is a solution that helps reduce unnecessary waste, disposal costs and the excessive use of raw materials and can also prove to provide alternative sources of income.

The focus of this work is an entirely new mass finishing product based wholly on thermally treated recycled glass. No other products similar to this are available. This innovation has been developed by a Northwest SME [re: Vibraglaz (UK) Ltd].The new abrasive media is a timely innovation and a most recent government commissioned review on international manufacturing research highlights the global importance and increasing need for sustainable, resource-efficient manufacturing technologies and research. The new media investigated within this research has been developed using only thermally treated recycled glass, which acts as both a bond and abrasive. The recycling of glass is excellent in respect of sustainability and environmental efficiency. Glasses can be recycled many times during their life without significant reduction to final quality. Glass recycling reduces landfill, reduces consumption of raw materials and imparts a lower carbon footprint in re-manufacture. The innovative-patented media possesses strong environmental credentials and will provide substantial economic benefit to consumers in the high-value sectors including aerospace, automotive and biomedical.

As an overview, there is very little published research on mass finishing and the process is presently poorly understood. Furthermore there is a new research opportunity residing in the use of glass as an abrasive media. This programme of work will improve understanding of the process, generate significant new knowledge and is innovative in a number of areas, specifically: new materials characterisation, new media performance evaluation, mass finishing modelling and simulation. The work will bring immediate benefit to the mass finishing community and enable the product innovator to achieve global market penetration.

1.1.3   Proposed solution

The most recent innovation in the process has been the production of preforms using recycled thermally treated glass. The manufacturing process yields a self-bonded abrasive produced solely from glass cullet. In preliminary studies, this novel media has demonstrated considerable promise as an alternative environmentally sensitive, sustainable abrasive finishing product. It has been reasoned that the performance capability of the media is a result of the high cutting edge density and relatively high toughness of the media, induced by the production process. If this can be demonstrated to be the case, the beneficial environmental credentials of the product will offer significant advantage to users and hence provide a potentially disruptive technology to a widening market. However, no quantitative evidence is presently available to support such conclusions and further investigations are needed.

The thermal treatment of the recycled glass is similar to that of conventional vitrified bonded products. The rate of temperature increase, maximum temperature, periods of steady state temperature and cooling rates for the media under investigation are confidential and patented. The raw material (cullet / new media) is set in a mould, in a 'dry' or 'wet' condition. The mould material is specific to the required output. It is important that for high precision items the thermal gradient of the mould be matched with the glass cullet to ensure uniformity of vitrification on cooling. Different mould materials and wall thicknesses will influence system-cooling rates. The glass is fired in an industrial linear transfer gas oven at furnace facilities within Vibraglaz UK. for a given time and temperature cycles.

The production process and how it impacts on media properties and tribological performance of the thermally treated recycled glass are not fully understood and this programme of work is designed to address these deficiencies. One of the key research tasks will be to establish the mechanical properties and crystallographic structure of the glass media and to then relate these properties to production parameters and to operational performance. A series of well-conditioned experiments will be developed to provide for the comparative evaluation of new and conventional media under a wide range of machining conditions. The mechanical properties of the new media will be investigated using an experimental indentation process supported by FEM analysis.

Results from such studies will be used to help explain performance output and to improve understanding of the material behaviour. Such information will be vital to continue development of the media and to ensure optimal abrasive/mechanical properties are achieved at the lowest environmental cost.

There is potentially a very large experimental matrix resulting from such a study, and as a consequence FEM simulation and statistical approaches will be employed to reduce the number of tests required to a manageable and achievable level. The research is a coupled programme of fundamental studies, from which important insights on the material properties and performance will be obtained, and the development of enabling technologies to aid technology integration into real production.

1.1.4   Aims and Objectives

The project aim is to establish the requirements for the high volume manufacture of thermally treated recycled glass preforms to satisfy stated performance criteria.

Principal Objectives:

- to design and assist in experimental tests (laboratory and on-site) to comprehensively characterise the recycled glass media range of products with respect to essential mechanical and physical properties based on experimental and numerical FEM of nano-indentation and micro-hardness testing techniques
- to determine optimal T-T-T production parameters to aid delivery of a product with a fully established capability in the finishing of aerospace and other engineering materials (predominantly: polishing, super-polishing and super-finishing operations)
- to design and evaluate a computer based particle flow simulation methodology (established from PVI and MATLAB methods) to predict element trajectory, velocity field vectors and to then extend this work to DEM for analysis of sliding and impact forces in vibratory operations
- to develop an optimization system tool that can be used to predict and optimise output quality, act as a design aid, or be utilised as a generic system for other manufacturing processes and operations
- to establish a framework for a future intelligent system for production quality control, process planning and product design.

1.1.5   Outline of the thesis

Chapter One, introduction

Chapter two, background information and the use of indentation methods for characterising the mechanical properties are reviewed. Several types of indentation techniques and instrumented methods are covered. A brief review of contact mechanics related to various indentations and factors affecting the analysis of indentation data are given. Different approaches to evaluate material properties based on forward and reverse indentation tests are critically reviewed, with discussions on the possibility of each method to be potentially used in characterising thermally treated recycled glass media.

Chapter three, reviews several powder characterization techniques to assess morphology, flowability and compressibility of various sizes of recycled soda lime glass beads (supplied by Potters Ballotini Ltd). The effect of particle shape, size and distribution on the parameters measured by powder characterisation techniques were critically reviewed with discussion of the influences on the manufacturing process in terms of flow and packing characteristics (manual and automatic mould filling) and glass media angularity.

Chapter four, investigates the nucleation and crystallization kinetics of various sizes of recycled soda lime glass beads supplied by (Potters Ballotini Ltd) by means of differential thermal analysis (DTA), and thermo-gravimetric analysis (TGA) experiments. A series of firing cycles were set-up to investigate the effect of heat treatment cycles on the final product of recycle glass media. Then, SEM, XRD, 3-D digital optical microscope, and stylus contact Profilometer were employed to examine the morphology, crystallinity, and surface roughness of the product for a given heat treatment cycle to evaluate the time-transformation temperature (TTT). This knowledge will aid delivery of a range of thermally treated recycled glass media with full capability in the finishing of aerospace and other engineering materials (predominantly: polishing, super-polishing and super-finishing operations) .

Chapter five, the numerical simulations of thermally treated recycled soda lime glass media were performed in two stages using uncoupled thermo-mechanical solidification analysis.

First, thermal analyses were created with the transient temperature of the solidification criteria taken into account. A parametric study was employed to determine the heat transfer coefficient of the specimen providing the best-fit numerical-experimental solidification measurements. Secondly, the thermal history obtained was used as an external force by means of a quasi-static mechanical analysis, using a well-known material model of elastic-viscoplastic constitutive law. The numerical analyses were verified by a comparison of experimental results obtained from X-ray diffraction analysis ($sin^2\psi$ method).

Chapter six, the area function of the Berkovich indenter was determined from continuous stiffness measurement (CSM) Berkovich nanoindentation tests with fused silica. FEM simulations were developed in order to aid determination of tip radius curvature and inclination angle distortion. The area function was analysed using experimental data coupled with FEM, and the deviation from the perfect Berkovich geometry was established. The outcomes are important for material characterisation of thermally treated glass designed for mass finishing processes

Chapter seven, the effect of variation in the tip geometry of the Vickers hardness stylus on the determination of contact area in instrumented microindentation tests were analysed and compared with different theories. This concentrated on the development of an inverse FEM approach to the microindentation test based on the parametric study technique. The newly proposed method, employed a 3-D optical Profilometer image processing technique to determine the contact area. Results are compared with the contact area determined through the Martin & Oliver method (actual indenter geometry from load displacement analysis), the Oliver & Pharr method (perfect indenter geometry), and a numerical approach which determines the contact area using the actual indenter geometry derived from FEM analysis. The accurate measurements are important in material characterization and fracture analyse.

Chapter eight, 2-D and 3-D axisymmetric FEM of four commonly used indenters in nano- and microindentation processes (Berkovich, Vickers, spherical, and conical) were developed. At each indentation process, the influences of a variation in sample size, tip geometry, frictional condition, mesh density sensitivity and material properties on the force displacement curves during the loading and unloading stages were determined using parametric studies. The convergence solutions resulting in optimum modelling parameters were established. The effect of projected area of different indenters on the predicted material properties were investigated; results were then compared to examine the effect of using different indenter geometries.

Chapter nine is mainly focused on a new approach of using inverse FEM accompanied with an optimization algorithm to obtain and optimize the elastic plastic properties (E, σ_y, n, ν) and Draüker-Prager material properties (E, σ_{yc}, β). The framework established would help to develop an approach for characterising complex material systems such as thermally treated glass. The new approach consists of three parts: in the first part an inverse FEM of continuous indentation of axisymmetric and 3-D commonly used indenter geometries were developed. The second part, an inverse program FEM interfaced with a non-linear MATLAB optimization algorithm was developed based on the load displacement results of single and dual indentation data of predefined material properties. In the third part, after a feasibility study and validation of combined FEM and optimisation algorithm with a wide range of material properties, the proposed method was applied to actual experimental load displacement curves for a range of thermally treated recycled glass material.

Chapter ten established an FEM method for detailed analyses of the stress intensity fields coupled with fracture toughness of both median and Palmqvist cracks during Vickers indentation of the brittle materials. The superposition technique was employed to determine the stress intensity factor (K) using dimensional analysis in order to establish the relationship between the material properties and different crack geometries and polar coordinates during the induced fracture. The results are also compared with the experimental cracking models developed by previous researchers. The proposed method was then applied to actual experimental load displacement curves for a range of thermally treated recycled glass material.

Chapter eleven, the first section focused on the evaluation of the machining performance of the new glass media compared to that of conventional media using a vibratory mass finishing process. The evaluation analyses were extended to include the on-site industry tests using turbine fan blades.

Performance measures used on-site were surface roughness (Ra), brightness and cycle time. The study was extended to include the effects of liquid compound solutions. The second area of this study focussed on the on-site comparative analysis of advanced mass finishing processes (disc centrifuge, drag, and stream) using conventional media. A series of experiments were developed over a wide range of manufacturing process conditions including various machining process and work material.

Chapter twelve, a new design of work holding for the mass finishing system is proposed in order to hold the part in free rotation within the media whilst reducing or removing the risk of shard generation. This design has been developed to provide a readily constructed portable and low-cost solution in order to carry the parts horizontally within the trough while allowing for variation in immersion depth and variation in position throughout the longitudinal or transverse directions in the vibratory trough machine. It is also hypothesised that work holding (jig arrangement) will result in improved process efficiency and this is to be evaluated as part of the work.

Chapter thirteen, discusses the development and optimization of the discrete element method (DEM) of bulk flow of thermally treated conical glass media in a vibratory finishing process. The predicted results were compared with experimental measurements of average flow velocity, bulk expansion, and vertical and horizontal velocity distribution along the horizontal axis of a vibratory finishing machine. The individual particle velocity measurements in the bulk flow were determined using particle image velocimetry adapted with MATLAB code (PIVLab).

Chapter fourteen, on the development of a software tool that is able to predict cycle efficiency over a wide range of parameters and identify an optimal set of parameters one should employ to deliver any stated target criteria. This information can then readily be extrapolated to give production cost.

Additionally, the system will also predict cost and efficiency when parameters are modified in any way and predict the consequence on achievable quality. This system was developed as an optimization tool and called process optimization system (POSY). POSY was applied to the advanced mass finishing applications: drag and stream finishing.

1.1.6   Scope of the thesis

The scope was constrained to the study of recycled glass supplied by Potters-Ballotini Ltd (world's largest glass beads producer) and Vibraglaz UK Ltd. The thermal treatment of the glass was constrained to the furnace facility within LJMU and an outsourced gas kiln provided by Vibraglaz. The range of materials and conventional media investigated were reasoned to be sufficient to facilitate evaluation of comparative performance and media characterization. Performance and application were directed by partners in an associated funded project (TSB – 101275; Manufacturing Technology Centre, Rolls-Royce, Finishing technique Ltd, Glass Technology Services, Vibraglaz UK Ltd, Potters-Ballotini Ltd, and LJMU). However, the study brings together key global partners in the competitive arena of advanced manufacturing process, glass production, super-finishing and Research and Technology.

This research will fully establish the potential of thermally treated recycled glass for vibratory finishing applications. The benefits and performance capabilities of the new media will be established through a comprehensive programme of experimental and theoretical research. This resource efficient and sustainable innovation will result in a reduction in the manufacturing cost of mass finishing media and will also serve to reduce the environmental impact of preform manufacture. The work has potential to yield important outcomes for the mass finishing industry and for the larger global abrasives community.

CHAPTER TWO

MECHANICAL ANALYSIS OF INDENTATION TEST METHOD

2.1　Indentation technique and application in characterizing material

Indentation testing, in many cases referred to as hardness testing, has for a long time been considered as a standard method for material characterization. Usually, the indenter of the hardness test instrument is made of diamond or any hard material such as tungsten carbide, which during the loading stage is pressed into the surface of material and force displacement data is used to represent the resistance of the material. In elastic-plastic (e.g. metal), brittle (e.g. ceramics, glass), materials the permanent indentation formed can be measured to represent the indentation resistance (i.e. hardness of the material) Giannakopoulos and Larsson (1997), while in a soft material (e.g. rubber, foams), the hardness of the material is measured by the indentation depth under load, Ren X. J. (2001). However, indentation hardness can be affected by many factors such as experimental environments, mechanical and physical properties of materials and indenter geometry. These factors should be carefully considered when using the indentation technique in material characterization.

The most important advantages of indentation hardness is that it only needs a small sample of material for properties identification, where a specimen is not available in standard size, such as in brittle or vivo test Youn and Kang (2005) , Delalleau, Josse et al. (2006). Moreover, the indentation technique is normally used in non-destructive testing procedures in research and industry because it offers an inexpensive and easy process for the development and evaluation of a new material.

The new approach of instrumented indentations is being widely used to search for the mechanical properties of material using the dynamic response technique Taljat, Zacharia et al. (1998). In such a technique, a continuous monitoring of the load displacement data and the indentation resistance of the material is represented by the loading unloading curve rather than a single value. The loading curve can be used to represent the resistance of the material over a selected interval of indentation depth; therefore this approach provides a more reasonable representation of the loading condition in service. This could be a unique advantage of continuous indentation over static indentation tests. The further levels of control, data acquisition and sensitivity, obtainable by instrumented indentation systems have resulted in numerous advances in materials properties characterization.

A number of studies have used continuous indentation to study the loading and unloading response of a wide range of material systems . The nanoindentation technique has been established as instrumented indentation, which is considered as a powerful tool for characterizing the mechanical properties of materials; this technique depends on high accuracy instruments that continuously monitor the loads and displacements of the indenter, usually a Berkovich type. Gong, Miao et al. (2004) employed the Nanoindentation technique with a Berkovich indenter to characterize three typical brittle materials, including a commercial soda-lime glass.

The indenter geometry is one important factor for indentation testing. Several types of indenters which are commonly used in the indentation process include pyramidal shape, conical shape and spherical shape indenters. The hardness of a material system is changed according to the indenter shape. There are five principal standard test methods for expressing the relationship between hardness and the size of the impression, these being, Vickers hardness, Berkovich hardness, Knoop hardness, Rockwell hardness and Brinell hardness testing. The following provides detail on these indentation systems.

2.1.1 Vickers hardness test

The Vickers indenter is a square based diamond pyramidal-shape, which has an angle of 136 degrees between the faces and diagonals ratio of 1:1 as shown in Figure 2.1. The Vickers hardness number is one of the most widely used measures of hardness in engineering and materials science. The Vickers hardness, H_V, is calculated using the indenter load F and the diagonals, d of the impression area left in the surface of the specimen after the indenter is removed. A microscope connected with the hardness instrument is used to measure the average value of d. The resulting quantity is usually expressed in, kgf/mm^2.

Where F is load in kgf, and d is the mathematical expression of the two diagonals, $d1$ and $d2$ and H_V represents Vickers hardness

$$H_V = \frac{2F \sin\frac{136}{2}}{d^2} = 1.854\frac{F}{d^2} \qquad (2.1)$$
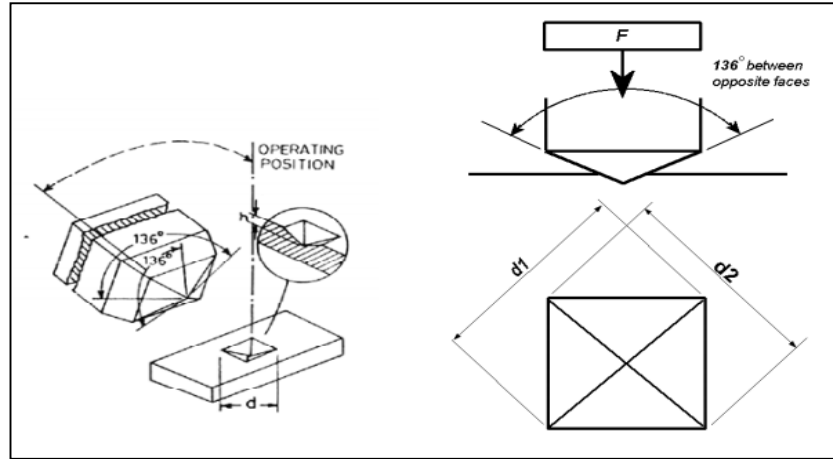
Figure 2-1 Schematic showing Vickers indentation test and impression

2.1.2 Berkovich indenter

The Berkovich indenter shape is commonly used for instrumented nano-indentation tests to measure the mechanical properties on the nano scale. The indenter has a three sided pyramid shape with the face angle of 65.3° as is shown in Figure 2-2. The Berkovich indenter tip has a large included angle of 142.3°, which minimizes the effect of friction between the tip and the specimen. The Berkovich hardness is calculated using the maximum indentation load F and the projected contact area A_{proj} of the surface impression. The projected contact area of the perfect indenter is calculated as follows (Eq.2.7)

$$tan60^o = \frac{l}{a/2} \equiv l\frac{\sqrt{3}}{2}a \tag{2.2}$$

$$A_{proj} = \frac{al}{2} \equiv \frac{\sqrt{3}}{4}a^2 \tag{2.3}$$

$$cos65.3^o = \frac{b}{h_c} \tag{2.4}$$

$$h_c = \frac{acos65.3^o}{2\sqrt{3}sin65.3^o} \tag{2.5}$$

$$a = 2\sqrt{3}h_c tan65.3^o \tag{2.6}$$

$$\therefore A_{proj} = 3\sqrt{3}tan^2(65.3^o)h_c^2 \approx 24.65h_c^2 \tag{2.7}$$

$$H_b = \frac{F}{A_C} \tag{2.8}$$
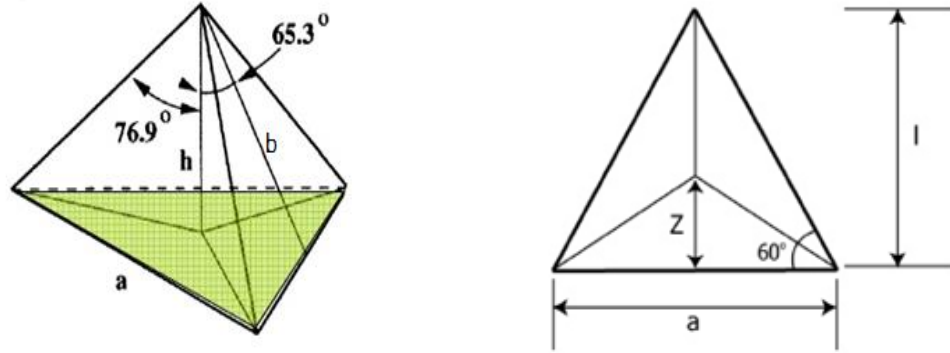
Figure 2-2 Schematic showing Berkovich indentation test: a) Indenter tip geometry with face angle 65.3^0, and b) Top view of projected area

2.1.3   Knoop hardness

Knoop indentation testing is generally used for the microhardness test scale. This technique is usually used for a brittle material with a small material thickness such as ceramic which requires a small indentation load, and for metallic material and plastic. The Knoop indenter has a four sided pyramid shape, with the angle between two of the opposite faces of $170°$ and the angle between the other two being $130°$ as shown in Figure 2.3. The indentation impression of the diamond shape produces a ratio between long and short diagonals of approximately 7: 1 and the short diagonal is about 4:11 times indentation depth. The long diagonal 'l'of the indentation is measured directly from the instrument. The short diagonal, w is calculated by Eq. 2.9

$$w = \frac{l\tan(130^o/2)}{\tan(172^o/2)} \tag{2.9}$$

The knoop indentation projected area $A_{(proj)k}$ is given by;

$$A_{(pro)k} = \frac{wl}{2} = \frac{l^2\tan(130^0/2)}{2\tan(172^0/2)} \tag{2.10}$$

The knoop indentation hardness, H_k is given by:

$$H_k = \frac{F}{Cl^2} \tag{2.11}$$

Where $C= \tan(130^o/2)\,/2\,\tan(172^o/2) \approx 0.07028$
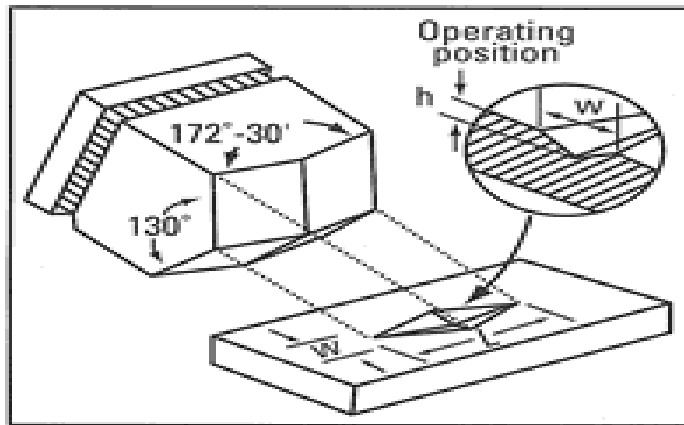
Figure 2-3 Schematic showing Knoop indentation test with face angle

2.1.4 Rockwell hardness

The Rockwell hardness test method characterises the indentation hardness of test materials with a diamond cone or spherical indenter. The indenter is loaded onto the test material under a minor load until a balance has been achieved, which is followed by movements of the indenter under a major load and the change in penetration depth of the indenter is compared, with reference to a datum position. When equilibrium has again been achieved, the added major load is removed but the initial minor load is still maintained. A partial recovery is developed due to removal of the additional major load, resulting in a reduction of the penetration depth. The permanent increase in depth of penetration, resulting from the initial load and removal of the additional major load is used to calculate the Rockwell hardness number given by Eq. 2.12.

$$HR = E - e \qquad (2.12)$$
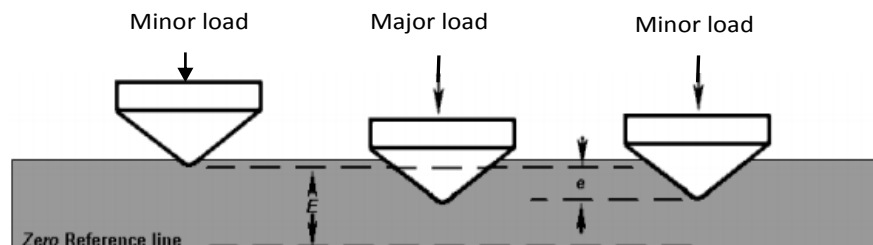
Figure 2-4 Schematic showing Rockwell hardness test

2.1.5   Brinell hardness

The Brinell hardness test method characterises the indentation hardness of the test material with a spherical indenter typically 10*mm* diameter, D, of carbide or hardened steel pressed using 30 *KN* force, f , for a period of 10 to15 seconds in the case of steel , 30 seconds and above in the case of other metals. For softer material, the indentation force can be reduced to 15 *KN* or 5 *KN* according to specimen material to avoid unnecessary indentation force. The diameter, d of the impression area left in the surface of the specimen after the indenter is removed is measured with a low powered optical microscope. The Brinell hardness number is calculated by dividing the force applied by the projected spherical surface area of the indentation tip.

$$H_B = \frac{2F}{\pi D(D - \sqrt{D^2 - d^2})} \tag{2.13}$$
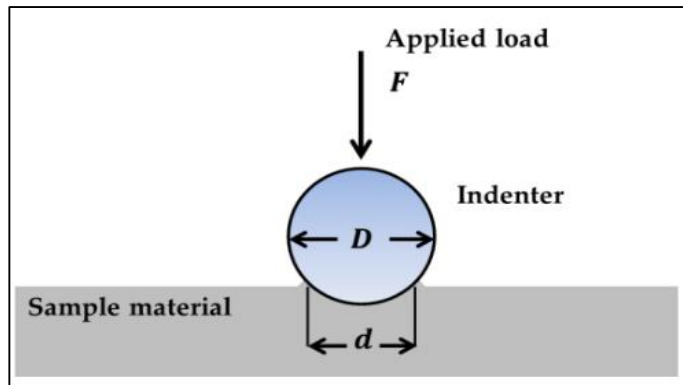
Figure 2-5 Schematic showing Brinell hardness test

2.2   Indentation data analysis

2.2.1   Tabor method (1948)

Indentation experiments using depth-sensing technique were conducted by Tabor (1948) to analyse the residual imprints using a profilemeter whose radius was bigger than the radius of the spherical indentation tip. The results show that the impression diameter did not recover during the unloading stage, while the indentation depth reduced significantly. The results also show that the second indentation process of the indenter under the previous load did not change the size and shape of imprint, confirming that the unloading stage is purely elastic and can be described by Hertz theory.

Thus, the elastic properties were extracted for materials exhibiting elastic plastic behaviour under deformation. Tabor introduced the following relationship to determine the representative strain.

$$\epsilon \approx 0.2 \, \frac{a_c}{R} \tag{2.14}$$

Where ϵ is the representative strain, a_c is the contact radius and R is the tip radius

2.2.2   Bulychev method (1975)

Based on the previous study made by Tabor and a contact law proposed by Sneddon (1948), Sneddon (1965), and Bulychev (1975) suggested an experimental procedure allowing the calculation of the reduced Young's modulus (Eq. 2.15). The proposed model is based on the contact stiffness, S, which is a function of the reduced modulus, *Er,* and projected contact area, *A*.

$$S = \frac{dP}{dh} = \frac{2}{\sqrt{\pi}} Er \sqrt{A} \tag{2.15}$$

where S = *dP/dh* is the experimentally measured stiffness of the upper portion of the unloading curve. Thus, the reduced modulus can be derived by measuring the initial unloading stiffness and assuming that the contact area is equal to the optically measured area of the hardness impression. Bulychev also demonstrated that the model given by (Eq. 2.15) is not only valid for a conical indenter, but also for spherical and cylindrical indenters. Though, Bulychev successfully measured the experimental stiffness of tested materials, he was able to relate the determined stiffness to the reduced modulus only, due to the difficulties preventing him from accurately determining the projected area.

2.2.3   Doerner and Nix method (1986)

Based on the stiffness equation proposed by Bulychev (1975) and the limited changes in contact area occurring during the early stage of the unloading curve. Doerner and Nix (1986) suggested that the indentation contact performs similarly to a flat cylindrical punch indentation in the beginning of the unloading phase (i.e. linear performance of the initial

portions of unloading curves). As previously stated, the accurate determination of the indentation contact area is the crucial factor in the calculation of contact stiffness.

Doerner and Nix (1986) proposed that the projected contact area (A) is a function of the contact depth (h_c), which is defined as the contact distance along which contact is made Figure 2-6 given by Oliver and Pharr (1992).

$$A = f\ (h_c) \tag{2.16}$$

The method developed to determine the contact area function is based on the extrapolation of the initial linear part of the unloading curve to the displacement axis. However, the extrapolated depth is used together with the indenter shape function to determine the contact area which allows for a better estimation of the contact area rather than the final indentation depth (h_f) or the maximum indentation depth (h_{max}) as is shown in Figure 2-6. The method developed by Doerner and Nix was considered as the first time elastic properties of materials could be extracted from nanoindentation experiments.
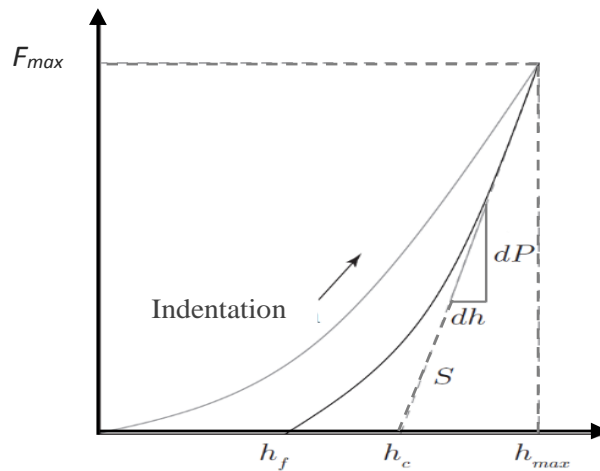
Figure 2-6 Typical load displacement curve Oliver and Pharr (1992)

2.2.4   Oliver and Pharr (1992)

Oliver and Pharr (1992) demonstrated that the contact stiffness model proposed by Bulychev (1975) is valid for any axisymmetric indenter. Further observation proved that the initial part of the unloading phase, originally considered as linearly by the Doerner-Nix method, would better be fitted by a power law expression given by Eq. 2.17.

$$F =\ \alpha h^m \tag{2.17}$$

where F is the indenter load, h is the elastic displacement, α and m (1.2 to 1.6) being constants relative to the indenter tip shape. The slope of this expression at maximum indentation load is defined as the contact stiffness.

The proposed power law presumes that the change in the contact area will occur during the unloading stage. Oliver and Pharr developed new area functions that better predicted the projected area using contact depth, *hc*, for different indenter tip geometries, which is defined by Eq. 2.18.

$$h_c = h_f - \epsilon \frac{F_{max}}{S} \qquad (2.18)$$

where ϵ is indenter geometry constant related to indenter tip shapes (0.72 for conical, 0.75 for spherical, and 1 for flat punch). The new method improved contact stiffness, and the projected area function were further enhanced the determination of the indentation elastic modulus using the contact stiffness equation. This method assumes purely elastic contact and perfect indenter tip geometry. The Oliver and Pharr model improved the Doerner and Nix (1986) method , and is still widely used as the standard model for extracting elastic materials properties from indentation tests.

2.3   Instrumented indentation test (IIT)

Instrumented indentation technique, also called depth-sensing testers are high precision instruments used for the characterisation of the mechanical properties of thin films, substrates, and coatings. The mechanical properties such as elastic modulus and hardness can be obtained for a wide range of material systems including ceramics, Polymers, metal and biological materials Fischer-Cripps (2005). The instrumented indentation systems offered additional levels of control, sensitivity, data acquisition, and full recording of load displacement data during the loading and unloading stage which makes this method more advanced in materials science applications . The typical principles of instrument operation are as follows: the indenter tip is normally driven into the specimen surface by applying and increasing force up to a predefined value, the force is then gradually released until partial or complete relaxation of material occurs. This instrument is capable of applying loads from the micro-newton range and measuring the displacement in the nano-metre range with high accuracy and resolution with ignoring the phenomenon of thermal drift which adds a false factor in the displacement signal yields.

Erroneous results especially occur in the low load and low indentation measurements. Another important issue is that, this method is able to sense when an indentation is performed and record the incremental increases in the depth causes by the indentation load.

The loading stage of instrumented indentation results usually follows Kick's law which is given by the following expression,

$$F = Ch^2 \tag{2.19}$$

where F, is the indentation load, h, is the indentation depth, and C, is a constant curvature of loading and unloading stages. Giannakopoulos, Larsson et al. (1994) proposed that the Kick's law model can be fitted with the data obtained from numerical simulations of elastic–perfect plastic and elastic–plastic materials. Larsson, Giannakopoulos et al. (1996) reported that the indentation force results obtained from the FEM using sharp Berkovich indentation on an elastic material is given by

$$F = 2.1891(1 - 0.21v - 0.01v^2 - 0.41v^3)\frac{E}{1 - v^2}h^2 \tag{2.20}$$

Moreover, for elastic plastic material the indentation force in the loading stage is equal to:

$$F = \frac{1.273}{(tan24.7^o)^2}\left(1 + \frac{\sigma_u}{\sigma_y}\right)\left(1 + ln\frac{E\,tan24.7^o}{3\sigma_y}\right)\sigma_y h^2 \tag{2.21}$$

The projected area of Vickers, conical, and Berkovich indenter geometry can be expressed with linear relationships between penetration depth, h, and contact radius Eq. 2.22

$$A_{proj} = kh^2 \tag{2.22}$$

where k, is a constant for a particular material and indenter geometry. The evaluation of the projected area should be calculated carefully which requires an accurate knowledge of the surface deformation stage, where errors can be introduced in the estimation of the projected area if the material piling-up and sinking-in is not taken into consideration. However, Oliver and Pharr (1992) developed a new method to determine the projected contact area by analysing the loading and unloading curves using an instrumented indentation mechanism Figure 2-6.

From the load displacement curve the maximum indentation force, F_{max}, maximum indentation depth, h_{max}, and residual depth h_f, can be measured (i:e the final depth after the indenter released and material relaxation is complete).

The other mechanical properties which it is possible to determine from the load displacement curve such as: material stiffness from the initial unloading slopee *dp/dh* at maximum indentation depth, total work done by maximum indentation load during the loading mode W_t, elastic work after the indenter is released in unloading mode, W_e , and the plastic work can be calculated using $W_p = W_t - W_e$.

Based on the load-displacement curve the material hardness can be calculated using average contact pressure P_{avr} , which is equal to maximum indentation force divided by true projected area. The effect of material properties on the load displacement curves has been studied by many researchers Oliver and Pharr (1992), Pharr, Oliver et al. (1992), Taljat, Zacharia et al. (1998), and Dao, Chollacoop et al. (2001) . These studies have concluded that the unloading stage is mainly influenced by the Young's modulus '*E*' which depends principally on the material stiffness. They also demonstrated that the loading part is influenced by the yielding strength 'σ_y' and strain hardening '*n*'.

2.4   Mechanical properties of indentation elastic plastic material

Since 1948 indentation techniques have been performed for measuring the mechanical properties including hardness of a wide range of material systems Tabor (1948). The need for measuring mechanical properties such as elastic modulus *E*, yield stress σy, and strain hardening *n*, of small scale material from load *vs* displacement curves, increases the interest in the indentation process. The development of micro and nano indentation equipment enhanced the possibility for monitoring with high accuracy force and indentation displacement during the whole indentation experimental cycle Pethicea, Hutchings et al. (1983), Bhushan and Koinkar (1994). Finite element methods have also been conducted to extract the mechanical properties of materials by determining the best fit numerical loading and unloading curves with the experimentally measured ones Bhattacharya and Nix (1988), Laursen and Simo (1992), Bolshakov and Pharr (1998).

Cheng and Cheng (1999) employed a dimensional and finite element method to analyse load-displacement data using a simple scaling relationship for indentation of elastic plastic and elastic perfectly plastic material. These scaling relationships provide a useful interpretation tool for the results of hardness, contact area, elastic, and plastic properties of solids obtained by instrumented indentation techniques including nano and micro

indentation measurements. In general, the uniaxial stress-strain relationship can be expressed as:

$$\sigma = \begin{cases} E\varepsilon, for\ \sigma \leq \sigma y \\ K\varepsilon^n, for\ \sigma \geq \sigma y \end{cases} \tag{2.23}$$

where E is the Young's modulus, K is the yield strength coefficient, n is the strain hardening exponent, σy is the initial yield stress and ε is the equivalent yield strain. The yield stress at the zero offset strain is equal to:

$$\sigma y = E\varepsilon = K\varepsilon^n \tag{2.24}$$

The true stress-true strain behaviour of an elastic plastic material has been developed by (Swaddiwudhipong, Tho et al. 2005) to be

$$\sigma = \begin{cases} \sigma y = E\varepsilon, \quad for\ \sigma \leq \sigma y \\ \sigma y = \left(\dfrac{E}{\sigma y}\right)^n \varepsilon^n, for\ \sigma \geq \sigma y \end{cases} \tag{2.25}$$

The fundamental principles for the dimensional analysis method can be introduced as follows. Firstly, the dependent variables should be selected and the independent dimensions should be then identified which contain all independent variables and parameters. Secondly, the dimensionless variables are created; thus the relationships among dimensionless variables can be formed.

2.4.1 Dimensional analysis of loading curve

The variables which change during the loading curve can be considered as dependent variables including indentation force, F, and contact depth at maximum indentation load, h_c, the number of relationships is related to the number of dependent quantities Figure 2-7.
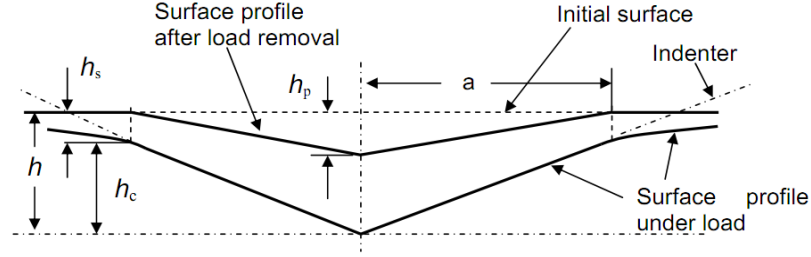
Figure 2-7 Schematic diagram of the indentation surface profile at loading and unloading stage Oliver and Pharr (1992)

The two dependent variables, F, and h_c, should be a function f_l, k of six independent governing parameters Young's modulus (E), initial yield stress (σy), work-hardening exponent (n), Poisson's ratio (v), the angle of indenter (θ), and indentation depth, h. Since the variables of n, v, and θ have no dimensions, then E or σy can be chosen, E and h_{max} are selected as the dominant parameters for dimensional analysis. Those can be expressed by the following:

$$[E] = [\sigma y], \ [F] = [E][h]^2, \ [v] = [E][h], \ [\theta] = [E][h], \ [n] = [E][h], \ [h_c] = [h]$$

Therefore, the load F and h_c for the loading curve stage can be expressed by:

$$F = f_l(\sigma y, E, n, v, h, \theta) \tag{2.26}$$

$$h_c = k\ (\sigma y, E, n, v\ h, \theta) \tag{2.27}$$

The Buckingham π theorem is applied in dimensional analysis Barenblatt (1996) as follows: The indentation force can be expressed as:

$$\pi_\alpha = \pi_\alpha(\pi_1, v, n, \theta), \text{ or equal to, } F = Eh^2 \pi_\alpha \left(\frac{\sigma y}{E}, v, n, \theta\right) \tag{2.28}$$

Where $\pi_\alpha = \frac{F}{Eh^2}$ and $\pi_1 = \frac{\sigma y}{E}$

The contact depth can be expressed as:

$$\pi_\beta = \pi_\beta(\pi_2, v, n, \theta), \text{ or equal to, } h_c = h\pi_\beta \left(\frac{\sigma y}{E}, v, n, \theta\right) \tag{2.29}$$

Where $\pi_\beta = \frac{h_c}{h}$ and $\pi_1 = \frac{\sigma y}{E}$

Based on the above dimensional analysis of the loading stage, the indentation force, F is proportional to the square of the indenter displacement, h.

The contact depth , h_c is proportional to the indenter displacement, h, and the depth ratio h_c/h is independent of the indenter displacement. In the elastic perfectly plastic material properties, the same dimensional analysis of the loading stage can be used excluding the strain hardening.

2.4.2 Dimensional analysis of unloading curve

The unloading stage takes place after the loading stage when the indenter penetrates at the maximum depth, h_m. Therefore, the force, F, can be expressed as a function, of seven independent dominant parameters.

$$F = f_{ul}(\sigma y, E, n, v, h, hm, \theta) \tag{2.30}$$

The Buckingham π theorem is applied in dimensional analysis as following:

$$\pi'_\gamma = \pi_\gamma(\pi_1, \pi_1, v, n, \theta), \text{ or equal to, } F = Eh^2\pi_\gamma\left(\frac{\sigma y}{E}, \frac{h}{h_m}, v, n, \theta\right) \tag{2.31}$$

where $\pi_\gamma = \frac{F}{Eh^2}$, $\pi_1 = \frac{\sigma y}{E}$, and $\pi_2 = \frac{h}{h_m}$

Based on the above dimensional analysis of the unloading stage, the indentation force, F is proportional to the square of the indenter displacement, h, and the ratio of indentation depth h/h_m. The initial unloading slope *df/dh* can be measured by the derivative of indentation force with respect to indentation displacement at h_m; the initial slope is given by the following expression:

$$\frac{df}{dh} = Eh_m\left[\pi'_\gamma(\frac{\sigma y}{E}, v, n, \theta)\right] + \left[2\pi'_\gamma(\frac{\sigma y}{E}, v, n, \theta)\right] \tag{2.32}$$

$$\frac{1}{Eh_m}\frac{df}{dh} = \pi_\delta\left(\frac{\sigma y}{E}, v, n, \theta\right) \tag{2.33}$$

The above analysis shows that the initial unloading slope is proportional to h_m. Again, for the elastic perfectly plastic material properties, the same dimensional analysis of the loading stage can be used excluding the strain hardening.

2.4.3 Work done by indentation

The total work done can be calculated by integrating the load indentation curves, which is equal to the area under the curve. The total work done by the loading stage (area under loading curve) is integrated up to h_m and it causes an elastic plastic deformation as is given by the following term:

$$W_t = \int_0^{h_m} F dh = \frac{E h_m^3}{3} \pi_\alpha \left(\frac{\sigma y}{E}, v, n, \theta \right) \tag{2.34}$$

The total work done by the unloading stage (area under unloading curve) is integrated between the final indentation depth h_f and h_m as is given by the following term:

$$W_u = \int_{h_f}^{h_m} F dh = \frac{E h_m^3}{3} \pi_\delta \left(\frac{\sigma y}{E}, v, n, \theta \right) \tag{2.35}$$

The above analysis shows both loading and unloading curves are proportional to the cube of maximum indentation depth h_m^3.

The energy ratio $(W_t - W_u)/W_t$ for a complete loading-unloading cycle can be written as :

$$\frac{W_t - W_u}{W_T} = 1 - 3 \frac{\pi_\alpha \left(\frac{\sigma y}{E}, v, n, \theta \right)}{\pi_\delta \left(\frac{\sigma y}{E}, v, n, \theta \right)} \tag{2.36}$$

FEM has been created by many researchers to investigate the relationship between the variables in the loading and unloading stages and also the framework of the dimensionless functions. These scaling relationships established in section 2.4.1, and 2.4.2 provide an opportunity for systematic investigation of the relationship between experimental variables within a theoretical structure, which can lead to better understanding of indentation in elastic-plastic solids. Using Eqs. (2.28), and (2.29) the ratio of hardness to elastic modulus and hardness to initial yield stress is given by:

$$\frac{H}{E} = \frac{\cot^2 \theta}{\pi} \left[\frac{\pi_\alpha (\frac{\sigma y}{E}, v, n, \theta)}{\pi_\beta{}^2 (\frac{\sigma y}{E}, v, n, \theta)} \right] \tag{2.37}$$

or, equivalently

$$\frac{H}{\sigma y} = \frac{cot^2\theta}{\pi}\left[\frac{\pi_\alpha(\frac{\sigma y}{E}, v, n, \theta)}{\frac{\sigma y}{E}\pi_\beta{}^2(\frac{\sigma y}{E}, v, n, \theta)}\right]$$ (2.38)

Figure 2-8 shows the scaling relationship between the ratio of hardness to elastic modulus and hardness to initial yield stress. Cheng and Cheng (1999) demonstrated that the above two equations show that hardness, *H*, is independent of indentation depth *h* in the elastic– plastic solids which follows the material constitutive law Eq. (2.25).This conclusion is valid for both elastic- plastic solids (*n*> 0) and for elastic perfectly plastic solids (*n*= 0)
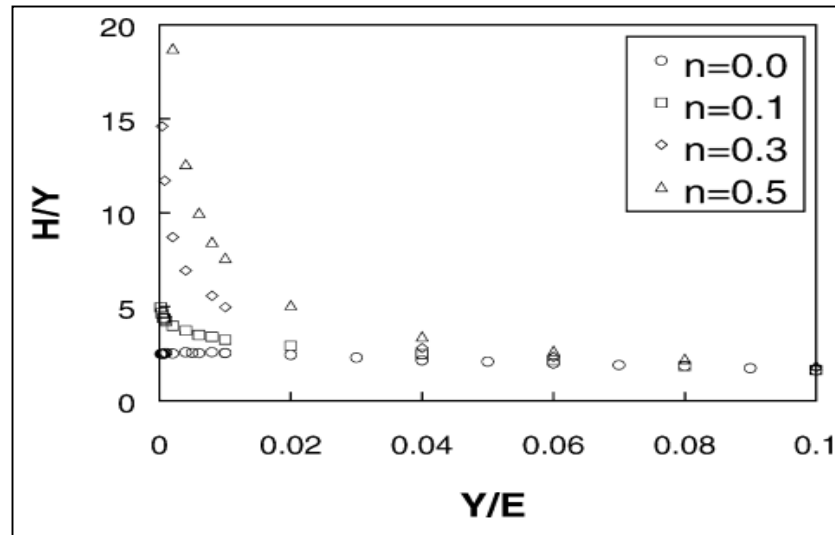
Figure 2-8 Scaling relationship between H/Y and Y/E for a number of values of n Cheng and Cheng (1999)

2.5 Glass deformation in an indentation process

The deformations of glasses as well as a wide range of crystalline ceramic and amorphous materials usually present an elastic behaviour up to failure. If the glass material is subjected to the tensile test, the critical crack will be initiated and propagated before any yielding condition. However, a high shear and compressive stress develops during the indentation resulting in failure and permanent deformation Evers (1967), Jahanmir (1993), and Lawn (1993). Commonly, two types of deformation are may take place, the first one is shear flow, which represents plastic deformation at constant volume (i:e volume conserving), the structural bonds are continuously being broken and reformed.

The geometry of the deformation zone, with the effect of the sharp indentation process shows that the impression volume is built up by the radial movement of the material and generates a hemispherical shape. This type of deformation occurs during the indentation of 'normal' glass types such as soda lime silica, lead alkali silica and alumina silicate glasses. Hagan (1980) reported that the plastic deformation of soda lime glass occurs due to the flow lines produced by shear displacements at the intersection points of some of the flow lines. Normal glasses can be used to represent the glasses with high thermal expansion coefficient, the pressure has a positive dependency on bulk modulus, with a negative dependency of bulk modulus on temperature Wiederhorn, Johnson et al. (1974) .

The second type of deformation is pressure-induced densification, which is based on the squeezing of the material structure and volume reduction. Spatial redistribution of the structural units occurs, where the displacement transformation of the individual units become closer (eg. SiO4 tetrahedral) resulting in a few bonds being broken Arora, Marshall et al. (1979) . This behaviour can be referred to as elastic more than plastic deformation. Thus, no shear flow developed and the original shape can be restored if enough energy is provided to the material for example by annealing to sufficiently high temperature as reported by Bridgman and Šimon (1953). The occurrence of such deformation is usually referred to as 'anomalous' glass such as vitreous silica and borosilicate glasses. Anomalous glasses can be used to represent the glasses with low thermal expansion coefficient, the pressure has a negative dependency on bulk modulus, and a positive dependency of bulk modulus on temperature Wiederhorn, Johnson et al. (1974), and Varshneya (2013).

Indentation methods with sharp indenters are considered the best technique to study the deformation of brittle material systems such as glasses, since the propagation of unstable cracks is prevented by high applied load. Hagan (1980) demonstrated that the plastic deformation in normal glass is due to high shear stress developed beneath the sharp indenter resulting in fault lines. The flow lines produced by the shear displacement can pile-up to create nuclei of median and radial cracks, if the indentation load reached a critical value. Based on the Hagan (1980) outcomes, the flow lines caused by shear displacement are not similar to those of metal material due to the densification effect, thus the lines intersect with another at 110° in glass, and 90° in metal.

The densification behaviour of anomalous glasses during the indentation process caused a blunting effect of the indenter tip geometry Lawn and Marshall (1979) resulting in stress generated around the indentation tip point similar to the Hertzian stress field generated beneath blunt indenters. This stress results in nucleation of cone cracks in addition to creation of some shorter median, lateral and radial cracks.

Figure 2-9 (a, and b) shows two images at different magnifications of the indentation deformation zone of normal and anomalous glasses where the cracks are highlighted out of the surface plane for the same glasses. Figure 2-9 (c) shows SEM image of normal glass, the flow lines related to the faulting deformation clearly appear within the deformation imprint producing median and radial cracks, and Figure 2-9 (d) shows the SEM image of anomalous glass, the densification phenomena is easily recognizable resulting in multiple cone cracking at high indentation loads.
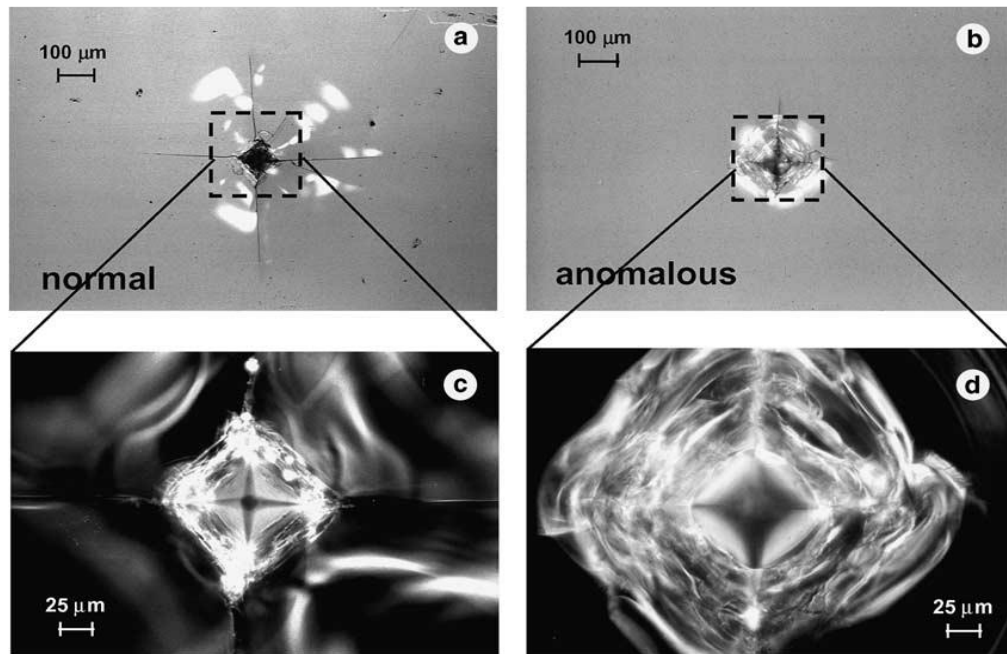
Figure 2-9 Magnification and SEM images of normal glasses (a , and c), magnification and SEM images of anomalous glasses (b, and d) Bertoldi and Sglavo (2004)

2.6   Pile-up and sink-in

During indentation of solid materials, a specimen's surface around the contact can be deformed either upwards or downwards; this material response is known as pile-up or sink-in as schematically shown in Figure 2-10.

For materials with a high ratio of final indentation depth, h_f, to the depth of the indentation at peak load, h_{max} such as metals, the plastic zone is a hemisphere with a radius larger than the contact radius. Most of the plastic deformation occurs near the indenter pushing additional material out of the normal specimen surface, but still within the plastic zone, to pile-up next to the indenter. However the vital material properties affecting pile-up are the ratio of the reduced modulus to the yield stress, E_r / σ_y, and work-hardening behaviour, n. For materials with a low ratio of final indentation depth, hf, to the depth of the indentation at peak load, h_{max} such as normal glasses, the plastic zone is generally controlled within the boundary of the contact radius. The surface is more likely to show sink-in behaviour with elastic deformations spread over a larger distance.
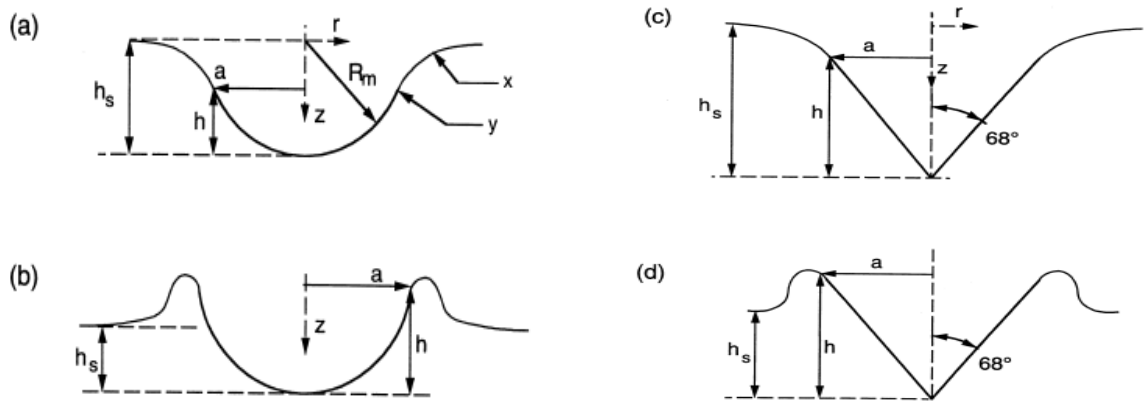
Figure 2-10 Schematic diagram of sinking-in (a, and c) and pilling-up (b, and d) of materials around spherical indents and sharp indents Alcala, Barone et al. (2000)

This piling-up or sinking-in of the specimen's surface must be taken into account when calculating the contact area. For a given contact depth, a surface with pile-up will have a larger contact area compared with material having sink-in behaviour. Oliver and Pharr (1992) investigated a wide range of materials numerically and experimentally to establish the relation between the normalized contact area and the experimental parameters such as, h_f / h_{max}. Two separate types of material were examined based on the work hardening value, the first case with no work hardening $n=d\sigma/d\varepsilon =0$, as in elastic perfectly plastic materials, the second case with strain hardening of $n=d\sigma/d\varepsilon =10\sigma_y$ as is shown in Figure 2-11.
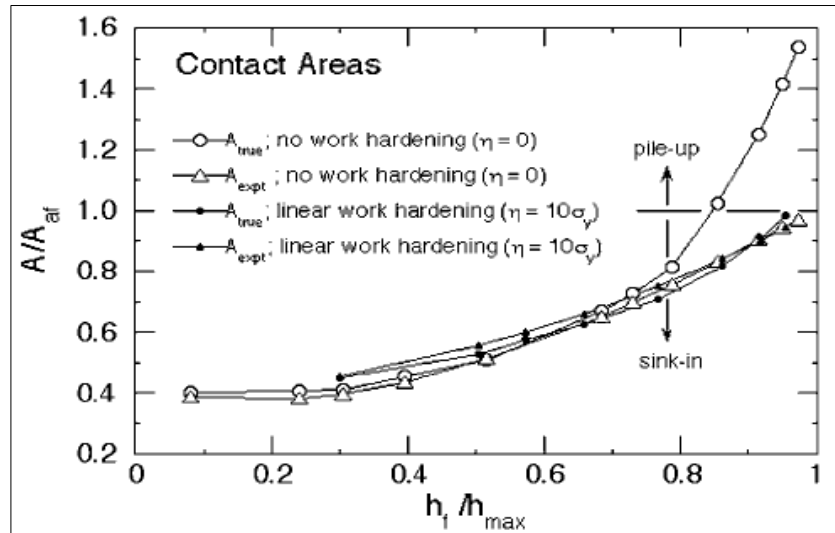
Figure 2-11 Comparison of numerical and experimental dependence of normalized contact areas on the experimental parameter h_f/h_{max} Oliver and Pharr (1992)

Two different contact areas were measured, the first one obtained directly from FEM mesh, A_{tru} , and the other one was obtained by applying the Oliver and Pharr (1992) method to the experimental load displacement data, A_{exp}. Both areas have been normalized with respect to, A_{af} ,the area given by the indenter area function measured at h_{max}, which normally takes place in the absence of piling up or sinking in. The comparisons between the numerical and experimental results shows that if A/A_{af}, is greater than 1 it indicates pile-up, while values less than 1 indicate sink-in. Moreover, when $h_f/h_{max} > 0.7$, the accuracy of the method depends on the amount of work hardening in the material.

2.7 Characterization of material properties by indentation tests

Determining the stress strain curve of a metallic and non-metallic material using simple hardness test is difficult, however this difficulty can be overcome by adapting an instrumented indentation test. Indentation load and depth sensing measurement of nano or micro scale are the most important technological tool for measuring the mechanical properties of material that only requires a small volume of structure and other material which may not be easily examined by normal tensile or compression test due to brittleness behaviour. This technique can be also used to track a small-scale mechanical reaction development of bulk material during its deformation process.

Wide ranging experimental, theoretical and numerical simulations have been focused on the mechanical properties characterization of material during the indentation test. FEM techniques have been used to compute very complex stress-strain fields of different material systems such as thin film or bulk materials in an indentation process. The first use of FE analysis for the indentation process was performed by Dumas and Baronet (1971), and Hardy and Baronet et al. (1972) and their FE analysis are in good agreement with the experimental results. Bhattacharya and Nix (1988) performed FEM of Al, Ni and Si to compare results with microindentation experimental tests, the comparison shows that using the continuum based FE approach; it is possible to simulate the load-unloading response during a micro and sub-micrometre indentation test. However, there are different methods used to extract material properties based on indentation tests which can be classified into two main approaches.

The first approach, forward and reverse analysis is performed based on load penetration-depth curves and reverse analysis, reported by various researchers Doerner and Nix (1986), Oliver and Pharr (1992), Dahmani, Lambropoulos et al. (1998), Cheng and Cheng (1999), Giannakopoulos A (1999) , Alcala, Barone et al. (2000), Dao, Chollacoop et al. (2001), Bucaille, Stauss et al. (2003), Bao, Wang et al. (2004), Sakai (2004), Tho, Swaddiwudhipong et al. (2004), Swaddiwudhipong, Tho et al. (2005), Ogasawara, Chiba et al. (2006), Shim, Oliver et al. (2007), Feng, Qu et al. (2009), Kang, Becker et al. (2012)

The second approach, inverse analysis is performed based on load penetration-depth curves and inverse analysis, reported by a number of researchers (Lichinchi, Lenardi et al. 1998, Cheng and Cheng 1999, Bolzon, Maier et al. 2004, Tho, Swaddiwudhipong et al. 2004, Tho, Swaddiwudhipong et al. 2005, Chen, Ogasawara et al. 2007, De Campos Velho, Ramos et al. 2007, Kang, Becker et al. 2012, Tikhonov, Goncharsky et al. 2013) .

2.7.1   Forward and reverse method

The forward analysis makes possible the prediction of indentation curves for a given set of material properties as an input data. The reverse analysis is used for the evaluation of material properties from the indentation curves. Different forward and reverse analyses have been associated to extract material properties during complete loading unloading curves.

Doerner and Nix (1986) developed a method for obtaining Hardness and Young's modulus from the data produced by the unloading microindentation test. Oliver and Pharr (1992) proposed a new technique for determining the Hardness and Young modulus's using the load displacement microindentation test. The accuracy of this method was validated for six materials exhibiting different responses. Dahmani, Lambropoulos et al. (1998) proposed the nanoindentation technique to determine the residual stresses development near laser-induced cracks in fused silica. Cheng and Cheng (1999) derived a set of scaling relationships for conical indentation into elastic perfectly plastic solids using dimensional analysis and finite element simulations. The results show that the force in the loading stage is proportional to the square of indenter displacement and the contact depth is proportional to the indenter displacement while, the initial unloading stage is proportional to indentation depth. Giannakopoulos, A (1999) suggested a new methodology to determine the elastic and plastic properties of materials using a unique relationships between penetration depth and true contact area taking into account the pile-up and the sink-in effects by employing instrumented sharp (i.e. Berkovich, conical, and Vickers) indenters. Alcala, Barone et al. (2000) measured the pile-up and sink-in of ceramics and metals around the imprint of spherical and Vickers micro-indenters in order to study the correlation between the uniaxial strain hardening exponent and the surface deformation under applied load and in the unloaded stages; it was found that the sinking-in was must dominate when the strain hardening increases.

Dao, Chollacoop et al. (2001) performed a large deformation finite element modelling to identify the elastic plastic properties of ductile materials using instrumented sharp indentation and to calculate the sensitivity and validity of such extracted mechanical properties for a wide range of measured indentation data. The analytical expressions were derived using dimensionless functions related to material properties, and elastic plastic finite element simulation; forward and reverse algorithms then established based on the identified dimensionless functions using numerical simulations as demonstrated in Figure 2-12. As is shown in Figure 2-12 the forward algorithms were allow the calculation of the indentation response for a given set of elastic-plastic properties, while the reverse algorithms enable the extraction of elastic-plastic properties from a given set of indentation data. A series of sensitivity analyses were performed for forward and reverse analysis; the results show a good agreement with experimental work for two types of examined materials, aluminium alloy (7075-T651 and 6061-T651 1).

The forward analysis shows the error in the predicted values to be less than $\mp\,0.6\%$ for the loading curvature profile, C, h_r/h_m, and stiffness, $S=df\,/\,dh$ at maximum indentation depth. The reverse analysis shows the predicted values of reduced modulus E_r, representative stress, $\sigma_{0.33}$, and average pressure, P_{avr}, is in good agreement with experimental results, while the predicted yield stress, σ_y, is reasonably accurate in some cases of indentation data. Based on the information provided by the reverse analysis, the value of, σ_y, and the strain hardening, n, can be determined, resulting in obtaining full uniaxial stress-strain response.

Ogasawara, Chiba et al. (2006) suggested that the representative plastic strain proposed by Dao, Chollacoop et al. (2001) is limited over a wide range of material properties and it is not associated with elastic or plastic deformations. Therefore, Bucaille, Stauss et al. (2003) proposed a large deformation microindentation numerical simulation in elastic plastic materials. The simulations were carried out accurately to determine the plastic properties of metals using a wide range of indenter-included angles. This method is also valuable to determine the value of the representative stress corresponding to a given representative strain depending on the included angle value of the sharp indenter. The outcomes from this work show that the accuracy of σ_y, n, and E increases with the use of Berkovich indenter and indenters having included angles equal to or lower than 70.3°.

Sakai (2004) used finite element simulations having different face angles to study the unloading stage behaviour of conical microindentation applied to numerous elastic plastic materials with predefined linear strain hardening. The analytical correlations between the hardness and reduced modulus exhibiting a wide range of plasticity were theoretically analysed and experimentally confirmed by Bao, Wang et al. (2004) based on Berkovich nanoindentation tests.

More recently, Tho, Swaddiwudhipong et al. (2004) developed a new method to extract the elastic plastic properties of materials obeying power law strain hardening during instrumented indentation tests using large deformation finite element analysis. This method investigated the effect of loading curvature C, yield stress σ_y, and the ratio of plastic work done to total work done (W_p/W_T) as a function of elastic plastic properties (E_r, σ_y, and n).

Swaddiwudhipong, Tho et al. (2005) presented a reverse analysis algorithm and FE simulation with dual indenters of microindentation load–indentation curves. It was demonstrated that accurate and unique elastic plastic material properties could be obtained from load displacement curves of two conical indenters with different apex angles. The uniqueness of the material properties based on dual indenters can be illustrated by the fact that the combinations of material properties resulting in the same indentation curve for one indenter will present different indentation curves for dual indenters. In another case, a reverse analysis technique to determine the elastic plastic material properties of a bulk material from the load displacement curve corresponding to only one conical microindentation test was developed by Ogasawara, Chiba et al. (2006).

Shim, Oliver et al. (2007) developed finite element simulations of 2D (conical) and 3D Berkovich indentation, the comparison of results shows minor differences at the maximum load and pile-up / sink-in behaviour of fused silica. Feng, Qu et al. (2009) proposed an analytical model which is validated with FE simulations, based on the so called embedded centre of dilatation (ECD) strength, to determine the stress field outside the plastic zone around a conical elastic plastic indentation. Matching the results of ECD with the expanding cavity model, provides analytical expression to predict the values of yield stress, and plastic zone radius.

The material properties predicted from reverse analysis of the loading and unloading curve can be affected by many factors. Firstly, the geometry of the indenter used in the numerical simulations has to be similar to that used in the indentation experiments. Therefore, for the indenters with blunting tips, the experimental indentation depth should be high enough to reduce the influence of the tip defect. Dao, Chollacoop et al. (2001) have shown that, there is a difference of 10% in the calculation of loading curvature for a Berkovich tip with a 10 degrees difference of inclination angle . This problem becomes particularly important for indenters with small inclination angles, due to the fact that tip geometry can be deformed much more easily. Secondly, the developed models may not accurately represent the force penetration curve during the loading phase over a wide range of material properties. This may be attributed to the fact that the load curvature C is influenced by many factors, such as indentation size effect resulting from load dependence hardness and indentation with a sharp indenter is not similar (Begley and Hutchinson 1998).

In conclusion, forward and reverse analysis methods can be considered as successful tools to estimate the material properties from the indentation test data, but there are many factors, such as the limitation from the wide-ranging finite element simulations, different indenter geometry, or material properties, that result in different functions between indentation test data and material properties. All such factors would affect the accuracy and sensitivity of the predicted results.
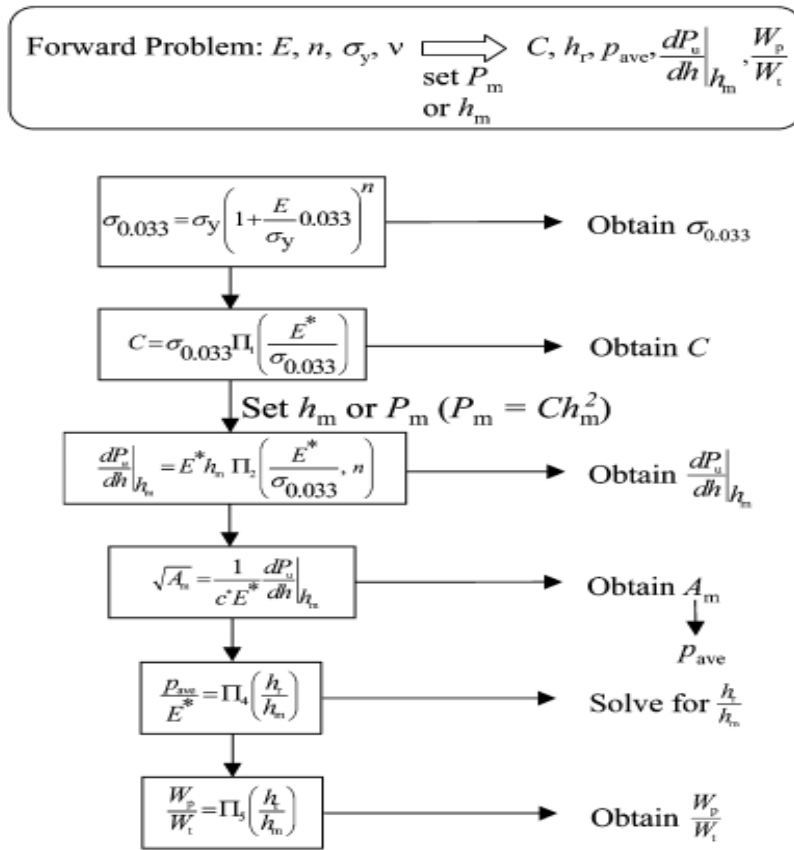
Chart 1: Forward Analysis algorithm
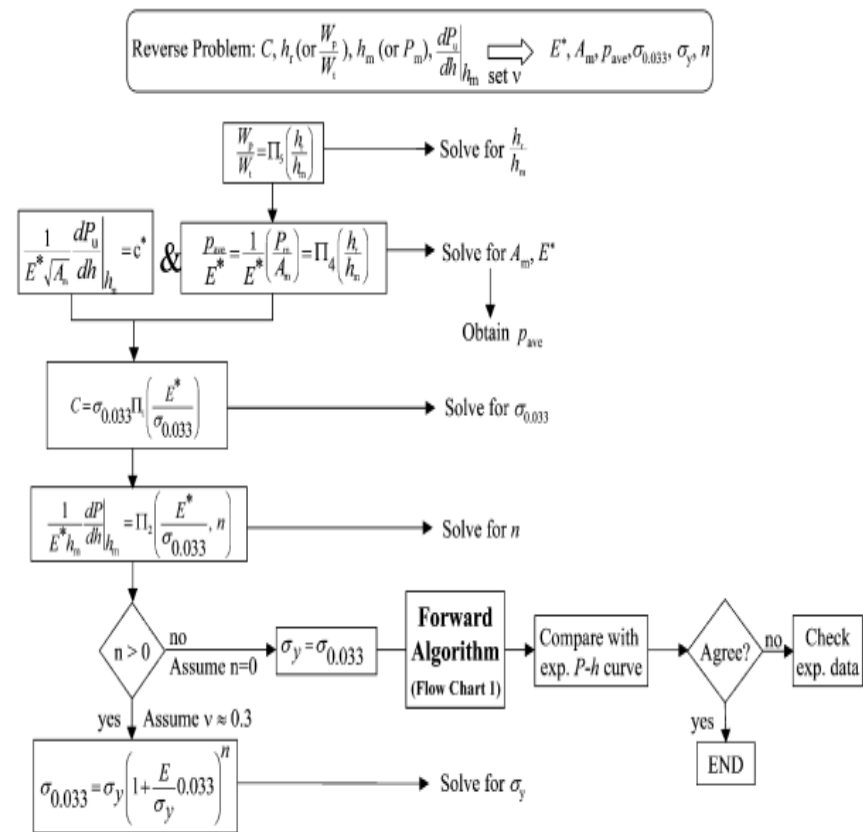
Flow Chart 2: Reverse Analysis algorithm

Figure 2-12 Flow chart showing typical procedures in forward (a) and reverse (b) algorithms Dao et.al, (2001)

2.7.2   Inverse FEM method

Inverse modelling has been widely applied in different subjects of engineering fields. Engineering mechanics is one of the important inverse problems applications which is focused on mathematical and computational aspects of inverse problems, system identification, shape determination, material property characterization, optimization processes, sensitivity analysis, destructive and non-destructive testing, thermal inverse problems, and other engineering applications (Tanaka and Dulikravich 1998). A successful programme for predicting a material parameter has to be accurate, efficient and robust and this depends on the experimental method used the inverse program, and optimisation method.

Direct measurements of unknown parameters can be difficult for a complex material and structural system. However the unknown variables can be estimated using inverse measurement of other influential parameters. Inverse finite element modelling is a combined numerical and experimental approach; the experimental results of load displacement are used as input data to FEM to predict the unknown material parameters. This approach can be searched for a wide range of input parameters until optimization is achieved. A technique of standard least squares is a reliable solution used for material property reconstruction, but could be unstable because the noise generation is a permanent feature in experimental data meaning that uniqueness and stability of such inverse solutions cannot be assured. In order to assure a final solution that is stable and physically acceptable, some previous information of material properties must be added to the quadratic difference term De Campos Velho, Ramos et al. (2007). According to Tikhonov and Arsenin (1977), ill-posed problems can produce stable solutions if sufficient previous information about the true solution is available. Such information is added to the least squares optimization by means of a quadratic difference term, in order to complete the solution for the inverse problem.

Figure 12-13 shows the typical procedure of inverse FE method. In this process a coupled FEM and optimisation algorithm is used to find the values of optimal parameters for a set of target variables, which produces the best-fit numerical and experimental results (minimum objective function). As displayed, the FEM is repeated with changing of material properties until convergence is achieved resulting in optimal material properties.
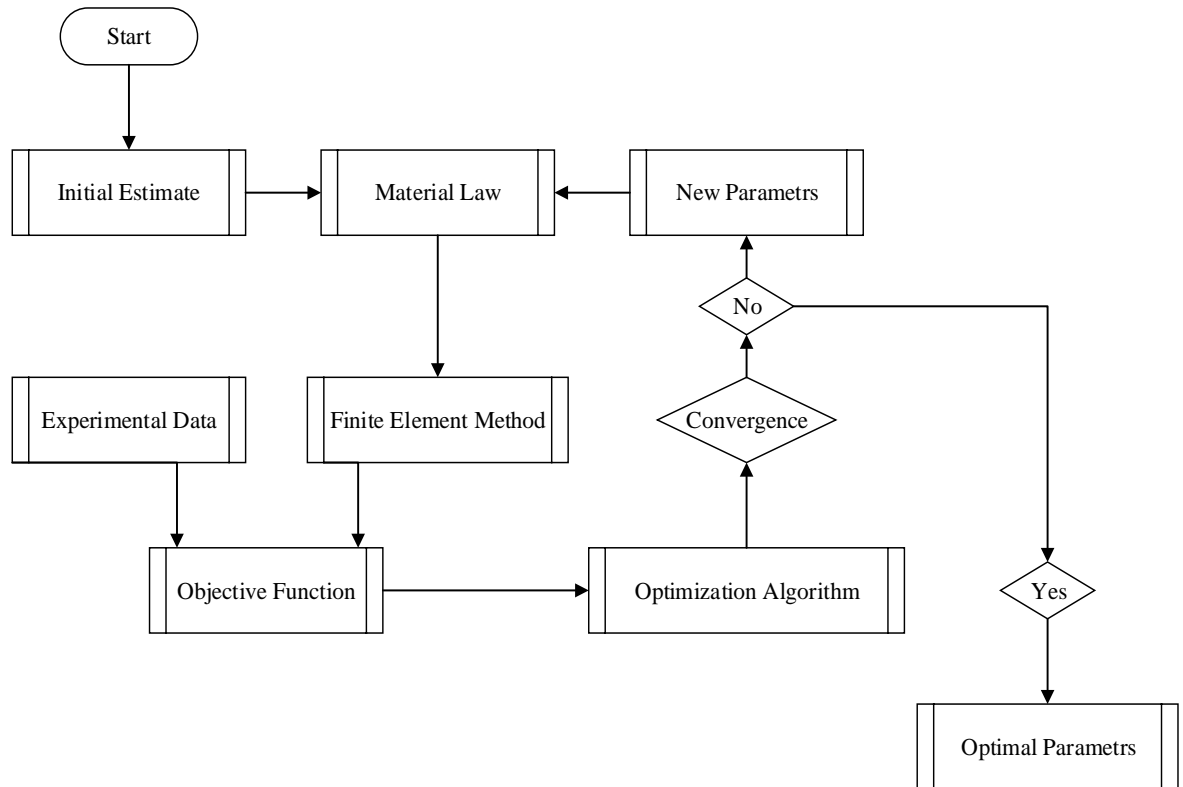
Figure 2-13 Flow chart showing procedure for inverse FEM solution

Lichinchi, Lenardi et al. (1998) found that the load-displacement curves from FE simulations using axisymmetric conical shape and 3D numerical models with Berkovich indenter and experimental data of nanoindentation measurement performed on titanium nitride on high-speed steel material system are generally in good agreement. Cheng and Cheng (1999) performed scaling relationships using numerical simulations for single conical indentation in elastic plastic material with strain hardening. The results show a range of calculated loading unloading curves matches uniquely with experimental results, which can produce multiple stress–strain curves for a given set of loading and unloading curves (i:e cannot uniquely determine tensile stress–strain relationships).

Tho, Swaddiwudhipong et al. (2004) developed a large deformation and large strain inverse FEM using two conical indentations system to investigate the relationships between the characteristics of the loading unloading indentation curves and elastic-plastic material properties, the elastic strain ratio (E_r / σ_y) ranging from 60 to 1000 and strain hardening (n) change from 0 to 0.6. The relationships between the curvature of the loading

curve, the slope at initial unloading curve, and the ratio of residual depth to maximum indentation depth h_f/h_{max} has been established.

The derived relationship shows that it is possible to achieve accurate elastic plastic material properties using at least two different indenter geometries.

Tho, Swaddiwudhipong et al. (2005) carried out large deformation FEM to investigate the uniqueness of elastic plastic materials those obeying power-law strain hardening properties during the loading and unloading processes using instrumented sharp microindentation test. It was established that a one-to-one relationship between load–displacement curve and elastic plastic material properties for a single indentation simulation could not be always unique.

Chen, Ogasawara et al. (2007) addressed important questions of the application range, limitations, and uniqueness of the mechanical response and microindentation technique to measure material constitutive properties. They found that for a given indenter geometry, the indentation test cannot successfully examine the material properties beyond a critical strain point, resulting in non-unique inverse FEM analysis solution of force-displacement curve. The results also demonstrated that the elastic plastic materials have different properties but with almost identical load displacement curve.

Kang, Becker et al. (2012) developed FE analysis interfaced with non-linear optimisation algorithms to determine and improve the accuracy of the elastic–plastic material properties obeying a power-law strain hardening behaviour without the concept of representative strain and dimensionless analysis. The optimisation approach shows that a unique set of four key material properties (Young's modulus, yield stress, work hardening and Poisson's ratio) can be predicted from the loading–unloading curve using only a single indenter, without the need for employing two indenters.

2.8   Potential use of inverse FE modelling for material parameter identification of thermally treated glass based on the indentation tests

The material characterization of complex systems can be estimated by using inverse finite element modelling, where the material properties are incrementally changed in FE modelling to find a set of material properties which give the best match with the experimental result. Different types of measuring data can be used in the comparison with

FEM results, such as load displacement curves, strain field around the indentation point, and surface deformation profile (Bolzon, Maier et al. 2004, Nakamura and Gu 2007). Although many Inverse analysis techniques have been introduced in various applications, the techniques are not efficient unless they assure convergence and stability conditions. In many inverse finite elements the unstable system can converge to a unique solution if sufficient information about the true solution is available. As discussed in the previous section, inverse modelling techniques are not efficient unless convergence and consistency is achieved. This requires a precise experimental work set up and proper FEM with the correct optimisation method. Many inverse FE modelling results were sensitive to initial setup values and in some cases, a wide range of initial data has to be used to produce robust values which lead to optimal parameters.

As in some inverse finite element analysis, the model is initially not able to achieve good convergence characteristics with a single indenter solution. This problem may be overcome by using an additional indenter, where the accuracy of the FEM reverse method can be significantly improved to predict the material properties by using dual or more indenters as compared to the single indenter method. Swaddiwudhipong, Tho et al. (2005) and many other researchers in the previous section demonstrated that the sensitivity of the reverse method can be significantly improved by using more than one indenter. Another solution might be available to predict unique material properties using a powerful optimization tool in conjunction with inverse FE analysis of the single indentation process. It is important to extend the application of single and dual indenters into material characterisation of other non-linear brittle material, which is difficult to obtain by standard uniaxial tensile or compression tests, such as recycled glass, based silica material treated in different heat treatment cycles as a novel material in manufacturing application of mass finishing processes.

2.9   References

Alcala, J., A. Barone and M. Anglada (2000). "The influence of plastic hardening on surface deformation modes around Vickers and spherical indents." Acta Materialia **48**(13): 3451-3464.

Arora, A., D. Marshall, B. Lawn and M. Swain (1979). "Indentation deformation/fracture of normal and anomalous glasses." Journal of Non-Crystalline Solids **31**(3): 415-428.

Bao, Y., W. Wang and Y. Zhou (2004). "Investigation of the relationship between elastic modulus and hardness based on depth-sensing indentation measurements." Acta Materialia **52**(18): 5397-5404.

Barenblatt, G. I. (1996). Scaling, self-similarity, and intermediate asymptotics: dimensional analysis and intermediate asymptotics, Cambridge University Press.

Begley, M. R. and J. W. Hutchinson (1998). "The mechanics of size-dependent indentation." Journal of the Mechanics and Physics of Solids **46**(10): 2049-2068.

Bertoldi, M. and V. M. Sglavo (2004). "Soda–borosilicate glass: normal or anomalous behavior under Vickers indentation?" Journal of non-crystalline solids **344**(1): 51-59.

Bhattacharya, A. and W. Nix (1988). "Analysis of elastic and plastic deformation associated with indentation testing of thin films on substrates." International Journal of Solids and Structures **24**(12): 1287-1298.

Bhattacharya, A. and W. Nix (1988). "Finite element simulation of indentation experiments." International Journal of Solids and Structures **24**(9): 881-891.

Bhushan, B. and V. N. Koinkar (1994). "Nanoindentation hardness measurements using atomic force microscopy." Applied physics letters **64**(13): 1653-1655.

Bolshakov, A. and G. Pharr (1998). "Influences of pileup on the measurement of mechanical properties by load and depth sensing indentation techniques." Journal of materials research **13**(04): 1049-1058.

Bolzon, G., G. Maier and M. Panico (2004). "Material model calibration by indentation, imprint mapping and inverse analysis." International Journal of Solids and Structures **41**(11): 2957-2975.

Bridgman, P. and I. Šimon (1953). "Effects of very high pressures on glass." Journal of applied physics **24**(4): 405-413.

Bucaille, J. L., S. Stauss, E. Felder and J. Michler (2003). "Determination of plastic properties of metals by instrumented indentation using different sharp indenters." Acta Materialia **51**(6): 1663-1678.

Bulychev, S. I., Alekhin, V. P., Shorshorov, M. K., Ternovskii, A. P. (1975). "Determination of young's modulus according to

indentation diagram." Industrial Laboratory **41**: 1409–1412.

Chen, X., N. Ogasawara, M. Zhao and N. Chiba (2007). "On the uniqueness of measuring elastoplastic properties from indentation: the indistinguishable mystical materials." Journal of the Mechanics and Physics of Solids **55**(8): 1618-1660.

Cheng, Y.-T. and C.-M. Cheng (1999). "Scaling relationships in conical indentation of elastic-perfectly plastic solids." International Journal of Solids and Structures **36**(8): 1231-1243.

Dahmani, F., J. Lambropoulos, A. Schmid, S. Burns and C. Pratt (1998). "Nanoindentation technique for measuring residual stress field around a laser-induced crack in fused silica." Journal of materials science **33**(19): 4677-4685.

Dao, M., N. Chollacoop, K. Van Vliet, T. Venkatesh and S. Suresh (2001). "Computational modeling of the forward and reverse problems in instrumented sharp indentation." Acta materialia **49**(19): 3899-3918.

De Campos Velho, H. F., F. M. Ramos, E. S. Chalhoub, S. Stephany, J. C. Carvalho and F. L. De Sousa (2007). "Inverse problems in space science and technology." Inverse Problems in Science and Engineering **15**(4): 359-372.

Delalleau, A., G. Josse, J.-M. Lagarde, H. Zahouani and J.-M. Bergheau (2006). "Characterization of the mechanical properties of skin by inverse analysis combined with the indentation test." Journal of biomechanics **39**(9): 1603-1610.

Doerner, M. F. and W. D. Nix (1986). "A method for interpreting the data from depth-sensing indentation instruments." Journal of Materials Research **1**(04): 601-609.

Dumas, G. and C. Baronet (1971). "Elastoplastic indentation of a half-space by an infinitely long rigid circular cylinder." International Journal of Mechanical Sciences **13**(6): 519-530.

Evers, M. (1967). "Glass Technol." Ber **40**(2): 41.

Feng, G., S. Qu, Y. Huang and W. D. Nix (2009). "A quantitative analysis for the stress field around an elastoplastic indentation/contact." Journal of Materials Research **24**(03): 704-718.

Fischer-Cripps, A. C. (2005). "The IBIS Handbook of Nanoindentation." Fischer-Cripps Laboratories.

Giannakopoulos A, a. S. S. (1999). "Determination of elastoplastic properties by instrumented sharp indentation." Scr. Mater. **40** (1191–1198).

Giannakopoulos, A. and P.-L. Larsson (1997). "Analysis of pyramid indentation of pressure-sensitive hard metals and ceramics." Mechanics of Materials **25**(1): 1-35.

Giannakopoulos, A. E., P. L. Larsson and R. Vestergaard (1994). "Analysis of Vickers indentation." International Journal of Solids and Structures **31**(19): 2679-2708.

Gong, J., H. Miao and Z. Peng (2004). "Analysis of the nanoindentation data measured with a Berkovich indenter for brittle materials: effect of the residual contact stress." Acta Materialia **52**(3): 785-793.

Hagan, J. (1980). "Shear deformation under pyramidal indentations in soda-lime glass." Journal of Materials Science **15**(6): 1417-1424.

Hardy, C., C.-N. Baronet and G.-V. Tordion (1972). "The Indentation of an Elastic-Perfectly-Plastic Half-Space by a Hard Sphere." Journal of Fluids Engineering **94**(1): 251-253.

Jahanmir, S. (1993). Friction and wear of ceramics, CRC Press.

Kang, J., A. Becker and W. Sun (2012). "Determining elastic–plastic properties from indentation data obtained from finite element simulations and experimental results." International Journal of Mechanical Sciences **62**(1): 34-46.

Larsson, P.-L., A. Giannakopoulos, E. Söderlund, D. Rowcliffe and R. Vestergaard (1996). "Analysis of Berkovich indentation." International Journal of Solids and Structures **33**(2): 221-248.

Laursen, T. and J. Simo (1992). "A study of the mechanics of microindentation using finite elements." Journal of Materials Research **7**(03): 618-626.

Lawn, B. and D. Marshall (1979). "Hardness, toughness, and brittleness- An indentation analysis." J. AM. CERAM. SOC. J. Am. Ceram. Soc. **62**(7): 347.

Lawn, B. R. (1993). Fracture of brittle solids, Cambridge university press.

Lichinchi, M., C. Lenardi, J. Haupt and R. Vitali (1998). "Simulation of Berkovich nanoindentation experiments on thin films using finite element method." Thin solid films **312**(1): 240-248.

Nakamura, T. and Y. Gu (2007). "Identification of elastic–plastic anisotropic parameters using instrumented indentation and inverse analysis." Mechanics of materials **39**(4): 340-356.

Ogasawara, N., N. Chiba and X. Chen (2006). "Measuring the plastic properties of bulk materials by single indentation test." Scripta Materialia **54**(1): 65-70.

Oliver, W. C. and G. M. Pharr (1992). "An improved technique for determining hardness and elastic modulus using load and displacement sensing indentation experiments." Journal of materials research **7**(06): 1564-1583.

Pethicai, J., R. Hutchings and W. Oliver (1983). "Hardness measurement at penetration depths as small as 20 nm." Philosophical Magazine A **48**(4): 593-606.

Pharr, G., W. Oliver and F. Brotzen (1992). "On the generality of the relationship among contact stiffness, contact area, and elastic modulus during indentation." Journal of materials research **7**(03): 613-617.

Ren X. J., H. R. M., Griffths C. and Henshall L. J. (2001). "An investigation of the effect of indenter heating on the indentation creep behaviour of single crystal MgO." Journal of Materials Science Letters **20**: 1819-1821.

Sakai, M. (2004). "Simultaneous estimate of elastic/plastic parameters in depth-sensing indentation tests." Scripta materialia **51**(5): 391-395.

Shim, S., W. C. Oliver and G. M. Pharr (2007). "A comparison of 3D finite element simulations for Berkovich and conical indentation of fused silica." International Journal of Surface Science and Engineering **1**(2-3): 259-273.

SNEDDON, I. (1948). "Bousslnesq's problem for a rigid cone." Proc. Cambridge Phil. Soc. M+ j if92-507 **19**(8).

Sneddon, I. N. (1965). "The relation between load and penetration in the axisymmetric Boussinesq problem for a punch of arbitrary profile." International Journal of Engineering Science **3**(1): 47-57.

Swaddiwudhipong, S., K. Tho, Z. Liu, J. Hua and N. Ooi (2005). "Material characterization via least squares support vector machines." Modelling and Simulation in Materials Science and Engineering **13**(6): 993.

Swaddiwudhipong, S., K. Tho, Z. Liu and K. Zeng (2005). "Material characterization based on dual indenters." International journal of solids and structures **42**(1): 69-83.

Tabor, D. (1948). A simple theory of static and dynamic hardness. Proceedings of the Royal Society of London A: Mathematical, Physical and Engineering Sciences, The Royal Society.

Taljat, B., T. Zacharia and F. Kosel (1998). "New analytical procedure to determine stress-strain curve from spherical indentation data." International Journal of Solids and Structures **35**(33): 4411-4426.

Tanaka, M. and G. S. Dulikravich (1998). Inverse problems in engineering mechanics, Elsevier.

Tho, K., S. Swaddiwudhipong, Z. Liu and K. Zeng (2005). "Simulation of instrumented indentation and material characterization." Materials Science and Engineering: A **390**(1): 202-209.

Tho, K., S. Swaddiwudhipong, Z. Liu, K. Zeng and J. Hua (2004). "Uniqueness of reverse analysis from conical indentation tests." Journal of materials research **19**(08): 2498-2502.

Tikhonov, A. N. and V. I. A. k. Arsenin (1977). Solutions of ill-posed problems, Vh Winston.

Tikhonov, A. N., A. Goncharsky, V. Stepanov and A. G. Yagola (2013). Numerical methods for the solution of ill-posed problems, Springer Science & Business Media.

Varshneya, A. K. (2013). Fundamentals of inorganic glasses, Elsevier.

Wiederhorn, S., H. Johnson, A. Diness and A. Heuer (1974). "Fracture of glass in vacuum." Journal of the American Ceramic Society **57**(8): 336-341.

Youn, S. and C. Kang (2005). "FEA study on nanodeformation behaviors of amorphous silicon and borosilicate considering tip geometry for pit array fabrication." Materials Science and Engineering: A **390**(1): 233-239.

3-1

CHAPTER THREE

POWDER CHARACTERISATION OF THERMALLY TREATED RECYCLED GLASS MEDIA FOR MASS FINISHING PROCESSES

3.1   Introduction

The main characteristics of powders are particle shape (morphology) and particle size and distribution (granulometry). The consistency and quality of powder is under investigation; the glass beads are supposed to be key process variables (KPVs) in the powder characterization of thermally treated recycle glass media. A full evaluation of powder properties requires the use of two approaches; (1) assessment of powders at a single particulate level and (2) via the behaviour of a mass of particles often referred to as 'bulk' assessment. The particulate assessment techniques include; particle size and particle size distribution, particle shape, particle structure, particle surface area and particle internal surface porosity. The bulk assessment techniques include; apparent density, tap density, flowability, cohesiveness, and chemical composition. For thermal applications, it is preferable to use spherical shape particles in order to ensure high flowability and optimal conditions of melting. Such preconditions are crucial for the manufacturer to produce high density and high wear-resistant abrasive tools. The wear resistance of abrasive tools depends on the particle shape, size, hardness, etc. Kulu, Mikli et al. (2005). Mikli, Kaerdi et al. (2001) confirm a direct correlation between the abrasive particle shape and the wear rate. Moreover, the abrasive tool produced from hard powder material will cause high abrasivity (angularity) particles resulting in a significant increase of abrasive wear.

There are different techniques presented by many researchers to determine the granulometry of powders such as (sieve analysis, laser analysis, image analysis, etc.). Kulu, Tümanok et al. (1998) proposed that the coarser powder granulometry (particle size > 50µm) provides sufficiently good results by means of sieve analysis. However, the sieve analysis does not describe adequately the powder granulometry of particles size < 50µm. Mikli (1998) proposed a comparison of powder granulometry determined by sieve and laser techniques. The results show that the laser analysis provides finer granulometry of the powder compared with the sieve analysis, which is insufficient and unsuitable for fine powder classification. Wojnar (2010) suggested that powder granulometry using image analysis increases the quality of the evaluation method due to its high speed and accuracy mainly for fine powders. The morphology of powders can be characterized by defining the particle shape such as (spherical, angular, dendritic, dish-shaped, irregular shape, etc.) or through quasi-quantitative analysis by means of geometrical shape parameters Kimura and Yamaguchi (1982).

However, the shape parameter characterizes the particles' shape, without considering the size. Qualitative descriptions of particle visual appearance, such as rounded, semi-angular or angular, have been used to identify and distinguish between various abrasive particle groups. However, several researchers have developed various numerical modelling methods to characterize the particle shape Stachowiak (1998), Wojnar (1998), and Wojnar (2010).

Large numbers of characterization methods are available to identify the flow performance of powder using classification charts and indices. Carr (1965) proposed a series of charts and indices that collect the results of flowability from several characterisation methods into a single score. Hausner (1967) developed an expression to define the flowability of powders that is equal to the ratio of bulk density to the tapped density. However, the Hausner ratio does not define a property of the material, the value can vary depending on the measuring instrument used. Geldart (1973) proposed one of the best powder classification systems through separating powders into four groups in terms of different fluidization behaviour based on medium particle size and density. Hosokawa Micron Ltd. for powder system analysis collected the indices from different characterization methods and implemented then into one powder tester. The application of such indices is valuable in describing the most basic powder properties. However, these indices cannot accurately identify the differences between powders, and they cannot accurately predict powder performance in different processes. Prescott and Barnum (2000) proposed that the flow behaviour of a powder is a multi-dimensional problem and the flowability performance comes from the combination of material physical properties and the equipment used for handling, storing, and/or processing the material

Although access to several powder characterization methods has made it relatively easy to characterize, care should be taken to identify the best characterization method for a specific application. This is because characterization methods are usually designed to measure a specific property and may have limited capability outside of their designed scope.

In this study, powder characterisations were carried out using the full range of traditional techniques including apparent / tap density, SEM, chemical composition and particle size distribution. In order to obtain a deeper level of understanding, advanced techniques were employed, which involved the utilisation of the Freeman FT4 Rheometer instrument.

This is a semi-automated powder testing system that allows precise measurement of shear and flow energy properties of powder samples (ASTMD6128–06 2006). These techniques are routinely applied during the characterisation of metal powders, the measured parameters have been found to be KPVs.

The outcomes from such an analysis will lead to suitable techniques to assess morphology, flowability, and compressibility of recycled soda lime-glass beads and critically analyse the effect of particle size and distribution of the glass beads on the parameters measured by powder characterisation techniques.

The overall aim of this study is to assess the suitability of these techniques as a method to compare and contrast four different samples of recycled soda lime glass beads with different particle size supplied by Potters Ballotini Ltd. The group particles coded by means of their sizes to (VG+450, VG+350, VG+250, VG+06), respectively. Characterisation of glass beads is an important issue to optimize the material properties throughout thermal analysis and the manufacturing process (automation filling process) and to evaluate other component properties such as glass media angularity.

3.2 Methodology

3.2.1 Powder sampling

In order to obtain representative powder samples for testing; the powder was blended and sampled in accordance with MTC technical instruction reference MTC-NSAM-TI-PC-01 standard. The powder was decanted into a secondary container before blending for 1 minute at 10 rpm. After the completion of the blending cycle, the powder was sub-divided into uniform volumes of powder suitable for testing using a chute splitter method. Two representative sub-samples were created for each test (i.e. fresh powder was used for every test).

3.3 Particle morphology

The particles' morphology was assessed at MTC / Coventry using optical methods with the utilization of a Keyence digital optical microscope and a scanning electron microscope (SEM) Hitachi TM3000.

3.3.1 Particle sizing

Particles' size analysis was performed at LSM (London and Scandinavian Metallurgy Co.) where a laser diffraction method (Malvern Mastersizer 2000) was employed. In this process, the powder was dispersed in a liquid suspension (water) and passed through a focus cell laser beam. The powder particles reflect light at an angle inversely proportional to their size. Each sample was run for five times, and the values of D_{10}, D_{50}, and D_{90} were calculated in addition to the cumulative distribution curve.

3.3.2 Chemical composition

Elemental analysis of the powder samples was performed at London & Scandinavian Metallurgical (LSM) Analytical Co Ltd, and Ceram Research Limited (CERAM). All the main elements were identified by x-ray fluorescence (XRF), except for sulphur trioxide, expressed as SO3 which was assessed by an inert gas diffusion technique at LSM and calculated from the remaining sulphur following loss on ignition (LOI) and fusion at CERAM.

3.3.3 Flow and packing properties

The apparent density was measured using the Hall Flowmeter funnel. A fixed mass of powder was allowed to flow into a container with volume of 25 cm^3 under controlled conditions. The mass of powder per unit volume was determined and reported as the apparent density (ADH). This is a measure of the packing density of the material in a low stress environment, such as in a manual die filling operation where no external stress is applied or a die filled from a gravity-fed hopper.

Tap density is the packing density of the powder after tapping against a firm base to obtain the maximum consolidation of the loose powder. Whilst still a relatively low stress environment the tap density represents the maximum, the packing density of material can achieve without application of any external influence, which would cause a change to the individual particles (i.e. heat or compaction pressure). A material would be much closer to its tapped density when using an automatic die filling system that uses an auger feeder.

The tap density of the powder was measured using an Auto tap machine, in accordance with (MTC TI reference: MTC-NSAM-TI-PC-05). A fixed mass of powder (20 g) held within a granulated glass cylinder is repeatedly tapped against a firm base. The tapping motion has amplitude of 1.5mm, and 3000 taps at 260 taps/min were conducted. The volume of powder before and after tapping was measured which is used to calculate the compressibility of powder. The ratio of tap to apparent density can be used to calculate the Hausner Ratio (HR) and Carr's Index (CI%), which have been developed as measuring tools of powder flowability using Eq. (3.1) and Eq. (3.2) , respectively. According to the Hausner Ratio and Carr's Index approaches, typically *HR* > 1.25 and *CI* > 25 suggests a powder with poor flowability whereas *HR* < 1.25 and *CI* < 15 indicates good flowability. *HR*, and *CI* were given by following expressions:

$$HR = \rho_t / \rho_a \tag{3.1}$$

$$CI = (1 - \rho_t / \rho_a) \times 100 \tag{3.2}$$

where ρ_t is the tap density, and ρ_a is the apparent density

3.3.4 Powder rheology

Particle rheology was carried out at MTC/ Coventry.The Freeman FT4 rheometer is not currently accredited with a professional standard, but is in the process of gaining accreditation from the ASTM international subcommittee D18.24 W42122. The Freeman FT4 is capable of measuring the dynamic, bulk, and shear properties of a powder. The vessel size chosen for this experiment was 25 ml, which was appropriate for the volume of powder samples provided.

3.4   Results and discussions

3.4.1   Particle imaging

In order to evaluate the particle morphology of the four samples, representative aliquots of powders were assessed using both a digital optical microscope and scanning electron microscope (SEM) at a range of magnifications.

3.4.1.1 Soda-lime glass particle (VG+450)

Figure 3-1 (a) shows optical microscope images of irregular and elongated particles. Based on the images most of the particle sizes comply with the specification (less than VG+450). However, there is evidence of elongated particles in the region with dimensions of 1157 μm (1). A higher magnification image is shown in Figure 3-1 (b) the image shows evidence of spherical glass particles ~500 μm (1). There is also evidence of irregular shap particles and elongated morphology particles.

The morphology of the particles can be observed in more detail by the SEM micrographs. Figure 3-2 (a), shows evidence of spherical particles ~500 μm (1), and 100 μm (2), Figure 3-2 (b) shows a higher magnification image of these cases. The infrequent occurrence of these spherical particles and their apparent inconsistency compared to the bulk sample indicates that they may be present as contaminants from other processes.

Potters manufacture a spherical grade of both soda lime silicate glass and borosilicate glass. Consequently, if the observed spherical particles are present as contaminants, there is a potential that they may be present as borosilicate glass. The issue here is that borosilicate glass has a higher melting temperature than soda lime silicate glass. As such during the melting process, these borosilicate beads may form areas of incomplete fusion within the final part. However, EDS analysis was carried out as is shown in Figure 3-3 to investigate the chemical composition distribution of the spherical and irregular particles. The comparison shows similar composition, mainly for silicon (Si), Sodium (Na), and Calcium (Ca). The results show, no evidence of other metallic component.

(a)   (b)
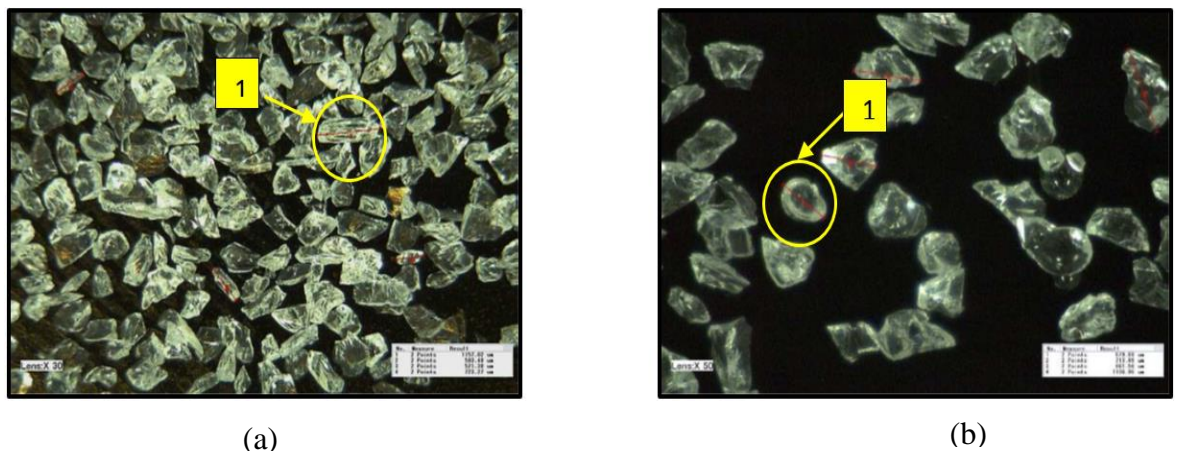
Figure 3-1 Optical microscope images of VG+450 at: a) 30x, and b) 50x magnifications

(a)   (b)
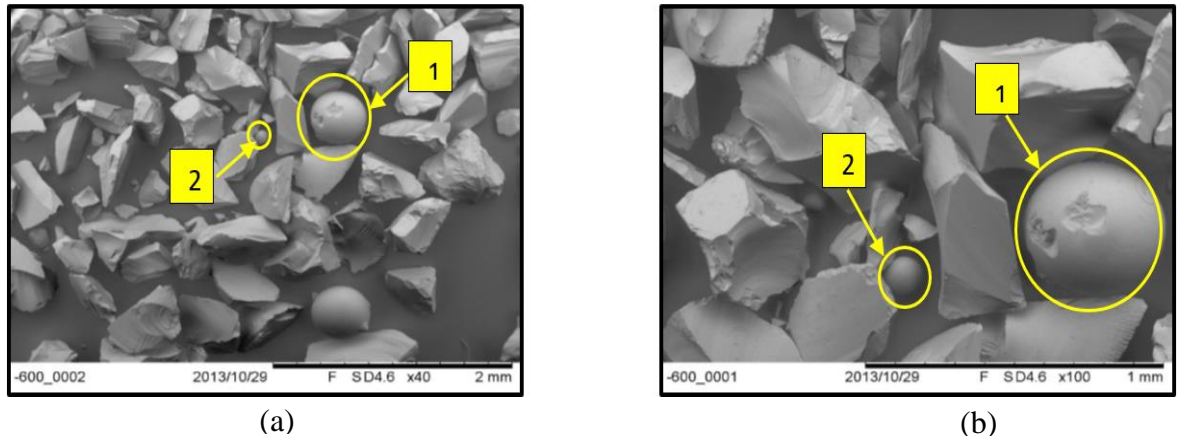
Figure 3-2 SEM micrographs of VG+450 at: a) 40x, and b) 100x magnifications
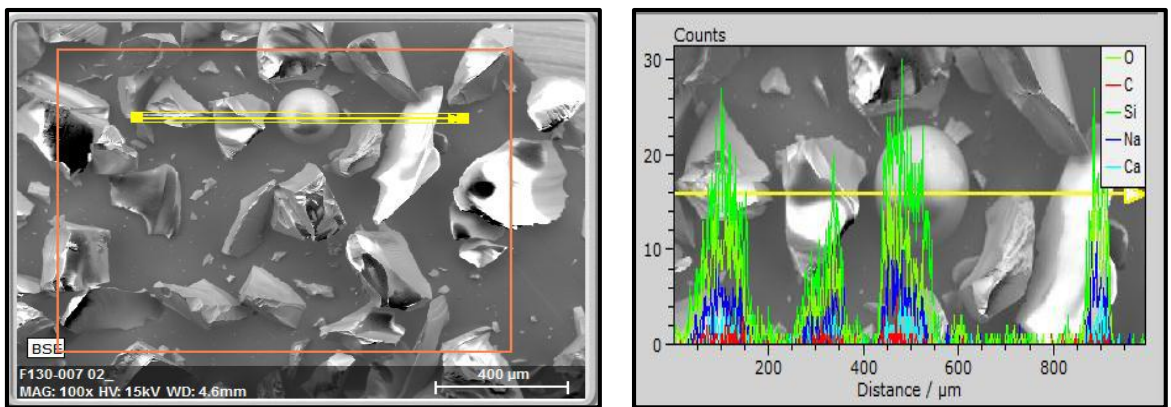
Figure 3-3 EDS analysis of spherical and irregular particles

3.4.1.2   Soda-lime glass particle (VG+350)

Figure 3-4 (a) shows the optical microscope image of VG+350 μm at a magnification of 30x, the particles are angular and irregular in shape. Figure 3-4 (b) shows higher magnification 50x image, the particles with dimension of ~ 450 μm (1) can be observed. Figure 3.5 (a) shows the SEM micrograph at 40x. There is an evidence of spherical particles with diameter of about300 μm (1). Figure 3.5 (b) shows SEM micrograph at higher magnification 100x, a semi spherical broken particle was found in this image (1).

(a)   (b)
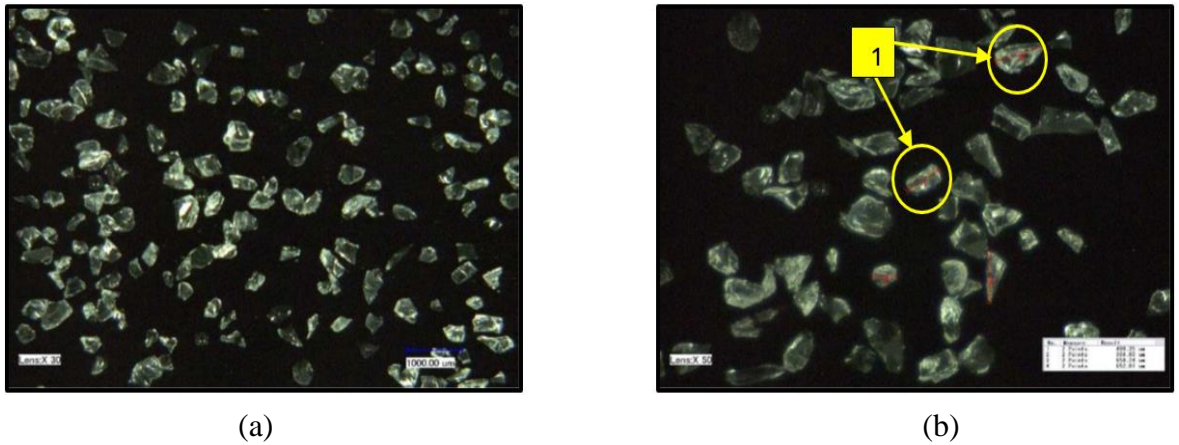
Figure 3-4 Optical microscope images of VG+350 at: a) 30x, and b) 50x magnifications

(a)   (b)
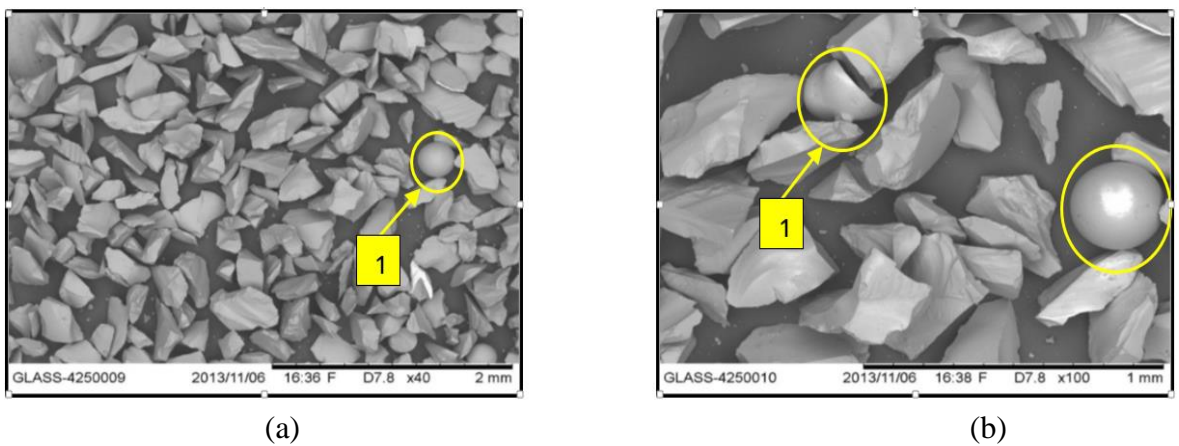
Figure 3-5 SEM micrographs of VG+350 at: a) 40x, and b) 100x magnifications

3.4.1.3   Soda-lime glass particle (VG+250)

Figure 3-6 (a) shows the optical image of VG+250 at 30x, the particles were observed to be angular and irregular in shape, some elongated particles with dimension up to 721μm (1) were observed in Figure 3-6 (b). Figure 3-7 (a) shows the micrographs using SEM, the results were similar to the previous examination; in the case of angularity and irregularity shape. However, in this size fraction there is evidence of thinner flake-like particles (1) that may fracture due to the stresses involved during powder handling which increases with the fine particles, there is also evidence of spherical particles ~100 μm in diameter (2). Figure 3-7 (b) show higher magnification at (100x), and the spherical particle of 100 μm in diameter was also observed.

(a)   (b)
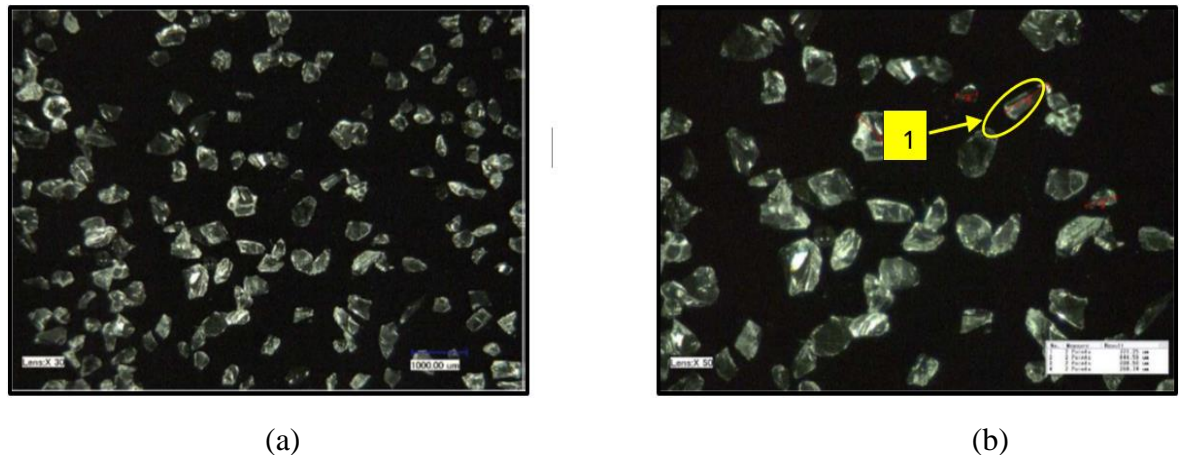
Figure 3-6 Optical microscope images of VG+150 at: a) 30x, and b) 50x magnifications

(a)   (b)
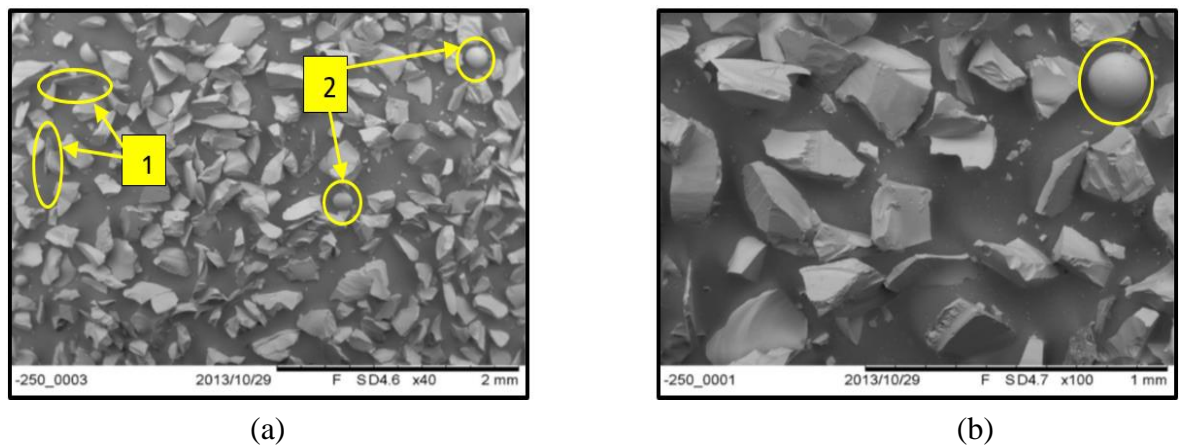
Figure 3-7 SEM micrographs of VG+150 at: a) 40x, and b) 100x magnifications

3.4.1.4 Soda-lime glass particle (VG+06)

Due to the small diameter of the VG+06 particles, a higher magnification optical microscope lens was required to attain morphological assessment. Figure 3-8 (a, and b) shows digital microscope images at 200x and 250x respectively. The Particles size were observed as angular and irregular shape, with some presence of spherical particles that can be appreciated at this magnification Figure 3-8 (a) (1). Elongated particles with dimensions of 178 μm were found in Figure 3.8 (b) (2). Figure 3-9 (a) shows the micrographs using SEM (100x), in Figure 3-9 (b) the sample shows evidence of both angular flat like particles and spherical particles around 40 μm (1).

<div align="center">(a)   (b)</div>
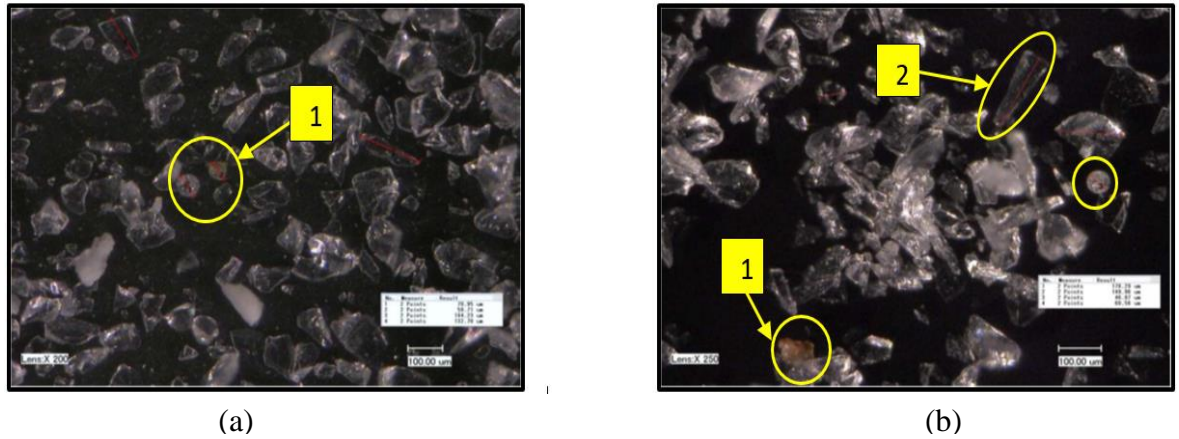
Figure 3-8 Optical microscope images of VG+06 at a) 200x, and b) 250x magnifications

<div align="center">(a)   (b)</div>
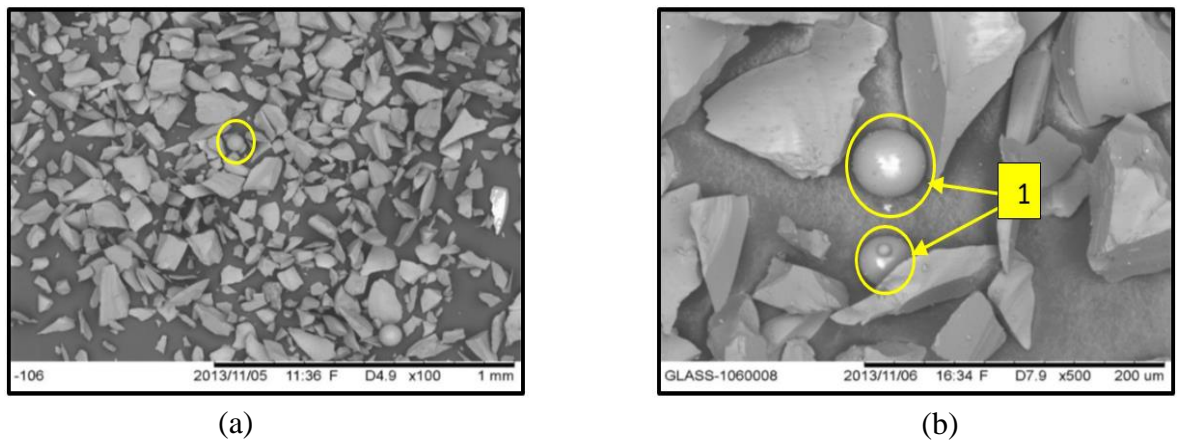
Figure 3-9 SEM micrographs of VG+06 at: a) 100x, and b) 500x magnifications

3.4.2   Particle size distribution

A particle size and width distributions curve is commonly used to define the particle size present in whatever proportions (relative particle amount as a percentage of total particles) in the sample particle group to be assessed. The frequency particle distribution can describe width distribution, which indicates the percentage of particles obtained in individual particle size intervals when the range of target particle sizes is divided into separate intervals. The standardized method to determine the width of frequency particle distribution is by estimating the values of D_{10}, D_{50}, and D_{90}, denotes 10%, 50%, and 90% of particles are smaller than the target particle value by volume, respectively. This approach is better to define the acceptable size distribution. The accumulative distribution of particles passing through the sieve can be expressed by the percentage amounts of particles below the target particle size.

Whereas, the cumulative distribution of particles remaining on the sieve can be expressed by the percentage amounts of particles at a specific particle size or above. Table 3-1 shows the results of D10, D50, and D90 measured by laser diffraction methodology of different recycled soda lime glass particles of (VG+06, VG+150, VG+350, and VG+450).

Figure 3-10 shows the cumulative percentage comparison of the four samples. The results demonstrated that the full distribution of VG+450 sample are within the range of 126-1000 μm. Whereas, the accumulative distribution analysis of VG+350, VG+250, and VG+06 show the cumulative particles range of (160-800, 90-600, 1.2-200) μm, respectively.

Figure 3-11 shows the comparison of frequency particle distribution of VG+450, VG+350, VG+250, and VG+06 glass powders. As presented, the particles of VG+06, and VG+450 show the widest particles distribution. Instead of using single point to describe the particle size distribution, it is suggested to include other size variable to define the distribution width. The span is commonly used to quantify the distribution width, given by Eq. 3.1:

$$D_{90} - D_{10}/D_{50} \hspace{3cm} (3.1)$$

However, it is unusual to suggest the span value within the particle size specification. Usual is to include points, which describe the coarsest and finest parts of the distribution.

Table 3-1 Particle size distribution of VG+06. VG+150, VG+350, and VG+ 450 glass powder

Index Value	VG+06	VG+150	VG+350	VG+450
	Mean (μm)	Mean (μm)	Mean (μm)	Mean (μm)
D_{10}	VG-63.59	VG+50.14	VG+109.74	VG+109.95
D_{50}	VG-22.33	VG+147.64	VG+242.22	VG+272.80
D_{90}	VG+44.36	VG+305.07	VG+455.00	VG+535.86
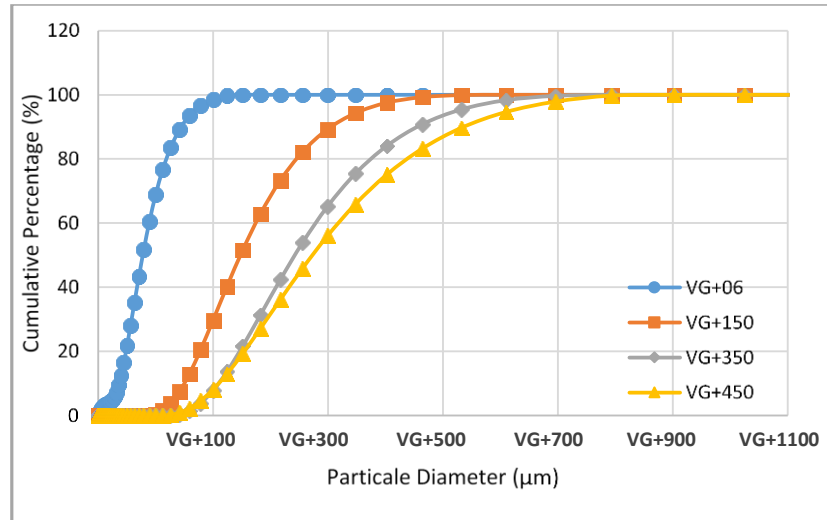
Figure 3-10 Cumulative percentage distribution of VG+06, VG+150, VG+350, VG+450 glass powder
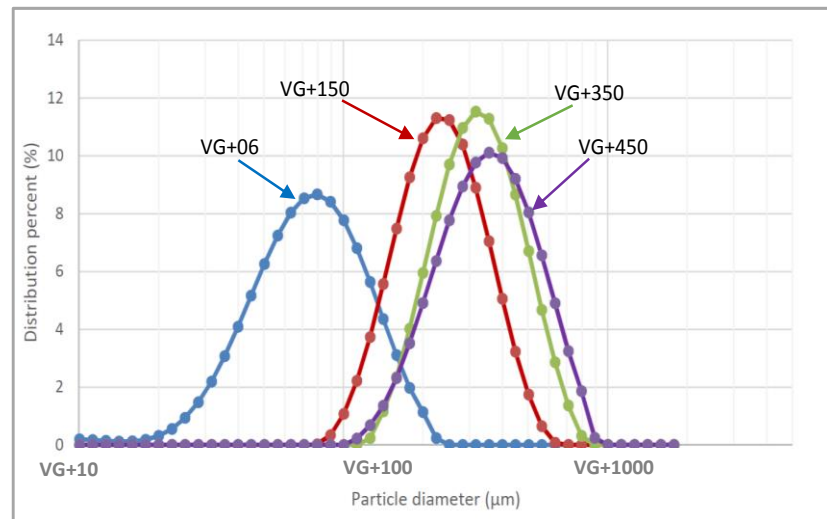
Figure 3-11 Particle size distribution of VG+06, VG+150, VG+350, and VG+450 glass powder

3.4.3 Chemical analysis

A single chemical composition measurement was performed for each sample. Table 3-2 shows the comparison of the chemical composition of VG+06, VG+150, VG+350, and VG+450 glass powder. The composition analyses were created based on comparing the results relative to reference material of soda lime glass. The VG+06 sample was analysed by two different laboratories in order to assess if there is any variation in the results due to the technique used, the results from the two laboratories are shown in Table 3-3.

The main elements were analysed using XRF except for the sulphur trioxide SO_3, which was assessed by the inert gas fusion technique at LSM and calculated from the remaining sulphur following LOI and fusion at CERAM. The analysis suggested that the powder material was identified as soda lime silica glass (SLSG) where the main elements are silica sand (silicon dioxide), soda (sodium oxide) and lime (calcium oxide), the four samples had very similar composition, and there was minimal variation in the percentage of the same elements measured from different samples. The variation observed might be within experimental error. Further testing with a repeatable trail is suggested to ensure that the variation is due to experimental error rather than variation in the element between different samples.

The comparison between labs results also shows minimal differences in the elements composition of VG+06. There is a minor difference in the SO_3 composite, this is associated with different technique being employed in the measurements. However, these differences will not affect the performance of material in the thermal applications.

Table 3-2 Comparison of the chemical composition of VG+06, VG+150, VG+350, and VG+450 glass powders

%w/w	SiO_2	Na_2O	CaO	MgO	Al_2O_3	K_2O	TiO_2	Fe_2O_3	Mn_3O_4	P_2O_5	Cr_2O_3	SO_3
VG+06	71.53	13.30	9.21	3.53	0.84	0.33	0.04	0.14	0.02	<0.02	<0.01	0.24
VG+150	72.16	13.45	9.20	3.62	0.81	0.32	0.04	0.13	0.01	<0.02	<0.01	0.25
VG+350	72.17	13.53	9.28	3.57	0.83	0.33	0.04	0.11	0.01	<0.02	<0.01	0.26
VG+450	71.90	13.37	9.12	3.65	0.83	0.35	0.04	0.11	0.01	<0.02	<0.01	0.24

Table 3-3 Comparison of the chemical composition results of VG+06 from two different laboratories

%w/w	SiO_2	Na_2O	CaO	MgO	Al_2O_3	K_2O	TiO_2	Fe_2O_3	Mn_3O_4	P_2O_5	Cr_2O_3	SO_3
VG+06 (CERAM)	71.53	13.30	9.21	3.53	0.84	0.33	0.04	0.14	0.02	<0.02	<0.01	0.24
VG+06 (LSM)	72.38	13.36	9.08	3.57	0.80	0.33	0.05	0.15	<0.05	<0.05	<0.05	0.17

3.4.4   Powder flowability

Two different methodologies were employed to evaluate flowability; traditional techniques that assess the bulk behaviour based on density, and advance techniques using the rheometer instrument to measure bulk, dynamic and shear properties.

3.4.4.1   Traditional Techniques

The flow time of a fixed mass (50 g) through a hopper with a specific outlet orifice was measured using a Hall flowmeter funnel. In metallic powder characterisation, a specification limit is placed on the maximum time permissible for the powder sample to flow. A powder batch that fails to flow through the Hall flowmeter within the maximum time specified would be rejected. The use of the Hall flowmeter funnel was considered unsuitable for the recycled glass beads; VG+06 and VG+450 were unable to flow through the Hall flowmeter funnel. However, if the powder is unable to flow through the Hall flowmeter, a Carney flowmeter funnel can be used. The Carney flowmeter funnel has the same set-up as the Hall flowmeter funnel but the diameter of the outlet orifice is doubled (0.2 in.). Table 3-4 shows a summary of Carney methods with apparent and tab density results of four glass powder samples. It is clearly noticed that VG+450,VG+350 and VG+150 samples show a very similar flow rate using the ASTM B964-09 method, where the time of 50g glass powder flow was measured. However, when the apparent densities were taken into consideration, the samples with the lower densities will give a greater volume of powder for each 50g test portion, thus more powder having to flow through the orifice. To evaluate Carney flowmeter results, a volumetric flow rate was performed, where each sample had the same 50cm^3 volume flowing through the orifice. The results were slightly contradictory to the values given by the Hausner Ratio and Carr's Index, rating the VG+150 sample the fastest flowing, followed by the VG+350 and then the VG+450 samples.

Based on the Hausner Ratio and Carr's Index values were calculated using relationships between the Bulk and Tapped densities. The results show that the powder flow characteristics increases with the increasing of particle size.

VG+450 was rated as good/free flowing powder, VG+350 is rated as fair flowing powder, VG+150 is rated as passable flowing powder and VG+06 is rated as poor/cohesive flowing powder (See Table 3-4).

In summary decreased particle size increases the specific surface area of the powder. This in turn leads to a greater area of contact between particles in the bulk and hence increases the friction between the particles. Increasing the friction between particles causes a stable packing structure to be developed between the particles leading to a reduction in apparent density. Furthermore, the higher packing density of VG+450 may be due to wider distribution of particle sizes. There is an order of magnitude between the smallest measured particles and the largest particles. In this case, the smaller particles can fit within the void volume that exists between the larger particles resulting in increasing the packing density. Though, the same is true for VG+06, due to the larger friction between the particles a more stable packing structure is developed which prevents the particles from arranging into a dense packing structure. The tapped density of VG+06 is similar to VG+150, and VG+350. In this case, the particles are quickly separated which allows the particles to rearrange, furthermore the force generated during the tap provides an external force, which can overcome the friction between particles.

Table 3-4 Bulk and flowability parameters of VG+06, VG+150, VG+350, and VG+450 glass powders in terms of traditional techniques

Sample	Apparent Density (g/cm^3)	Tap Density (g/cm^3)	Carney Flowrate ASTM B964-09 (FR_c s/50g)	Carney Flowrate (volume) (FR_c s/25g)	Hausner Ratio	Carr's Index
VG+450	1.24	1.42	15.92	9.76	1.18	15.57
VG+350	1.15	1.39	15.59	8.64	1.24	19.1
VG+150	1.09	1.36	15.78	8.26	1.26	20.54
VG+06	0.89	1.32	No Flow	No Flow	1.37	26.92

3.4.4.2 Advanced FT4 rheometer techniques – compressibility

The compressibility analysis was performed using the Freeman FT4 rheometer, in this case normal stresses were applied to the bed of preconditioned glass powder samples. At each level of normal stress, the height of the bed is measured, when the normal stress increases the height of the bed decreases resulting in increased packing density.

The packing density (or % porosity) of the bed as a function of applied normal stress is defined as the compressibility of the sample. Consequently, compressibility gives an indication of how easily a bed of powder can be reduced in volume. The compressibility test differs from the tap density test because the particles remain in constant contact. Figure 3-12 shows the compressibility results of soda lime glass powders. It is clearly observed VG+06 was the most compressible material. This observation is consistent with the tap density results, and is likely due to the distribution of particle sizes within the sample explained previously.
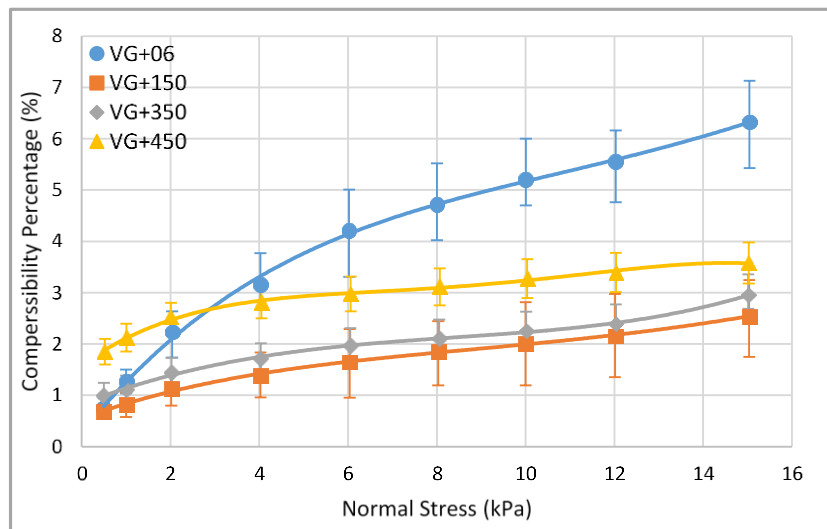
Figure 3-12 Compressibility percentage of VG+06, VG+150, VG+350, and VG+450 glass powders as a function of applied normal stress

3.4.4.3 Advanced FT4 rheometer techniques – basic flow energy

The basic flow energy BFE is the energy required to displace a conditioned and stabilised powder at a given flow pattern and flow rate. The flow pattern is a download anti-clockwise motion of the spindle blade, which generates a compressive stress in the powder. The BFE is calculated from the work done of download movement of the spindle blade through the powder.

Figure 3-13 and Table 3-5 shows the powder flowability parameters comparison of BFE, stability index SI, Flow rate index FRI, and specific energy SE derived by means of stability and variability flowrate measurements of VG+06, VG+150, VG+350, and VG+450 glass powders using the rheometer flowrate test.

The results of BFE were correlated perfectly with the Hausner Ratio and Carr's Index values obtained in the previous section. The flowability rank of the VG+450 sample was excellent / very free flow followed by VG+350 and then VG+150. The VG+06 sample exhibited considerably higher BFE agreeing with the poor/cohesive rating obtained by the Hausner Ratio, the size range also showed a greater variance in results, suggesting that the sample may have changed during the test. The results follow a simple general rule for powders, where smaller particles have greater specific surface area, which increases the friction between the particles. In the case of VG + 06, the friction between the particles increases significantly compared with the other three samples, which show minimal variation in BFE.

The stability index (SI) indicates whether the powder behaviour changes as a function of repeated testing (*SI= test8/test1*). Particle attrition, segregation, (de)agglomeration, and (de)aeration are examples of affects that could result in instability. As illustrated in Table 3-5 and Figure 3-13, the three coarser samples were very stable (SI ≈1.0) and exhibit very little change in flow energy over the course of the repeated tests. This suggests that the powders are robust and stable. However, VG+06 shows the least stable condition and may have changed during the test.

Flow rate index (FRI) is the factor by which the flow energy requirement is changed when the flow rate is reduced by a factor of 10 (*FRI = test 11 / test 8*). In other words, FRI can measure the sensitivity of powder to flow at different rates by varying the blade tip speed. The sensitivity of powder to flow rate is usually an important parameter when describing its flow properties. It is common that cohesive powders are more sensitive to changes in flow rate than non-cohesive or granular materials. This may be attributed to the high air content in the non-cohesive materials. As illustrated in Table 3-5 and Figure 3-13, the three coarser samples show flow rate insensitive values (FRI ≈1.0) which is common amongst free flowing samples or samples with a larger particle size, while VG+06 has a higher FRI value, agreeing that it is a more cohesive sample .

Specific energy (SE) is the energy needed to displace a conditioned powder using a gentle shearing and lifting mode of displacement divided by the split mass. SE is measured during the upward movement of the blade through the powder. The flow pattern is identical to that used during the downward flow pattern but because it is being established on the upward traverse and because the powder is now unconfined, the energies measured are more dependent on the cohesive forces between the particles and less influenced by other factors

such as compressibility. When comparing different materials, a higher SE is usually associated with greater cohesiveness of the powder. However, it is recommended that the SE be used as a tool for comparison and correlation with process experience rather than an absolute measurement. The results in Table 3-5 shows that the SE of VG+06 was significantly higher than the other glass samples, indicating that it was the most cohesive sample. In this case, the SE supports and correlates well with the results of BFE.

Table 3-5 Powder flowability parameters by means of stability and variability flowrate measurements of VG+06, VG+150, VG+350, and VG+450 glass powders

Sample	BFE (mJ)	SI	FRI	SE (mJ/g)
VG+06	2230.7	1.08	1.18	6.68
VG+150	1478.4	1.02	0.91	3.77
VG+350	1387.5	1.00	0.94	3.41
VG+450	1230.9	1.01	0.95	3.28
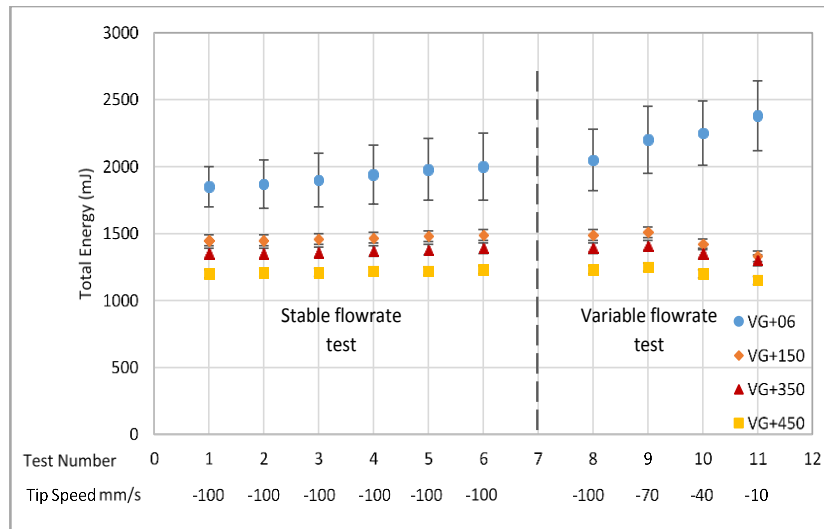
Figure 3-13 Comparison of powder flowability parameters by means of stability and variability flowrate measurements of VG+06, VG+150, VG+350, and VG+450 glass powders.

3.4.4.4 Advanced FT4 rheometer techniques – shear cell

Figure 3.14 shows the powder flowability parameters comparison based on shear cell measurements of VG+06, VG+150, VG+350, and VG+450 glass powders using rheometer technique.

The results suggested no significant differences were observed between the measured shear properties of the four recycled soda lime glass samples. This may be attributed to the level of shear cell selected for the tests. The internal friction measured during the shear cell test is a function of the applied normal stress. Thus, increased normal stress causes increasing the friction between particles. The level of pre-shear selected during this test might be too low to extract the differences in shear properties between the four samples. The method is development to achieve a suitable shear cell test to characterize the glass samples. However, in this study shear cell tests were designed to determine the shear stress required to initiate flow in a pre-consolidated glass powder, providing an indication of how easily a powder will move from a static condition to dynamic flow. Therefore, the flow function (FF) and cohesion should be investigated to evaluate this phenomenon. FF is the ratio of the normal stress and the yield stress; higher values of FF indicate a more free flowing material. Consequently, the description of flow as a function of measured FF value is given by: FF ranking as free flowing when FF>10, FF ranking as easy flowing when 4<FF<10 and FF ranking as a cohesive when 2<FF<4. Table 3-6 shows the summary results of FF, and cohesion parameters derived by means of shear cell measurements of VG+06, VG+150, VG+350, and VG+450 glass powders using the rheometer flowrate test. The results suggested that the VG+150 sample show the better properties with the lowest cohesion value and the highest flow-function (FF) values. The VG+06 sample showed the next best properties followed by the VG+350 and VG+450 samples, the latter two showing very similar values.

Table 3-6 Comparison of powder flowability parameters derived by means of shear cell measurements of VG+06, VG+150, VG+350 and VG+450 glass powders.

Sample	Cohesion (kPa)	FF
VG+06	0.16	9.67
VG+150	0.11	14.41
VG+350	0.19	8.26
VG+450	0.19	7.98
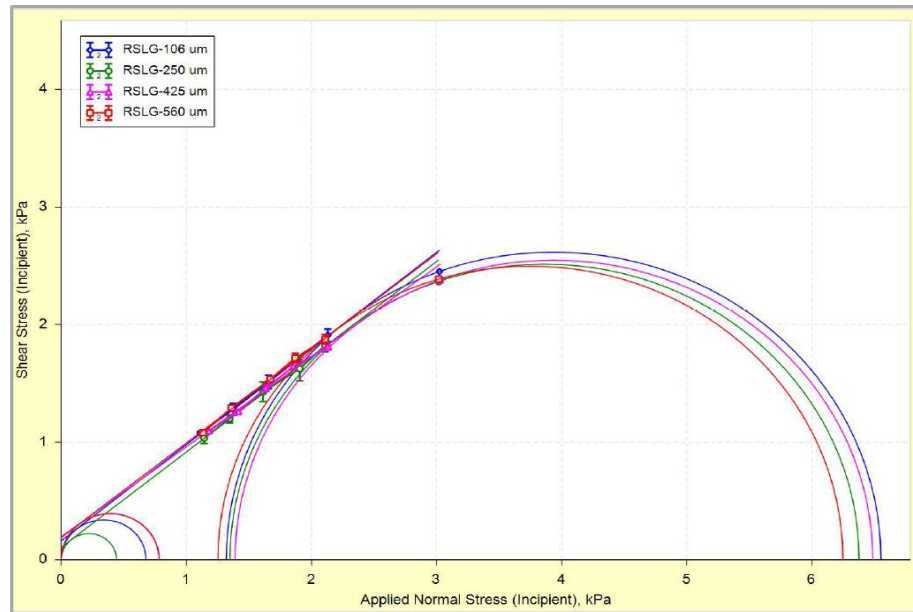
Figure 3-14 Comparison of powder flowability parameters derived in terms of shear cell measurements of VG+06, VG+150, VG+350, and VG+450 glass powders

3.5 Conclusion

In this study, the experimental investigation of various powder characterization techniques of powder sampling, particle morphology, particle sizing, chemical composition, flow and packing properties, and powder rheology were successfully employed to analyse the recycled soda lime glass powders. Based on the particle size and morphology analysis, the recycled soda lime glass exists as irregular and elongated particles. There was some occasional evidence of spherical particles, which could potentially be cross-contamination from other processes. However, further analysis would be required to confirm this. From the particle size data a number of oversized particles were observed in each of the powder samples, this is likely to occur due to the elongated particle shape where the smallest particle dimension can pass through a sieve screen size smaller than the longest dimension. From the chemical analysis, all four samples appear to have an identical chemical composition. In terms of flowability, increased particle size had the better flow properties and increased apparent and tap density. The flow energy measured, using the FT4 rheometer test, also showed that samples with increased particle size exhibited a higher level of free flowing behaviour. The flowability results follow the general rule of powder flow, the smaller particles the larger surface contact area, which increases the friction between the particles

Based on the data presented in this study, VG+350, and VG+150 would be the recommended recycled glass samples. However, this is based purely on the powder performance in terms of flow and packing characteristics (manual and automatic mould filling). Further work assessing the effect of particle size on the melting and fusion process would be required to ensure that this particle size range would be suitable for the process.

3.6 References

ASTMD6128–06 (2006). "American Society for Testing and Materials, Standard test method for shear testing of bulk solids using the Jenike shear cell."

Carr, R. L. (1965). "Evaluating flow properties of solids." Chem. Eng **72**(2): 163-168.

Geldart, D. (1973). "Types of gas fluidization." Powder technology **7**(5): 285-292.

Hausner, H. (1967). FRICTION CONDITIONS IN A MASS OF METAL POWDER, Polytechnic Inst. of Brooklyn. Univ. of California, Los Angeles.

Kimura, T. and T. Yamaguchi (1982). "Morphology of Bi2WO6 powders obtained in the presence of fused salts." Journal of Materials Science **17**(7): 1863-1870.

Kulu, P., V. Mikli, H. Kaerdi and M. Besterci (2005). "Angularity evaluation of milled WC-Co powder." International Journal of Materials and Product Technology **22**(4): 289-298.

Kulu, P., A. Tümanok, V. Mikli, H. Käerdi, I. Kohutek and M. Besterci (1998). "Possibilities of evaluation of powder particle granulometry and morphology by image analysis." Proc. Estonian Acad. Sci. Eng **4**: 3-17.

Mikli, V., H. Kaerdi, P. Kulu and M. Besterci (2001). "Characterization of powder particle morphology." Proceedings of the Estonian Academy of Sciences: Engineering(Estonia) **7**(1): 22-34.

Mikli, V., Kulu, P., Tümanok, A., and Käerdi, H. (1998). "Comparative investigation of disintegrated WC-Co powders by the methods of sieving and image processing." In Proc. VII International Baltic Conference "Materials Engineering – 98". Jurmala, Latvia: 9–13.

Prescott, J. K. and R. A. Barnum (2000). "On powder flowability." Pharmaceutical technology **24**(10): 60-85.

Stachowiak, G. (1998). "Numerical characterization of wear particles morphology and angularity of particles and surfaces." Tribology International **31**(1): 139-157.

Wojnar, L. (1998). Image analysis: applications in materials engineering, Crc Press.

Wojnar, L. (2010). Image analysis: applications in materials engineering, Crc Press.

CHAPTER FOUR

THERMAL ANALYSIS OF GLASS MEDIA FOR MASS FINISHING PROCESSES

Chapter Four / Thermal Analysis

4.1   Introduction

Glass material is one of the oldest industrial manufactured products. The desired mechanical properties are achieved by controlling manufacturing process conditions throughout adjusting the chemical composition and heat treatment cycle. The soda lime silica system is the largest group of the commercial glasses used for a wide range of applications such as containers, windows and insulations due to its workability at moderate temperature, chemical stability and it can be produced from cheap raw materials Kingery (1960). Although this material system is well known, it is still difficult to control during the thermal treatment process because a small change in chemical composition ratio Na2O, CaO and SiO2 causes the glass thermal properties to behave differently and consequently vary the glass transition point, crystallization, and melting point.

The general simplified composition in weight-percent for conventional soda-lime-silica system is 15 Na_2O, 13 CaO and 72 SiO_2. The material elements are mixed and heated to 1093°C, creating Glass. The material under such conditions becomes viscous. However, with rapid cooling, the atoms do not have the time to rearrange themselves resulting in an amorphous (non-crystalline) structure. The amorphous structure increases the tendency of glass to brittleness. However, the glass viscosity increases if enough thermal heat is available and transforms to a crystalline stable structure resulting in glass-ceramic material. The crystalline glass forms if it consists of the formation of devitrite ($Na_2O. 3 CaO. 6SiO_2$) and wollastonite ($CaO. SiO_2$). Thus, SiO_2 polymorphs tridymite or crystobalite can be recognized. Strand (1986) investigated the crystalline growth in soda lime silica glass $Na_2O-CaO-3SiO_2$, with 60% weight of SiO_2 under isothermal conditions and microscopy. The results show that the crystal structure grows from the surface to the interior of the glass sample. Ray and Day (1996) studied the same material composition using the differential thermal analysis (DTA) technique; the results also demonstrated that crystallization was superficial.

Glass-ceramics are crystalline materials developed in the 1950s by controlled crystallization of glasses, giving increases in a wide range of technological applications such as microelectronic, biomedical, optical, sensors, and composite materials Partridge (1994), and Holand and Beall (2012). Controlled crystallization is possible for certain glass chemical composition types and generally takes place in two stages, nucleation and crystallization.

A powder processing technique has been developed recently to produce glass ceramic materials, similar to that for a conventional bulk glass route in which the glass is processed into a fine powder shape and heated. Thus, the glass particles densify by action of viscous flow development and then new nucleation and crystallisation is obtained Rincón (1992). The powder- processing technique shows a stronger tendency for surface crystallization compared with the conventional bulk material route, thus the glass – ceramic microstructure is different in the two approaches.

Optimal glass-ceramic properties and microstructure can be achieved by controlling the thermal history of the original glass powder, particularly the heat treatment cycle (Time-Temperature). Therefore, the time-temperature-transformation (TTT) diagram is extremely useful to present the nucleation and crystal growth data for a particular chemical composition of glass; additionally it is used as a guide for heat treatment improvement in the manufacturing of glass ceramics.

Moreover, differential thermal analysis (DTA) has been widely used to determine the glass transition, optimum nucleation temperature, and crystallization temperature. This consists of the determination of crystallisation peak temperature after isothermal treatments at different nucleation temperatures. The nucleation curve within the DTA trajectory follows a convex shape representing the temperature where the nucleation rate has a maximum value Ray, Ranasinghe et al. (2001).

In this study, the nucleation and crystallization kinetic was evaluated by means of differential thermal analysis (DTA), and thermo-gravimetric analysis (TGA) experiments. Then, the optimal time temperature transformation (TTT) production parameters were determined, to aid delivery of a range of thermally treated recycled glass media with full capability in the finishing of aerospace and other engineering materials (predominantly: polishing, super-polishing and super-finishing operations), was established.

4.2   Glass formation and crystallization

4.2.1   Nucleation and crystallization growth

Nucleation can occur homogeneously or heterogeneously. Homogeneous nucleation is random nucleation without special sites in the phase of homogeneous material.

Heterogeneous nucleation occurs from suitable sites in the phase such as grain boundaries, surfaces, second-phase particles, etc. Most glass materials have a tendency to crystallize on the surface due to a concentration of impurities and defects, which enhance the creation of heterogonous nucleation, Marotta, Buri et al. (1981).

The crystal growth kinematic starts when a nucleus continues to grow by adding atoms from different surrounding orientations, resulting in the creation of a crystal particle which can grow to a certain limit depending on a range of parameters such as chemical composition and heating environment Zarzycki (1991). These crystal particles bind together to create molecules, chains of molecules which will finally form a lattice Vogel (1979). A number of models have been developed by many researchers based on the interface between the atoms and spaces available for growth, assuming different mechanisms such as, normal growth, screw dislocation growth, and 2-D surface nucleated growth Lieth (1977). In the normal growth model, the interface between atoms should be rough, which is characterized by a large section of step locations where atoms can easily be added and removed in different crystal steps. Screw dislocation growth, the interface between atoms is relatively smooth but still imperfect; the crystal growth takes place in steps spirally. Fokin, Nascimento et al. (2005) suggested that this model is good to interpret the crystal growth in silicate glass. It depends upon the requirement of balancing the forces between atoms at crystal steps. However, when the crystal growth takes place at sites in the perfect atoms interface condition, 2-D surface nuclei will be formed on the interface and will be developed by distribution of a monolayer across the surface until the surface is covered Paul (1990).

Figure 4-1 shows a schematic diagram describing the nucleation and crystal growth rates with temperature for a glass material system. When glass temperature is elevated to a particular value the viscosity decreases, which increases the tendency to structural rearrangement and crystallization. However, when the temperature is increased high enough, usually above the softening point, crystal cores begin to form. The cores are tiny regions in the glass structure where the crystalline structure has formed and started to grow. The more likely region for crystallization to develop, both during cooling and reheating, is in the region under the over-lapping curves for nucleation and crystal growth Beall and Duke (1983). Consequently, with further temperature increases, the rate of nucleation increases to a maximum value at a certain temperature either by homogeneous or heterogeneous nucleation, subject to the glass composition.

Additional thermal energy at higher temperature levels causes the nucleation to grow by crystal growth mechanisms; some nuclei can become oversized and melt-out. The rate of crystal growth increases with increasing temperature to a certain value, and then the rate decreases to zero at the liquidus temperature Beall and Duke (1983).
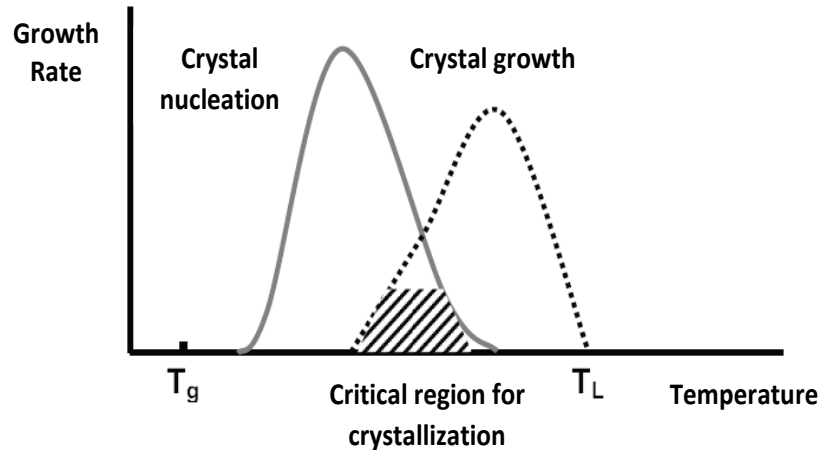
Figure 4-1 Temperature effect on the nucleation and crystallization growth rate of typical glass material

4.2.2 Crystalline phases of heat treated soda lime glass

Heat treatment provides a preferable condition for atoms rearrangement at the nucleation phase, which grows at a certain temperature level to define the crystal structure. The crystal structure growth rate is dependent on the thermal conditions and glass chemical composition. The glass can transform to the stable crystalline state if enough thermal energy is available. However, there are several possible outcomes, which can be predicted as it shown in Figure 4-2. Firstly, the binary system of $Na_2O \cdot SiO_2$ is considered, then crystalline structure of $Na_2O \cdot SiO_2$, α-$Na_2O \cdot 2SiO_2$ and β-$Na_2O \cdot 2SiO_2$ are possible to form. Secondly, if the carbon element composition changes into graphite or diamond elements, then SiO_2 might be possible to form tidymite or cristobalite, quartz Cook, Roth et al. (1978).The probability of crystal growth increases if the triple system $Na_2O \cdot SiO2CaO \cdot SiO_2$-$SiO_2$ is considered. In glass compositions with $SiO_2 > 75\%$ only the crystalline silica is may form. The glass compositions with $(0 < SiO_2 < 20)$ %, then only Na_2O, α and β - wollastonite $(CaO \cdot SiO_2)$ or devitrite $Na_2O \cdot 3CaO \cdot 6SiO_2$ are can form as the main crystalline phase Cook, Roth et al. (1978).

However, the actual percentage weight of SiO_2, CaO, and Na_2O in these crystalline phases and their recognition with X-ray diffraction analysis is quite difficult, because several strong peaks are common for two or more compound systems Backman, Karlsson et al. (1997). Fokin, Zanotto et al. (2003) identified $Na_2O \cdot 2CaO \cdot 3SiO_2$ (NC_2S_3) ratios as the main crystal phase during the XRD analysis due to continued composition change during the crystallization phase transition.
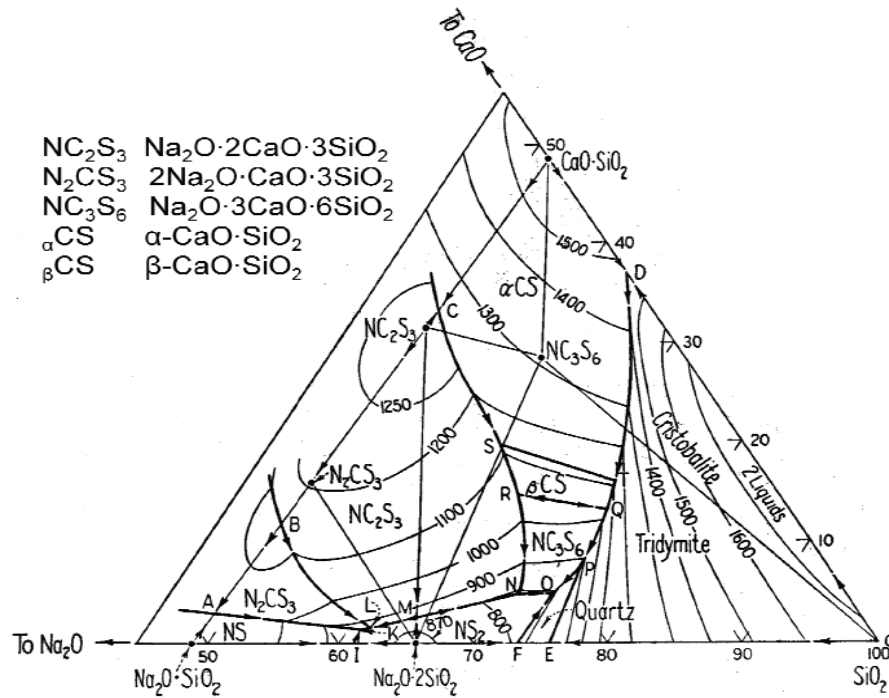
Figure 4-2 Possible heat treatment outcomes from Na2O-CaO-SiO2 phase digram (Cook, Roth et al. 1978)

4.3 Glass powder densification and viscous phase sintering

Sintering is a production procedure for making glass particles adhere together randomly during the heating process. During sintering, the glass particle surface becomes soft, as a result the sharp edges convert to a round shape and particles approach each other. Thus, the particles are bound together through viscous flow and an object with a certain porosity is created. This porosity might be able to be eliminated by extending the sintering process for longer time. Zanotto and Prado (2001) reported that the sintering mechanism for transforming glass particles to dense product could be controlled in addition to viscous flow by glass chemical composition, contaminations, surface area, heat treatment cycle, glass particles packing and crystallization growth.

The main reason for controlling the sintering parameters is to avoid natural crystallization, which delays the viscous flow sintering process and developed residual porosity Zanotto and Fokin (2003). However, the crystallization and viscous flow usually take place at the same temperature range. The crystal growth will lead to increase a viscosity and densification for a certain sintering conditions. Further addition of impurities or crystalline material to the glass particles will also unfavourably influence the sintering behaviour. As a result, some glass compositions can densify easily by viscous phase sintering, whereas other material compositions do not densify well.

On the other hand, increasing the particles' surface area by decreasing the particle size will tend to promote viscous phase sintering. Increasing the glass particles packing density will also help sintering. This can be achieved by increasing particle size distribution, optimal particle size, and mould shaking [Ref. Chapter 3]. Moreover, additional melting glasses or flux can also be enhancing the viscous phase sintering. Sometimes, the multiphase composite system allows the production of unique material properties through improving viscosity and the sintering process, which are not possible with single-phase material systems

Recently, Boccaccini and Maquet (2003) suggested an approach that uses a constant heating rate to achieve acceptable sintering results in order to gain full densification prior to crystallization. In this study, heating microscopy and DTA have been employed to investigate the interaction between densification and crystallization over a range of heating rates.

The Boccaccini approach has been further developed by Vedel, Arstila et al. (2008) by using heating microscopy to determine the viscosity temperature dependence of glasses to control the sintering process, which results in enhancing the bonding response of the porous glass matrix such as bioactive glass composition. The development of the specific volume as a function of the temperature for different cooling rates is shown in Figure 4-3. When the glass is subjected to a low cooling rate from above its melting temperature T_m, it might crystallize when reaching T_m. This may be attributed to the fact that the re-arrangement process suggests that the reorientation or relocation of local molecules may lead to sintering or crystal growth process of the crystalline dislocated material Hancock and Zografi (1997). It is also seen that for a relatively high cooling rate, the density in the solid state becomes smaller (higher volume) than for a relatively intermediate cooling rate. In this case, the rate of crystallization is very low and crystallization is unlikely to occur.
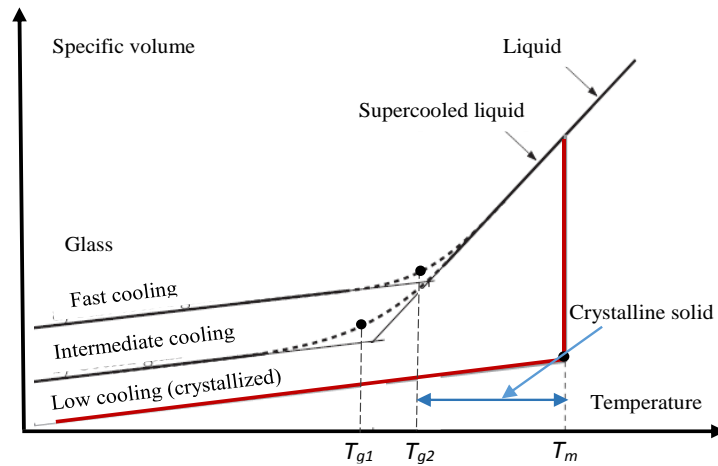
Figure 4-3 Specific volume as a function of the temperature for different cooling rates

4.4   Materials and methods

4.4.1   Preparation of the glass powder

The glass powder used in this study was obtained from recycled glass supplied by Potters Industries LLC / UK leading producer of engineered glass materials. The procedure of manufacturing starts with strong automated shaking to ensure mixing of the raw material powder. For consistency, the powder batches were melted at 1200ºC, and annealed at 570ºC for an hour before cooling to the room temperature. The glass blocks were crushed to a different particle grain size.

In this study, four different particle sizes VG+06, VG+150, VG+350, and VG+450 were used. The chemical combustion of the glass powders was analysed using X-ray fluorescence spectroscopy. The analyses showed that all glass powder samples were a typical soda lime glass [Ref. Chapter 3]. The effect of particle size, shape, and distribution on the crystalline phase transformation as a function of temperature was established by aid of (DTA), (TGA), (XRD), and powder characterisation [Ref. Chapter 3].

4.4.2   Characterization of thermally treated glass powders

Thermal analysis has been defined by the International Confederation of Thermal Analysis (ICTA) as a general term which covers a variety of techniques that record the physic-chemical changes occurring in a substance as a function of temperature Ashraf, Khan et al. (2009).

Two common complementary techniques in this category are differential scanning calorimeter (DSC) and thermo-gravimetric analysis (TGA). DSC measures heat flow to or from a sample as a function of temperature and time, TGA continuously measures the weight of a sample as a function of temperature and time. Differential thermal analysis (DTA) is a method similar to DSC, where the difference in temperature between the sample and a reference material is recorded while both are subjected to the same heating programme. For assessing the moisture and instability, decomposition kinetics and composition thermo- gravimetric analysis is widely used; whereas, DTA is used to determine the presence of exothermic or endothermic reactions. In this study, TGA and DTA were employed to investigate the thermal properties of soda lime glass powder product. These analyses will be used together with results obtained from Chapter 3 (powder characterization) to identify the optimal glass grain size and distribution for actual heat treatment cycles (crystallization point of view) and enhancing the productivity through the automated filling of the mould cavity in the mass production process.

4.5   Results and discussions

4.5.1   Thermogravimetric analysis (TGA)

Thermogravimetric analysis (TGA) is an analytical solution used to determine the thermal stability and instability fraction component for materials by recording the weight change occurrence during the heat treatment process. The measurement is usually carried out in air or inner purging gas such as helium, argon, or nitrogen, and weight is monitored over a linear temperature ramp. The weight change over specific temperature ranges provides information about the desolvation or decomposition, but it does not provide any information about the material lost from the sample. Such a measurement provides two important pieces of analytical information: Ash content (residual mass, M_{res}) related to the weight loss, and oxidation temperature (T_o), associated with phase transformation that occurs at particular temperatures.

The glass powder samples VG+06, VG+150, VG+350, and VG+450 were used for measurements with a Perkin Elmer TGA7 (TGA) analyser at LJMU. The glass powder sample of 20mg was heated in a tungsten crucible at a constant rate of 10°C/min using inert nitrogen gas in the temperature range from 20°C to 900°C. Commercial software Pyrism was used to quantify the mass loss and identify M_{res}, and T_o, from TGA instrument.

Figure 4-4 shows the TGA results of the three soda lime glass powder samples VG+150, VG+350, and VG+450 received from Potters. The TGA results show that the weight loss starting at higher temperatures is caused by thermal degradation of recycled soda lime glass due to the decomposition of calcite ($CaCO_3$) to lime CaO with continued generation of CO_2. The result also shows that the oxidation temperature of VG+150 starts at 330^OC, mass loss continues to $\approx 700^O$C, the residual mass, $M_{res} \approx 17\%$. The oxidation temperature of VG+350 starts at 370^OC, mass loss continues to $\approx 730\ ^O$C, the residual mass, $M_{res} \approx 20\%$. The oxidation temperature of VG+450 starts at 380^OC, mass loss continues to $\approx 770\ ^O$C, the residual mass, $M_{res} \approx 33\%$. The discrepancy in the results may be attributed to the amount, morphology, and distribution of catalyst particles and other carbon impurities, which increased in larger powder grain size.
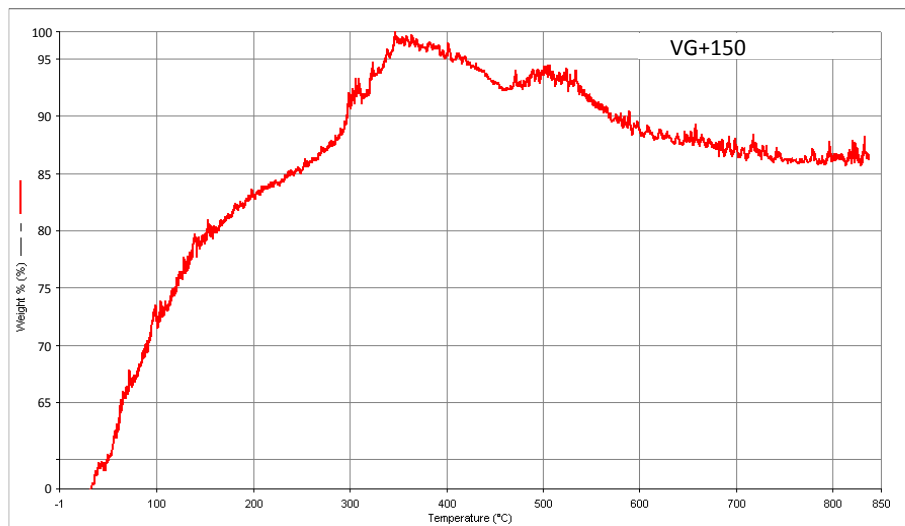
(a)
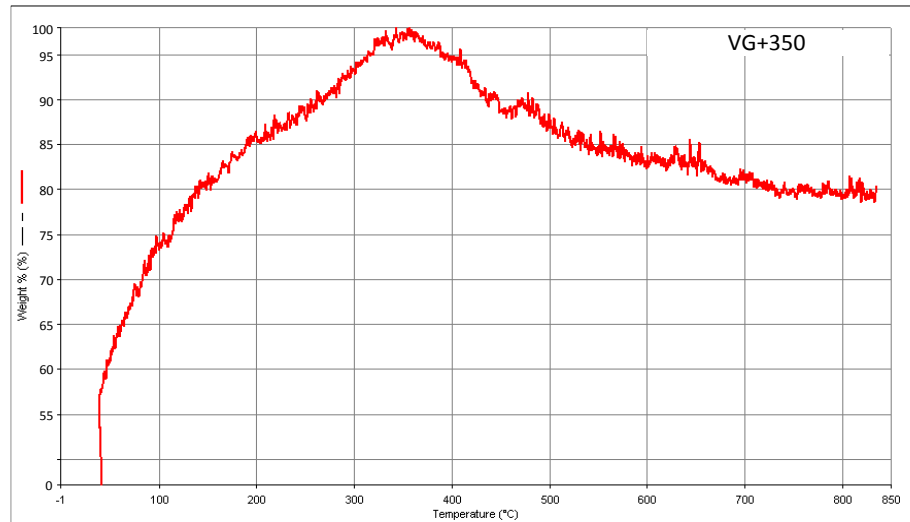
(b)
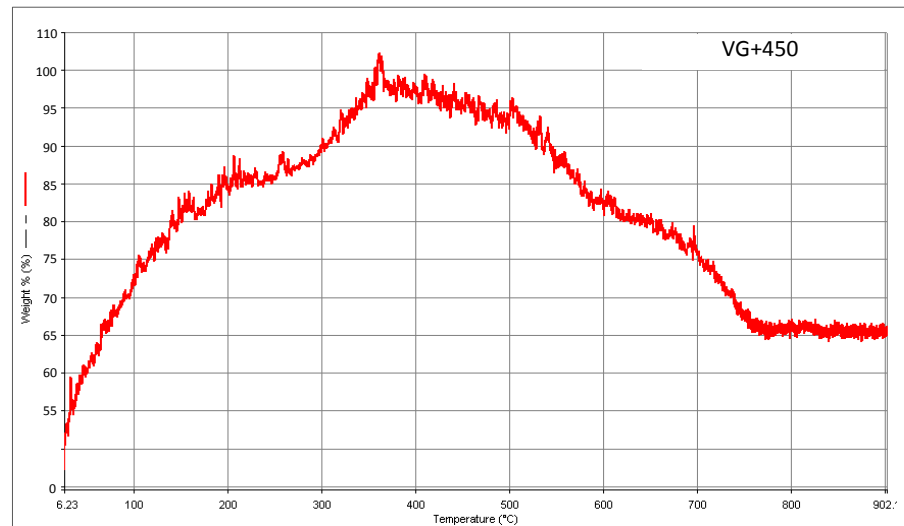
(c)

Figure 4-4 TGA for a) VG+150, b) VG+350, and c) VG+450 glass powder samples

4.5.2   Differential thermal analysis

Differential thermal analysis (DTA) is usually used to determine the characteristic temperatures related with specific phase transitions that occur during the heat treatment cycle. The differences in the phase transition between the glass powder samples and setting reference material were measured over a linear ramp temperature change with time. During analysis, the first considerable thermal parameter which occurs at lower temperature is the glass transition temperature, T_g. The T_g is indicated by the endothermic variation point on the heating curve history, which is caused by the increased heat capacity. Glass materials exhibit an elastic material property below its, T_g breaking point.

With a further increase in the heating rate just above the softening point, the material viscosity decreases, which enhances the possibility for structure rearrangement and crystallization, crystal nuclei begin to form at, T_n temperature. Additional thermal energy causing an exothermic peak is usually started due to the crystallization at temperature, Tx on the heating curve. More crystallization peaks might be generated if various crystallization phases are present F.W. Wilburn (1972). The rate of crystallization decreases to zero at the liquidus temperature, T_1 which corresponds to the offset of the endothermic peak Zanotto (1992). At higher temperature, an endothermic peak is observed as a peak valley due to the melting point at temperature, Tm.

The differential thermal analysis (TPI Perkin Elmer DTA 1700) at Glass Technology Services Ltd (GTS) was conducted to determine the nature of crystallization mechanism of glass powder samples VG+150, VG+350, VG+450 over a programmable heat treatment cycle. The glass powder sample of 20mg was heated from 20°C to 1000°C in a tungsten crucible at a constant temperature rate of 10°C/min. The reference material used to compare the results was soda lime glass.

Figure 4-5 shows the DTA curves for VG+150, VG+350, VG+450 glass powder samples. Figure. 4-5 (a) illustrates that the first transition was an endothermic inflection, through approaching 550ºC , associated with the glass transition temperature, T_g. The next visible transition is exothermic peak at 705ºC, associated with the crystallization temperature, T_x. The results also show, that no further exothermic peaks were observable at higher temperatures, which suggested that the glass can be transformed into a glass-ceramic at a relatively low temperature. The intensity of the exothermic crystallization peak of a glass is dependent on the rate at which the glass devitrifies F.W. Wilburn (1972) . This is followed by an endothermic peak at close to 900 °C, which indicates formation of the liquid stage corresponding to the melting temperature, T_m . The DTA curves of VG+350, and VG+450 samples Figure 4-5 (b), and 4-5 (c) respectively show a similar trend but the corresponding endothermic and exothermic peaks have lower intensity and higher temperature compared with the finer grain size VG+150. The first endothermic peak appeared between 600 ºC and 630 ºC, a second exothermic peak between 750°C and 790 °C, which is demonstrated by the occurrence of volumetric crystallization phase , the endothermic peak was visible between 930 °C, and 970 °C, which indicate the melting point.
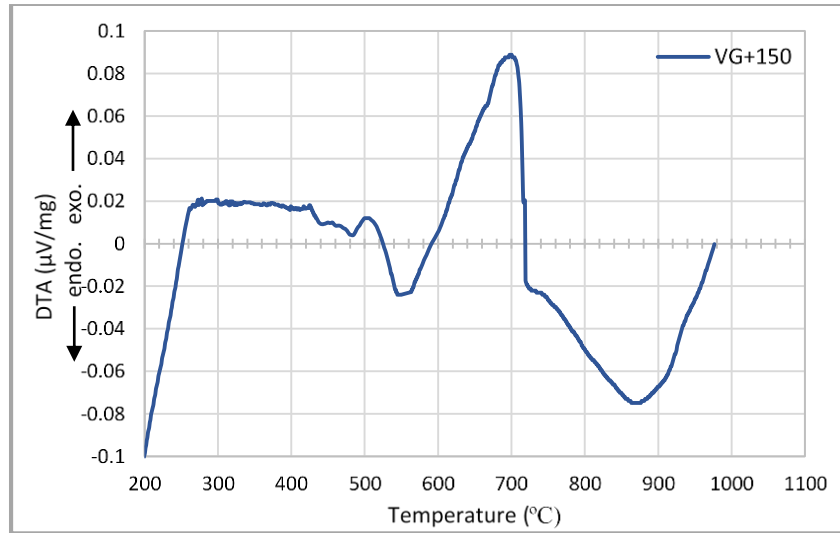
(a)
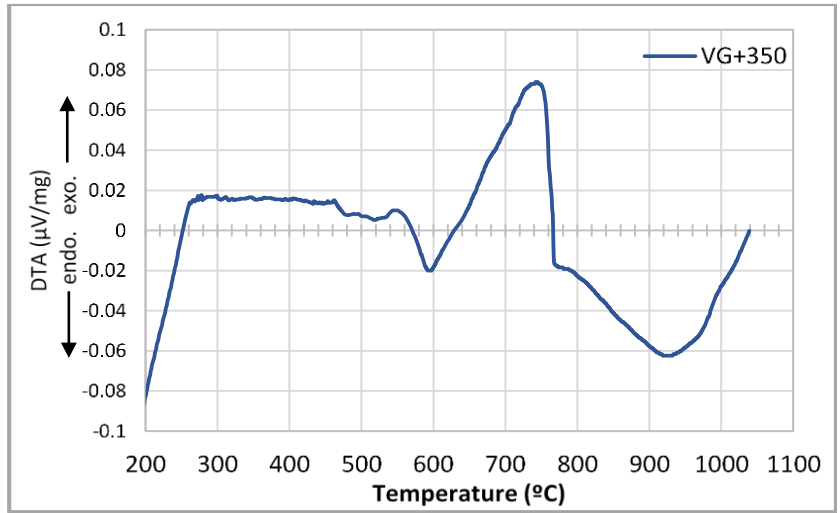
(b)
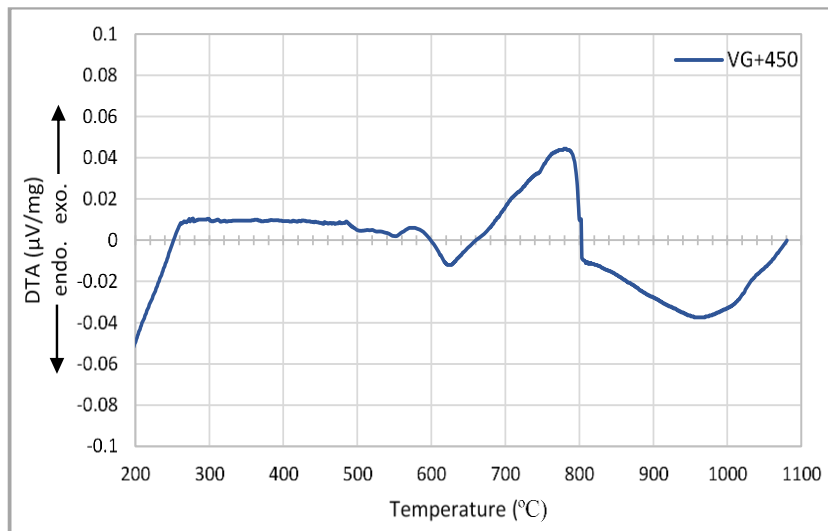
(c)

Figure 4-5 DTA for a) VG+150, b) VG+350, and c) VG+450 glass powder samples

Figure 4-6 shows a comparison between transition, nucleation, crystallization, and melting temperatures of various particle size samples. As displayed, when the particle grain size increases the intensity of crystallization decreases and crystallization temperature increases. The trends of variations are similar to the other phase transition parameters. This may be attributed to fact that the surface broken chemical bond is increased during crushing glass to fine grain size particles. This makes the particle surface highly reactive to bind to other particles that will fulfil these broken bonds. The chemistry structure of what is bonded on the material surface has a great influence on the core material crystallization and affects the sintering behaviour. Furthermore, sintering finer glass powder into a bulk material usually results in increasing the microstructure interfacial region between the particles. Such, interfacial regions increase the tendency of material to crystallize similar to the surface broken chemical bond. However, material surface chemistry, particle grain size and heat treatment conditions are also very important in controlling the crystallization behaviour.
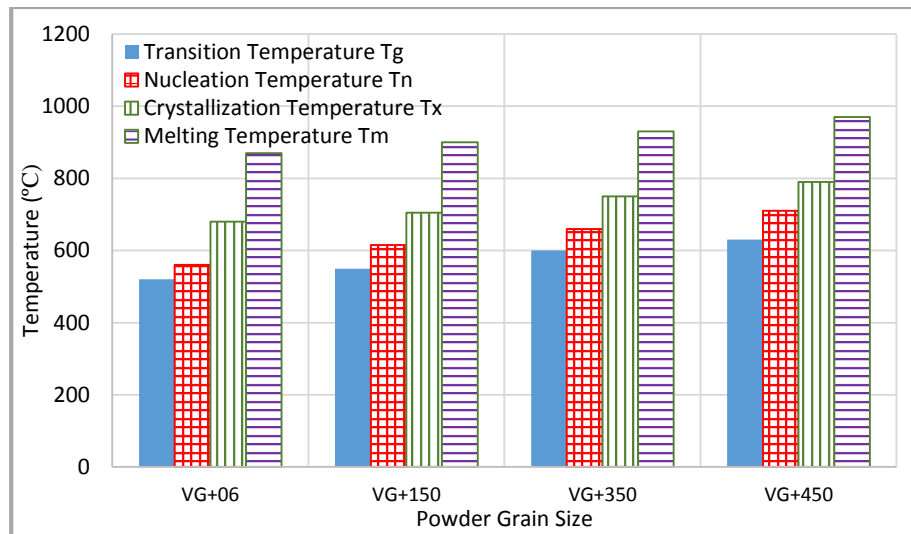
Figure 4-6 Comparisons between transition, nucleation, crystallization, and melting temperatures for range of grain size samples

4.6   Thermal treatment of recycled powder glass

Thermal treatment is the transfer of energy to the material to be heat-treated. Generated energy can be conducted by two methods. Direct heat-treated method, the energy transfer to material itself such as (induction, infrared microwave, and exothermic reaction). Indirect method, the heat generated in the material by the action of the heat source during conduction, convection, and radiation or a combination of these parameters.

Commonly, the industrial heat treatment process is employed by combustion or electric heating systems. Time and temperature are the most important parameters, which should be controlled during the heat treatment process, which is significantly affected by the material properties of specimens. Although, several heat transfer numerical simulation tools are available to predict the heat transfer of the specimens in the furnace, such numerical simulations require complex boundary condition parameters, and therefore the industry thermal treatment cycle design and optimizations are based on experience and empirical rules.

In this study, a range of mould materials has been used to investigate the effect of mould material on the heat transfer and sticking behaviour between specimen and moulds. For optimal mould material, a set of experiments has been conducted to investigate the effect of the heat treatment cycle on the final product of recycle a glass media. Then, SEM, XRD, 3-D digital optical microscope, and stylus contact Profilometer were employed to examine the morphology, crystallinity, and surface roughness of samples for a given heat treatment cycle to evaluate the time- transformation temperature (TTT) of glass media. The flow chart in Figure 4-7 shows the procedure of the heat treatment cycles and optimal TTT curve evaluation for thermal treated recycled glass media

4.6.1 Experimental setup and procedure

The experimentel setup is shown in Figure 4-8. The system consists of an electrical programmable furnace of 3-ramps heating rate programme, the maximum working temperature to within 1000 ±10 ºC. The temperature control and data recording solution permit to space the heating rate, maximum temperature, dwell time and cooling rate according to the heat treatment cycle requirements as is shown in Figure 4-8 (1). K–type (1.5×1000 mm , up to 1000°C) thermocouple has been connected between the mould and data acquisition device to measure the temperature variance of the mould during the heat treatment cycle as is shown in Figure 4-8 (2). Figure 4-8 (3) shows the TC-08 Thermocouple Data Logger (data acquisition) connected between the thermocouple and PC by USB port to record temperatures over a permissible range from -270 °C to 1760 °C with an accuracy of ± 0.5 °C.

The data acquisition system used to convert the electrical signal imported from the thermocouple to °C values with a milli-second interval time. Figure 4-8 (4) show the Picolog software tool. This software is a powerful data acquisition programme that is used to extract and record the temperature change with time from the data logger, analysis, sampling data, and export the results for interpretation in other software programmes such as Microsoft office. The experimental procedure consists of many stages. The first stage was furnace calibration without loading a part throughout distinguish the actual temperature measured by the k-type thermocouple adapted inside the furnace chamber and the reading recorded from the furnace gauge during a full heat treatment cycle setup of [(heating rate=21.5°C / min), L1 (maximum temperature=860°C), d1 (dwell time=50min) , C1 (cooling rate 15°C / min)]. The difference between the two readings was ± 10 °C, which is considered as an acceptable accuracy. The second stage was the mould preparations for test starting with drilling a Ø1.5mm hole at position in the centre of the media cavity in order to let the thermocouple probe go through the mould and interface with media for temperature measurement requirement. For sticking behaviour, the mould cavities were sprayed with a release agent (boron nitride), then filled by glass powder size VG+350. The third stage can be summarized by assembling all parts together and placing the mould inside the furnace chamber at the bottom where the temperature is always homogenous.
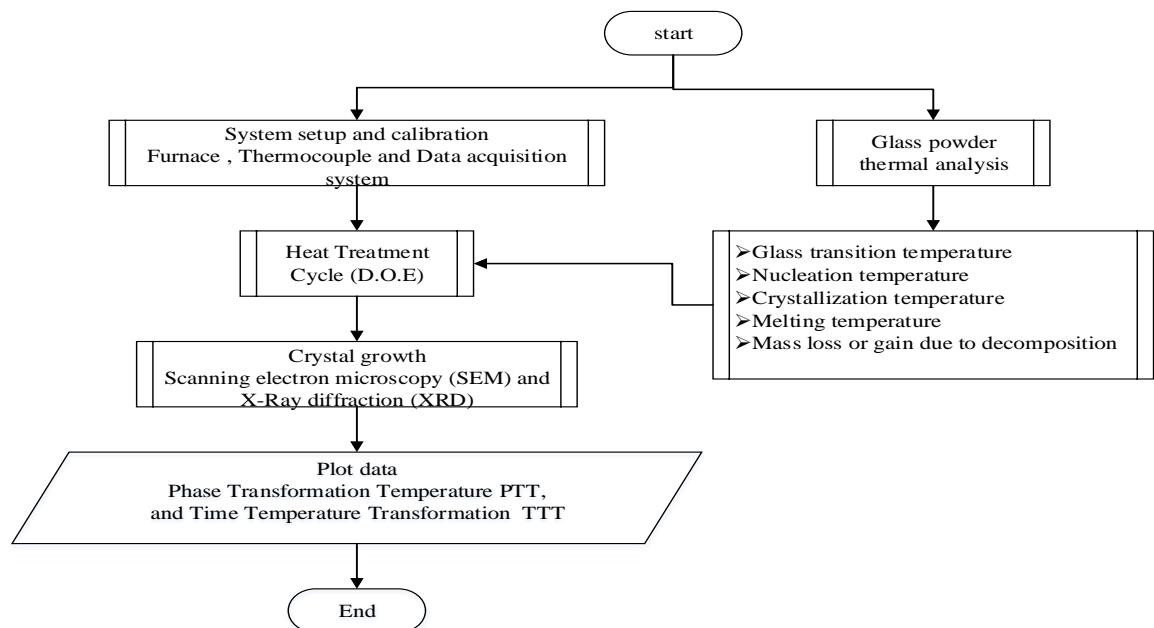
Figure 4-7 Flow chart of optimal TTT curve determination for thermal treated recycled glass media
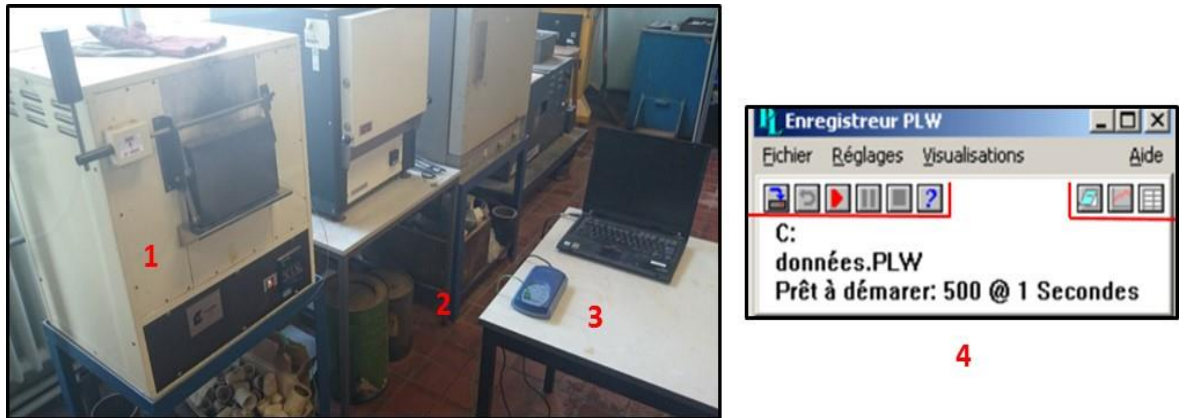
Figure 4-8 Experimental setup of heat treatment cycles including 1) Furnace, 2) Thermocouple, 3) Data acquisition, and 4) Data analysis software

4.7   Refractory mould analysis and sticking behaviour

Sintering the glass powder into dense material at high temperature may be accompanied with glass particles tend to stick to the refractory mould due to the wetting phenomena of the surface that is in contact.

This will be overcome by controlling the differences of the surface tension between materials. Surface tension of particles in contact is the energy required to increase the surface of an interface by a unit area. The surface tension of liquid (or glass) might be affected by the attraction of particles in the surface by the bulk material, which leads to minimizing the surface area. Three different surface tension interfaces are involved in the sintering mechanism between the glass powder and mould (wettability), liquid-solid, liquid–vapour, and solid-vapour. Differences in control between these interface surfaces are very important to prevent sticking behaviour. Wetting surface is controlled when liquid –vapour surface tension has to be less than solid- vapour surface tension to ensure ease of removal of the dense part from the mould. Therefore, the surface tension of the release agent should be less than that of the glass powder, such conditions mean that the glass spreads across the mould to lower the energy of the system.

The surface tension of soda lime glass varies with the change of material composition, however it is relatively low compared with other materials due to dynamic behaviour at high temperature .Therefore, there is a limited range of materials that can act as a release agent for glass and other material systems Kingery (1960), and Bansal and Doremus (2013).

There are many other factors that have an influence on the release agent performance in addition to the surface tension, such as: the release agent particles should strongly bind together and then to the refractory mould to keep the release as a separating layer when the glass particles tend to stick; the rate of diffusion and dissolution into the glass particles, a good release agent should have low rates of diffusion and dissolution; high melting temperature and not form low melting structure when interfaced with glass particles; stability and reliability, the release agent should be designed to maintain the composition unchanged during the repeated firing process.

The mould stiffness is also an important parameter in the sticking phenomena, mould distortion, and/or erosion due to the high temperature, or repeated firing process may lead to weakening the bond between release and solid particles. With these conditions, a release agent will separate from the mould when some sticking occurs. The refractory mould material should have a very strong atomic bonding, which will tend to resist dissolution and diffusion into the glass particles.

Commercial release agents are typically made from mixtures of kaolin and silica or kaolin and alumina hydrate (Nelson 1966). A series of reactions and phase changes occur during firing at high temperature.

This continuous change during repeat firing will have an effect on the release performance. Boron nitride release provides better performance with glass materials compared with kaolin & silica or kaolin & alumina hydrate. Moreover, the surface tension at elevated temperature is less than the surface tension of soda lime glass. The main properties of boron nitride coatings are: Excellent release properties with low layer thicknesses, excellent heat resistance, not wetted by most molten glasses, short drying times corrosion resistance to molten metals and molten glasses, release particles strongly bonded together at high temperature.

4.7.1   Results and discussions

To reduce the number of variables involved, a single glass source was used throughout the experiments. Potters crushed recycled glass VG+350 was chosen because it provides the best material properties as described in the previous Chapter (3). Boron nitride was selected as a release agent in all firing trials.

A standard firing profile was used for all firings involved in this study. The heat treatment experiments were carried out using a programmable time-temperature cycle with the following setup parameters: heating rate of 19°C /min up to 760°C, holding time at 760°C for 50 min, cooling rate of 8.5°C/min. Because there is no cooling fan adapted with this furnace, the cooling rate was adjusted by controlling the gap of the furnace gate using different sizes of shim spacer. When the heating temperature reduces to 250°C, the mould is removed from the furnace and allowed to cool down to room temperature in the static air. Figure 4-9 shows different cooling rate profiles based on the different gaps of the furnace gate using three shim sizes. Natural cooling, the gate is fully closed, cooling cycle 1 (2mm shim) cooling cycle 2 (4mm shim), cooling cycle 3(6mm shim). The results suggested that the cooling cycle 3 satisfied the cooling rate of 8.5°C/min; therefore, the shim size of 6mm was adopted in all experimental works. The experimental cooling rate profile will validate the cooling rate of FEM (Chapter 5) in order to predict the residual stress after Heat treatment cycles and the results were compared with XRD experimental data.

Figure 4-10 shows the four different types of refractory mould materials used with the same dimensions of cavities (Ceramic, Ceramic pre-coated, silicon carbide, and vermiculite) to investigate the mould stiffness and sticking behaviour over the same heat treatment cycle. All moulds were sprayed with the same amount of Boron nitride.

The release-coated moulds were then filled with glass powder. The stick-ability of moulds was examined after repeat firings, without recoating the release, and with new glass powder filled in the moulds after each firing. A semi-quantitative rating system was used to evaluate the release performance with different mould materials, as listed in the Table 4-1. Ratings of 1.5, 2.5, 3.5, and 4.5 were used to further distinguish the differences in performance. The experimental error in ratings is estimated to be < 0.5 of a rating point.

Table 4-1 Semi-Quantitative mould rating system

Rating	Descriptions
1	No sticking
2	Slight sticking visible
3	Moderate sticking
4	Severe sticking
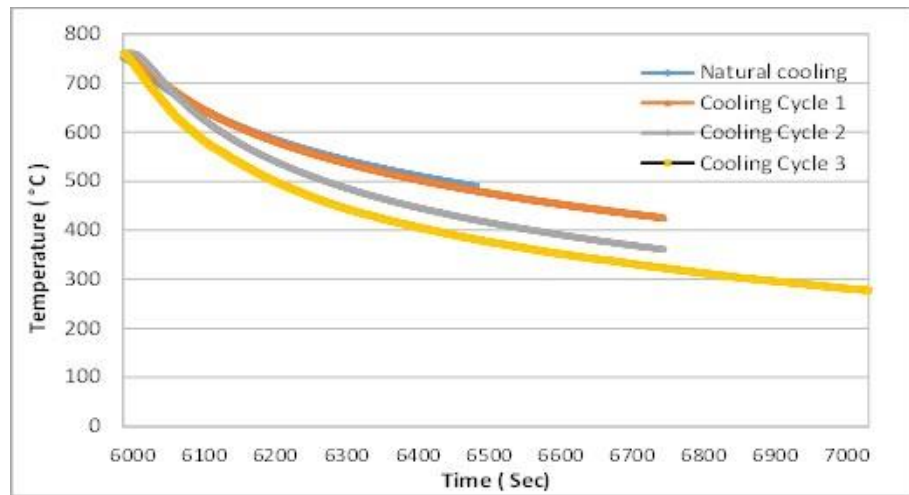
Figure 4-9 cooling rate profiles at, Natural cooling, cooling cycle 1, cooling cycle 2, Cooling cycle 3
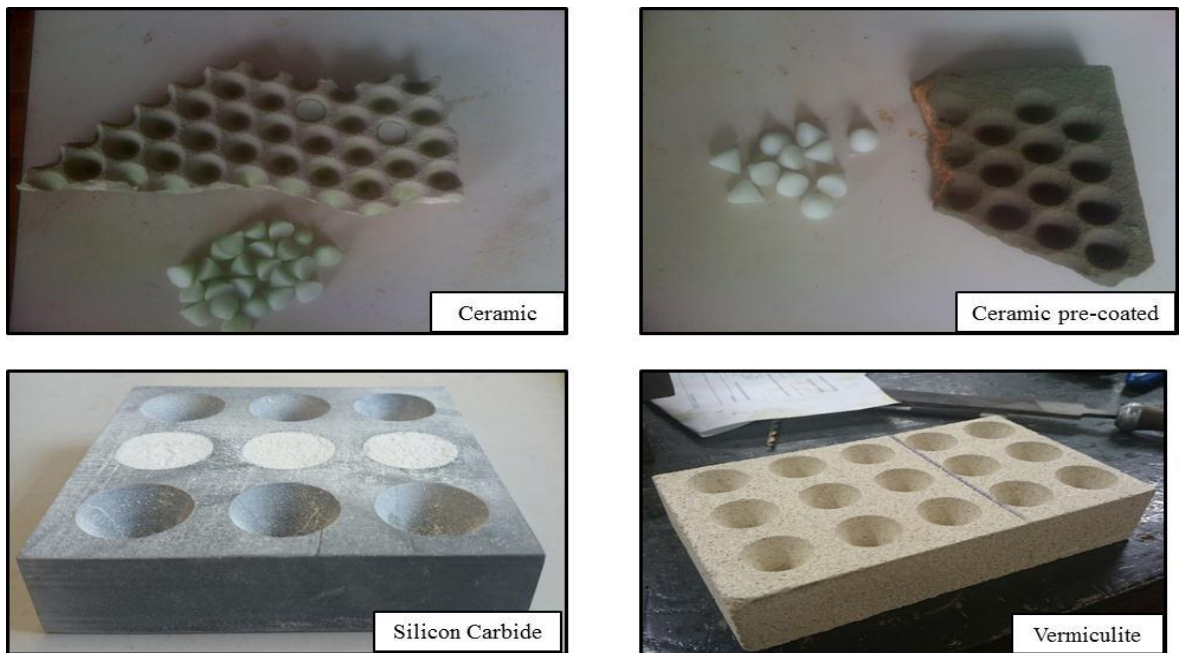
Figure 4-10 Refractory mould images of (Ceramic, Ceramic pre-coated, Silicon carbide, and Vermiculite)

Figure 4-11 shows the relationship between moulds rating versus the number of firings using boron nitride agent. For more accuracy, the data plotted were for running averages of five data points and measurement settings rate every half point after firing. The (Ceramic, Ceramic pre-coated, and vermiculite) moulds stuck severely to the glass with different numbers of firing and rating values, while no sticking has been occurred from the silicon carbide mould over 10 times of firing.

Ratings of 2 and below indicate acceptable sticking, while ratings 3 and above are considered unacceptable. The results demonstrated that the release agent with vermiculite degraded more rabidly at firing number 4 resulting in severe sticking occurrence , while the Ceramic, Ceramic pre-coated moulds degraded at firing number 7, and 8 respectively. These results indicated that the surface tensions vary with the mould composition. The surface tension of vermiculite, Ceramic or Ceramic pre-coated is greater than silicon carbide surface tension, resulting in greater bonding and diffusion with the release compound in comparison with silicon carbide. The observation after repeat firing suggested that the silicon carbide stiffness was much higher than other moulds, which show micro-cracks initiated and propagated during continued firings.
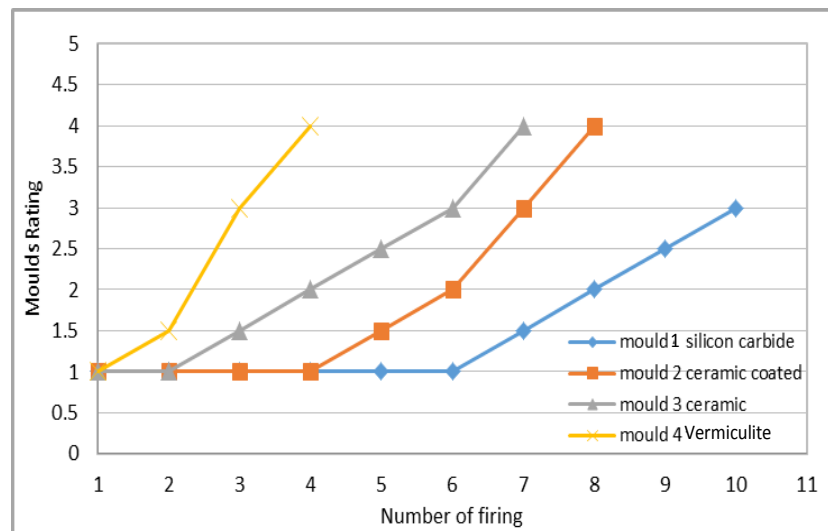
Figure 4-11 Relationship between moulds rating versus the number of firings using boron nitride agent

Figure 4-12 shows the thermal history output of the moulds under investigation using same heat treatment cycle parameters of, heating rate 20.5 C/min to maximum temperature of 820°C, holding time at 820°C for 50 min, cooling rate of 9.5 using 6mm shim to 250°C. As displayed the thermal conductivity for the silicon carbide was better than ceramic and vermiculite moulds. The maximum temperature of 820°C was achieved at the end of ramp 1 with an error of -20°C. While, the ceramic and vermiculite moulds reached 760°C and 730°C, respectively at the end of the holding time. Therefore, the outcome from sticking, stiffness, and thermal analyses suggested that the silicon carbide mould together with boron nitride agent has been identified as the most appropriate solution for the thermally treated recycled glass powder process.
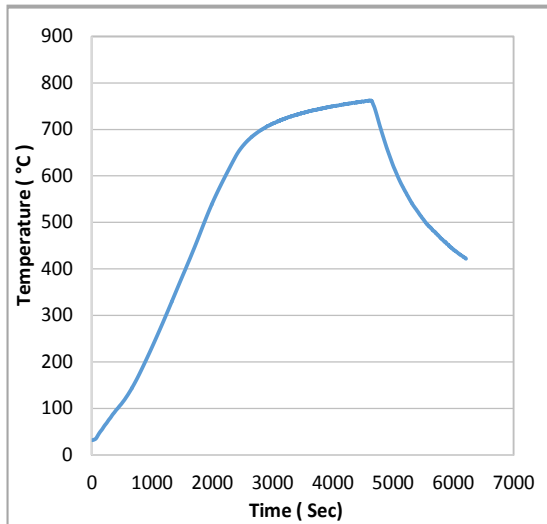
(a) Ceramic Mould
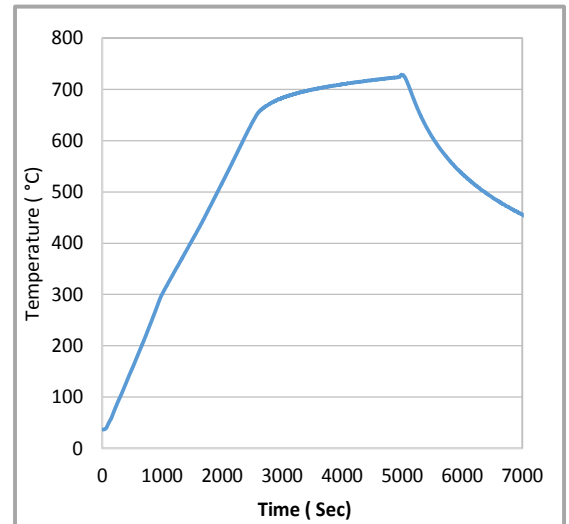
(b) vermiculite moulds
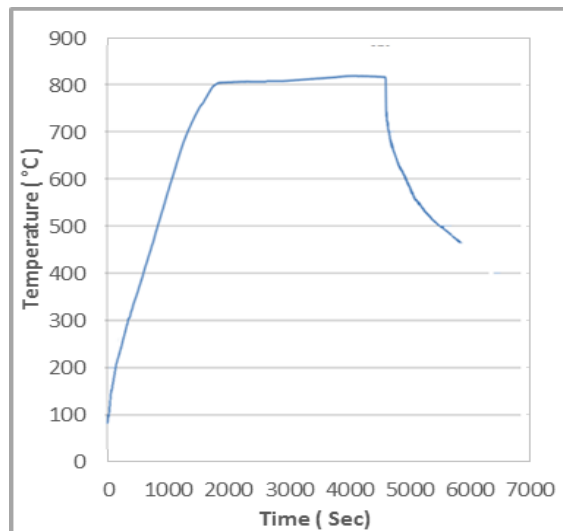
(c) Silicon Carbide Mould

Figure 4-12 Thermal history output of a) Ceramic Mould, (b) vermiculite moulds, and (c) Silicon Carbide Mould

4.8   Heat Treatment Cycles (Design of experiments)

Heat treatment cycles were carried out on glass powder VG+350 using a matrix of 36 experiments, heating time range $(40 < r1 < 60)$min maximum temperature range, $(VT + 60 \geq VT \geq VT - 100)$ºC. The maximum temperatures for the heat treatments were chosen according to crystalline temperature Tx value $(Tx \pm 100 \,°C)$ obtained from DTA. The holding time range $(10 \leq d1 \leq 60)$min. cooling rate fixed for all experiments using 6mm shim.

The mould cooled down inside the furnace to about 230°C - 300°C depending on maximum temperature range, then removed outside the furnace to cool down to ambient temperature. However, this difference is acceptable from the glass cooling rate point of view. These firing conditions produced dense samples with different crystalline and surface roughness values. Microstructural analysis was performed by running averages of three samples of glass media from each patch using XRD, and SEM. The outcomes are concluded on the TTT graph. Moreover, 3-D X-ray computed tomography was employed to detect inclusions and voids of three samples at different heat treatment cycles.

4.8.1   X-ray diffraction and crystallographic structure

X-ray diffraction (XRD) is a non-destructive technique used to characterize the crystallographic structure of manufactured materials. This technique is widely used in material characterization and process control as it provides fundamental details about lattice structure of single crystal, phase transformation, residual stress evaluation of crystalline materials, and texture analysis. The crystallinity phases formed were identified using XRD, (mini-Flex). The radiation CuKα type was used in the 2θ range from 3° to 90° (with 0.02° sampling width) on glass powder samples before and after heat treatments. Continued scan mode was employed with scan speed of 2°/min. The samples were prepared for XRD test by sintering the glass powder at different thermal cycles as described in the previous section (4.8). After heat treatment cycles, the media samples were ground to a fine powder corresponding to the XRD requirements.

Figure 4-13 shows the XRD analysis determined on amorphous glass powder sample and heat-treated samples at various temperatures. Figure 4-13 (a) illustrates the crystallinity phase of the glass powder before heat treatment, the material exhibited a fully amorphous property. The XRD analysis in Figure 4-13 (b) suggested that the first crystalline phases were developed at maximum temperature of VT-70, and holding time of d1=50 second. This is in agreement with results obtained from DTA in Figure 4-5 (b). At VT-70 the binary system of $Na_2O \cdot SiO_2$ began to form and then the crystalline structure of α-$Na_2O \cdot 2SiO_2$ and β-$Na_2O \cdot 2SiO_2$ developed, this amount increased with the increase of the heat treatment temperature. Figure 4-13 (c) shows heat treatment at VT-10, d1= 40 second, another $Na_2O \cdot 2CaO \cdot 3SiO_2$ (NC_2S_3) phase was identified and become the main crystalline phase, although there was no evidence of this response in the DTA data.

This phase began to precipitate increasing intensity (cps) with increasing heat-treatment temperature as is shown in Figure 4-13 (d). The most dramatic phase change occurred at VT+100, were the relative amount of NC_2S_3 crystal has dropped during the endothermic transition as described in the DTA Figure 4-5 (b).
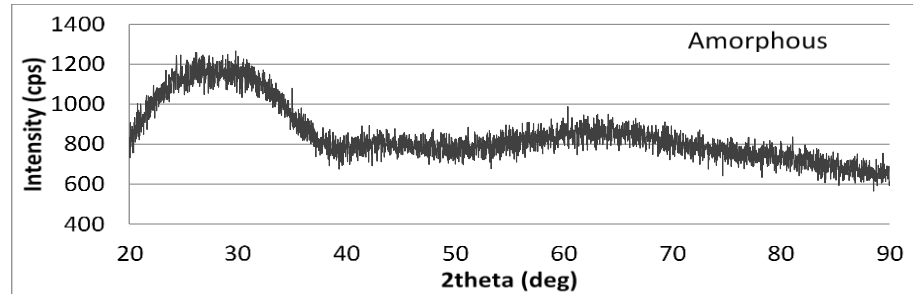
(a)
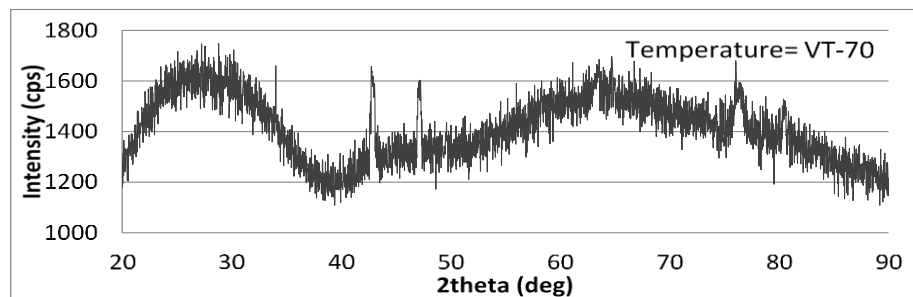
(b)
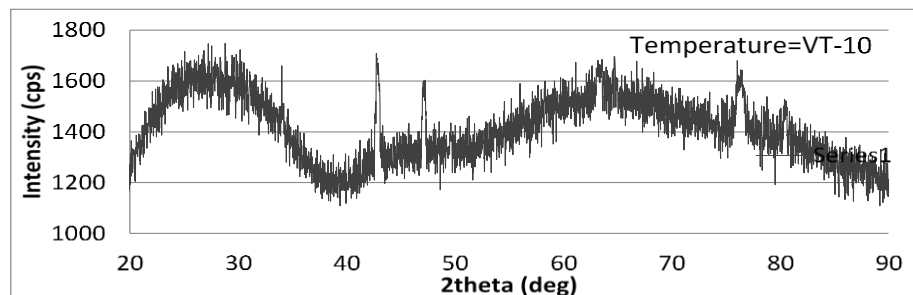
(c)
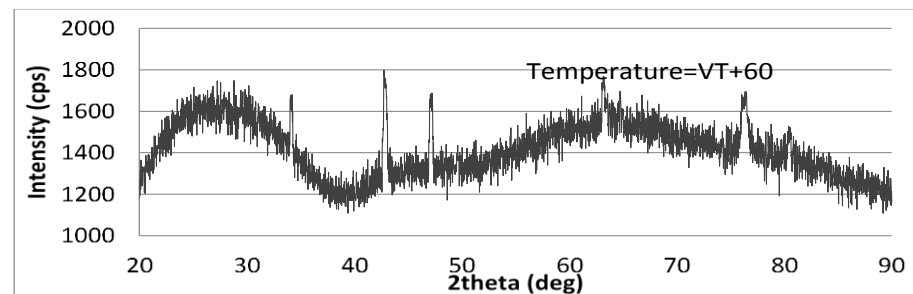
(d)

Figure 4-13 XRD analysis of a) amorphous VG+350 glass powder, and heat treated at b) VT-70, c) VT-10, and d) VT+60

4.8.2   Scanning electron microscopy and micrograph analysis

Scanning electron microscopy Hitachi TM3800 at LJMU was performed for the microstructure analysis of thermally treated recycled glass media obtained from different heat treatment cycles. The glass media samples were prepared for SEM analysis by grinding the surface with silicon carbide paper, then polishing with diamond paste. The polished samples were immersed into a HF solution for 30 seconds; this solution is used as an etching medium to enhance the grain structure and thus remove enough of the residual glass. Due to the reflection behaviour of glass, the media samples were finally coated with a thin layer of titanium or gold. Figure 4-14 shows the SEM images sequence of glass media obtained from amorphous and thermally treated recycled glass powder within the range of elevated temperature, $VT + 60 \geq VT \geq VT - 100$, and keeping the holding time and cooling rate unchanged of 50sec., and 9.5°C/min., respectively. It is clearly observed that the crystallization growth gradually increases as sintering temperature increases, the complete crystalline phase being reached at a temperature around, $VT + 60$. This crystal size increases because of gradual development of irregular clusters of smaller grains. This behaviour is in good agreement with XRD results.
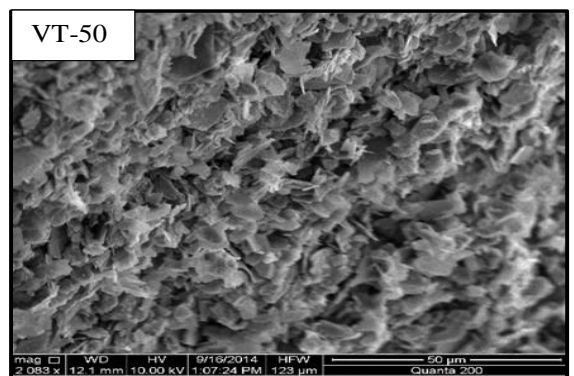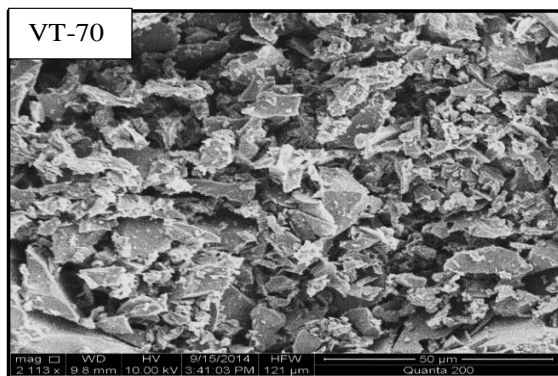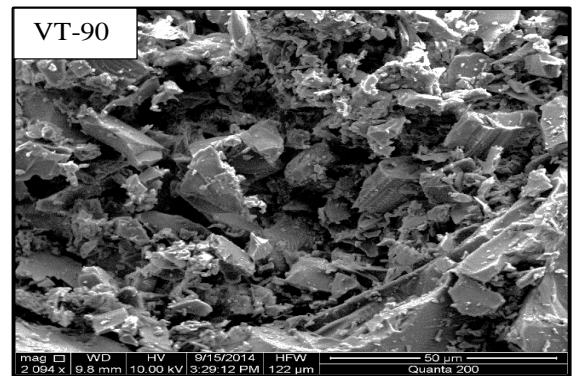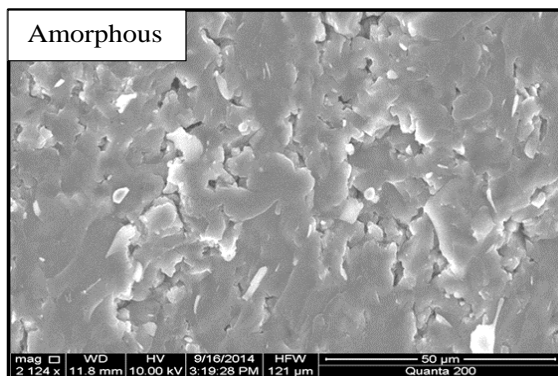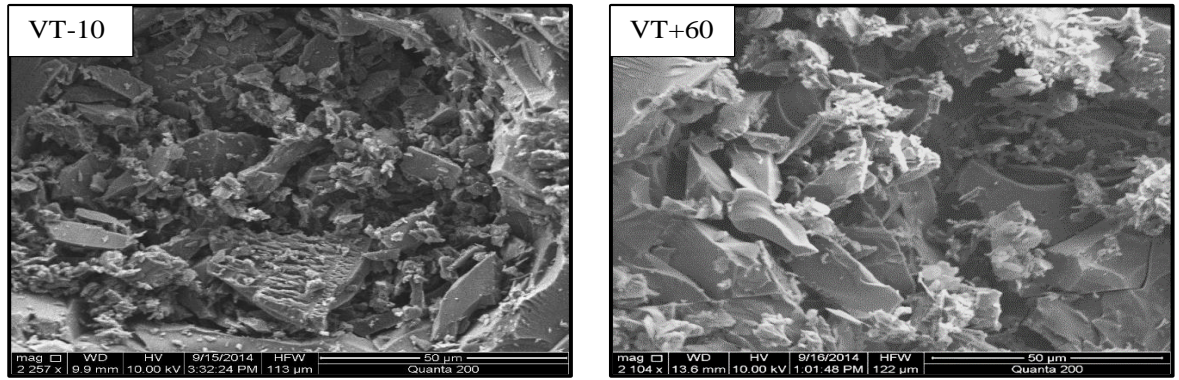
Figure 4-14 SEM images of VG+350 amorphous glass powder sample sintered at different temperatures of VT-90, VT-70, VT-50, VT-10, and VT+60.

4.8.3   Surface roughness measurements of glass media

The surface roughness of the three glass cones obtained from various heat treatment cycles VT-70, VT-10, and VT+60 (Figure 4-15) were measured using two different techniques. The first was a non-contact method using 3D digital optical microscope Keyence VHX-600. This method gives a semi-quantitative value with high-resolution 3-D images in a large depth of field. The data can be processed to generate a precise 3-D profile measurement with 5000× magnification. The second method is a stylus contacts Profilometer (Mar-Surf LD 120), which consists of combined contour and surface roughness measurements. The measurement accuracy is about 0.01μm.
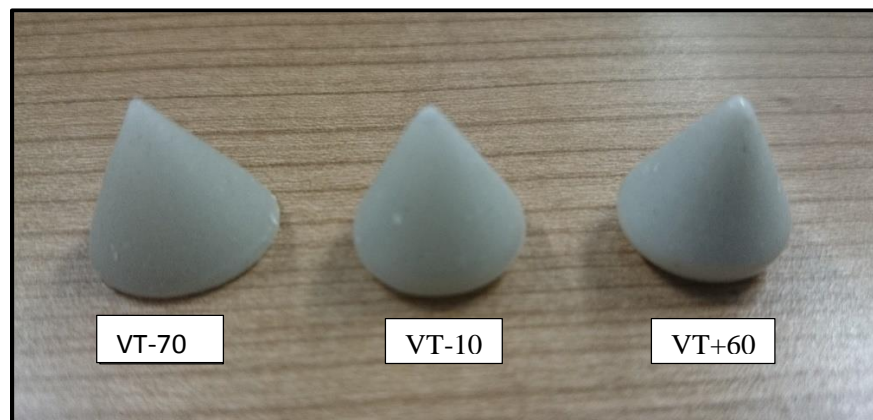
Figure 4-15 images of glass cone media produced by different heat treatment cycles

Figure 4-16 shows the 3-D microscopic scanning images covering an area of 0.5mm×0.5mm obtained by Keyence VHX-600 digital optical microscope of three different glass media samples determined from different heat treatment cycles of VT-70,

VT-10, and VT+60 using recycled glass powder VG+350. The colour mapping images show gradual increase of crystalline size represented by reducing peaks values when the heat treatment temperature is increased, this change developed significantly at VT-50 and above. Figure 4-17 shows the surface roughness measurement obtained by Mar-Surf LD 120. The surface roughness measurements agree with the results obtained from 3-D microscopic images. Five surface measurements were performed for each sample at different orientations, the average of the group results are presented in Table 4-2. Figure 4-17 present the surface roughness values (*Ra*) for three different glass media samples. As displayed, the surface roughness decreases when the heat treatment temperature increasing.
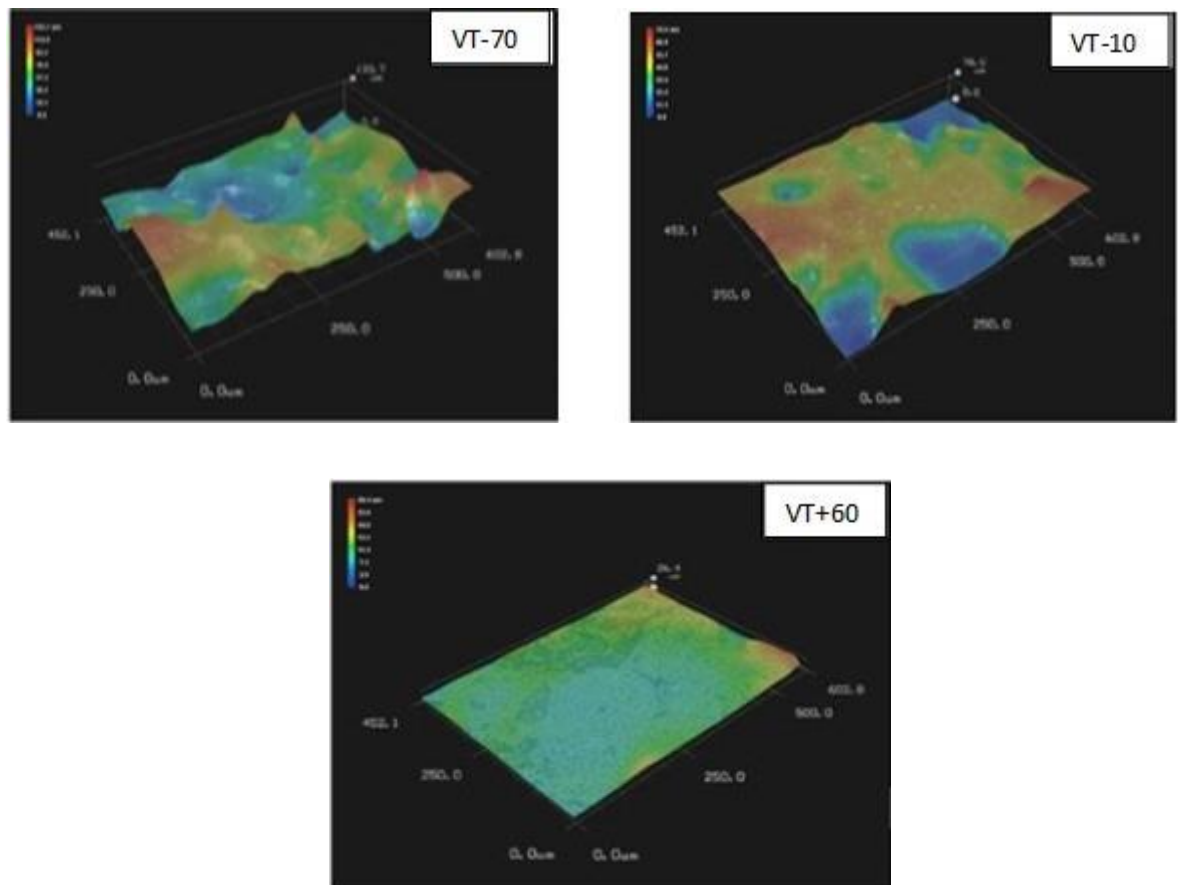
Figure 4-16 3-D microscopic scanning images of VG+350 glass powder sample sintered at different temperature VT-70, VT-10, and VT+60.

Table 4-2 Average surface roughness results of thermally treated glass samples

Sample	Ra (µm)	Rq (µm)	Rt (µm)
Cone (VT+60)	0.21	0.36	5.26
Cone (VT-10)	9.87	13.25	92.41
Cone (VT-70)	16.82	21.21	108.65
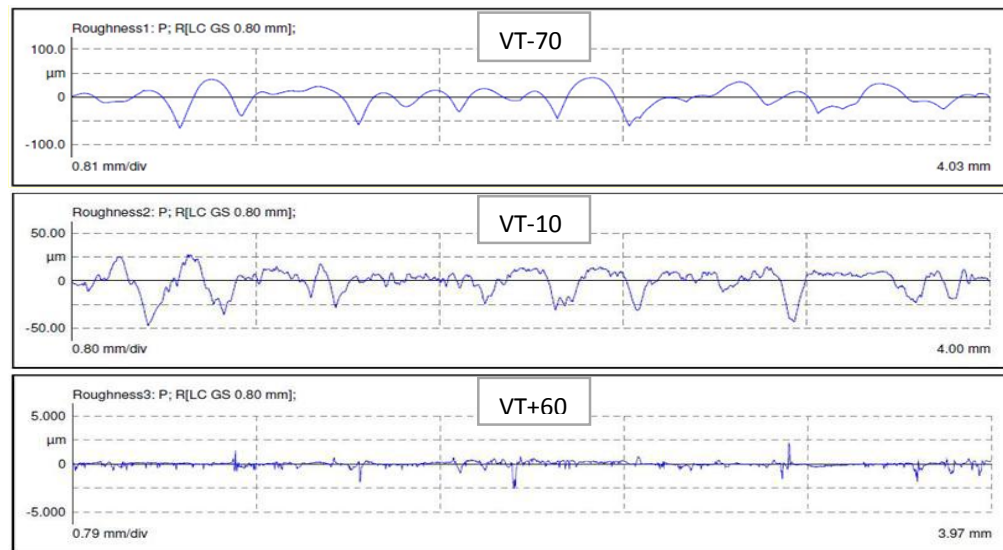
Figure 4-17 Surface roughness results of VG+350 glass powder sample sintered at different temperature VT-70, VT-10, and VT+60

However, the results from (36) heat treatment cycles can be concluded in Figure 4-18. Figure 4-18 shows that the mean crystallizing size was determined together with surface roughness as a function of maximum sintering temperature. The influence of temperature on the surface pattern of the media can be clearly observed. It is clearly observed that the present crystallization size (SEM) increases as the sintering temperature increases especially above VT-100, which yields a change in the number of cutting edges. This may be attributed to the fact that the growth of grains size takes place resulting in enhancing the clustering of crystallization phases. It is evident that even small changes in temperature vary the structure and hence properties of the glass media. Furthermore, by controlling temperature one can produce media that will function as either a cutter or polisher.

As consequence, the surface roughness decreases with increasing sintering temperature. This could be associated with the grain size increases, resulting in decreasing the differences between the peaks and valleys of the profiles detected by stylus contact Profilometer. However, the results demonstrated in Figure 4-18 can be used as control tool to manufacture a particular glass media suitable for industrial application. The change in temperature leads to a change in the rate of crystallinity. The lower temperature, in general, will generate a higher number of smaller crystals, and thus impact positively on the number of crystal edges on the surface of the media (cutting edges). However, this is not always the case because the mould volume, cullet size, mould material and quench rate also have an important role in determining rate of crystallinity and crystal size.
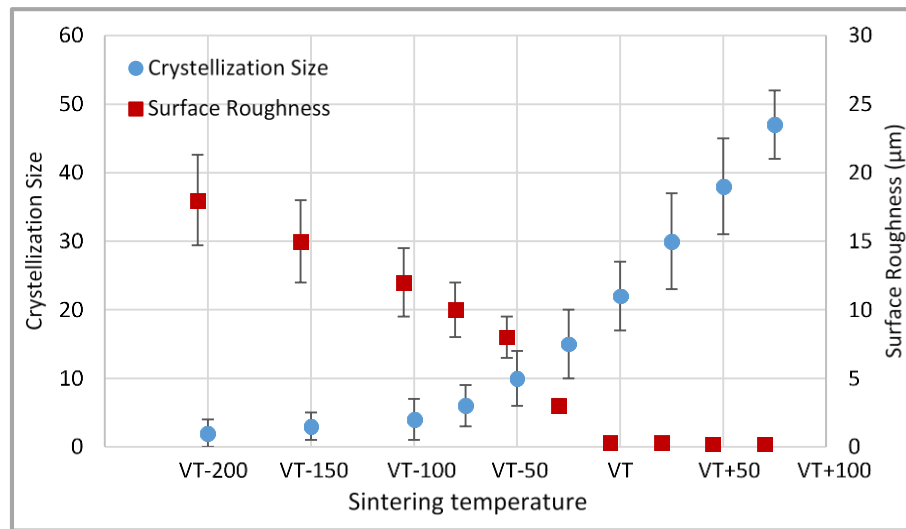
Figure 4-18 Crystallization size and surface roughness of the recycled glass powder sintered in the range of temperatures between VT-200 and VT+100

4.9   Time Temperature Transformation results

Figure 4-19 shows the TTT diagram for the crystallisation of the thermally treated recycled media illustrating in a C-shaped curve, which represents the characteristic of nucleation and growth processes. Partial crystallization of the glass material is observed after thermal treatment of VT-100ºC, and 50 minutes holding time. The start of crystallisation is recognized after 60 minutes holding time with heat treatment temperature of VT-70ºC. This could happen at lower holding times, but the sintering temperature need to increase. The samples are fully crystallised at 40 minutes holding time and VT-30ºC. At or above VT+10ºC, full crystallisation is reached within a very short heating time of 30 minutes.
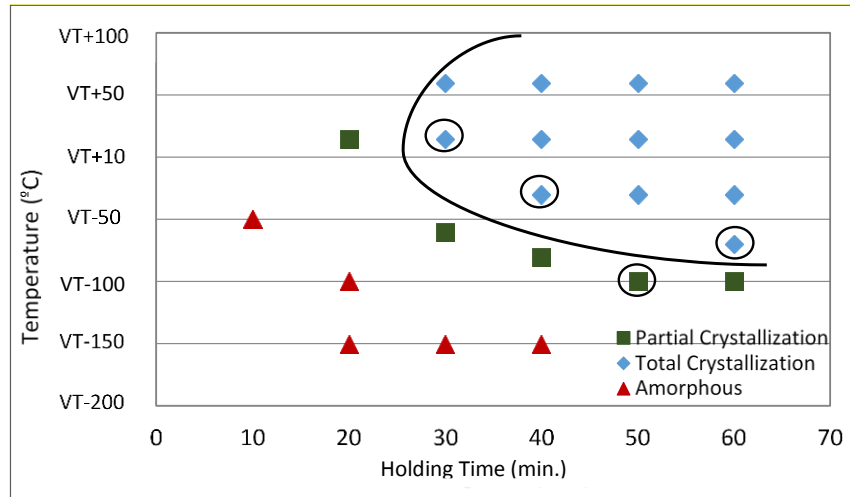
Figure 4-19 TTT diagram for the crystallisation of thermally treated recycled media (▲ amorphous, ■ partial crystallisation, and ◆ total crystallisation).

4.10 3-D X-ray computed tomography (CT) analysis

3-D X-ray computed tomography CT (Nikon XT H) at the MTC was employed to investigate the porosities and inclusions of three-glass cone samples which were heat treated at different thermal cycles of (VT-70, VT-10, and VT+60). The porosity/or void was determined by the feature as a low-density region, and looked darker on the CT image. Whereas, the inclusion showed as a high density region compared with the surrounding zone, and looked brighter than the base material.

All samples were scanned under the same parameter conditions of power (215KV, 185μA), filter material (copper), and filter size (0.1mm), exposure (250ms), number of projections (3142) with one frame per projection. The sample was placed on a plastic surface to separate it from the fixture, and moved as close as possible to the X-ray source to ensure maximum magnification. The 3-D CT PRO software package was employed for reconstructing the projected images and building a 3-D volumetric scan. A beam hardening pre-set and noise pre-set were applied to the reconstruction for optimum image quality.

Figure 4.20 shows CT images of the three glass media samples at different heights from the bottom of the cones. The heights were determined by fitting a plane to the cone base and aligning the slices to this plane, thus the fitted plane represents the reference point. The positions of the images were taken approximately 2mm, 5mm, and 10mm above the reference point. The surface for the high-density regions (inclusions) was identified, and then the auto detection tool was used to pick out the high-density regions.

The regions were then stored sequentially, according to the surface area size, the four largest regions were measured using the calliper tool adjusted in the same software. These inclusions generate a crystalline phase change in smaller form and are fixed within the material structure upon cooling. Such an occurrence is usually used negatively such as when the region could act as a fatigue crack nucleus or/and area of high stress intensity. The same procedure has been used to pick out the low-density (voids) regions from the surface by the auto detection tool and compared using the adjusted calliper. These measurements are not to scale, and only give an estimate of the size. The results from the software based on the image analysis suggested that the sample with heat treatment cycle VT-70 showed the most high-density regions and most low-density regions, indicating that there were many inclusions and porosities, respectively. The results proposed that the inclusion and void defects were reduced by increasing the sintering temperature due to the diffusion phenomena. The outcomes from 3-D X-ray CT analysis agree with results obtained from contact surface roughness (Mar-Surf LD 120) where the increases of the porosities size will lead to increases in the differences between the peaks and valleys resulting in high surface roughness values. The images also demonstrated that the voids and inclusions increase with the increasing of height from the bottoms, regardless of thermal cycle. If the grayscale intensity value was similar to that of the material then there is a possibility that the area could be noise or just not picked up from a surface determination. This may attributed to fact that the porosity can also be determined by grayscale values.

2mm height from the bottom

| VT-70 | VT-10 | VT+60 |

5mm height from the bottom
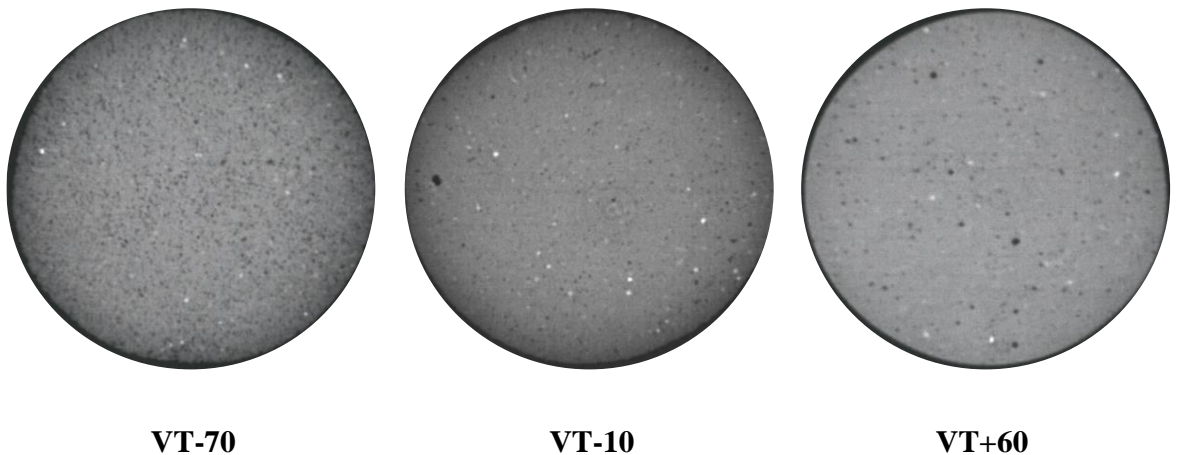
| VT-70 | VT-10 | VT+60 |
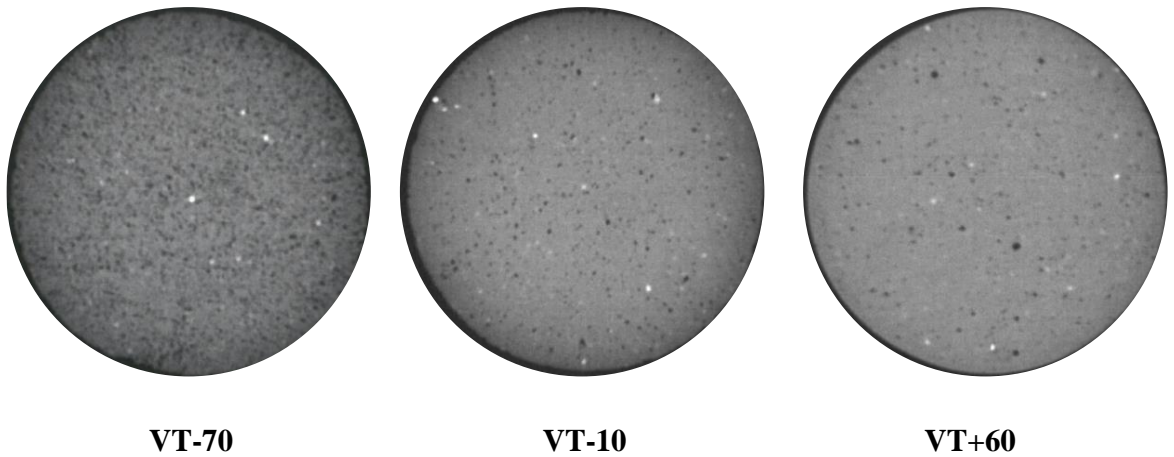
10mm height from the bottom
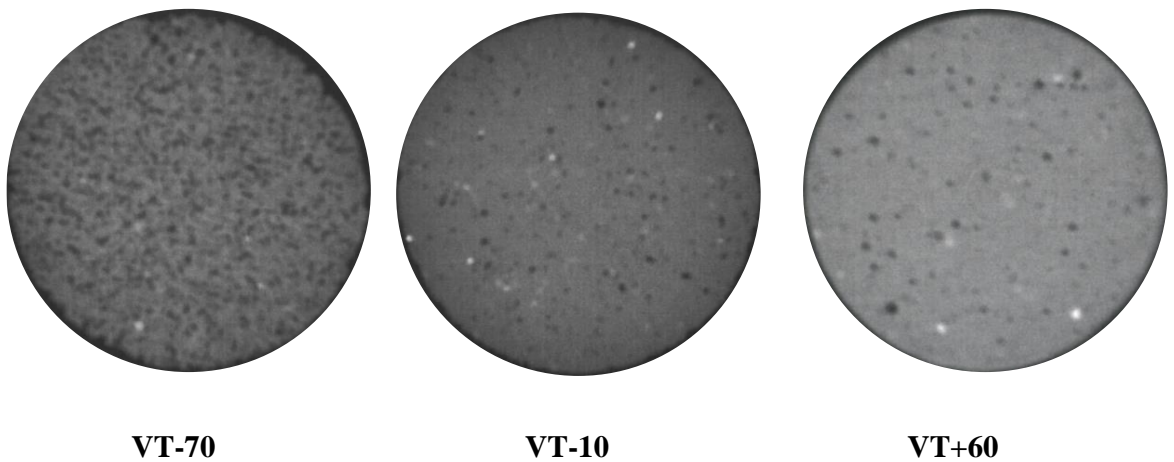
| VT-70 | VT-10 | VT+60 |

Figure 4-20 3-D X-ray computed tomography images of the three glass media samples VT-70, VT-10, and VT+60 at 2mm, 5mm, and 10mm height from the cones bottom

4.11 Conclusion

Thermal analysis of recycled soda lime glass powder has been successfully applied to determine the optimal particle size parameter for heat treatment cycles. TGA analyses of a range of particle sizes suggested that the weight loss increases with the increasing particle size due to the catalyst particles and other carbon impurities. DTA analyses demonstrated that the particle size increases as the intensity of crystallization decreases and crystallization temperature increases. The trends of variations are similar for the other phase transition parameters (T_g, T_n, and T_m). This may be associated with the fact that the surface broken chemical bond is increased for the fine grain size particles.

The heat treatment cycles set up were selected corresponding to the phase transition temperature information obtained from TDA analysis. The outcomes from TGA, TDA, and Rheology analyses suggest that the particle size VG+350 is considered as a best grain size solution for the production of glass media in terms of decomposition, nucleation and crystallization growth, flow-ability and packing characteristics.

The effects of different mould material on the heat transfer and sticking behaviour between the specimen and mould have been investigated. A semi-quantitative rating system was developed to compare the sticking behaviour and a special experimental arrangement was also established to distinguish the thermal histories. The outcome from sticking, stiffness, and thermal analyses suggested that the silicon carbide mould together with boron nitride agent was the most appropriate solution than other material moulds for thermally treated recycled glass powder process.

Design of experiments (DOE) has been used to investigate the effect of heat treatment cycle on the final product of recycle glass media. Then, SEM, XRD, 3-D digital optical microscope, and stylus contact Profilometer were employed to examine the morphology, crystallinity, and surface roughness of the product for a given heat treatment cycle to evaluate the time- transformation temperature (TTT) to aid delivery of a range of glass media used as abrasive tools in the mass finishing process of engineering materials.

The microstructural evolution suggested that the crystallisation starts with a heat treatment cycle of (VT-70ºC, and d1= 60 minutes). Further increases in temperature resulting in gradual increases in the grain and crystallite sizes, the optimal heat treatment cycle to transform the partial crystalline glass to the fully crystalline was within 30 minutes holding time and VT+10ºC sintering temperature. The tendency of crystals' growth increases significantly at VT+50. This may be attributed to increased diffusion phenomena favoured by the high temperatures. Meanwhile, the surface roughness decreases with increasing sintering temperature due to the grain size increases. However, the results proposed in Figure 4-17, and Figure 4-18 can be used as a quality control tool to distinguish the glass media and to identify the correct media size and grain for different industrial application.

3-D X-ray computed tomography was conducted to investigate the porosities and inclusions developed in thermally treated recycled glass media. The results shows the most high density (inclusion) and low-density (porosity) area were identified in glass media sample under the VT-70 heat treatment cycle.

It is clearly observed that the inclusion and void defects were reduced by increasing the sintering temperature due to the diffusion phenomena.

Consequently, by selecting the suitable heat treatment cycle, it will be possible to obtain glass media with optimal mechanical properties and microstructure to satisfy the requirements of specific applications. Thus, VT-70, VT-10, and VT+50 can be defined as cutting media, general-purpose media, and finishing media, respectively.

4.12 References

Ashraf, M., A. N. Khan, Q. Ali, J. Mirza, A. Goyal and A. Anwar (2009). "Physico-chemical, morphological and thermal analysis for the combined pozzolanic activities of minerals additives." Construction and Building Materials **23**(6): 2207-2213.

Backman, R., K. Karlsson, M. Cable and N. Pennington (1997). "Model for liquidus temperature of multi-component silicate glasses." Physics and chemistry of glasses **38**(3): 103-109.

Bansal, N. P. and R. H. Doremus (2013). Handbook of glass properties, Elsevier.

Beall, G. H. and D. A. Duke (1983). Glass-ceramic technology. Glass: Science and Technology.

Boccaccini, A. R. and V. Maquet (2003). "Bioresorbable and bioactive polymer/Bioglass® composites with tailored pore structure for tissue engineering applications." Composites Science and Technology **63**(16): 2417-2429.

Cook, L., R. Roth, T. Negas and G. Cleek (1978). Phase diagrams for ceramists. Applications of Phase Diagrams in Metallurgy and Ceramics: Proceedings of a Workshop Held at the National Bureau of Standards, Gaithersburg, Maryland, January 10-12, 1977, US Department of Commerce, National Bureau of Standards.

F.W. Wilburn, J. B. D., in: R.C. Mackenzie (1972). "Differential Thermal Analysis." Applications, Academic Press,London **Vol. 2**: p. 238.

Fokin, V. M., M. L. Nascimento and E. D. Zanotto (2005). "Correlation between maximum crystal growth rate and glass transition temperature of silicate glasses." Journal of Non-Crystalline Solids **351**(10): 789-794.

Fokin, V. M., E. D. Zanotto and J. W. Schmelzer (2003). "Homogeneous nucleation versus glass transition temperature of silicate glasses." Journal of Non-Crystalline Solids **321**(1): 52-65.

Hancock, B. C. and G. Zografi (1997). "Characteristics and significance of the amorphous state in pharmaceutical systems." Journal of pharmaceutical sciences **86**(1): 1-12.

Holand, W. and G. H. Beall (2012). Glass ceramic technology, John Wiley & Sons.

Kingery, W. D. (1960). "Introduction to ceramics."

Lieth, R. (1977). Preparation and crystal growth of materials with layered structures, Springer Science & Business Media.

Marotta, A., A. Buri and F. Branda (1981). "Nucleation in glass and differential thermal analysis." Journal of materials science **16**(2): 341-344.

Nelson, G. C. (1966). "Ceramics: a potter's handbook."

Partridge, G. (1994). "An overview of glass ceramics. I: Development and principal bulk applications." Glass technology **35**(3): 116-127.

Paul, A. (1990). Chemistry of glasses, Springer Science & Business Media.

Ray, C. and D. Day (1996). "Identifying internal and surface crystallization by differential thermal analysis for the glass-to-crystal transformations." Thermochimica acta **280**: 163-174.

Ray, C. S., K. S. Ranasinghe and D. E. Day (2001). "Determining crystal growth rate-type of curves in glasses by differential thermal analysis." <u>Solid state sciences</u> **3**(6): 727-732.

Rincón, J. M. (1992). "Principles of nucleation and controlled crystallization of glasses." <u>Polymer-Plastics Technology and Engineering</u> **31**(3-4): 309-357.

Strand, Z. (1986). "Glass Ceramic Materials." <u>Elsevier, Amsterdam</u> **vol. 8**.

Vedel, E., H. Arstila, H. Ylänen, L. Hupa and M. Hupa (2008). "Predicting physical and chemical properties of bioactive glasses from chemical composition. Part 1: Viscosity characteristics." <u>Glass Technology-European Journal of Glass Science and Technology Part A</u> **49**(6): 251-259.

Vogel, W. (1979). "Glass chemistry."

Zanotto, E. and M. Prado (2001). "Isothermal sintering with concurrent crystallisation of monodispersed and polydispersed glass particles. Part 1." <u>Physics and Chemistry of Glasses-European Journal of Glass Science and Technology Part B</u> **42**(3): 191-198.

Zanotto, E. D. (1992). "Crystallization of liquids and glasses." <u>Braz. J. Phys</u> **22**(2): 77-84.

Zanotto, E. D. and V. M. Fokin (2003). "Recent studies of internal and surface nucleation in silicate glasses." <u>Philosophical Transactions of the Royal Society of London A: Mathematical, Physical and Engineering Sciences</u> **361**(1804): 591-613.

Zarzycki, J. (1991). <u>Glasses and the vitreous state</u>, Cambridge University Press.

CHAPTER FIVE

DETERMINATION OF THE RESIDUAL STRESS OF THERMALLY TREATED RECYCLED GLASS MEDIA SUPPORTED BY FEM SIMULATION

5.1 Introduction

Residual stresses are unavoidable phenomena, which are introduced during the manufacture of engineering components through inelastic deformation, heat treatment, and cooling. Residual stresses are developed in the bulk material in tension or compression without effect from external load, which remain after the original cause(s) has/have been removed. In the heat treatment process, during the cooling stage, the glass undertakes a second order phase transition from a viscoelastic solid to an amorphous or crystalline solid at room temperature. As a result, residual stresses are induced due to temperature gradients across the whole process, mechanical constraints given by the mould during the shrinkage and volumetric change of the material, and phase transformation plasticity. Therefore, residual stresses are a function of the mould and specimen shapes and the cooling rate of the heat treatment cycle.

Generally, compressive residual stresses are a desirable component as they enhance the fatigue life and reduce the stress corrosion-cracking tendency because they offer resistance to crack initiation and propagation. Performance and longevity of brittle material can be enhanced largely by introducing residual stress. Whereas, tensile stresses tend to adversely affect the mechanical properties of materials as they promote internal failure.

Generally, thermal treatment of glasses requires rapid cooling (quenched) from high temperatures usually above the glass transition temperature, as a result residual compressive stresses on the surface and tensile stresses in the mid-plane surface are developed, Narayanaswamy and Gardon (1969). The residual stress distribution is different over the glass thickness based on the cooling rate distribution. Any surface defect caused by surface compressive stress produces in-plane compression that may lead to a delay in crack propagation. This defect will grow readily if initiated in the mid-plane surface by the effect of tensile stress, as a result glass might shatter in tiny pieces in different directions. Such distribution of the residual stresses can be obtained in the tempering process of the glass in which the heated glass is rapidly cooled. The strength of tempered glass is significantly higher than untreated glass (Haldimann, Luible et al. 2008). Therefore, control of the solidification phase throughout cooling is very important to predict and optimize the residual stress to acceptable mechanical performance.

Tempered glasses are considered as pre-stressed materials because their thermal treatment induces a certain amount of compressive and tensile residual stress. A conventional simple destructive test method is used for determining the glass stiffness after the heat treatment cycle and classifies the glass as a tempered or not. However, such a test does not provide information about the residual stress variations near corners, edges, and holes. Knowledge of the 3D residual stress in the whole plate geometry is necessary for failure assessment. The advantage of the conventional method is that it is easy to use, but it is limited to some general cases of geometry and boundary conditions (Soules, Busbey et al. 1987). The FE numerical simulation tool to evaluate and predict the residual stress will be a valuable solution for optimizing the thermal process as well as an important tool for product design (Carre and Daudeville 1996).

In this chapter, the numerical simulation of thermally treated recycled soda lime glass media was performed in two stages using uncoupled thermo-mechanical solidification analysis. First, thermal analysis was performed, and the transient temperature of the solidification criteria are taken into account. A parametric study was employed to determine the heat transfer coefficient of the specimen providing the best-fit to numerical-experimental solidification measurements. Second, the thermal history obtained was used as an external force by means of a quasi-static mechanical analysis, using a well-known material model of elastic-viscoplastic constitutive law. The numerical analyses were verified by comparison with experimental results obtained from X-ray diffraction analysis ($sin^2\psi$ method).

5.2 Residual stress supported by FEM analyses

Due to the difficulties raised during the glass heat treatment process and the accuracy required to be achieved, the glass thermal treatment process is investigated by considering the relation between mould design and material properties, glass media profile, residual stress etc. Extensive experiments are necessary to achieve the required accuracy of the media profile and to optimize the cooling rate to have the residual stress within an acceptable range. This heat treatment cycle and design optimization is performed by experimental trial and error using an iterative procedure. FEM simulation of the heat treatment process can help to predict the optimal profile of the media and predict the residual stress at the end of the process.

Although, the heat treatment process of glass material has been significantly developed, limited work has been established in the field of FEM numerical simulations of the thermally treated glass moulding process. This may be attributed to the fact that the heat treatment of glass material by the moulding process is dependent on time and temperature, boundary condition dependent temperature, and large deformation phenomena, all these facts makes the material model behave in a nonlinear mode.

Cesar de Sa (1986) developed FEM to simulate the glass container forming process using 2-D thermo-mechanical analysis with a time dependent boundary condition. The analysis showed the temperature distribution at different stages of the forming process. Rekhson (1993) employed a viscoelastic with structural relaxation material model in the FEM simulation. The glass sample was bonded to a metal substrate and subjected to a hysteresis loop. The comparison was in a good agreement with the numerical and analytical results. Krishna, Harper et al. (1995) investigated the residual stress development in polymers bonded on to elastic substrates using the viscoelastic material model. The results showed that the time dependent stress is very important in the residual stress analysis because no stress has been captured in the elastic material model. These results demonstrated that the failure mode is not expected in the pure elastic analysis.

Dang and Brüggemann (2005) developed FEM numerical simulations using ANSYS code to predict residual stress during the annealing process of glass bottles based on the Narayanaswamy model of viscoelasticity and structural relaxation. The results suggested the soaking phase is very important in the annealing process, to ensure the whole glass sample is at a uniform temperature. The results also show that the growth of the residual stresses is dependent on the cooling rate during the glass transition phase. For the optimal annealing process, rapid cooling should be performed once the temperature is below the glass transition phase.

Jain and Allen (2004) implemented a commercial FEM programmes, DEFORM 3D and MSC Marc to simulate the glass moulding process. The DEFORM 3D software does not have capability to employ the viscoelasticity and structural relaxation material model, however, the author built his model assuming the glass to be an elastic material during the whole heat treatment cycle. The result showed a reasonable thermal history profile but could not predict residual stresses.

Hyre (2002) developed FEM method to simulate the glass-forming process. The author used the assumption that the glass bottle formation at high temperature behaves as a Newtonian fluid, where the viscosity is temperature-dependent, and the material model is rigid-viscoelastic. The results suggested that a particular interest must be given to the selection of appropriate nonlinear thermal boundary conditions and the contact between the glass and mould. Yi and Jain (2005) also attempted to utilize the rigid-viscoelastic model in FE analysis of the glass moulding process in order to investigate the deformed behaviour of glass in the moulding stage.

5.3 Mechanical performance of heat-treated glass

Several models have been developed to characterize the behaviour of glass during the heat treatment cycle. Carre and Daudeville (1996) proposed that the first theory of (freezing instant), that had been developed from the work of Bartenev (1948). This hypothesis suggested that the liquid glass is rapidly changed into an elastic solid at the glass transition temperature. Narayanaswamy and Gardon (1969) developed a new model of viscoelastic behaviour by introducing the stress relaxation and structural relaxation phenomena, which represents the variation of the stresses with time and temperature.

5.3.1 Viscoelastic mechanical behaviour of glass

Viscoelasticity is defined as the time dependent response of a material to a mechanical load. The viscoelastic material exhibits both elastic response and viscous response. The instantaneous response of a viscoelastic material to an applied mechanical load followed by viscous dependent time causes part of the long material molecular chain to change composition. This phenomenon is known as creep. In this case, the material state remains as a solid structure while rearrangement happens in order to complement the applied stress. This leads to development of back stress in the solid, the back stress causes the material to return to its original form when the applied stress is taken away (McCrum, Buckley et al. 1997).The standard one-dimensional Hooke's material law for elastic material is represented in Eq. (5.1).

$$\sigma = E\varepsilon \tag{5.1}$$

For an ideal Newtonian fluid, the shear stress is a function of the temperature related viscosity η, and strain rate $d\varepsilon/dt$, Eq. (5.2)

$$\sigma = \eta \frac{d\varepsilon}{dt} \tag{5.2}$$

Narayanaswamy (1971) suggested that the glass behaves as an elastic solid at room temperature 20ºC, the glass can be considered as viscoelastic at the transition temperature which is a thermorheological simple material; for a higher temperature 1100ºC, the glass becomes a viscous fluid. Narayanaswamy (1971) proposed that the stress strain dependent temperature for the viscoelastic material can be written in two different ways: stress relaxation and creep. The stress relaxation with time is given by (Eq. 5.3)

$$\sigma(t) = \int_0^t G(t - t_i) \frac{d\varepsilon(t_i)}{dt_i} dt_i \tag{5.3}$$

where, t_i is known as the dummy variable at past time, and $G(t - t_i)$ is called the relaxation shear modulus which expressed by Eq. (5.4):

$$G(t) = G_\infty + G_{exp}\left(-\frac{t}{\tau}\right) \tag{5.4}$$

The standard linear viscoelastic model can be easily described as an arbitrary number of Maxwell elements arranged in parallel, which is known as the generalized Maxwell model Figure 5-1. In reality, the viscoelastic material does not respond as a standard linear model. However, distribution of stress relaxation times has been established to conform to the generalized Maxwell model. The viscoelastic behaviour is described in terms of stress relaxation by means of a generalized Maxwell model (Daudeville and Carre 1998). Relaxation shear modulus (G) and bulk modulus (K) can be described with instantaneous and deferred shear modulus and expanded into Prony's series of six terms (Daudeville and Carre 1998).The deferred shear modulus value is considered to be zero. The generalized Maxwell model in terms of relaxation function $\Psi_i(t)$, can be expressed by (Eq. 5.5):

$$G(t) = 2G_g\Psi_1(t), and\ K(t) = 3K_e - \left(3K_e - 3K_g\right)\Psi_2(t) \tag{5.5}$$

where

$$\Psi_i(t) = \sum_{j=1}^n W_{ij} \exp\left(-\frac{t}{\tau_{ij}}\right) \quad i = 1,2,.. \tag{5.6}$$

Where K_e is the deferred bulk modulus, K_g is the instantaneous bulk modulus, G_g is the instantaneous shear modulus
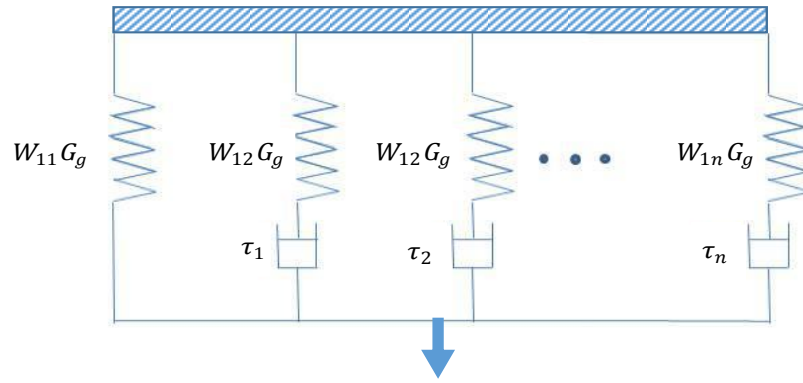
Figure 5-1 Schematic representation of generalized Maxwell model for viscoelasticity

5.3.2 Glass transition temperature influence

Glasses are vitreous materials, which behave like plastic when heated. The glass viscosity is significantly decreased with an increase in temperature. At a certain temperature level, the glass viscosity is ideal to duplicate the mould surface, usually by the compression moulding process.

The rearrangement of glass composition at a molecular level occurs at the glass transition temperature, T_g region to achieve equilibrium (liquid state) in a short time, thus the change of phase transition profile occurs at a rate that is easy to recognize. The mechanical load at this temperature, and stress relaxation will lead to time-dependent change in dimensions. Meanwhile, a sudden change in temperature causes time-dependent change in properties (like volume, density etc.). At this point structural relaxation is developed resulting in phase transition.

Figure 5-2 shows the specific volume change of a glass cooled through the glass transition region. When the material is in the liquid state, the viscosity of glass is low, hence equilibrium is achieved immediately with a step change in temperature. Further decrease in temperature, the viscosity of the glass liquid increases, thus the time increases to attain equilibrium. The temperature range in which the material leaves the equilibrium state is shown as region AB. The viscosity at point B is too high causing the internal structure to be frozen into the glassy state. The region AB is defined as a transition range between liquid and solid state where the equilibrium can take place. DTA experimental results can help identify the transition range with time in more detail.

However, the glass transition temperature is defined as the point at the centre of the glass transition region; the expansion coefficient is measured by the slope change from higher value in the liquid state to a lower value in the solid state at the transition temperature.
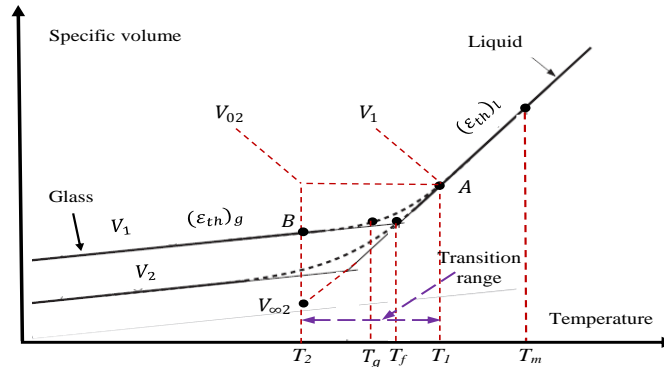
Figure 5-2 specific Volume versus temperature for a viscoelastic material like glass, and definition of fictions temperature

5.3.3   Structural relaxation

Structural relaxation is defined as a time dependent change in properties such as volume, density, etc. like viscoelastic glass material when subjected to an instantaneous step change in temperature.

The structural arrangement of the molecules and structure dependent density are considered as the most important effects on the residual stresses (Narayanaswamy 1978). The instantaneous changes in volume at the glassy state and after liquid are characterized by the coefficient of thermal expansion $(\varepsilon_{th})_g, and (\varepsilon_{th})_l$, respectively. As is shown in Figure 5-2, several possible glassy states for the same temperature are close to the transition region depending on the cooling rate. Thus, the structure material at these temperatures cannot be stabilized (Narayanaswamy and Gardon 1969, and Narayanaswamy 1971). The response of material to a step change in temperature is defined by the structural relaxation volume function M_v, represented in Eq. (5.7)

$$M_v(t) = \frac{V(t) - V_2(\infty)}{V_2(0) - V_2(\infty)} = \frac{T_f(t) - T_2}{T_1 - T_2}$$
(5.7)

The instantaneous and high values of volume (*V*) are represented by 0 and ∞ respectively, during the step temperature change. The fictitious temperature T_f , is defined as the temperature of the liquid which is in the same structural state with the glass at the temperature (T) (Tool 1946). Thus, if the material is in the liquid state at temperature T_f, and then rapidly cooled to T_2, the phase transition change along the slope line$(\varepsilon_{th})_g$, in this case no structural rearrangement would occur. Figure 5-2 illustrated that the fictitious temperature T_f is measured by extrapolating a line from *V(T₁)* with a fitting slope $(\varepsilon_{th})_g$ to intersect line from *V(T₀)* with a fitting slope $(\varepsilon_{th})_l$.

The structural relaxation volume function Eq. (5.8) is derived in terms of stress relaxations and expanded to Prony's series (Carre and Daudeville 1996) .

$$M_v(t) = \exp\left(-\left(\frac{t}{\tau_s}\right)^b\right) \tag{5.8}$$

Where τ_s is structural relaxation time, b is, is experimental fitting parameter in the from 0 to 1. Moreover, the structural relaxation volume can be fitted more accurately by using extensive experimental data of relaxation times and weights similar to the Maxwell model as stated in Eq. (5.9)

$$M_v(t) = \sum_{i=1}^{n} W_i \exp\left(-\frac{t}{\tau_{si}}\right) \tag{5.9}$$

However, in order to estimate the structural relaxation time and stress relaxation time dependent temperature, the thermorheological simplicity should consider estimating the variation of these quantities.

5.3.4 Thermorheological Simplicity

The stress and structural relaxation times vary significantly with temperature change. thermorheological simplicity behaviour considers the temperature and time as two dependent variables. Figure 5-3 show the plot of stress relaxation curves versus *log (t)*. As displayed the stress relaxation curves are similar in shape, but shifted along X-axis.

The stress relaxation curves can shifted along the X-axis to allow overlay to single suitable temperature known as reference temperature $T_{ref.}$, this temperature dependence into a new

time variable known as the reduced time ξ , (Schwarzl and Staverman 1952) Reduced time is given by Eq. (5.10)

$$\xi = \int_0^t \frac{\tau_{ref}}{\tau[T(s)]} ds \qquad (5.10)$$

where, τ_{ref} is the relaxation time for suitable reference temperature. Thus, structural relaxation volume function $M_v(t)$ takes a new form of Eq. (5.11) after substitute t by ξ

$$M_v(\xi) = \sum_{i=1}^{n} W_i \exp\left(-\frac{\xi}{\tau_{si}}\right) \qquad (5.11)$$

The fictitious temperature T_f , can be calculated by substituting Eq. (5.7), in Eq. (5.11) as a function of temperature and time (or reduced time) by using the Boltzmann principle and integrating over the thermal history. The T_f, is given by Eq. (5.12)

$$T_f(t) = T(t) - \int_0^t M_v\left[\xi(t) - \xi(s)\right]\frac{dT}{ds} ds \qquad (5.12)$$

The relaxation times τ and weight are assumed constant with temperature. Narayanaswamy (1978) proposed a mathematical model to be used with the viscoelastic tempering materials; this structural model is capable of describing the property changes for different cooling rates. Hence τ , is given by Eq. (5.13)

$$\tau = \tau_{ref} \exp\left[-\frac{H}{R}\left(\frac{1}{T_{ref}} - \frac{x}{T(t)} - \frac{(1-x)}{T_f(t)}\right)\right] \qquad (5.13)$$

where, *T(t)* is the current temperature , R is the universal gas constant, H= Hg + HS is the activation energies associated with temperature Hg and structure HS, and x is a factor controlling the relative influence of Hg and HS, x typical range is $0< x < 1$. There are two assumptions for the fictitious temperature value: When $T(t) > T_g, T_f \approx T(t)$, and For $T(t) < T_g, T_f \approx T_g$.
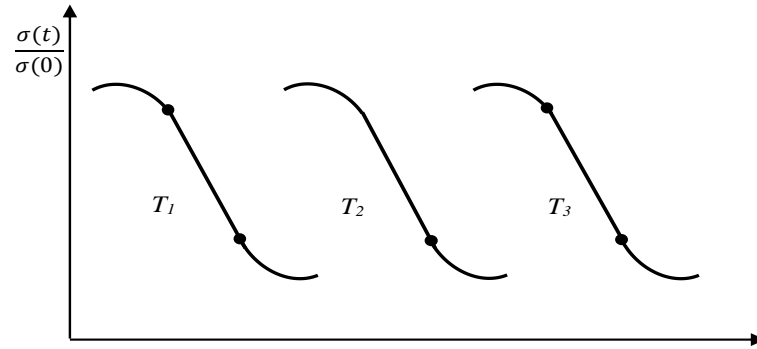
Figure 5-3 the plot of stress relaxation curves versus *log (t)*.

5.4   Methods for measurement of residual stresses

The methods used in residual stress measurement are usually monitored by the changes in the distortion of components. The methods are classified into destructive and non-destructive testing.

5.4.1   Hole Drilling (destructive testing)

The hole drilling method is based on the hypothesis that the sample will relax into a different shape in the machining process due to the residual stress, this will allow for back calculation of the residual stress. This technique involves drilling in a location where a strain gauge is attached to measure the strain change. Eq. (5.14) is used to determine the residual stress based on the drilling approach.

$$\sigma = (\sigma_{max} + \sigma_{min})\bar{Q} + (\sigma_{max} + \sigma_{min})\bar{P}cos\ 2\partial \qquad (5.14)$$

where $\bar{Q}$, and $\bar{P}$ are hole drilling constant. ∂ is the angle from x-axis to the direction of maximum stress σ_{max}

The reliability of measurement is reduced when the depth is greater than the hole diameter. In this technique, only three strain gauges will allow for measurement within two in-plane directions. The error increases significantly when the residual stress is 50% greater than the yield stress due to localised yielding (Schajer 2011). This method is considered as destructive testing unless the sample size is much larger than the hole diameter, and the testing location does not influence the sample functionality.

5.4.2   Curvature Measurements (destructive testing)

The Curvature measurement method is useful to determine the stress within coating and multi-layers material (Clyne and Gill 1996). It is possible to measure the stress variation from the changes in substrate curvature generated when a substance is deposited on a sample surface Kuroda, Fukushima et al. (1987). The curvature can be measured using a strain gauge. The residual stress can be calculated using Stoney Eq. (5.15) Totten (2002).

$$\sigma = -\frac{4}{3}E\frac{t^2}{l^2}\frac{\partial g}{\partial t} \qquad\qquad (5.15)$$

Where t is the current thickness, g is the deflection of the thin beam of l length.

5.4.3   Crack compliance Methods (destructive testing)

The crack compliance method is also known as successive cracking method, slotting method and termed fracture mechanics based approach (Prime 1999). This technique involves introducing a small slot in a sample to monitor the stress relaxation around the slot. Cheng, Finnie et al. (1991) proposed that the crack compliance method is better than the other residual stress measurement methods for many reasons, such as improved resolution of residual stress variation with depth; measurement on a large component is possible; ability to measure stress intensity factor caused by the residual stresses; ability to measure stresses in non-crystalline materials

5.4.4   XRD analysis of residual stress (non-destructive testing)

The main objective of the XRD experiments residual stress analyses was to compare the FEM predicted residual stress to experimental observation. The residual stress is determined by measuring the angle θ, at which the maximum diffracted intensity takes place in a set of lattice planes (*hkI*), when a crystalline sample is subjected to X-ray (Noyan and Cohen 1986). From these angles, it is possible to calculate the inter-planar spacing *d*, using Bragg's law. The atoms in a crystalline material are arranged in regular molecules, such arrangement is scattered radiation undergoes interference either constructively or destructively, based on the d spacing and wavelength of X-ray beams.

The scattered beams remain in the same phase since the path length is equal to an integer multiple of wavelength. Figure 5-4 illustrated, the Bragg's law that represents, the difference in the path length between two constructively interference beams. Eq. (5.16) gives the expression of Bragg's law.

$$2d\ sin\theta = n\ \lambda \qquad\qquad (5.16)$$
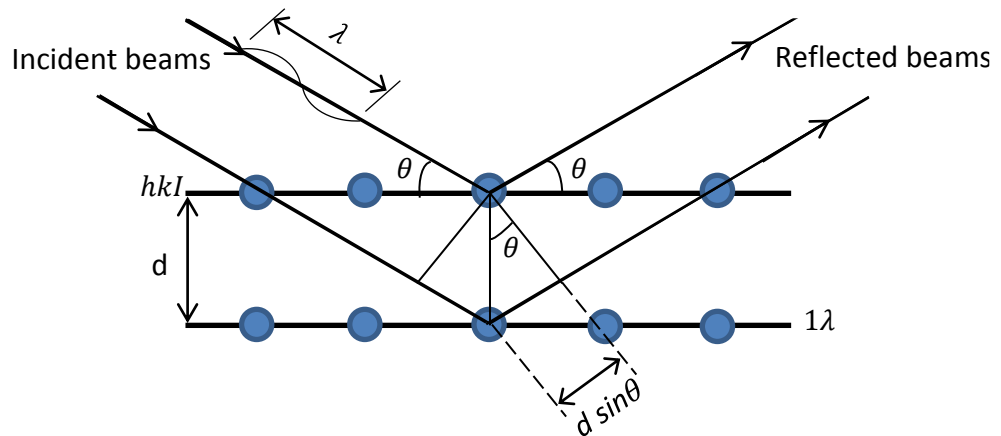
Figure 5-4 Diffraction in crystal lattice according to Bragg's law

Figure 5-4 illustrated that the crystal lattice consist of clusters of grains, each grain has plains of atoms parallel to the surface separated with inter-planer spacing d . The incident beam diffract from the atomic planes given a wavelength λ , the reflection not only from the surface atoms but also from the atoms underneath the top surface to some considerable depth. However, the interaction depth is a thin surface layer of about 20µm depending on the X-ray beam energy. The Bragg's law demonstrated that the inter-planer spacing of stressed material is different from that of unstressed state. The value of d is proportional to the magnitude of the residual stress. If the specimen is tilted corresponding to the incident beam, new grains will contribute in diffraction. The orientation of diffraction beams is more likely perpendicular to the stress direction. As a result, the Bragg's angle increases and d- spacing decreases. In this case, the inter-planar spacing acts as a strain gauge.

Two characteristic methods have been developed by Prevey (1977), and Noyan and Cohen (1986) to determine the residual stress using XRD techniques. Direct measurements of inter-planar spacing normal to the surface result in obtaining residual elastic strain component normal to the material surface.

The $sin^2\psi$ method was employed to determine biaxial residual stress developed in crystal lattice. In this method, the assumption of free strain material is not required in considering the residual stress.

5.4.4.1   Strain measurements

There is a clear relationship between the diffracted X-ray beams through the crystal lattice and inter-planar spacing, d. The strained material produced elongation and shrinkage within the crystal lattice, thus the d-spacing of the lattice planes will be changed accordingly resulting in different d values in comparison with strained free material. Such differences will cause a shift in the diffraction pattern. Under the assumption of symmetric diffraction, the incident and reflected beam through the crystal lattice are in equal angle with reference to the specimen surface. The residual elastic strain, ε_{zz} normal to the specimen surface can be evaluated by comparing the d-spacing of the stress region to that of unstressed reference material.

Figure 5-5 show the schematic diagram of 3-D stress ($\sigma_1, \sigma_2, and \ \sigma_3$) and diffraction planes parallel to the surface and at an angle of φψ. In the first case, the assumption of normal stress $\sigma_3 = 0$, $\sigma_1, and \ \sigma_2$ both lie in the plane of specimen surface. The normal strain can be measured experimentally by determining the peak position 2θ, and solving Bragg's Eq. (5.16) for a value of d_n. The residual elastic strain is obtained from Eq. (5.17) for a given value of unstressed d-spacing, d_0.

$$\varepsilon_{zz} = \frac{d_n - d_0}{d_0} \qquad\qquad (5.17)$$

In the second case, the measurements were performed by tilting the specimen within the diffractometer. The inter-planar spacing measurement at an angle ψ of each plane can be made, and thus the residual elastic strain along that direction can be calculated using Eq. (5.18)

$$\varepsilon_\psi = \frac{d_{\varphi\psi} - d_0}{d_0} \qquad\qquad (5.18)$$
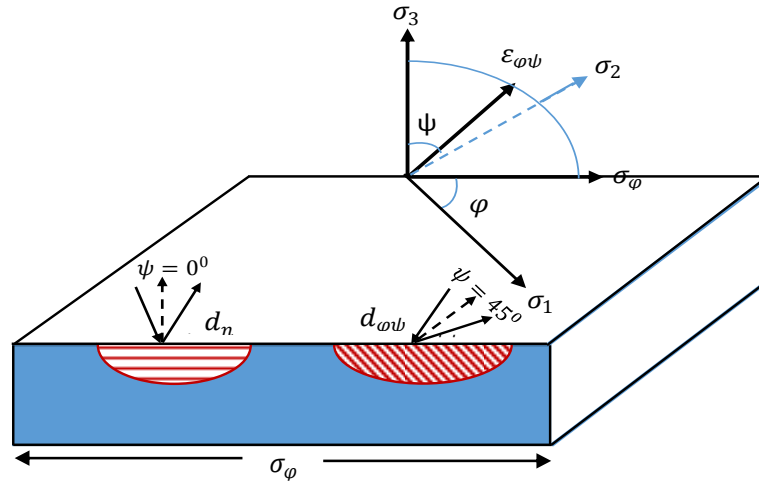
Figure 5-5 Schematic diagram of $\sigma_1, \sigma_2, and\ \sigma_3$ and diffraction planes parallel to the surface and at an angle of ψ

This technique provides direct residual strain comparison under various conditions (material, velocity, indenter size, etc.). For the purpose of conversion the ε_ψ, or ε_{zz} to stress component, pre-knowledge of stress at that location is required. However, for FEM validation requirement, it is may not be necessary to convert to stress, rather than directly compare the numerical and experimental elastic strain distribution.

5.4.4.2   Stress measurements by $sin^2\psi$ method

In this study, the well-known $sin^2\psi$ method (Prevey 1977, and Noyan and Cohen 1986) was employed to determine the local stresses in the plane of glass media. The $sin^2\psi$ method does not require a free strain surface when considering biaxial residual stress. However, when samples are tilted by angles ψ from the normal surface, the crystallographic planes are no longer parallel to the specimen surface. Figure 5-5 shows the tilted sample under a given range of ψ will allow the measurements of normal and shear strain. As a result, the differences in inter-planar spacing with tilt angle ψ, are related to the development of the stress component in the region of interest. The schematic diagram also illustrated that the specimens can be rotated through an angle of φ, around the centre to determine the main strains in the orthogonal direction. The assumption of equilibrium should be considered in $sin^2\psi$ method, where the normal stress σ_3 to unstrained surface is equal to zero.

Hauk, Oudelhoven et al. (1982) suggested that the slope of the linear relationship between the inter-planar spacing and $sin^2\psi$ is proportional to the biaxial stress component Eq. (5.19).

$$\frac{d_{\varphi\psi} - d_0}{d_0} = \frac{1 + v}{E} \sigma_\varphi \, sin^2\psi \qquad (5.19)$$

where, $d_{\varphi\psi}$ is the d-spacing when the specimen is tilted by angle ψ, and rotated by φ, d_0 is d-spacing of unstressed reference material, and σ_φ is the residual stress component.

Equation (5.19) is the common residual stress equation, it predicts a linear relationship between, $d_{\varphi\psi}$ and $sin^2\psi$. Experimental results are used to determine regression least square line. The biaxial residual stress σ_φ is derived from the slope of the least square line for given material properties E, and v and unstressed d spacing (d_0) values. The slope of the least square line increases indicating a tensile region and slop decreasing indicating a compressive region. There are different ways used to calculate the d_0 value (Totten 2002). In this study, the d spacing measured at $\psi = 0$, is used as a d_0 value. This substitution is attributed to the fact that, in a wide range of material properties, the elastic strain does not exhibit greater than 0.1% differences between the d_0 , and d at any tilted angle ψ. In such cases, the error is less than 0.1% because d_0 is a multiplier to the least square line slope.

Therefore, when the linear relationship between the d spacing and specimen-tilted angle ψ is satisfied, the related residual stress in the plane can be calculated using Eq. (5.20). A nonlinear relationship may be related to the wrong assumption of equilibrium surface, or strong surface texture, which requires more analysis. Advanced explanation of the assumptions and potential error associated with $sin^2\psi$ method is given by Noyan and Cohen (1986).

$$\sigma_\varphi = \left(\frac{E}{1 + v}\right)\frac{m}{d_0} \qquad (5.20)$$

5.5 Experimental setup

In this study, XRD residual stress analysis was conducted by a miniFlex X-ray crystallographic analyser with parallel beam optics including a multi-capillary collimator and a vertical collimator with a graphite flat crystal analyser in the incident beam and diffracted beam, respectively.

Measurements were made using CuKα radiation, the X-ray tube operated at 30 kV and 15mA. The Kb filter was used to reduce ground signal noise. The spot size of X-ray beam was adjusted such that the projected imprint on the sample was $250\times250\mu m^2$. This spot size was a mix between the small spatial scale to map the strain gradient change over several millimetres, and the need of large scale to sample many grains of powder diffraction analysis. The adjustment was repeated in each tilting ψ experiment to ensure consistent measurements.

5.6   Results and discussions

Residual stress measurements were performed on the Cutting media (VT-70) base along the longitudinal X-axis as illustrated in red marks in Figure 5-6. The method of inter-planer measurements $(sin^2\psi)$ using XRD as a function of tilting angle ψ, were employed. The residual stresses were calculated from the shift in the high intensity peak location of a specific set of inter-planers with respect to stress free inter-planer spacing d_0. Linear relationship between d vs. $sin^2\psi$ behaviour is valid for isentropic and homogenous material, low or moderate texture, and negligible normal stress. The material properties such as Elastic modulus and Poisson's ratio are assumed the same in tension and compression. Six separate tilting angles were made at each position within range $0^o \leq \psi \leq 45^o$. The angle of rotation φ of the sample about a normal axis is considered zero. Data were collected on the Cutting media sample over the range of diffraction peaks 2θ=42°-43° using 0.02 ^{o} of 2θ step. This is because the most appropriate diffraction peak in a glass media samples was 42.78$\mp$ 0.05.

(a)   (b)
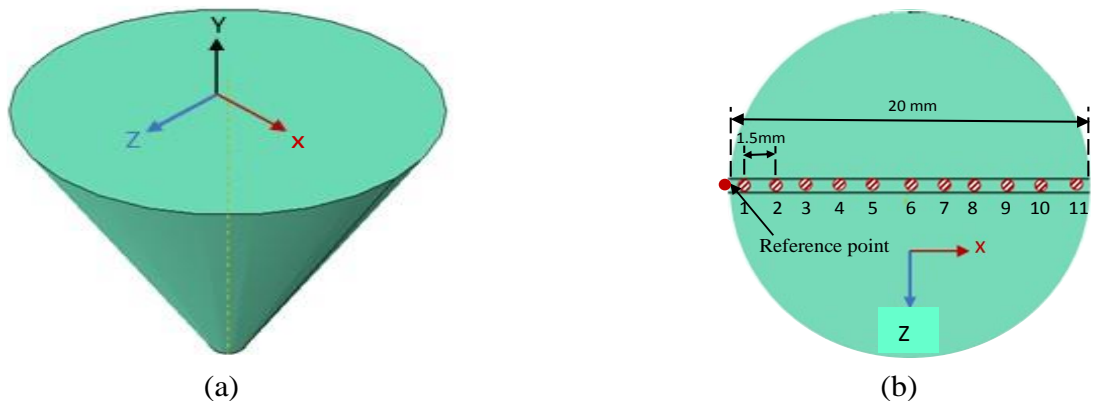
Figure 5-6   a) 3-D glass media geometry, b) positions of measurements on the base of media

The intensity and location of diffraction peaks are crucial parameters for peak fitting purpose. The peaks must be free of interference from other surrounding peaks. However, the occurrence of residual stress in the material produces a shift in the x-ray diffraction peak 2θ position when tilting the sample of various ψ angles. Figure 5-7 (a) shows Forward shift in diffraction peak during the interval change in ψ angle positions causes tensile stress while in Figure 5-7 (b) backward shift diffraction peak is noticed in various ψ angles and causes a compressive stress.
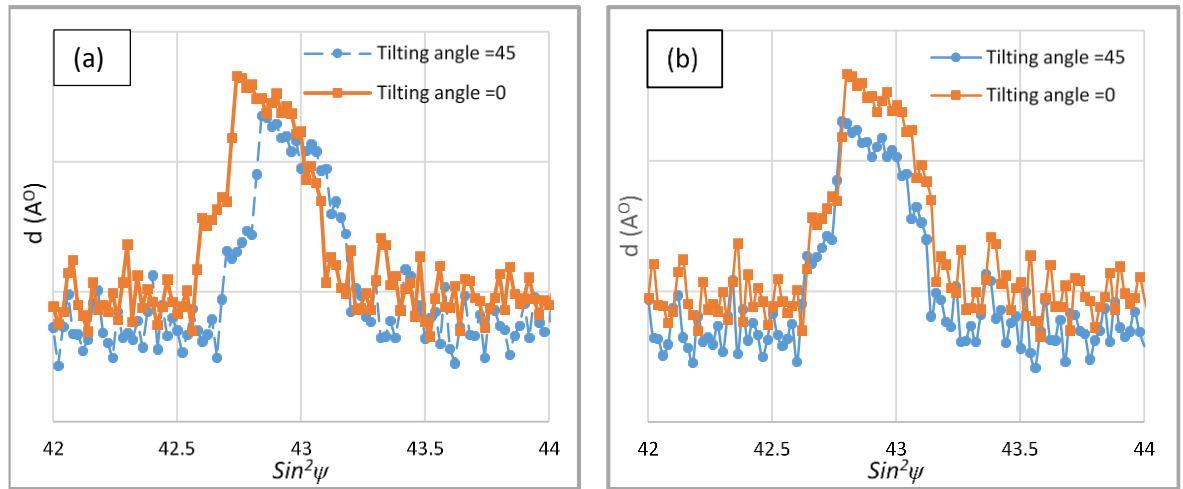
Figure 5-7 2θ diffraction peak shift during a) Tension stress, and b) Compression stress

Figure 5-8 shows samples of d vs. $sin^2\psi$ diagram. The results were obtained from XRD method (Bragg's law) throughout measuring d spacing at six-tilted ψ angle along the longitudinal axis on the media surface. The results exhibit a regular linear d vs. $sin^2\psi$ behaviour, which suggests using Eq. (5.20) to determine the residual stress. Slope can be derived from this graph and longitudinal residual stress was calculated by using the $sin^2\psi$ method.

Figure 5-8 (Position 1, and Position 2) shows the slope of d-spacing decreases with the increasing tilting angle, $sin^2\psi$, this indicates these positions exhibit compression resulting in negative residual stress. The longitudinal compression residual stresses calculated at Position 1, and Positon 2 were about -306 MPa, and -246 MPa, respectively. Whereas in Figure 5-8 (Position 5, and Position 6) the slope of d-spacing increases with the increasing tilting angle $sin^2\psi$, this indicates these positions are in tension resulting in positive stress.

The longitudinal tension residual stresses calculated by the method were about 41 MPa at Position 5, and 72 MPa at Position 6. The magnitude of these stresses either in compression or tension are depending on the slope value, the residual stress increases with the increase in the slope value of the least square regression line for given material properties and unstressed d spacing values (E, v, and d_0).

Figure 5-9 shows the distribution of residual stresses along the longitudinal X-axis of Cutting media measured by XRD technique. All the presented measurements are near the material surface, because the penetration depth of incident X-ray beams is about 10-20μm depending on the material under investigation (Hauk, Oudelhoven et al. 1982). The distribution of longitudinal residual stresses is shown as a parabolic shape. The residual stress becomes compressive near the media edges with value of -306MPa, this stress reduces gradually toward the media centre. The longitudinal residual stress developed to tension stress beyond 7mm from reference point at the edge of the media (see Figure 5.6), this stress increases gradually to reach 70MPa at the mid plane of the media. Because the media base is of a symmetric shape, no big change in the residual stress has been observed between the left and right sides from the media centre. The compressive residual stress at the edge is about four times greater than the tension residual stress at the mid-plane.
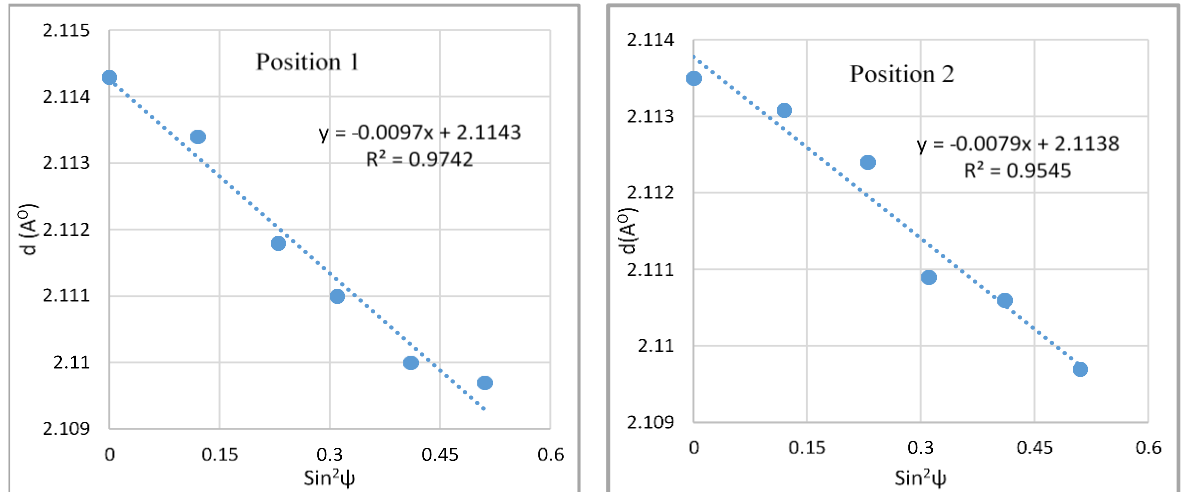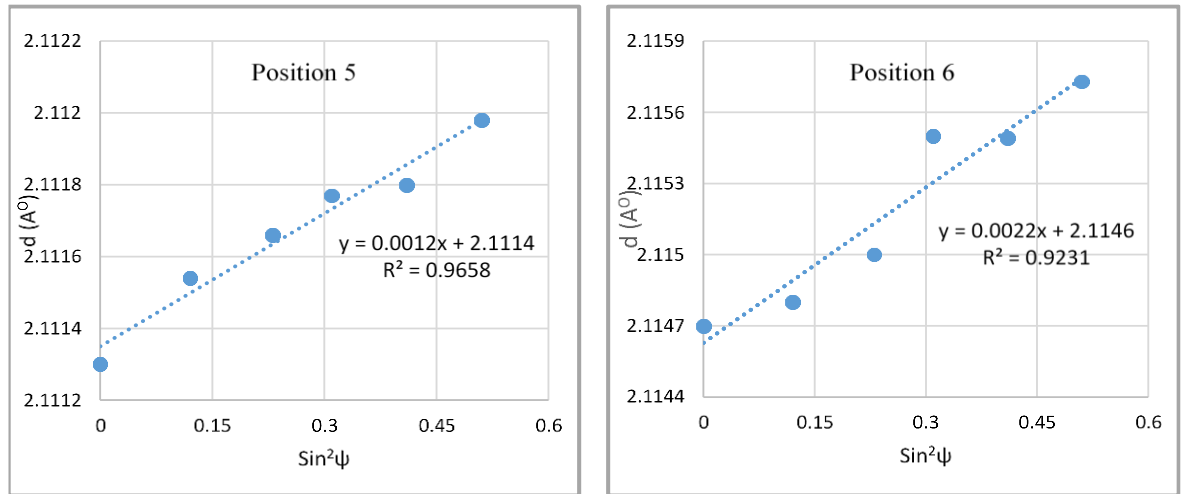
Figure 5-8 Variation of d-spacing with $\sin^2\psi$ at position1, 2, 5, 6 along the longitudinal axis
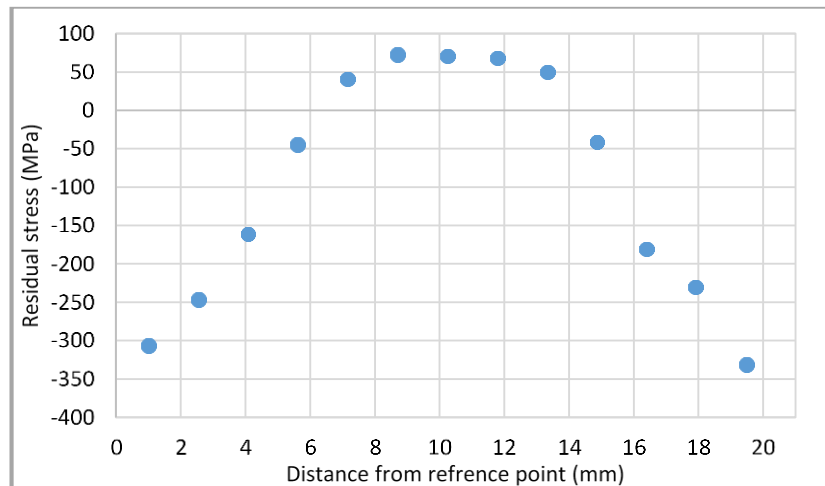
Figure 5-9 Biaxial residual stress profile σ_φ along the longitudinal shown in Figure 5-6b

5.7 Numerical investigation of thermally treated glass media

Numerical simulation of thermally treated recycled soda lime glass media was performed in two stages using uncoupled thermo-mechanical solidification analysis. Firstly, thermal analysis was performed and the transient temperature of the solidification criteria taken into account. A parametric study was employed to determine optimal heat transfer coefficient HTC of the specimen that provide the best-fit to numerical-experimental solidification measurements.

Although, the heat flow and HTC varies from location to location, which plays an important part in influencing the solidification results, for simplicity, the assumption of uniform HTC is considered. Initial HTC data were assigned and thermal simulation was conducted to obtain temperature-time curves. The HTC values were adjusted based on the differences between the simulated time- temperatures and the experimentally measured time- temperatures using an objective function algorithm. The HTC values were then modified based on the objective function results. After several iterations, the HTC can converge to values when the objective functions fall into accepted design tolerance. Accordingly, the optimal thermal histories based on optimal HTC data for selected glass media types were determined. Secondly, for residual stress analysis, the thermal history obtained was used as an external force by means of a quasi-static mechanical analysis.

In this case, a temperature interpolation was performed from the thermal to the mechanical using a well-known material model of elastic-viscoplastic constitutive law. The numerical analysis was verified by comparison with experimental results obtained from X-ray diffraction analysis ($sin^2\psi$ method). Figure 5-10 shows the flow chart of the numerical and experimental steps sequence for the residual stress analysis.
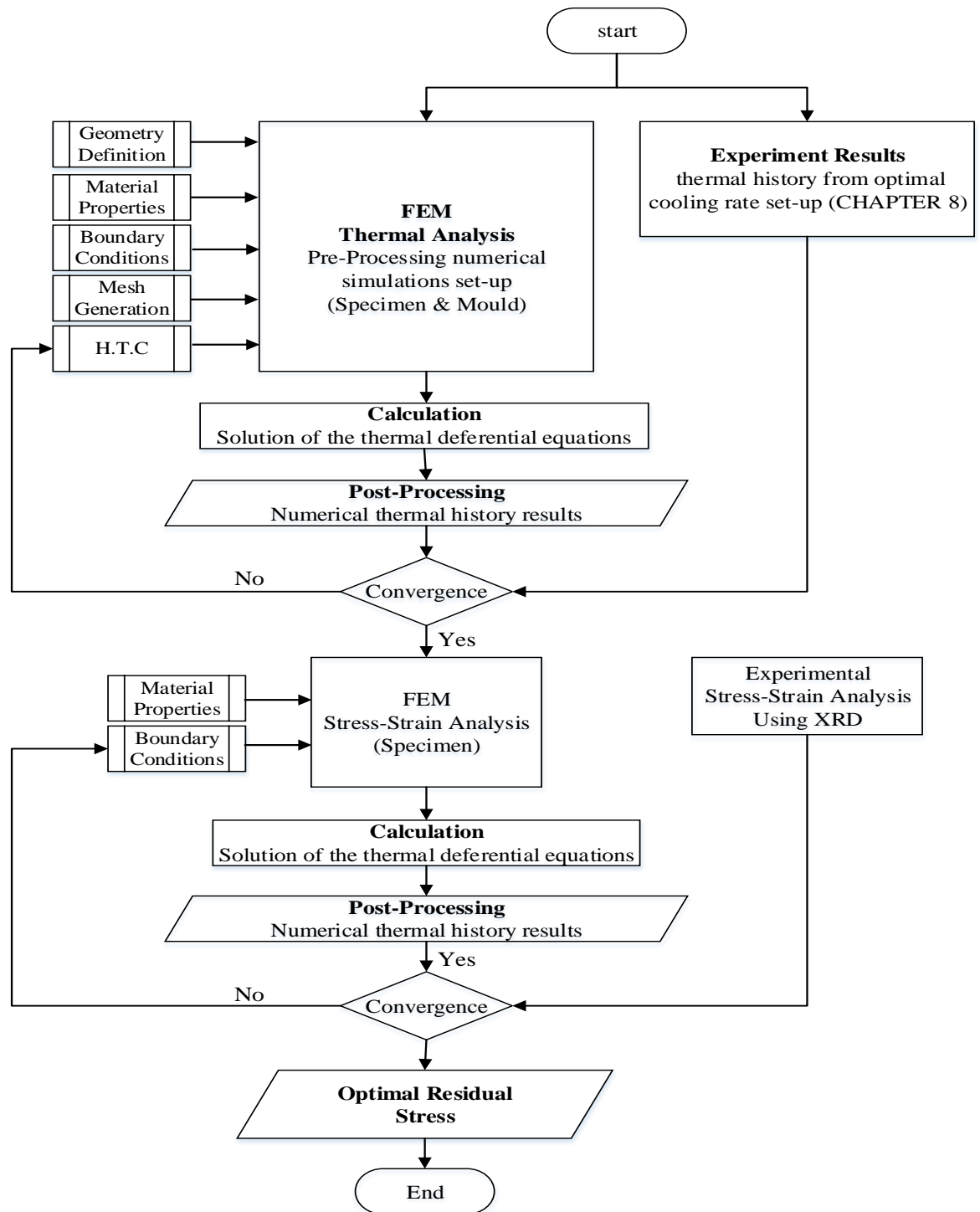
Figure 5-10 Numerical and experimental steps sequence for the residual stress analysis

5.7.1 FE - numerical simulation

The purpose of the numerical simulation is to determine the value of the dependent variable at various predefined points called (node points). The resulting equation systems of the dependent variables are written so that for each node point there is an equation for every dependent variable. FE numerical simulations of heat transfer and residual stress of various glass media samples were carried out using ABAQUS/CAE code. Figure 5-11 (a, and b) shows 3-D geometries of the glass media and mould, respectively used for thermal simulations. In the thermal analysis stage, the geometry of glass media was modelled with 8-node linear heat transfer brick (DC3D8) of 3,916 elements, the geometry of the mould was performed with a 4-node linear heat transfer brick (DC3D4) of 1,348 elements.

Figure 5-11 (c) shows the glass media in the stress analysis stage was modelled with an 8-node linear brick, reduced integration (C3D8R) of 5,586 elements. The mesh density was refined for the glass media in the mechanical analysis stage in order to increase the accuracy of predicting residual stress while the mesh density in the thermal analysis was kept small due to the complex interaction thermal model between the mould and media, which required more computational time.
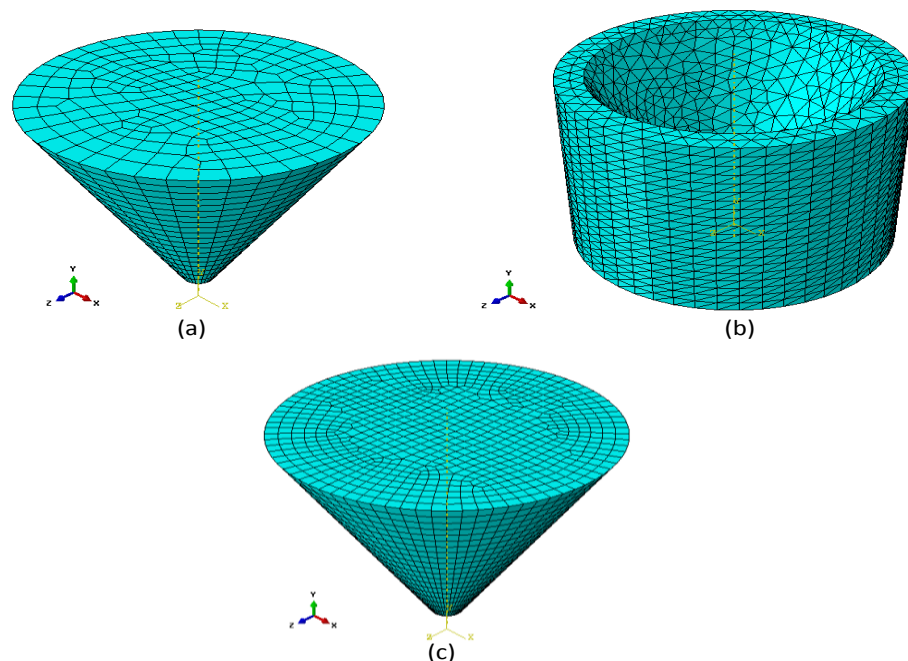
Figure 5-11 3-D FEM geometries a) Media geometry in the thermal analysis mode, b) Mould geometry in the thermal analysis mode, c) Media geometry in the stress analysis mode

5.8   Material properties implementation

As described in previous sections, the glass can be modelled as linear elastic solid at room temperature, and for high temperature, the glass is a viscous fluid. At intermediate temperature, the viscoelastic properties of glass (viscosity and relaxation time) are significantly temperature dependent.

There are several methods to determine the viscoelastic and structural relaxation time properties of glass. The most common method is to fit the experimental results to an analytical or mathematical constitutive model using a least squares method or nonlinear regression analysis method (Johnson and Quigley 1992). However, the mechanical, thermal, and viscoelastic properties of soda lime glass used in FEM simulations were directly obtained from the literature.

5.8.1   Thermal properties of soda lime glass dependent temperature

Carre and Daudeville (1996) developed a mathematical relationship for the thermal properties of soda lime glass varying with temperature based on extensive experiments. The soda lime glass material properties dependent-temperature used in the FEM simulations are given in the following expressions:

5.8.1.1   Thermal conductivity (W/m.K), T in K
Thermal conductivity is the ability of a material to conduct heat. It is defined as the quantity of heat, Q, transmitted during a period of time through a specific thickness in a direction normal to the surface area; for a given temperature difference ΔT.

$$\lambda = \frac{\Delta Q}{\Delta t}\frac{t}{A\Delta T} = 0.975 + 8.58 \times 10^{-4}T \qquad (5.21)$$

5.8.1.2   Specific heat (J/Kg.K), T in K
It is defined as the heat energy required to increase the temperature of a unit quantity of a substance by a defined temperature step.

Specific heat of liquid glass for $T > T_g \approx 850K$

$$C_{p,l} = \frac{\partial H}{\partial T} = 1433 + 6.5 \times 10^{-3}\, T \tag{5.22}$$

Specific heat of solid glass for $T < T_g$

$$C_{p,g} = \frac{\partial H}{\partial T} = 893 + 0.4T - 1.8 \times 10^{-7}/\, T^2 \tag{5.23}$$

5.8.1.3 Thermal diffusivity (J/m^3K), T in K

It is defined as the ratio of the thermal conductivity to the volumetric specific heat capacity. Materials with high thermal diffusivity reach thermal equilibrium quickly with their surrounding medium due to their capacity of rapid heat transfer compared with their mass.

$$D = \frac{\lambda}{\rho C_p} \tag{5.24}$$

5.8.2 Thermomechanical properties of soda lime glass

Saint-Gobain Recherche proposed the Thermomechanical properties of the existing model; they are given by Carre and Daudeville (1996) in the following mathematical relationships and tables:

5.8.2.1 Elastic modulus dependent temperature

Elastic modulus of liquid glass for $T > T_g \approx 850K$

$$E_l = -4.916 \times 10^6 T + 7.11 \times 10^{10} \tag{5.25}$$

Elastic modulus of solid glass for $T < T_g$

$$E_g = -3.61 \times 10^7 T + 9.67 \times 10^{10} \tag{5.26}$$

5.8.2.2 Thermal Expansion *(1/k)*

It is defined as the amount of deformation undergone during heating or cooling. The thermal expansion value is a function of fictitious temperature T_f .

Thermal expansion coefficients:

Solid glass (room temperature) $\beta_g = 9 \times 10^{-6} \ K^{-1}$

Liquid glass (high temperature) $\beta_l = 32 \times 10^{-6} \ K^{-1}$

$$\epsilon_{th} = \beta_g \big[T(t) - T_f(t) \big] + \beta_l \big[T_f(t) - T_0 \big] \qquad (5.27)$$

5.8.2.3 Viscoelastic and structural relaxation

Carre and Daudeville (1996) suggested that the weight and relaxation times can be determined for a given Bulk modulus ratio $K_e/K_g = 0.18$, reference temperature $T_{ref} = 869K$, and $-H/R{=}55000K$, and summarized in table 5.1

Table 5-1 Viscous and structural relaxations, weights and relaxation times

i	1	2	3	4	5	6
$W_{1i}G_g(GPa)$	1.5845	2.3539	3.4857	6.5582	8.2049	6.4980
τ_{1i} (s)	6.658$\times 10^{-5}$	1.197$\times 10^{-3}$	1.514$\times 10^{-2}$	1.672$\times 10^{-1}$	7.497$\times 10^{-1}$	3.292

5.8.2.4 Viscous properties

The viscosity of soda lime glass is dramatically changed with the temperature distribution, thus the final shape of the glass product is essentially affected by the values of viscosity it contains. The temperature range of the glass forming process is 700 to 1200 ºC. The glass viscosity dependence on temperature was determined in previous work of Carre and Daudeville (1996). It is an empirical relationship of Vogel-Fulcher given by Eq. (5.28).

$$\log_{10} \eta = A + B/(T - T_o) \qquad (5.28)$$

where A=-1.993, B=4003.5, and T_o=542 are empirical constants

In this study, the thermo-mechanical properties of soda lime glass were adopted in the FEM stress analysis by using a UMAT subroutine. This subroutine covers the elastic modulus dependence temperature, thermal expansion, viscoelastic and structural relaxation properties for temperatures distribution $T \leq 700$ ºC; for temperatures $T > 700$ ºC, the UMAT subroutine will switch to the viscoplastic property condition.

5.8.3 Thermal properties of silicon carbide dependent temperature (mould)

Sintered SiC has been developed as a major structural material used for mould applications at high temperature and aggressive environments. Several reviews of the mechanical properties of silicon carbide have contributed to it development by defining the ranges of performance characteristics that can be expected from this material. Sintered silicon carbide SiC material is typically manufactured from sub-micron powders. Boron and Carbon are used as an aid material to enhance the densification during sintering process at 2,500 ºC. The SiC material properties dependent-temperature used in the FEM simulations are given in the following expressions (Muro, 1997):

5.8.3.1 Thermal conductivity (W/m.K), T in K

$$\lambda = 52000 \times e^{-1.24 \times 10^{-5}T}/T + 437 \tag{5.29}$$

5.8.3.2 Specific heat (J/Kg.K), T in K

$$C_P = 1110 + 0.15T - 425 \times e^{-0.003T} \tag{5.30}$$

5.8.3.3 Thermal diffusivity (J /$m^3 K$), T in K

$$D = 121 \times e^{-6.98 \times 10^{-5}T}/T + 219 \tag{5.31}$$

5.8.3.4 Density with temperature

$$\rho = \rho_O[1 + \epsilon_{th}(T - T_O]^{-3} \tag{5.32}$$

Where ρ_O is the density at reference temperature, T_O

5.8.3.5 Elastic modulus (GPa) and Poisson's ratio dependent on temperature

$$E = 415 - 0.023T, \quad v = 0.16 - 2.62 \times 10^{-6}T \tag{5.33}$$

5.8.3.6 Thermal Expansion *(1/k)*

$$\epsilon_{th} = 4.22 + 8.33 \times 10^{-4}T - 3.51 \times e^{-0.00527T} \tag{5.34}$$

5.9 Boundary and initial condition set-up

The boundary and initial conditions together with the heat conductance are used to define the thermal transient behaviour of solidification mode during the heat treatment cycle. The initial conditions can be used to identify the initial temperature distribution through the mould and specimen. In the solidification simulation process, the assumption of constant temperature distribution is used throughout the mould, given by predefined temperature field with the start of the cooling phase.

For simplicity, when there is no requirement for the mould filling simulation, a constant predefined temperature distribution throughout the specimen can be assumed and the maximum temperature achieved by the heat treatment cycle was employed as the initial condition for the solidification simulation. Three types of boundary conditions relevant to the simulation modelling of the solidification process are introduced together with their mathematical relationship.

5.9.1 Thermal boundary conditions

5.9.1.1 Convection boundary condition

The heat flux across the contact surfaces at instantaneous time *t*, is proportional to the difference between the temperature of the mould surface at point P, $T(P,t)$ and the temperature of the surrounding medium $T_{sm}(t)$. The second law of thermodynamics, Newton's convective law of cooling can define the convection boundary condition in Eq. (5.35)

$$\lambda \frac{\partial T}{\partial n}(P,t) = h\left(T_{sm}(t) - T(P,t)\right) \tag{5.35}$$

Where, *n* is the plane normal to the surface at point *P*, h is the heat transfer coefficient. Figure 5-12 (a) shows the FEM convection boundary condition set up between the external surface of the mould and ambient

5.9.1.2 Radiation boundary condition

Thermal radiation is the heat transfer by the action of emission of electromagnetic waves from the mould surface due to the difference between the temperature of this surface at point $T(P, t)$ and the temperature of the surrounding medium $T_{sm}(t)$. Thermal radiation will transmit the energy away from emitting surface. The Stefan-Boltzmann law can be used to represent the boundary surface received heat by radiation.

$$\lambda \frac{\partial T}{\partial n}(P, t) = h_{rad} \left(T_{sm}(t) - T(P, t) \right) \qquad (5.36)$$

Where h_{rad} is the radiation heat resistance given by Eq. (5.37) , ϵ is the coefficient of emissivity ($\epsilon = 1$ for ideal radiation), σ is the Boltzmann constant (σ=5.669× $10^{-8}(W/m^2 K^4)$). Figure 5.12 (b) show the radiation boundary condition set up between the external surface of the mould and ambient.

$$h_{rad} = \epsilon \sigma \left(T^3 + T^3 \times T_{sm} + T \times T_{sm}^2 + T_{sm}^3 \right) \qquad (5.37)$$

5.9.1.3 Conduction boundary condition

Conduction boundary condition is defined as the heat transfer by physical contact of the particles within a medium or between two mediums. This transference take place in gases, liquid, and solids. The Fourier's law can be used to represent the boundary of heat conduction and it expresses that the heat flow is proportional to the surface area and normal temperature gradient for a given the thermal conductivity value.

$$\rho \frac{\partial H}{\partial T} \frac{\partial T}{\partial t} = \frac{\partial}{\partial x}\left[\lambda \frac{\partial T}{\partial x} \right] + \frac{\partial}{\partial y}\left[\lambda \frac{\partial T}{\partial y} \right] + \frac{\partial}{\partial z}\left[\lambda \frac{\partial T}{\partial z} \right] \qquad (5.38)$$

Where $\partial H/\partial T = C_p$ is the amount of heat per unit mass dependent temperature, $\partial T/\partial x$ $\partial T/\partial y, \partial T/\partial z$ is the heat flux travel in *x, y,* and *z* directions. Figure 5.12 (c) shows the conductance boundary condition set up between the surface of the mould cavity and the external surface of the specimen.

(a) Convection (mould& ambient)

(b) Radiation (mould& ambient)

(c) Conduction (mould cavity surface & specimen external
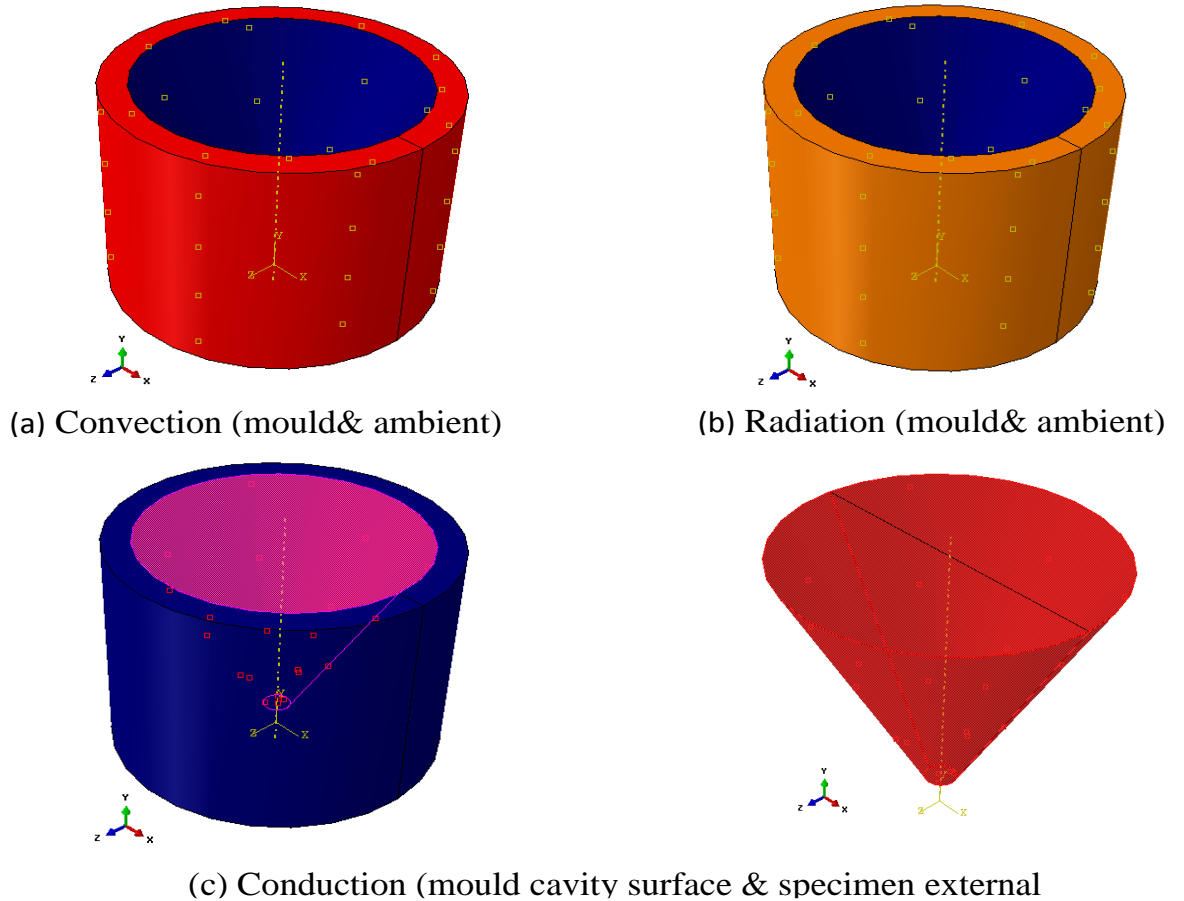
Figure 5-12 FEM boundary condition set-up a) convection (mould& ambient) , b) radiation (mould& ambient), and c) conduction (mould cavity surface & specimen external surface)

5.9.2   Contact boundary condition

The thermal contact can be represented as a perfect contact, where the two surfaces touch each other or a gap separates the surfaces in contact. In the FE simulations, the contact boundary condition is defined between two nodes or a node from the master surface and the nearest element face from the slave surface. In case of the contact surfaces with a gap, gap conductance coefficient should be considered for achieving the required HTC between the two interfaces bodies in contact.

In this study, perfect thermal contact was considered; the heat transfer from one body must be equal to that entering the other. Thus, point, P in the perfect contact surfaces is equal to:

$$\lambda_1 \frac{\partial T_1}{\partial n}(P, t) = \lambda_2 \frac{\partial T_2}{\partial n}(P, t) \tag{5.39}$$

The subscripts 1 and 2 refer to the two solid bodies in perfect contact condition.

5.9.3   Coupled Thermomechanical boundary conditions

5.9.3.1   Define the initial boundary condition

Two boundary conditions were defined. Firstly, the initial temperature of the specimen similar to that in the thermal analysis. Secondly, load output data base file (odb. File) of the nodal thermal history developed in the numerical thermal simulation as a predefined field in the stress analysis simulation.

5.9.3.2   Define the mechanical boundary conditions

The mechanical boundary condition involves constraining the specimen body by translations and rotations in X, Y and Z, but allowing the specimen body to deform in all directions. In the optimized glass media model the six degrees of freedom has been considered as follows:

5.9.3.3   Translation of the specimen body in the X, Y and Z axes

The translation is selected in the flat base surface of the media, a node with coordinates of vortex (0.01, 0, 0) is constrained in X, Z and Y. Figure 5-13 (a) shows the X, Y and Z coordinates, where X is the horizontal axis, Z is the vertical axis, and Y is the perpendicular axis. Fixing this point in the space, means the 3-degrees of freedom body translations are constrained. This constraint will allow the specimen to shrink toward this node. The remaining constraint tasks are related to the specimen rotations in three degrees of freedom.

5.9.3.4   Rotations of the specimen body in the Y and Z axes

Figure 5-13 b illustrates the constraint rotations in Y and Z- axes. As displayed, the fixed node (marked in red circle) at the same Y=0 of the fully constrained one and in Z=0, but in the opposite side of the specimen with respect to fixed node is constrained in Y and Z-axes. In this case, the constraint in Y-axis prevents the rotation in Z-axis and the constraint in Z-axis prevents the rotation in Y-axis. Thus, the node is free to move and rotate along the X-axis; this arrangement will allow the node to follow a correct shrinking trajectory.

5.9.3.5   Rotations of the specimen body in the X axis

Figure 5-13 (c) illustrated the constraint rotation in X-axis. As displayed, the selected node (marked in red circle) aligned in the Y- axis with the totally fixed one, that is with the same X coordinate and Z=0. The opposite side of the specimen with respect to the selected node is constrained in X and Z-axes. Such an arrangement will allow the rotation in Y-axis, this also means all vertical axes of the specimen are fixed to remain parallel to the Y-axis.

(a)   (b)   (c)
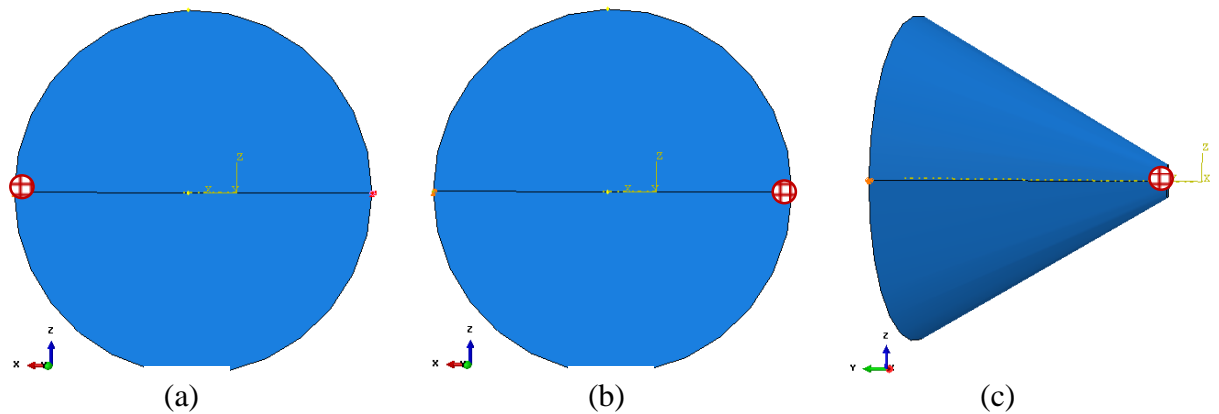
Figure 5-13 Mechanical boundary conditions: a) Concentrating translation of the specimen body in the X, Y and Z-axes, b) Concentrating rotations of the specimen body in the Y and Z axes, and c) Concentrating rotations of the specimen body in the X axis

5.10   Thermal analysis results and discussion

In this study, the numerical residual stress analysis was performed on three different glass media Finishing media, General purpose media, and Cutting media. Parametric study was employed to determine the optimal heat transfer coefficient HTC of specimens (optimal cooling rate) in order to optimize thermal history results that provide the best-fit numerical-experimental solidification measurements and consequently optimal residual stress. Samples of development results were presented by the following Figures for the optimal HTC (750 $W/m^2.K$) which is obtained throughout an extensive numerical simulations.

The material properties dependent on the temperature of mould and specimens were implemented into ABAQUS solver by using UMAT subroutine. The predefined field condition and the contact interactions were considered in the first stage of thermal analysis. The assumption of homogenous temperature distribution of VT+50, VT-10, and VT-70 ºC was applied to the Finishing media, General-purpose media, and Cutting media,

respectively and the same temperatures were also applied to the mould. The contact interaction properties were defined by conduction between the specimen and mould by means of surface-to-surface perfect contact using a predefined HTC property. The effect of the release agent layer on the heat transfer performance was neglected in these analyses. However, the interaction was activated in the initial step. A convective interaction between the mould and the ambient was assigned through a predefined surface film condition. A radiation interaction between the mould and the ambient was assigned through a predefined surface radiation to ambient interaction. The emissivity value was assigned in this step.

The thermal history of the solidification criterion was performed during the quenching process which is based on monitoring the temperature variation of the specimen. Figure 5-14 shows the temperature distribution during the quenching process to room temperature at different time intervals throughout cooling rate of (HTC=750 W/m^2.K). The mechanical properties dependent on temperature of mould and Finishing media were employed in the numerical simulation analyses. A perfect contact interaction at the initial step was considered, this condition would allow for instantaneous heat transfer between the specimen and mould during the quenching process. The main concept of solidification thermal analysis is to define the number of steps when the specimen solidified at a specific temperature and started separating from the mould. When that step number is defined, then the thermal history data is saved as shown in Figure 5-16 and transferred as an input data to the stress analysis where the specimen expansion and shrinkage takes place, as a result the residual stresses are calculated for a full time quenching process. The number of steps required for solidified Finishing, General purpose, and Cutting media were 195, 173, 147 respectively for a full quenching process (2,500 seconds).

Figure 5.15 shows the 3-D mould and specimen model during the thermal simulation with the positions of nodes I, II, and III under investigation. Figure 5.16 shows the temperature history distribution over 1000sec. of solidification cycle at different node (node I, node II, and node III) positions of various product (Finishing, General purpose, and Cutting) media. As displayed the thermal history distribution varies throughout the nodes for a particular type of product based on the distance of the selected node from the contact point with the mould. This change may be attributed to the effect of HTC. It is clearly noticed that the cooling is more rapid at the edge (node I) than in the mid plane part (node III).

Thus, the gradient of temperature throughout the distance along the longitudinal axis causes the residual stress state.

It is clearly noticed that for the first 10 second of the quenching process, the difference of temperature between the edge and mid plane is about 50 ℃. The results also show the same nonlinear trend of temperature distribution throughout the nodes of various product during the cooling process.
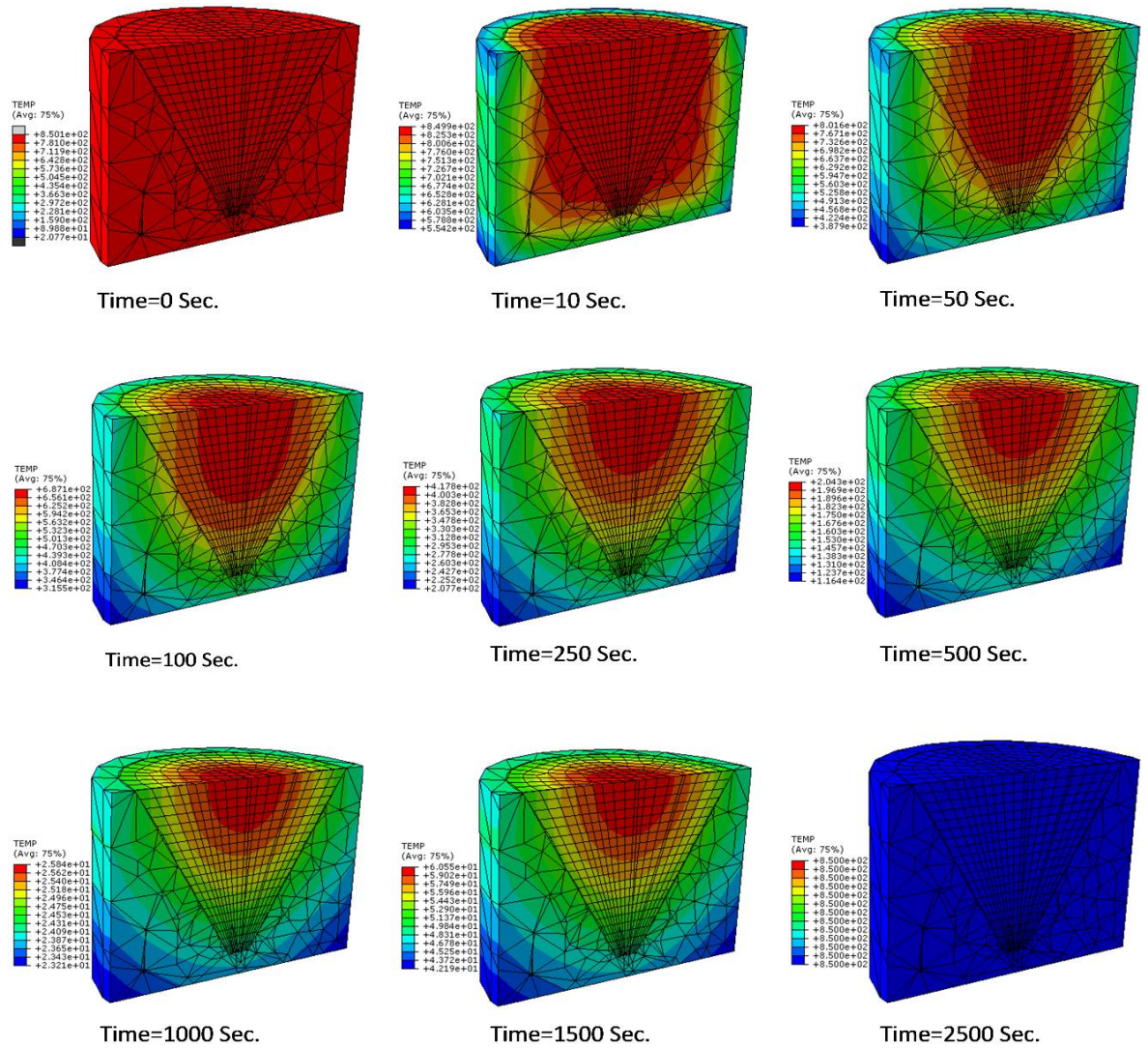
Figure 5-14 Temperature distributions of the 3-D Finishing media during a full quenching process to room temperature at 195 steps in 2500 second
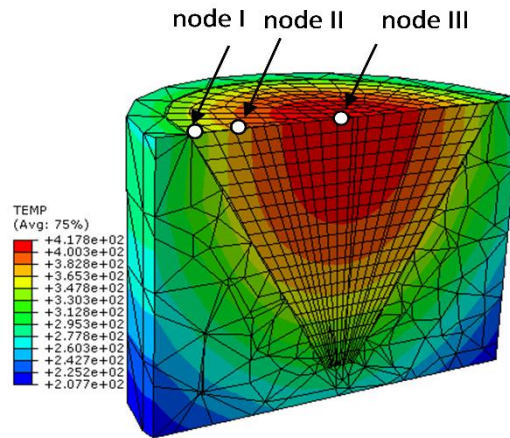
Figure 5-15 3-D mould and specimen model of thermal simulation with the positions of nodes under investigation
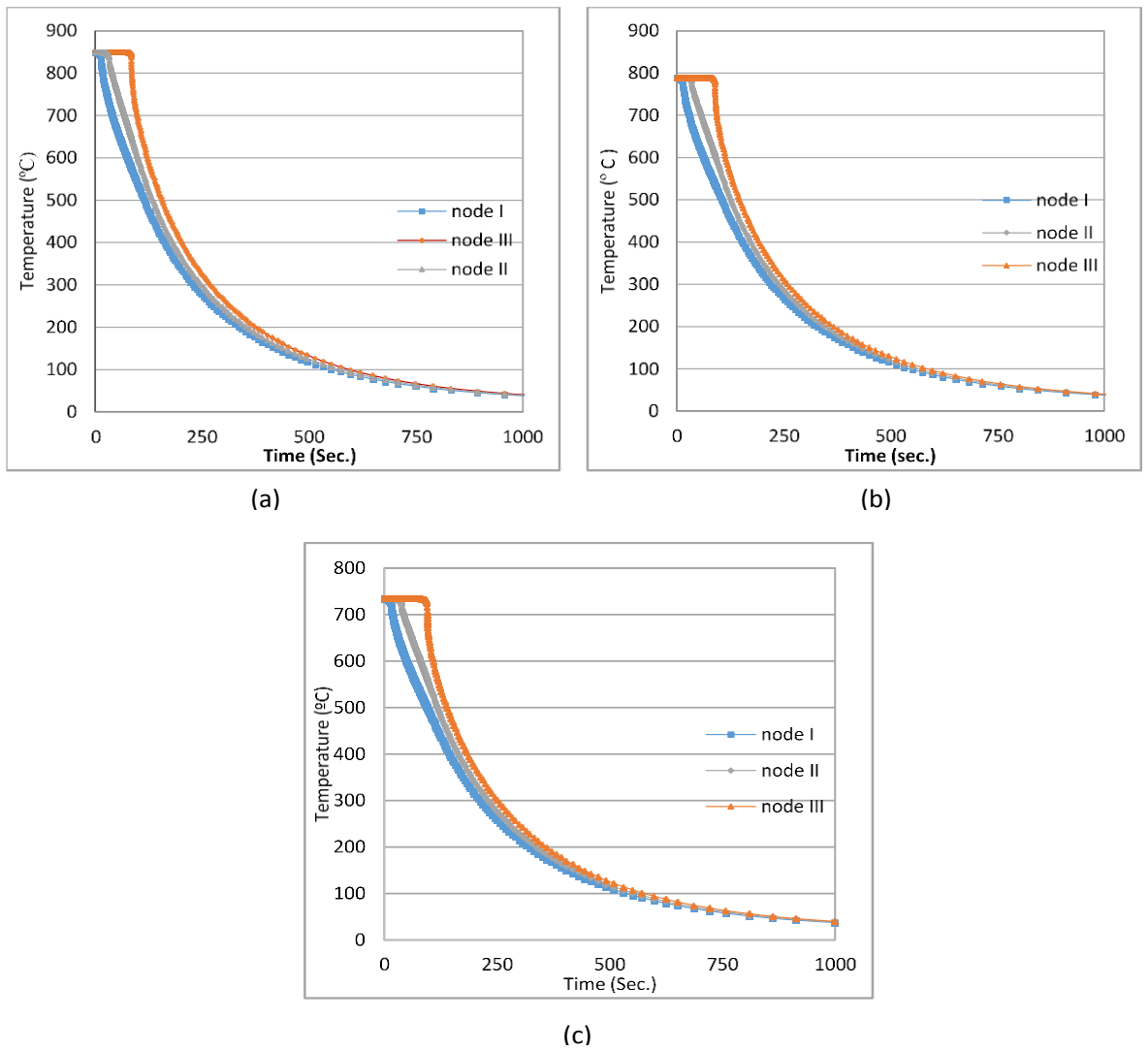
Figure 5-16 Temperature histories over 1,000 sec of cooling process for three nodes (I, II and III) positions of a) Finishing media, b) General purpose media, and c) Cutting media

Figure 5-17 shows the temperature distribution at times 0, 10, 50, 100, 250, 500, 1,000, and 1,500 seconds along the longitudinal axis during the quenching cycles of Finishing, General purpose, and Cutting media. The results demonstrated that the temperature contour distribution was changed at different quenching steps. These temperature distributions agreed with the results from Figure 5-16, which is associated with the HTC effect along the longitudinal distance. The results also show the same trends of temperature contour distribution throughout the longitudinal axis of various products and a homogenous temperature can be achieved at 1000sec. of the cooling cycle. These differences in the temperature distribution throughout the longitudinal axis of the media will lead to the generation of various compressive residual stresses at the edge and various tensile residual stresses in the mid plane.
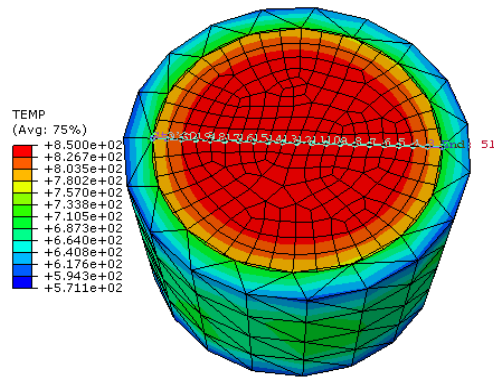
3-D Mould and specimen model of thermal simulation showing the temperature distribution contour along the longitudinal axis.
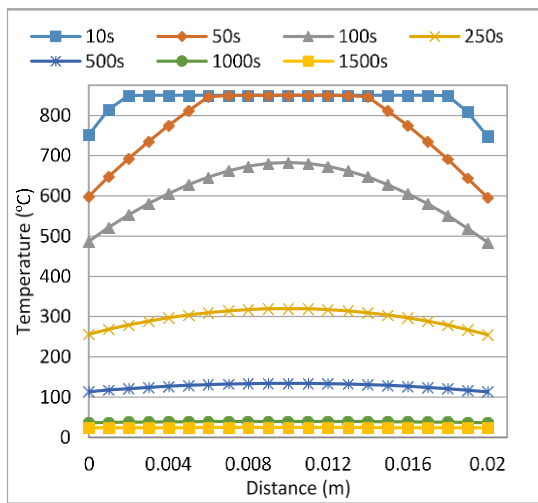
(a)
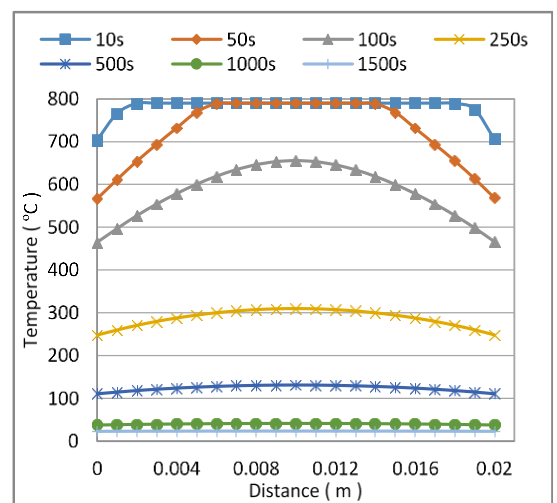
(b)
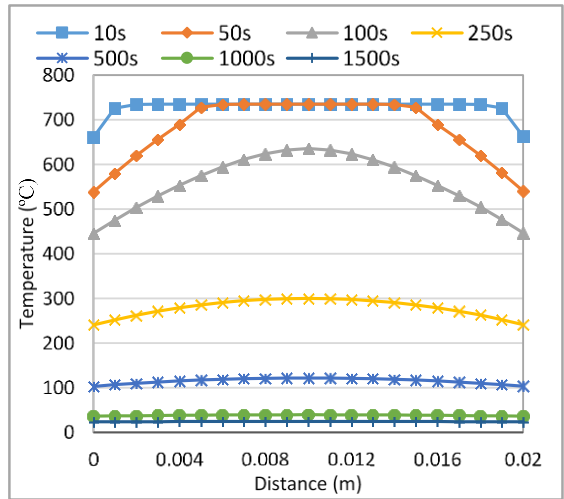
(c)

Figure 5-17 Temperature distributions along the longitudinal axis at different times during the quenching process of a) Finishing media, b) General purpose media, and c) Cutting media

Figure 5-18 show a validation of the thermal history numerical simulation of Cutting media obtained from optimal HTC of (750 W/m^2.K) with the results from the thermocouple arrangement system throughout the experimental work, both results were extracted from edge node position. This analysis is needed for accurate prediction of the residual stress. The agreement of temperature change with time is sufficient for the purpose of this comparison, however it does not demonstrate a perfect agreement. This may attributed to thermocouple location and/or the HTC variation due to the gap conductance generation between the mould and specimen during the solidification process.
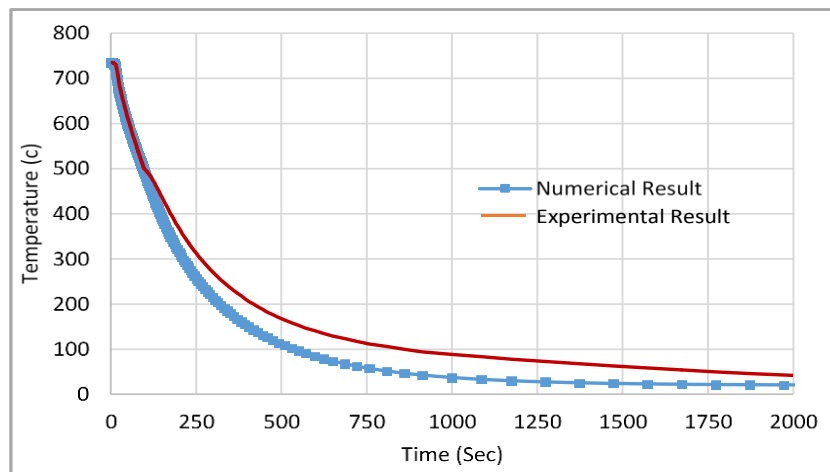
Figure 5-18 Comparison of the experimental thermocouple result to the numerical simulation data over 2000sec. of cooling cycle

5.11 Stress analysis results and discussions

The stress analysis was performed in ABAQUS/Standard by importing the temperature history from the thermal analysis as a predefined initial condition into the stress analysis using odb. file through the solidification cycle to room temperature. The specimen viscoelastic and viscoplastic material properties dependent temperature were implemented into ABAQUS solver by using UMAT subroutine. The boundary conditions were applied as described in section (5.9.3) using translation body in X, Y and Z axes, rotations in Y and Z axes, and then rotation in x axis. The numerical stress analyses were carried out on three different products produced by different thermal treatments such as; Finishing media, General-purpose media, and Cutting media.

Figure 5-19 illustrated the numerical simulations of the residual stress contours distribution of three different media using thermal histories of optimal HTC value. Different residual stress distributions were noticed from the contour plots results. This may attributed to the fact that different thermal histories were employed as a predefined initial condition into the stress analyses. Three nodes (I, II and II) were selected to investigate the numerical residual stress values in FE code. The residual stress distribution according to the contour plots suggested a compressive stress at the edge node I, and tensile stress at the mid node III.
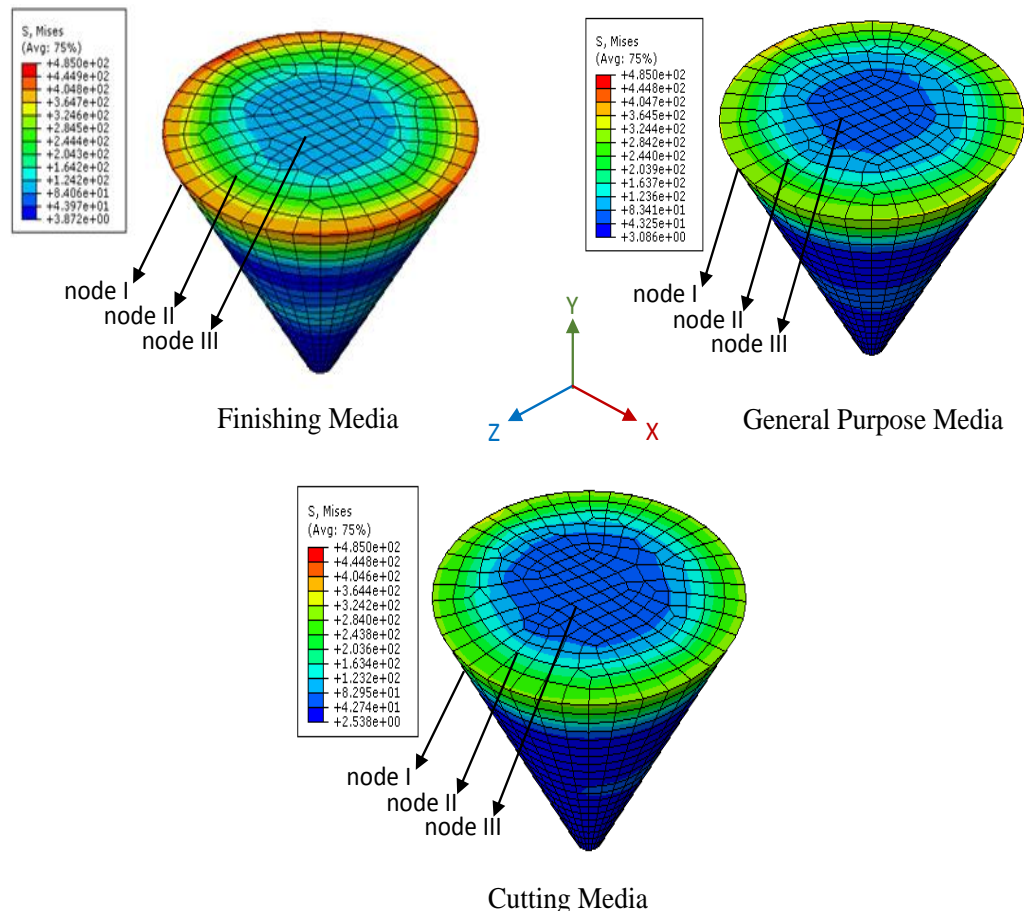
Figure 5-19 Contour Von Mises residual stress distribution of Finishing media, General-purpose media, and Cutting media.

Figure 5-20 shows the Von Mises residual stresses distribution in node I, node II and node II calculated over 1,250sec. of solidification cycles. It can be seen that for a particular node the residual stresses obtained from various products have the same trend during cooling process. The numerical results shows that the Von Mises residual stresses reach their maximum values when cooling cycles exceed 1,000sec. These results agree with the outcomes from Figure 5-17 where a homogenous temperature can be achieved at 1000sec. It is clearly observed that the residual stress concentration is dependent on the cooling rate, a rapid cooling rate at the edge (node I) will lead to a higher residual stress concentration compared with node II and node III. The residual stresses in nodes I, II and II at the end of cooling process obtained were higher in the case of the Finishing media. The Von Mises residual stresses distribution of the General purpose media in node I, node II and node II were about 73%, 70%, and 68%, respectively of the same node position in the Finishing media, and about 65%, 56%, and 54% for the Cutting media relative to the Finishing media.

(a)

(b)

(c)
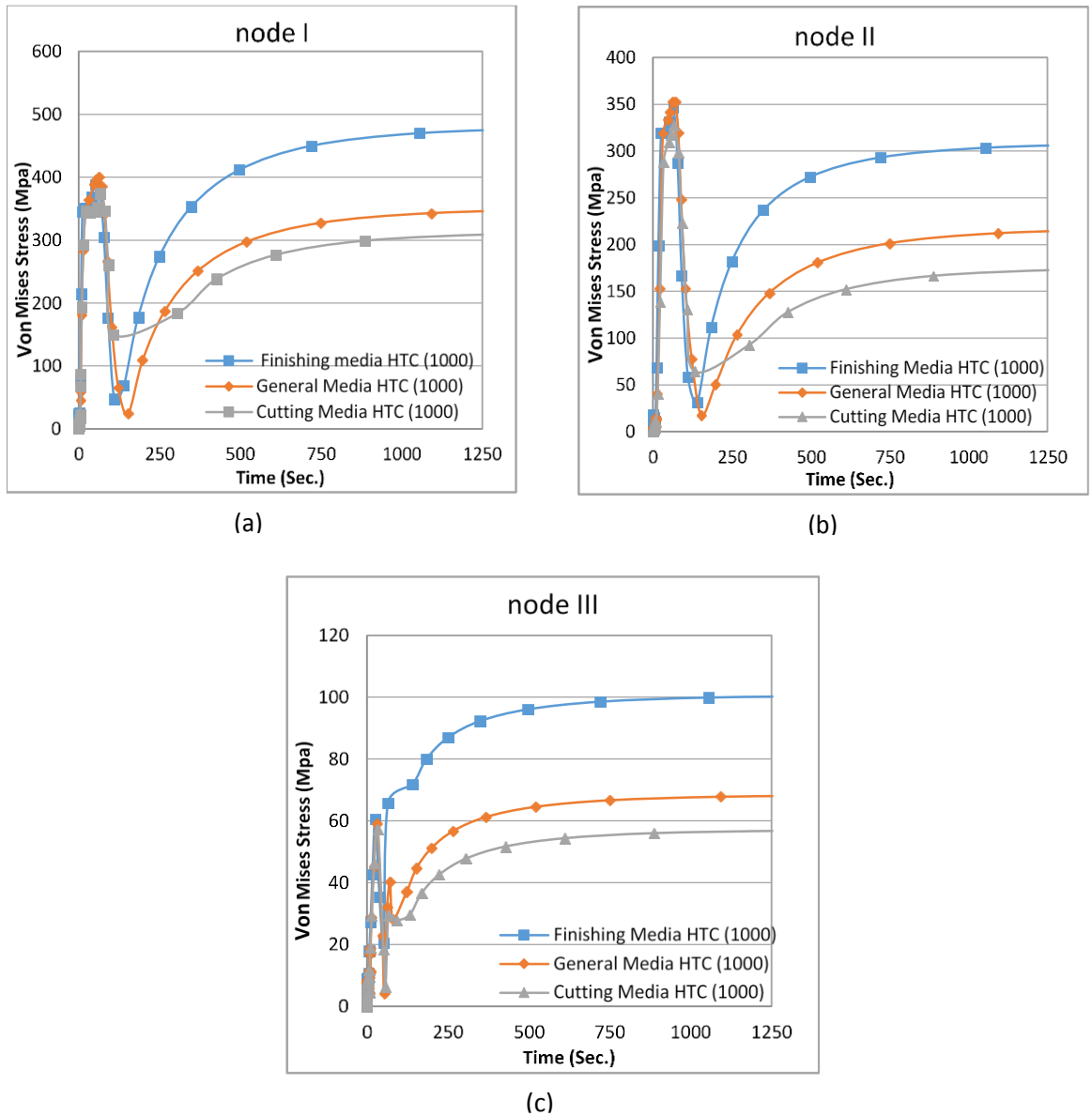
Figure 5-20 Von Mises residual stresses of Finishing media, General purpose media and Cutting media calculated over 1250sec. of solidification cycles at a) node I, b) node II and c) node II

Figure 5-21 represents the variation of Von Mises residual stress along the longitudinal axis of Finishing, General purpose and Cutting media. It is clearly noticed that the residual stresses reduce significantly in the first 5 mm from the edges, these stresses become equal in the mid plane. However, the Von Mises residual stress distribution in all products follows a positive parabolic shape. This stress distribution gives the media better mechanical strength.

The variations of Von Mises stresses follow the same trends in all products where maximum values in the edges are about four times the stresses in the mid plane. The stress distribution along the longitudinal axis was higher in the Finishing media followed by General purpose media and then Cutting media.
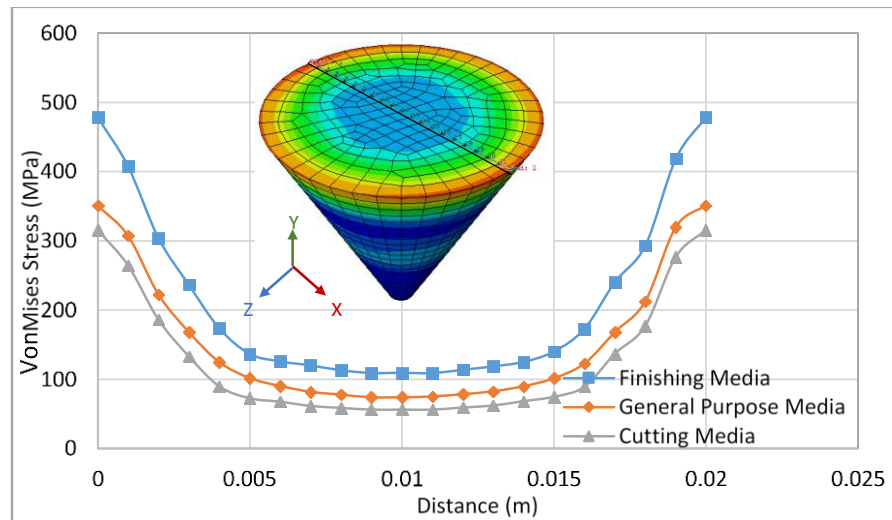
Figure 5-21 Von Mises stress variation along the longitudinal axis of Finishing media, General-purpose media, and Cutting media.

The previous analyses proposed that the initial temperature is a parameter of great importance on the residual stress values because it controls the viscoelastic and plastic behaviour, thus it is a very important variable influencing the classification of media products. However, in order to study the influence of thermal characteristics parameter values during the quenching process, residual stresses calculations were carried out by varying the HTC and initial temperature within the solidification cycle on different media products. Figure 5-22 shows the numerical Von Mises residual stresses prediction with different cooling rate HTC and initial temperature measured at different node locations (edge node I and mid plane node III). It is clearly noticed the higher the HTC, the higher the residual stress concentration. The results also expose a dependence on the initial temperature, the Von Mises residual stress increases with the increasing the initial temperature up to 820ºC, where it become virtually constant with initial temperature.
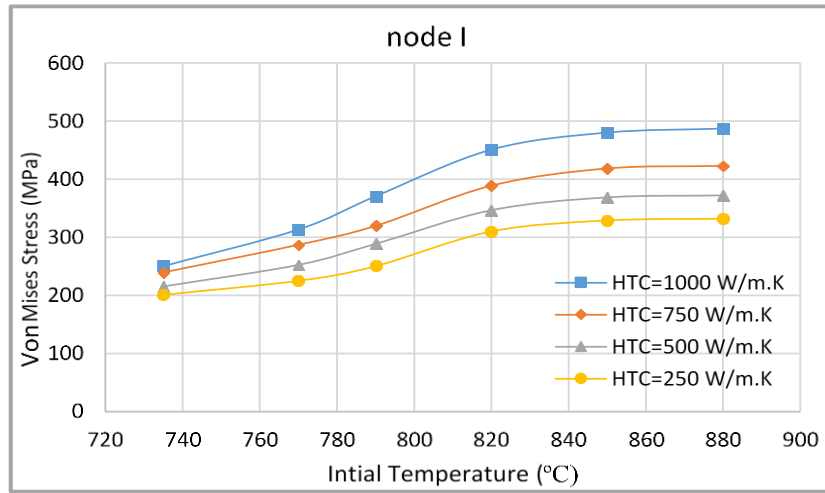
(a)
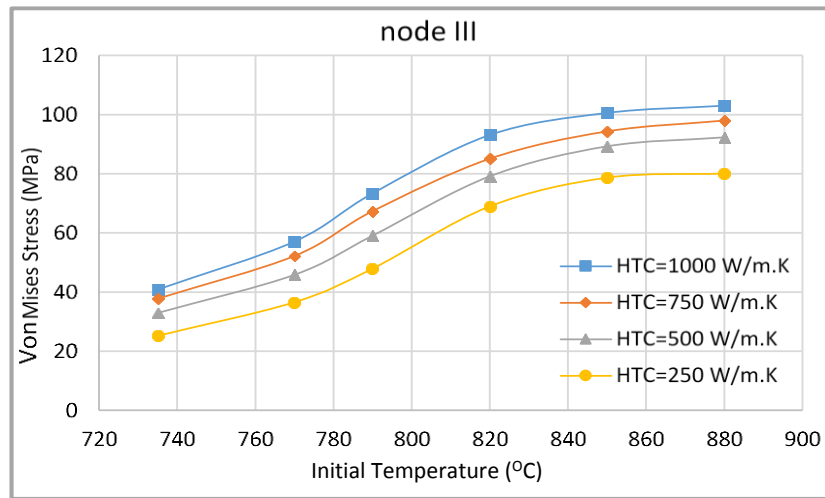
(b)

Figure 5-22 Von Mises residual stress variation with quenching parameters in (a edge node I, and b) mid plane node III

The heat flux across node positions varies with instantaneous time change. The edge node I cools down more rapidly than the mid plane node III. Thus, during the quenching process to within 560ºC the edge of the glass media becomes suddenly solid, while the mid plane media still remains liquid .This phenomenon will lead to compressive stress in the edge and by equilibrium; the mid plane is in tensile stress. The mid plane remains to cool down, then due to the convection, the edge media moves to compressive and the mid plane remains in tension. However, the residual stress measurements on the longitudinal axis σ_{xx}, should be considered in order to estimate the magnitude of compressive and tensile residual stresses developed during the quenching process. Figure 5-23 shows the variations of the longitudinal residual stresses at the edge node I and mid plane node III measured at optimal HTC of 750 (W/m^2.K) of different glass media products.

As displayed the sign of longitudinal residual stresses changes during the quenching process. All media products follow the same trend of compressive residual stress in the edge node I and tensile stress in the mid plane node causes a pre-stressed glass media at the end of quenching to room temperature. The longitudinal residual stresses generation in Finishing media is higher, compared with General and Cutting media samples. This may be attributed to the fact that for the same cooling rate value, the Finishing media needs more time to cool down and achieve equilibrium resulting in a higher compressive and tensile stress concentration. The results also show the same trends of longitudinal residual stresses variation throughout the nodes of various products. These stresses become stable after several tens of seconds.
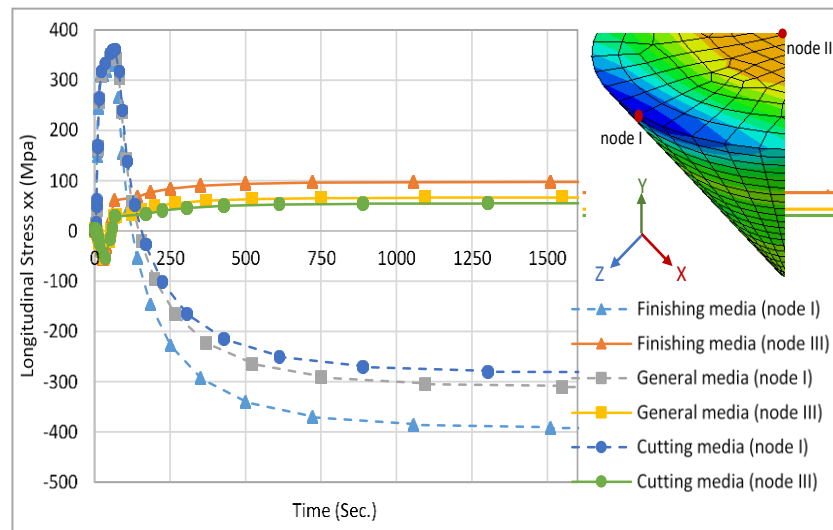
Figure 5-23 Variations of the longitudinal residual stresses at the edge node I and mid plane node III of Finishing, General purpose, and Cutting media

Figure 5-24 shows the variations of predicted longitudinal residual stresses along the X-axis of Finishing, General purpose and Cutting media. The results are in agreement with the results obtained from Figure 5-21. The tensile stresses are equal in the mid plane; the sign of longitudinal residual stresses changing to compressive near the edges generated a parabolic shape. The variations of longitudinal residual stresses follow the same trends in all products where the compressive values in the edges are about three times the stress in the mid plane.
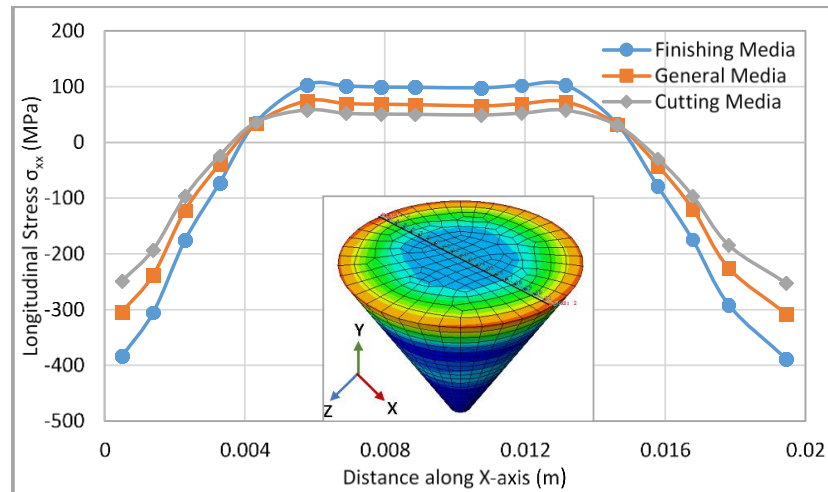
Figure 5-24 Variations of predicted longitudinal residual stresses along the X-axis of Finishing, General purpose and Cutting media

Figure 5-25 shows a validation of the numerical longitudinal residual stress σ_{xx}, obtained from optimal HTC with the result from experimental residual stress obtained by X-ray diffraction along the X-axis of Cutting media. The agreement of residual stress with distance is sufficient for the purpose of this comparison; however, the results do not illustrate a perfect agreement. This may be related to the discrepancy in the thermal history that is used as input data to the numerical simulation associated in Figure 5-18. The results in both measurements follows similar trends of parabolic shape that the residual stress become compressive near the media edges, these stresses reduced gradually toward the media center and are converted to tensile stresses. Moreover, the media base is symmetrical in shape, therefore there are no great changes in the residual stress between the left and right sides from the media centre. It is clearly noticed that the experimental compressive residual stress in the edge node was about 86% of the same node in the numerical simulation, this difference changes with the distance along x-axis however, the experimental tensile residual stress in the mid plane node was about 71% of the same node in the numerical simulation.
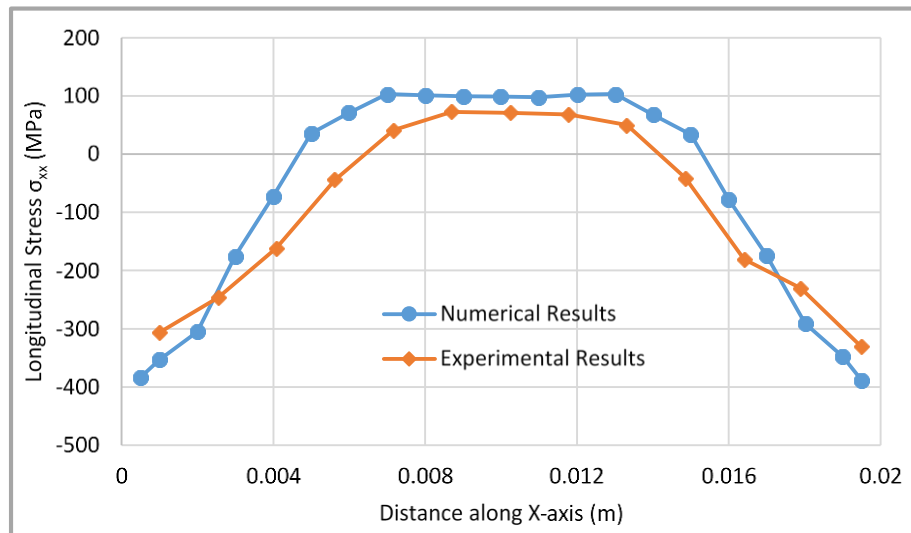
Figure 5-25 Comparison between the experimental and numerical longitudinal residual stresses variations along the X-axis.

5.12 Conclusion

Residual stresses for the thermally treated recycled glass products of Finishing, General purpose, and Cutting media have been obtained using commercial numerical FE code (ABAQUS) throughout the uncoupled thermo-mechanical solidification analysis. Narayanaswamy's model has been employed to describe the behaviour of soda-lime glass material properties using a well-known material model of elastic-viscoplastic constitutive law. The thermal numerical histories (solidification criteria) were obtained by developing a parametric study of HTC. A solidification criterion was performed based on the temperature variation development of the specimen. The optimal HTC was determined that provided the best fit to numerical-experimental quenching measurements. The optimal thermal histories determined were successfully implemented as an input external force into residual stress analysis.

It is clearly noticed from numerical simulations that the thermal history distribution varies throughout the nodes across the longitudinal axis for a particular type of product depending on how far the selected node is from the contact point with the mould. As a consequence the contour of numerical residual stress distributions varied accordingly, a compressive stress was observed at the edge node, and tensile stress at the mid plane node. The residual stress concentration is dependent on the cooling rate, a rapid cooling rate at the edge will generate a higher residual stress concentration compared with mid plane node.

The residual stress is also affected by the sintering temperature, the higher the temperature, the higher the residual stress. Thus, higher residual stress was recognized in the Finishing media followed by General-purpose media and then Cutting media

The numerical residual stress was compared with experimental data obtained by the XRD ($sin^2\psi$ method). The measurements follow the same trend line of parabolic shape, the residual stress in a compressive state at the edge node and tensile condition at the mid plane node. The results demonstrated that the discrepancy in stress was about 14% at the edge node and 29% at the mid plane node. However, the results do not show a perfect agreement but are sufficient for the purpose of this comparison.

5.13 References

Carre, H. and L. Daudeville (1996). "Numerical simulation of soda-lime silicate glass tempering." Le Journal de Physique IV **6**(C1): C1-175-C171-185.

Cesar de Sa, J. M. A. (1986). "Numerical modelling of glass forming processes." Engineering Computations **Vol. 3**(Iss 4): pp. 266- 275.

Cheng, W., I. Finnie and O. Vardar (1991). "Measurement of residual stresses near the surface using the crack compliance method." Journal of engineering materials and technology **113**(2): 199-204.

Clyne, T. and S. Gill (1996). "Residual stresses in thermal spray coatings and their effect on interfacial adhesion: a review of recent work." Journal of Thermal Spray Technology **5**(4): 401-418.

Dang, C. P. and D. Brüggemann (2005). "Optimizing the cooling parameters for annealing of glass bottles by stress simulation according to the viscoelastic theory." Glass science and technology **78**(4): 141-146.

Daudeville, L. and H. Carre (1998). "Thermal tempering simulation of glass plates: Inner and edge residual stresses." Journal of Thermal Stresses **21**(6): 667-689.

Haldimann, M., A. Luible and M. Overend (2008). Structural use of glass, Iabse.

Hauk, V., R. Oudelhoven and G. Vaessen (1982). "The state of residual stress in the near surface region of homogeneous and heterogeneous materials after grinding." Metallurgical Transactions A **13**(7): 1239-1244.

Hyre, M. (2002). "Numerical simulation of glass forming and conditioning." Journal of the American Ceramic Society **85**(5): 1047-1056.

Jain, A. and Y. Y. Allen (2004). Numerical simulation of compression molding of aspherical glass lenses. MATERIALS PROCESSING AND DESIGN: Modeling, Simulation and Applications-NUMIFORM 2004-Proceedings of the 8th International Conference on Numerical Methods in Industrial Forming Processes, AIP Publishing.

Johnson, A. and C. Quigley (1992). "A viscohyperelastic Maxwell model for rubber viscoelasticity." Rubber chemistry and technology **65**(1): 137-153.

Krishna, A., B. Harper and J. Lee (1995). "Finite element viscoelastic analysis of temperature and moisture effects in electronic packaging." Journal of Electronic Packaging **117**(3): 192-200.

Kuroda, S., T. Fukushima and S. Kitahara (1987). "Insitu measurement of coating thickness during thermal spraying using an optical displacement meter." Journal of Vacuum Science & Technology A **5**(1): 82-87.

McCrum, N. G., C. Buckley and C. B. Bucknall (1997). Principles of polymer engineering, Oxford University Press.

Muro.R.G. (1997) "Material Properties of a Sintered α -SiC".J. Phys. Chem. Ref. Data 26, 1195

Narayanaswamy, O. (1971). "A model of structural relaxation in glass." Journal of the American Ceramic Society **54**(10): 491-498.

Narayanaswamy, O. (1978). "Stress and structural relaxation in tempering glass." <u>Journal of the American Ceramic Society</u> **61**(3-4): 146-152.

Narayanaswamy, O. and R. Gardon (1969). "Calculation of residual stresses in glass." <u>Journal of the American Ceramic Society</u> **52**(10): 554-558.

Noyan, I. C. and J. B. Cohen (1986). "Residual stress."

Prevey, P. S. (1977). "A method of determining the elastic properties of alloys in selected crystallographic directions for X-ray diffraction residual stress measurement." <u>Adv. in X-ray Analysis</u> **20**: 345-354.

Prime, M. B. (1999). "Residual stress measurement by successive extension of a slot: the crack compliance method." <u>Applied Mechanics Reviews</u> **52**(2): 75-96.

Rekhson, S. M. (1993). "Thermal stresses, relaxation, and hysteresis in glass." <u>Journal of the American Ceramic Society</u> **76**(5): 1113-1123.

Schajer, G. S. (2011). "Destructive Methods for Measuring Residual Stresses: Techniques and Opportunities." <u>Conference Proceedings of the Society for Experimental Mechanics Series</u> **Volume 6**: 221-231.

Schwarzl, F. and A. Staverman (1952). "Time-temperature dependence of linear viscoelastic behavior." <u>Journal of Applied Physics</u> **23**(8): 838-843.

Soules, T. F., R. F. Busbey, S. M. Rekhson, A. Markovsky and M. A. BURKE (1987). "Finite-Element Calculation of Stresses in Glass Parts Undergoing Viscous Relaxation." <u>Journal of the American Ceramic Society</u> **70**(2): 90-95.

Tool, A. Q. (1946). "Relation Between Inelastic Deformability and Thermal Expansion of Glass in Its Annealing Range*." <u>Journal of the American Ceramic society</u> **29**(9): 240-253.

Totten, G. E. (2002). <u>Handbook of residual stress and deformation of steel</u>, ASM international.

Yi, A. Y. and A. Jain (2005). "Compression molding of aspherical glass lenses–a combined experimental and numerical analysis." <u>Journal of the American Ceramic Society</u> **88**(3): 579-586.

CHAPTER SIX

MATERIALS CHARACTERISATION OF THERMALLY TREATED RECYCLED SILICA BASED GLASS. PART I: CONTACT AREA OF THE BERKOVICH INDENTER

6.1 Introduction

Nanoindentation techniques are widely used to investigate the mechanical behaviour of a broad range of materials at the nanoscale. The load–displacement relationship is obtained from a plot of recorded information on forces and depth. The results of such tests (Doerner and Nix 1986, Oliver and Pharr 1992, Dao, and Chollacoop et al. 2001) among many others, are used to determine the elastic-plastic material properties: yield stress (σ_y), Young's Modulus (E), work hardening exponent (n) and hardness *H*. Several methods have been developed to analyse the loading-unloading curves of nanoindentation tests, the most important being those of Doerner and Nix (1986) and of Oliver and Pharr (1992). According to Oliver and Pharr, the reduced modulus *Er,* and the hardness are obtained from

$$H = \frac{P_{max}}{A} \tag{6.1}$$

$$S_s = \frac{2\delta}{\sqrt{\pi}} Er \sqrt{A} \tag{6.2}$$

$$Er = \frac{1 - v^2}{E} + \frac{1 - v_i^2}{E_i} \tag{6.3}$$

where P_{max} is the maximum indentation load, *A* is the projected contact area, S_s is stiffness at maximum indentation depth, and δ is a correction factor of the indenter uniaxial symmetry (Hay, Bolshakov et al. 1999). *E* and *v* are the Young's Modulus and Poisson ratio for the test material, E_i and v_i are the Young's Modulus and Poisson's ratio for the indenter.

Due to inconsistency in manufacture and because of wear through use in measurements, the indenter tip will invariably possess a finite radius of curvature. When the indentation depth is small, most, if not all, of the contact occurs in the highest spherical depth range, and the real contact area is different from that assumed for the indenter. In the case of nanoindentation tests, where penetration depth is comparatively small, this difference has a greater effect on accuracy. Therefore, in such a case, the area function needs to be calibrated for a range of indentation depths. Moreover, in the FEM simulation of nanoindentation and microindentation processes, the corresponding indenter tip radius needs to be fully specified in order to obtain a precise and simple geometrical shape of indenter.

Experimental investigations conducted over many years on many material systems have shown that the projected area *A* is an important parameter for obtaining mechanical properties. The projected area is considered to be a function of contact depth, $f(h_c)$ - obtained by calculating the shape of the indenter at intervals of contact depth. A calibration method has been proposed to estimate $f(h_c)$ prior to analysis of the projected area, (Oliver and Pharr 1992). The estimation employs a pre-defined material of a known Young's Modulus and also takes into account compliance of the load structure. The area function is then estimated from the best fit for the A versus h_c data using the relationship:

$$A(h_c) = C_0 h_c^2 + C_1 h_c^1 + C_2 h_c^{1/2} + C_3 h_c^{1/4} + C_4 h_c^{1/8} + C_5 h_c^{1/16} \qquad (6.4)$$

-where h_c is the contact depth, C_O is the tip geometry coefficient (C_O= 24.5 for a perfect Berkovich indente, $C_1 - C_5$ are variable coefficients obtained from the indentation instrument at the calibration stage through a best fit of the experimental data. The Oliver and Pharr method is reported to be highly accurate in determining the area function of both simple and complex imprint shapes, however, in the actual application it is very difficult to understand the physical meaning of the coefficients introduced in Eq. (6.4).

Oliver and Pharr (1992) focussed on the calibration process to determine the area function; other researchers have suggested imaging techniques of the residual imprint for obtaining the tip geometry. Transmission electron microscopy (TEM) was employed by Doerner and Nix (1986) who adapted a method developed earlier by Pethicai, Hutchings et al. (1983) using two-stage carbon replicas to determine the indenter shape calibration. McElhaney, Vlassak et al. (1998) advocated a new indenter calibration technique based on measurement of the compliance of both contacts and use of scanning electron microscopy (SEM) measurements for the areas of large indentations. Herrmann, Jennett et al. (2000) proposed a method to determine the indenter area function from direct measurements obtained using a scanning force microscope (SFM). The SFM data for tungsten and fused silica reference materials were reported to exhibit good agreement with results obtained from the compliance method of Oliver and Pharr. The mathematical analysis of the load-displacement curve such as that described by Oliver and Pharr is relatively difficult for a complex material model and hence the strength of the interactions of the system are difficult to discern.

However, finite element modelling simulations are now more commonly employed to aid in the analysis of mechanical properties over a wide range of material systems using load-displacement curves obtained from experiments.

In this study, the area function was determined from continuous stiffness measurement (CSM) Berkovich nanoindentation tests with fused silica. It was reasonably assumed that the test material possessed a load-independent hardness. A FEM simulation was developed in order to aid determination of the tip radius curvature and inclination angle distortion. The area function was analysed using experimental data coupled with FEM, and the deviation from the perfect Berkovich geometry was determined. The deviation being attributed to indenter tip blunting and inclination angle distortion. The developed FEM was subsequently adapted with a root mean square optimization algorithm in order to obtain the most accurate values of tip geometry for a range of target curvatures and apex angles. The method results in a best match (curve fitting) of both numerical and experimental results for a minimum value of objective function. This new approach will be shown to improve the correlation between measurement and theory.

6.2   Experimental procedure

A fused silica sample was employed as the test specimen. The specimen was prepared to standard metallographic and nanoindentation test specification. The specimens were mounted using a hot compression thermosetting resin, machine type: Struers Prontopress-2. The specimen was positioned in the press mount, and the resin was added to a pre-defined level. Heat and pressure were then applied to set the specimen. The mounted specimen was finish prepared by wet grinding using a Metaserv rotary grinding machine with abrasive papers of grade P120 to fine grade P1200A. Nanoindentation experiments were carried out using a calibrated Nano indenter CSM equipped with a standard Berkovich indenter. For each loading unloading cycle, an approach speed of 3,000 nm/min and dwell time of 3 seconds at each load interval was programmed. Tests were carried out at ten pre-determined maximum load values in the range 6.5-250 mN. Three indentation tests were performed at each load, the average of the group results are presented in this study with thermal drift neglected. Typical load indentation curves obtained from this experimental work are shown in Figure 6-1 and Figure 6-2.
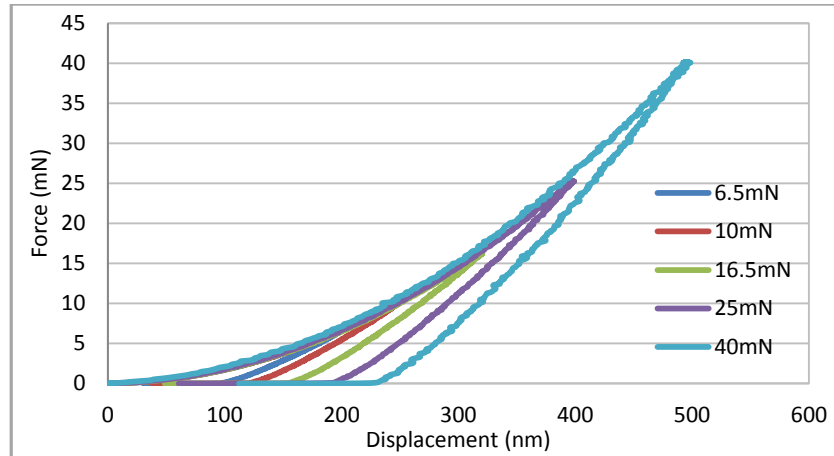
Figure 6-1 Typical loading- unloading curves for fused silica with indentation load of (6.5-40) mN
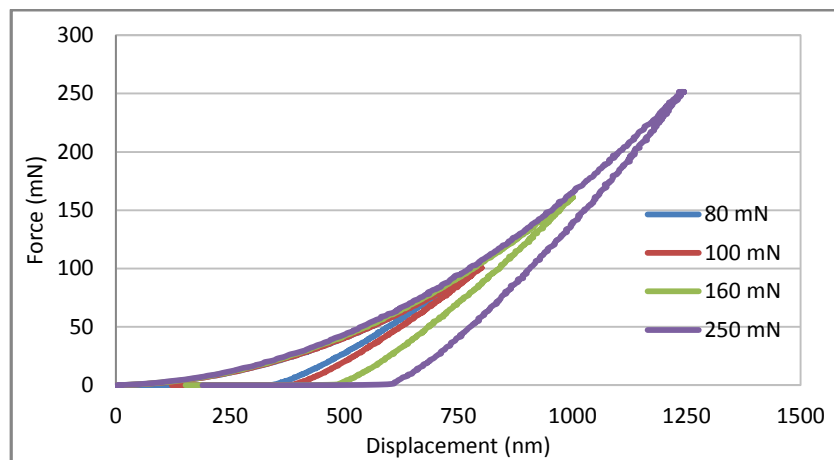
Figure 6-2 Typical loading- unloading curves for fused silica with indentation load of (80-250) mN

6.3   Results and discussion

Fused silica was selected as the reference material because it has elastic isentropic properties and presents no significant plow profile (pile-up), for an indentation ratio of $h_f/h_{max} < 0.7$ - such properties can be expected to give an accurate projected area result from the Oliver and Pharr method. Beyond this value the correlation deteriorates (Bolshakov and Pharr 1998, Cheng and Cheng 1998) .

The method to determine the area function is based on the assumption of (a) load independent hardness for an elastic plastic material and (b) an elastic modulus independent of indentation depth.

Substitute Eq. (6.1) in Eq. (6.2) to give

$$S_s = \frac{2\delta}{\sqrt{\pi}} E_r \sqrt{\frac{P_{max}}{H}} \tag{6.5}$$

Based on the assumptions of (a) and (b) above

$$\beta = \frac{\sqrt{\pi}}{2\delta} \frac{\sqrt{H}}{E_r} \tag{6.6}$$

The Oliver and Pharr (1992) method proposes the load frame and specimens as two springs in series

$$C_T = C_S + C_F \tag{6.7}$$

where C_T is the total compliance and is the sum of compliance of the specimen C_S and compliance of the frame structure, C_F. Based on the guiding principle given in Annex B of ISO (14577-1 2002) it is possible to calculate the indenter area function following the series of equations expressed therein. The specimen compliance during the elastic contact is specified by the inverse of the contact stiffness, and the total compliance is determined by the inverse of the initial region of the experimental unloading slope

$$\frac{1}{S_T} = \frac{1}{S_S} + C_F \tag{6.8}$$

Substitute Eq. (6.5) and Eq. (6.6) into Eq. (6.8) gives

$$\frac{1}{S_T} = \beta \frac{1}{\sqrt{P_{max}}} + C_F \tag{6.9}$$

To calculate the contact stiffness at maximum load S_T, Oliver and Pharr (1992) suggested that the first portion of the experimental unloading curve can be fitted to a power law mathematical expression,

$$P = \alpha (h - h_f)^m \tag{6.10}$$

-where h is the indentation depth, h_f is the final indentation depth obtained by curve fitting, α and m are constants and can be determined using a least squares fit. The initial experimental unloading slope will be then obtained by differentiating Eq. (6.10) at maximum indentation depth

$$S_T = \left(\frac{dp}{dh}\right)_{h_{max}} = m\alpha (h - h_f)^{m-1} \tag{6.11}$$

Different indentation loads were applied to the fused silica specimens and the load displacement curves were analysed using Eq. (6.10) and Eq. (6.11) to determine the slope of the initial unloading curve S_T. Figure 6-3 shows the relation between the initial loading curve S_T and maximum applied load, P_{max}. As displayed, there exists a very good linear relationship between the inverse of the slope of the initial unloading curve, $1/S_T$ and the inverse of the square root of maximum load $(1/P_{max})^{0.5}$. The linear regression fitted data obtained from Eq. (8) gives $C_F = 0.128$ nm/mN, and $\beta = 32.05$ nm/mN. The load frame compliance shows a reasonable value for an instrumented nanoindentation measurement when compared with published data, for example: $C_F = 0.196$ nm/mN (Gong, Miao et al. 2004) and $C_F = 0.1$ nm/mN, (Troyon and Martin 2003).
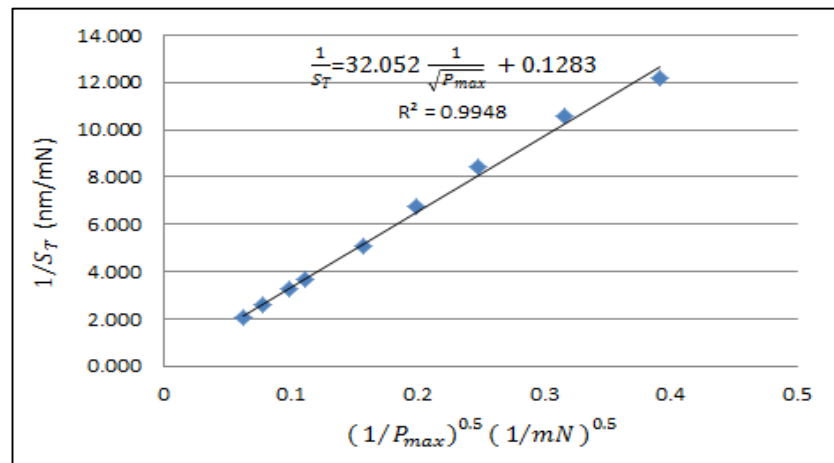
Figure 6-3 Relation between $1 / S_T$ and $(1/P_{max})^{0.5}$

6.4 Berkovich indenter correction factor

The value of the correction factor δ has a great effect on the elastic modulus, hardness and contact area function. For a small deformation of an elastic-plastic material caused by an indenter of a rigid asymmetric smooth profile, the value of δ is approximately unity, however for a Berkovich indenter with non-symmetric profile, the value of δ should be carefully considered in order to achieve a high accuracy in properties of hardness and Young's modulus. The latest studies have shown that for an elastic-plastic material and a perfectly elastic deformation by a rigid cone all estimated values of δ deviate from unity due to departures from the small strain approximation. King (1987) used a numerical method to study the effect of flat ended punches on the elastic material.

The analysis showed that δ has a value of approximately 1.034 for a triangular punch and approximately 1.012 for a square based indenter. Vlassak and Nix (1994) proposed a new numerical method using a triangular punch; and found a higher value of δ equal to 1.058. Hay, Bolshakov et al. (1999) employed both an analytical technique and FEM to examine the deformation of elastic material by a conical indenter with a half induced angle of 70.3°, results show that in the case of Poisson's ratio of 0.3, δ deviates from unity by 0.067. They developed the following expression to calculate δ based on the conical indenter, induced angle size and Poisson's ratio

$$\delta = \pi \frac{[\frac{\pi}{2} - 0.8312 \, cot \, \theta \, \frac{1 - 2v}{4(1 - 2v)}]}{[\frac{\pi}{2} - 0.8312 \, cot \, \theta \, \frac{1 - 2v}{4(1 - 2v)}]^2} \qquad (6.12)$$

From the review of previous works and removing the value derived from a flat half space, values for δ lie in the range $1.022 < \delta < 1.083$. However the value of $\delta = 1.05$ is considered a best target for this study given that the possible error has a minimum value of approximately $\pm$ 0.05.

6.5   Contact area of CSM load–depth sensing for a Berkovich indenter

Determining the tip area function is essential to calculate the hardness and Young's modulus of the indented material, Oliver & Pharr (1992), and Herrmann (2000). There are different methods described in ISO 14577-4 (2002); that explain the procedure for tip area function calibration based on the mechanical properties of the indented material and prior understanding of the frame compliance.

The Young's Modulus and Poisson's ratio for fused silica are: $E = 70.2$ GPa and $v = 0.22$ respectively, Gadelrab (2012). The properties of the Berkovich indenter used in the experiment were Young's Modulus, $E_i = 1147$ GPa and Poisson's ratio $v_I = 0.07$ (as shown in the CSM data sheet). Based on this information the reduced modulus E_r from Eq. (6.3) was calculated to be 69.15 GPa. The hardness of the fused silica material employed in experiments was found from Eq. (6.6) to be $H = 6.96$ GPa and $\beta = 32.057$ nm/mN. Using this hardness value and value of β, the projected area can then be calculated using Eq. (6.1). It is first necessary to determine the contact depth h_c at each load for the relationship between h_c and P_{max}.

The contact depth h_c is given by the expression.

$$h_c = h_{max} - \varepsilon \frac{P_{max}}{S_s}$$

(6.13)

-where ε is a constant depending on indenter geometry. The contact depth was calculated based on the Oliver and Pharr (1992) least square fitting procedure taking into account the correction factor. The exponent *m*, appearing in the Oliver Pharr method was calculated from curve fitting the first portion of the unloading curve and it has a great effect on the value of ε as indicated from Eq. (14).

$$\varepsilon = m \left[1 - \frac{2\Delta \left(\frac{m}{2(m-1)} \right)}{\sqrt{\pi}\Delta \left(\frac{1}{2(m-1)} \right)} (m-1) \right]$$

(6.14)

Over the expected range of 1.2<*m*<1.6, the value of ε has been found to change in magnitude. The two values: ε= 0.75 proposed by Oliver and Pharr (1992) and ε= 0.785 proposed by Martin and Troyon (2002), and Troyon and Martin (2003), were reported as the maximum limits for ε variation. Figure 6-4 shows the relationship between the unloading curve exponent *m,* and the maximum indentation depth with a fused silica specimen. A systematic relationship was observed where the exponent *m,* increased with a decrease in maximum indentation depth for an elastic-perfectly plastic material and the trend line remains relatively constant at maximum depths greater than 1,000nm. These results agree with results obtained by Oliver and Pharr (1992), and Bolshakov and Pharr (1998)
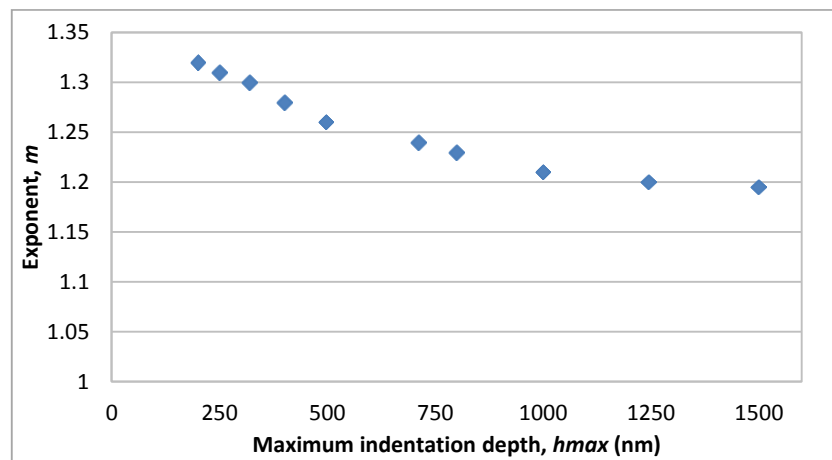
Figure 6-4 Relationship between the unloading curve exponent, *m,* and the maximum indentation depth for fused silica material

The hardness number obtained from Eq. (6.1) was used to calculate the projected contact area A as a function of the contact depth h_c, Eq. (6.13) and the results are shown in Figure 6-5. A linear relationship between $\sqrt{A}$ and h_c for the actual and a perfect indenter is evident from the regression analysis.
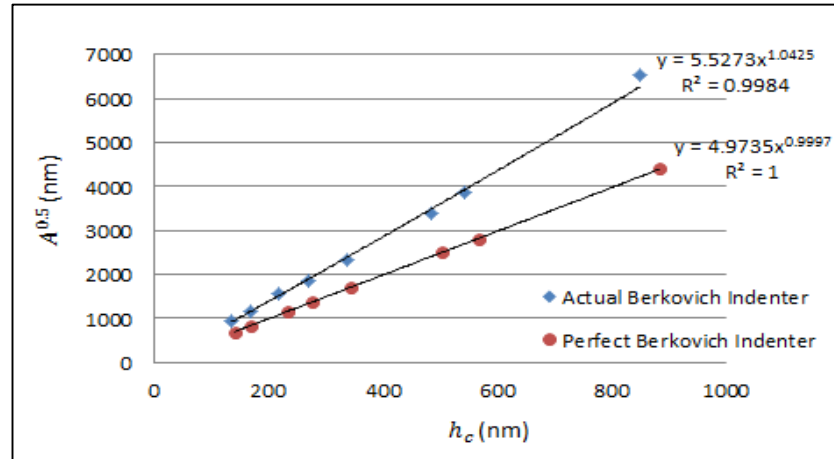
Figure 6-5 Tip area function values for a Berkovich tip determined from experiment compared to those for a perfect indenter

The Berkovich indenter is usually modelled as a rigid body with a perfect pyramidal shape having a half induced angle φ of 70.3º , the projected contact area / depth relationship proposed by Doerner and Nix (1986) is:

$$A_p = \pi\, h_c{}^2 tan^2\varphi = 24.5h_c{}^2 \qquad (6.15)$$

As demonstrated in Figure 6-5 the actual indenter is in practice never an ideal indenter due to tip blunting. In the case of a non-perfect indenter, the indenter area functions as described by Martin and Troyon (2002) and Oliver and Pharr (1992) can be determined from

$$A_P = C\,(h_c + h_d)^2 \qquad (6.16)$$

Where h_d is the distance between the blunted edge and the cone-end as is shown in Figure 6-6. The area function results of the indenter used in our experimental work deviates from that expected for an ideal indenter; this may be attributed to the indenter deforming under the action of the localized contact stress field. In such a case, the effective half included angle of the indenter would increase to $\theta^{'}$, thus resulting in a higher calibration value, C as shown in Figure 6-6. The expression of A_P in Eq. (6.16) is the projected area for a conical shape satisfying $h_c > \partial$.

The regression analysis data shown in Figure 6-5 were obtained according to Eq. (6.16) using Sigma plot software, yielding values of $C = 30.55$ and $h_d = 12.5$.
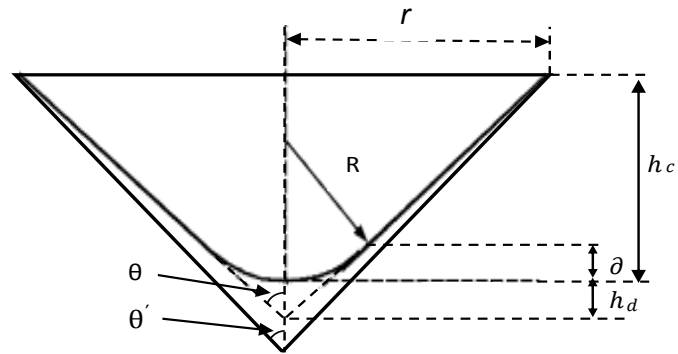
Figure 6-6 Schematic diagram shows the geometry of blunt indenter

The projected area of the spherical part A_{PS} of the indenter was calculated using Pythagorean theory for the case of $h_c \leq \partial$

The radius r of the spherical area is given by

$$A_{PS} = \pi\, r^2 \tag{6.17}$$

$$r^2 = R^2 - (R - h_c)^2 \tag{6.18}$$

$$h_d = \frac{R}{sin\varphi} - R \tag{6.19}$$

Substituting Eq. (18) into Eq. (17), the area function for the spherical parts are given by

$$A_{PS} = \pi\, h_c(2R - h_c) \tag{6.20}$$

In this study a series of nanoindentation, experimental tests were performed at different indentation loads. However, the spherical part of the area function was neglected based on the very reasonable assumption of all applied loads being performed with $h_c > \partial$.

The deviation in the area function results may be due to indenter tip blunting and this is supported from regression analysis. The h_d value obtained from the curve best fitting, $h_d = 12.5\ nm$. Troyon and Martin (2003) consider the value of h_d to be approximately 6.5 nm for the case of a blunted Berkovich indenter with half induced angle of 70.3^0 and tip radius of 105 nm. Sawa and Tanaka (2001) determined the distance for four different materials using four different indenters and found it to vary in the range 6.1nm$< h_d <$ 28.8 nm.

However, tip roundness is not the only factor found to contribute to deviations in values of the area function of an actual indenter. Deformation due to the concentrated residual field stress during indentation will also have effect on the half-induced angle, θ resulting in change in the value of the constant C. The difference can be noted physically in Eq. (6.16) between the two values determined from experiment, C = 30.55, and theory, C=24.56.

6.6   FEM supported determination of tip radius value

Numerical simulations were performed using ABAQUS finite element code. This code was developed to simulate the Berkovich indentation test. The Berkovich indenter geometry is that of a three sided pyramid with total included angle of 142.3 degrees. The Berkovich indenter was modelled as a 2-D asymmetric feature with a spherical cap having a specific tip radius. Figure 6-7 (a) shows the tip radius modelled with values of projected area function and contact depth obtained from experiment data for a real indenter. As is shown in Figure 6-7 (b) the specimen was modelled with a linear axisymmetric triangular element type (CAX4R). All specimen sizes used in the simulation were greater than 10 times the maximum indentation depth, which is satisfactorily large, in order to avoid any specimen size effect and boundary effect (Knapp, Follstaedt et al. 1999). The lower surface of the specimens was fixed for all degrees of freedom and one side face was symmetrically fixed in the y-direction. The contact constraint between the indenter and material was defined as the master surface (indenter) and slave surface (material)   interaction with a normal contact, to allow the master surface to move and contact the material at all times during the simulation. The contact direction is then obtained in relation to the master surface.
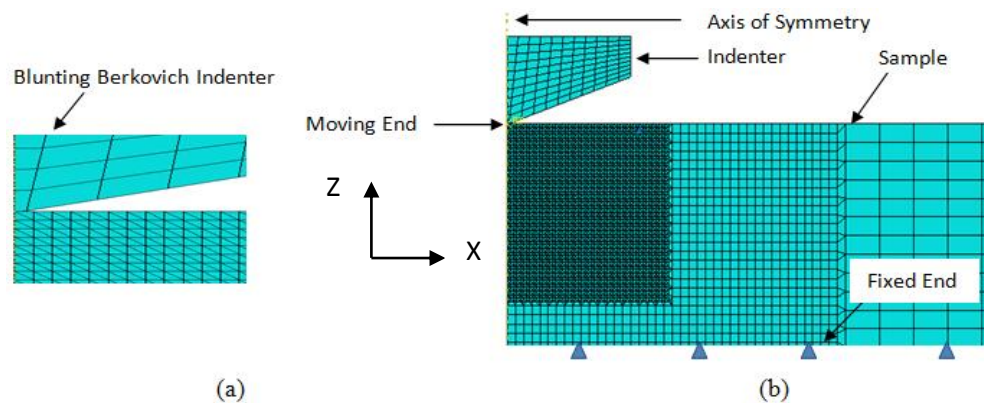
Figure 6-7 Finite element boundary conditions and mesh density of the indentation process

Mesh density under the indenter tip was refined in order to achieve the deformation and stress gradients during indentation to a very high accuracy. The indentation method was simulated in two alternating steps. During the loading step the indenter was moved in the z-direction in ramp mode and penetrated the specimen until the maximum depth was achieved. The reaction force was recorded at a reference point representing the overall load on the specimen. During the unloading step the indenter was returned to the initial position and same reference point. The loading curve represents the resistance of the material, while the difference between loading and unloading represents the energy (Swaddiwudhipong, Tho et al. 2005). Nano-indentation finite element modelling was performed based on the assumption of there being no exponent to the value of strain hardening of the material. Commonly, amorphous materials do not present a predictable strain hardening behaviour (Youn and Kang 2005, Gadelrab, Bonilla et al. 2012). Consequently, the fused silica was assumed an isotropic, linear elastic-perfectly plastic material.

6.7 Numerical simulation of Berkovich indentation

The tip radius calculation using best fitting regression analysis of experimental results is very difficult for the Berkovich indenter type due to the size of tip radius (100 nm -200 nm)-which is considered large if compared with the other indenter tip radii. Since the mechanical properties of fused silica are known from the prior instrumented indentation tests, these data were used as input parameters to the FEM simulation. The elastic modulus, estimated from experimental data was $E = 69.91$GPa. This value is very close to the value used by Gadelrab, Bonilla et al. (2012) of $E = 70.1$GPa. The yield strength is calculated from a parametric study of the FEM simulations, matching the force displacement curve to the one obtained from a typical experimental result (Gadelrab, Bonilla et al. 2012). This analysis delivered a value of $\sigma_y = 6.1$GPa, closely matching the value reported by Shim, Oliver et al. (2004) of $\sigma_y = 5.8$ GPa.

The effect of tip radius on the load displacement curves is shown in Figure 6-8 and is consistent with conventional understanding that a blunted tip will require greater force to penetrate a stated material when compared to a sharp indenter. Furthermore, the loading curve of the elastic-perfectly plastic material is more strongly affected by tip roundness if compared with the unloading curve.

Yu, Polycarpou et al. (2004) reported that the accuracy of mechanical property measurement is principally affected by tip radius blunting especially in nanoindentation. Wang, Fang et al. (2007) reported that the change in the tip radius results in significant effect on the load displacement data. The authors found the load to increase with a larger tip radius at the same maximum indentation depth.
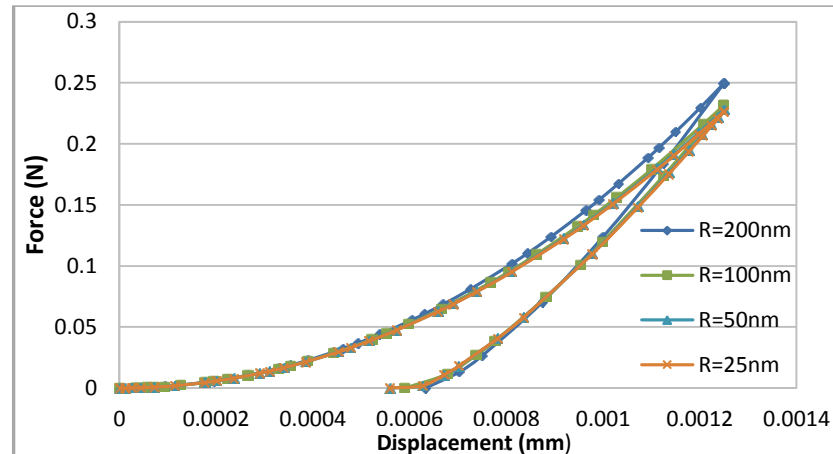
Figure 6-8 Effect of tip radius on the load displacement curves of fused silica

Figure 6.9 shows a flowchart of the FEM-based algorithm for determining the indenter tip geometry and the indenter inclination angle. The approach associates experimental results, numerical results and an optimization algorithm with the FEM in order to obtain the optimal value for a wide range of simulation space and target parameters leading to a best match between experiment and theory (minimum objective function). Within this approach, a parametric study was undertaken to determine the tip radius and inclination angle for a given set of indentation data using script-programming language (python) interfaced with ABAQUS FEM. In this arrangement, the programme automatically searches for a range of values of tip radius and inclination angles until minimum convergence of load displacement is achieved. In the searching process, the input data was transformed to a discrete form with equally spaced points at each indentation depth (indentation points). At each indentation point, the objective function values are calculated for each set of tip radius and inclination angle using a predefined program in Microsoft Excel. The final objective function was determined by the sum of objective functions at each indentation point. The final tip geometry is given by the minimum objective function value, defined as the optimal solution.

```
                              ┌──────────────────────┐
                              │ Indenter with unknown │
                              │     tip radius        │
                              └──────────────────────┘
                                         │
        ┌──────────────────┐   ┌────────────────────────────────┐
        │ Initial estimate │   │ Experimental nanoindentation at │
        │  of tip radius   │   │ depth h≤ 100nm on reference    │
        └──────────────────┘   │ material with known E, and H   │
                 │             └────────────────────────────────┘
        ┌────────────────────────┐
        │ Fem simulation results of │
        │     p-h, E, and H         │
        └────────────────────────┘
                      │
        ┌──────────────────────────────────────────────┐
        │ Objective function RMSE optimization algorithm │
        └──────────────────────────────────────────────┘
```
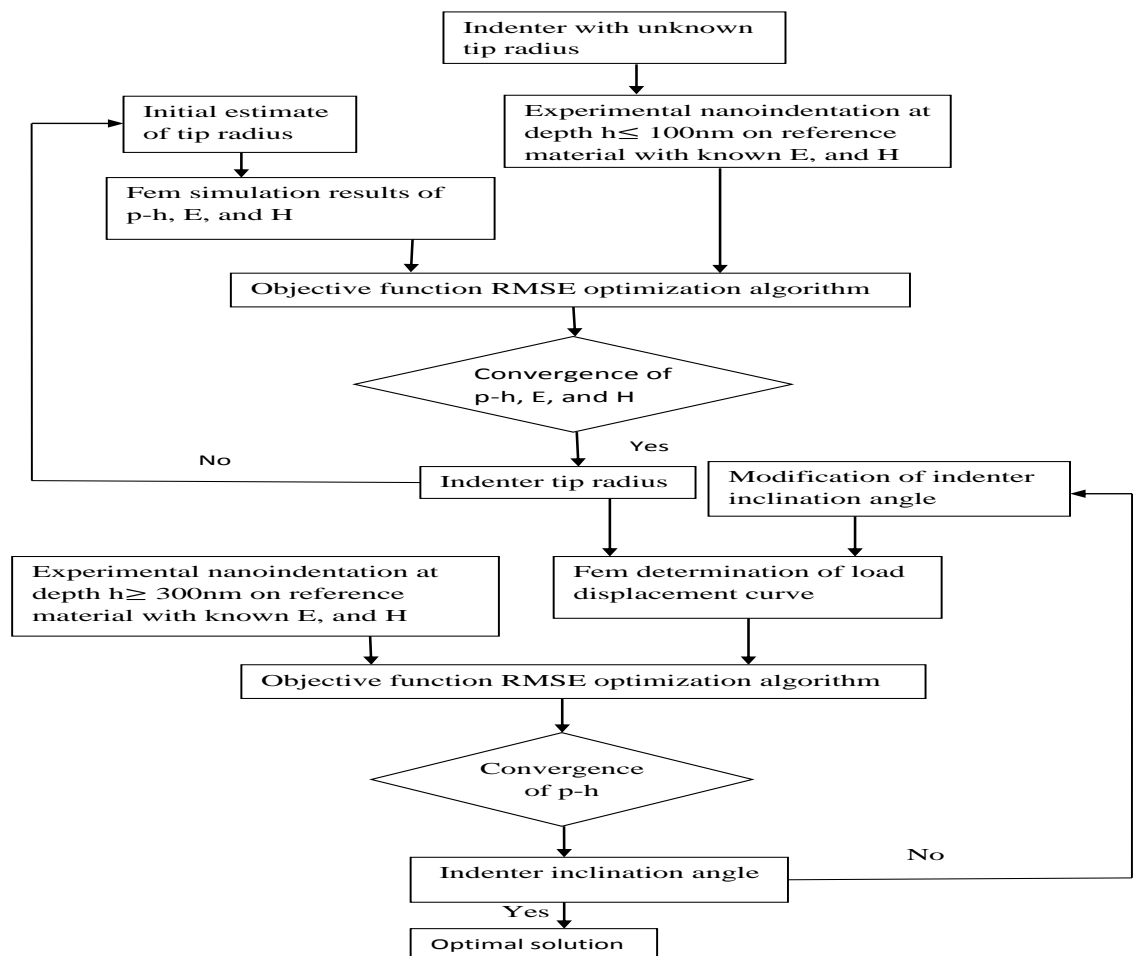
Figure 6-9 Flowchart of the FEM-based algorithm for determining the indenter tip geometry and indenter inclination angle

6.8   Optimization method for obtaining area functions and tip radius

A series of FEM simulations were performed for a Berkovich indenter using a wide range of tip radii and indenter inclination angles. Load displacement curves from numerical modelling were compared with experimental results at different indentation loads, with best match results obtained employing an objective function. Many optimization methods have been used by researchers to predict the best parameters using single- or multi-objective functions, for example Luo, Lin et al. (2006), and Kang, Becker et al. (2012). The main purpose of optimization techniques in our context is to achieve a best fit between the load displacement curve obtained from real measurement results and the curve obtained from numerical analysis.

The objective function used in this study is the root mean square error (RMSE). The RMSE value is obtained from determining the difference between experimental and numerical loads for the nano-indentation test Eq. (6.21)

$$MIN_{OF} = \left[\frac{1}{N}\sum_{i=1}^{N}\left(F_{exp-l}^{i} - F_{num-l}^{i}\right)^2 + \frac{1}{N}\sum_{i=1}^{N}\left(F_{exp-ul}^{i} - F_{num-ul}^{i}\right)^2\right]^{1/2} \qquad (6.21)$$

-where F_{exp-l}^{i} is the measured Force applied in loading at a particular depth, F_{num-l}^{i} is the value of Force obtained from theory for the loading section of the curve at the same depth predicted by FEM, F_{exp-ul}^{i} is the measured Force in unloading at a particular depth, F_{num-ul}^{i} is the value of Force obtained from theory for the unloading section of the curve at the same depth predicted by FEM, and N is the number of sampling points in each test.

Figure 6-10 shows the comparison between the load displacement curve for numerical theory and experimental results for two different maximum loads. The two curves exhibit good correlation and only a minor deviation occurs in small loads due to the elastic-perfectly plastic material constitutive material law used in the FEM, which is not fully adequate in explaining the behaviour of fused silica material. Gadelrab, Bonilla et al. (2012) reported that the Drucker–Prager model of material densification is more appropriate than the full plastic model in the nanoindentation of fused silica. However, the overall effect of this deviation on the Young's modulus and yield stress is extremely small and thus is ignored in this study. The minimum objective function was determined for the case of tip radius equal to 175 nm, and inclination angle of the Berkovich indenter being within the given tolerance of $70.1^0 \pm 0.15^0$.
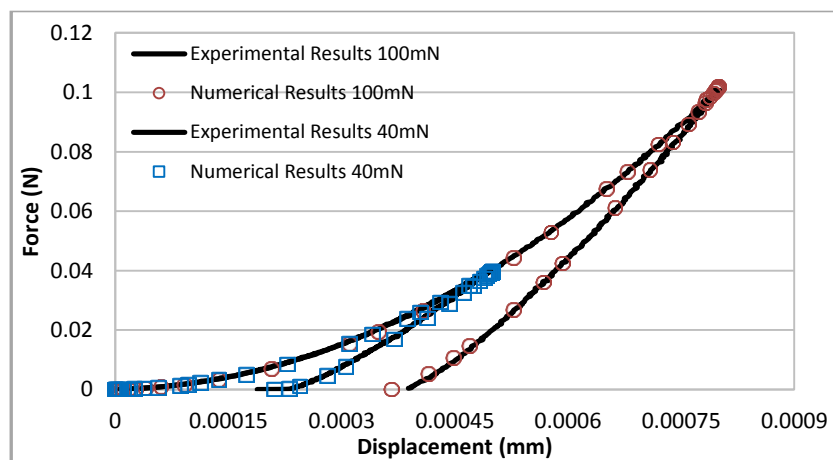
Figure 6-10 Comparison between numerical and experimental curves using optimal Berkovich tip geometry

6.9   FEM supported determination of the area function

Figure.6-11 (a) shows the 2-D asymmetric FEM employed to calculate the projected area function between the indenter and the specimen. To conduct this method, the nanoindentation load displacement data on the practical reference material with known Young's modulus and Poisson ratio, as well as the corresponding properties of the indenter have to be available. The indenter geometry of tip radius and inclination angle is modelled corresponding to the dimensions obtained using the algorithm developed in the previous section. Figure.6-11 (b) shows the indenter tip calibration methodology according to guidelines given in Annex B of ISO14577, taking into consideration the Young's modulus and Poisson's ratio of a reference material and $C_f \cong 0$. The projected area and contact depth were calculated using the following series of equations

$$A_P = \pi \, r_c^{\,2} \tag{6.22}$$

$$C_t = C_s = tan\theta \; when \; C_f \cong 0 \tag{6.23}$$

$$C_t = \left|\frac{dh}{dp}\right|_{P_{max}} = \frac{\sqrt{\pi}}{2\,E_r\sqrt{A_P}} \tag{6.24}$$

$$h_c = h_{max} - \varepsilon P_{max}C_t \tag{6.25}$$
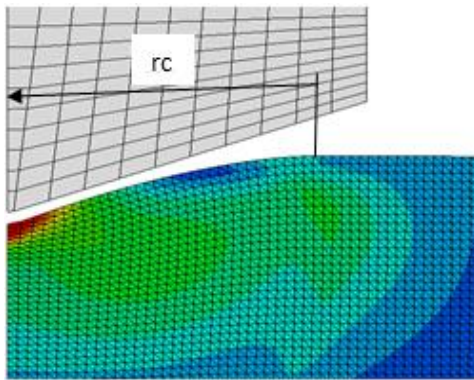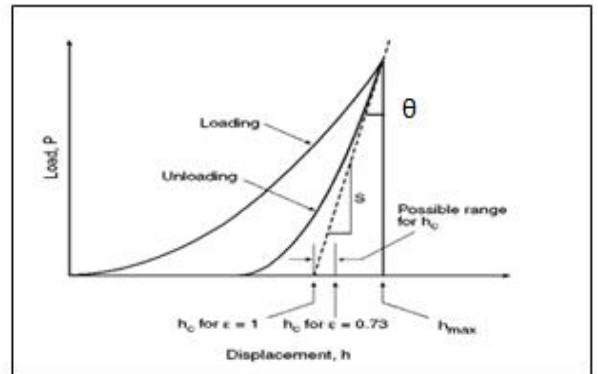
(a)	(b)

Figure 6-11 FEM supported determination of the area function a) Screenshot of 2-D asymmetric FEM used to calculate the projected area function , and b) Indenter tip calibration methodology

A series of FEM simulations were carried out at various indentation loads enabling the indenter projected area A_P to be plotted against contact depth h_c for the examined fused silica reference material. The indenter area function values, determined from the tip geometry and area function algorithm, exhibit only a small dispersion, with the corresponding scatter satisfying ISO14577K-D. Bouzakis and Michailidis (2008) reported that nanoindentation FEM supported simulations were carried out using a trial and error methodology, enabling the determination of materials stress-strain constitutive laws and an accurate mathematical explanation of corresponding indenter tip geometry.

Figure 6-12 shows the comparison of the indenter projected areas A_P versus the contact depth h_c, according to experimental results and the developed tip geometry FEM algorithm, for the examined reference material. A close correlation is observed between the numerical and experimental data. This informs us that an accurate value of tip geometry and area function can be predicted using the developed FEM based algorithm and reference material. The area function obtained from fitting experimental force displacement curves is found to be larger than the tip metrology from the FEM results. Outcomes of the numerical optimization are also very similar to those obtained with the experimental results, and further, both results yield an area function significantly larger than that for a 'perfect' Berkovich indenter.
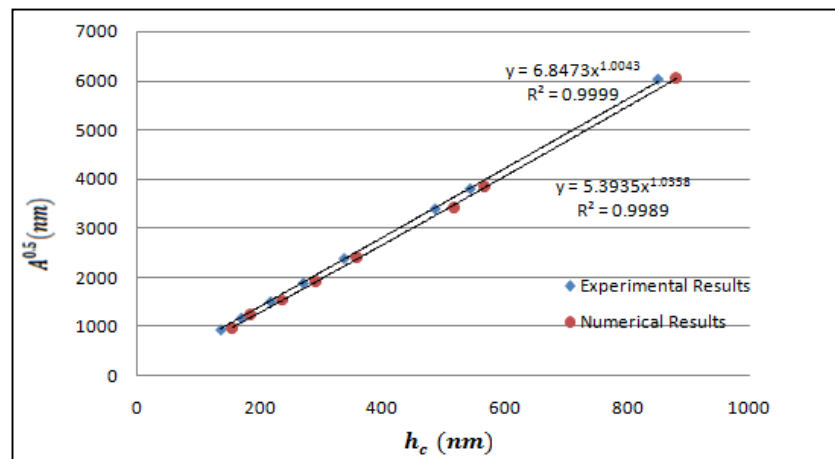
Figure 6-12 Comparison of the indenter projected areas A_P versus the contact depth h_c, according to experimental results and the developed tip geometry FEM based algorithm

Under all load conditions in this study the elastic modulus determined for fused silica was found to be the same. Based on our findings, indenter calibration using fused silica is deemed a reliable method and overcomes many of the problems encountered with other common materials during indentation testing (Shuman, Costa et al. 2007).

6.10 Conclusions

Results of nanoindentation measurements for fused silica were analysed and compared with theory. It was found that a linear relationship exists between the total measured compliance, i.e. the inverse of the measured initial unloading slope, $1/S_T$, and the inverse square root of the peak load $(1/P_{max})^{0.5}$. In the case of a known reduced modulus, E_r, and using the assumption of hardness independent load and elastic modulus independent contact depth. The projected area can be determined from the slope of the fitted $1/S_T$ vs $(1/P_{max})^{0.5}$ straight line. Using the hardness value found from this relationship the projected contact area, A can be determined. Finally, the area function is established by analysing the variation of the projected contact area with the contact depth, h_c.

An important finding in this study is that deviations in the value of the Berkovich indenter area function determined from measurement compared to those for an indenter of perfect geometry may be attributed to the factors: tip blunting and inclination angle deformation, - attributes which are included in the new analysis.

An FEM based algorithm was developed to determine tip geometry and indenter area functions. A parametric study of the simulations allowed a methodology to be developed for calculation of indenter tip geometry and inclination angle, taking into consideration both the Young's modulus and the hardness of reference materials. In this way, the exact contact between the indenter and the specimens can be determined. The calculated indenter area function according to this method is almost identical to the corresponding one expected from ISO14577-4, using fused silica as reference material. A close correlation is observed between the numerical and experimental data for indenter projected areas A_P versus the contact depth h_c.These outcomes are important for the analysis and characterisation of thermally treated glass designed for mass finishing processes.

6.11 References

14577-1, I. (2002). Metallic materials-instrumented indentation test for hardness and materials parameters-Part 1: test method, International Organization for Standardization Geneva, Switzerland.

Bolshakov, A. and G. Pharr (1998). "Influences of pileup on the measurement of mechanical properties by load and depth sensing indentation techniques." <u>Journal of materials research</u> **13**(04): 1049-1058.

Bouzakis, K. and N. Michailidis (2008). "Indenter tip geometries and calibration procedures: Deviations in determining coatings „and other materials "mechanical properties." <u>Proc: 3rd International Coference on Manufacturing Engineering ICMEN</u>: 391-398.

Cheng, Y.-T. and C.-M. Cheng (1998). "Relationships between hardness, elastic modulus, and the work of indentation." <u>Applied physics letters</u> **73**(5): 614-616.

Dao, M., N. Chollacoop, K. Van Vliet, T. Venkatesh and S. Suresh (2001). "Computational modeling of the forward and reverse problems in instrumented sharp indentation." <u>Acta materialia</u> **49**(19): 3899-3918.

Doerner, M. F. and W. D. Nix (1986). "A method for interpreting the data from depth-sensing indentation instruments." <u>Journal of Materials Research</u> **1**(04): 601-609.

Gadelrab, K., F. Bonilla and M. Chiesa (2012). "Densification modeling of fused silica under nanoindentation." <u>Journal of Non-Crystalline Solids</u> **358**(2): 392-398.

Gong, J., H. Miao and Z. Peng (2004). "On the contact area for nanoindentation tests with Berkovich indenter: case study on soda-lime glass." <u>Materials letters</u> **58**(7): 1349-1353.

Hay, J. C., A. Bolshakov and G. Pharr (1999). "A critical examination of the fundamental relations used in the analysis of nanoindentation data." <u>Journal of Materials Research</u> **14**(06): 2296-2305.

Herrmann, K., N. Jennett, W. Wegener, J. Meneve, K. Hasche and R. Seemann (2000). "Progress in determination of the area function of indenters used for nanoindentation." <u>Thin solid films</u> **377**: 394-400.

Kang, J., A. Becker and W. Sun (2012). "Determining elastic–plastic properties from indentation data obtained from finite element simulations and experimental results." <u>International Journal of Mechanical Sciences</u> **62**(1): 34-46.

King, R. (1987). "Elastic analysis of some punch problems for a layered medium." <u>International Journal of Solids and Structures</u> **23**(12): 1657-1664.

Knapp, J., D. Follstaedt, S. Myers, J. Barbour and T. Friedmann (1999). "Finite-element modeling of nanoindentation." <u>Journal of Applied Physics</u> **85**(3): 1460-1474.

Luo, J., J. Lin and T. Dean (2006). "A study on the determination of mechanical properties of a power law material by its indentation force–depth curve." <u>Philosophical magazine</u> **86**(19): 2881-2905.

Martin, M. and M. Troyon (2002). "Fundamental relations used in nanoindentation: Critical examination based on experimental measurements." <u>Journal of materials research</u> **17**(09): 2227-2234.

McElhaney, K., J. Vlassak and W. Nix (1998). "Determination of indenter tip geometry and indentation contact area for depth-sensing indentation experiments." Journal of Materials Research **13**(05): 1300-1306.

Oliver, W. C. and G. M. Pharr (1992). "An improved technique for determining hardness and elastic modulus using load and displacement sensing indentation experiments." Journal of materials research **7**(06): 1564-1583.

Pethicai, J., R. Hutchings and W. Oliver (1983). "Hardness measurement at penetration depths as small as 20 nm." Philosophical Magazine A **48**(4): 593-606.

Sawa, T. and K. Tanaka (2001). "Simplified method for analyzing nanoindentation data and evaluating performance of nanoindentation instruments." Journal of Materials Research **16**(11): 3084-3096.

Shim, S., W. C. Oliver and G. M. Pharr (2004). A critical examination of the Berkovich vs. conical indentation based on 3D finite element calculation. MRS Proceedings, Cambridge Univ Press.

Shuman, D. J., A. L. Costa and M. S. Andrade (2007). "Calculating the elastic modulus from nanoindentation and microindentation reload curves." Materials characterization **58**(4): 380-389.

Swaddiwudhipong, S., K. Tho, Z. Liu and K. Zeng (2005). "Material characterization based on dual indenters." International journal of solids and structures **42**(1): 69-83.

Troyon, M. and M. Martin (2003). "A critical examination of the P-h2 relationship in nanoindentation." Applied physics letters **83**: 863.

Vlassak, J. J. and W. Nix (1994). "Measuring the elastic properties of anisotropic materials by means of indentation experiments." Journal of the Mechanics and Physics of Solids **42**(8): 1223-1245.

Wang, T. H., T.-H. Fang and Y.-C. Lin (2007). "A numerical study of factors affecting the characterization of nanoindentation on silicon." Materials Science and Engineering: A **447**(1): 244-253.

Youn, S. and C. Kang (2005). "FEA study on nanodeformation behaviors of amorphous silicon and borosilicate considering tip geometry for pit array fabrication." Materials Science and Engineering: A **390**(1): 233-239.

Yu, N., A. A. Polycarpou and T. F. Conry (2004). "Tip-radius effect in finite element modeling of sub-50 nm shallow nanoindentation." Thin solid films **450**(2): 295-303.

CHAPTER SEVEN

MATERIALS CHARACTERISATION PART II: TIP GEOMETRY OF THE VICKERS INDENTER FOR MICROINDENTATION TESTS

7.1   Introduction

The elastic properties of a target material can be calculated by applying a solution proposed by SNEDDON (1948), on the assumption that indentation depth exceeds the radius of curvature of the indentation tip. However, the method has limited use for materials exhibiting linear elastic behaviour under indentation load. The method, based on the elastic plastic constitutive material law, can be applied when the following two assumptions are satisfied. Firstly, the unloading phase of the load displacement curve is assumed elastic, having an elastic recovery depth he. Secondly, the reloading path is expected to follow the unloading phase of the first indentation until maximum indentation depth of the previous indentation is achieved. Figure 7-1 (a) shows the indentation load displacement relationship for elastic plastic materials with linear elastic behaviour. In the case of an infinitely hard conical indenter and linear elastic half-plane, then Figure 7-1 (b) is a more representative schematic, (Fischer-Cripps 2011). To verify this assumption, a series of nanoindentation experiments were first carried out on a fused silica material using a calibrated Nano indenter (CSM) equipped with a standard Berkovich indenter. For each loading-unloading cycle, an approach speed of 3000 nm/min and dwell time of 3 seconds at each load interval was programmed, and then reloaded with a higher load at the same speed and dwell rate before the final unloading stage.

(a)   (b)
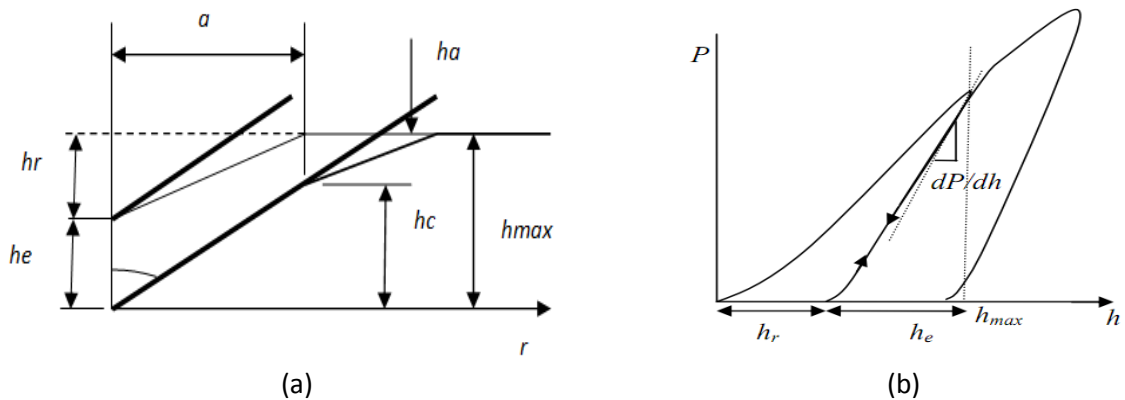
Figure 7-1 (a) Schematic diagram of elastic plastic loading unloading indentation, (b) Schematic diagram of load displacement curve for linear elastic material (Fischer-Cripps 2011)

Figure 7-2 shows results obtained from the experimental work. In this figure, the unloading and reloading curves are seen to lie on the same path and demonstrate that the unloading curve is following an elastic behaviour.

Thus, satisfying the assumption of the unloading phase being part of the elastic reloading curve under elastic-plastic indentation is crucial requirement for Sneddon's approach. These results are reported in full in the earlier [Chapter 6].
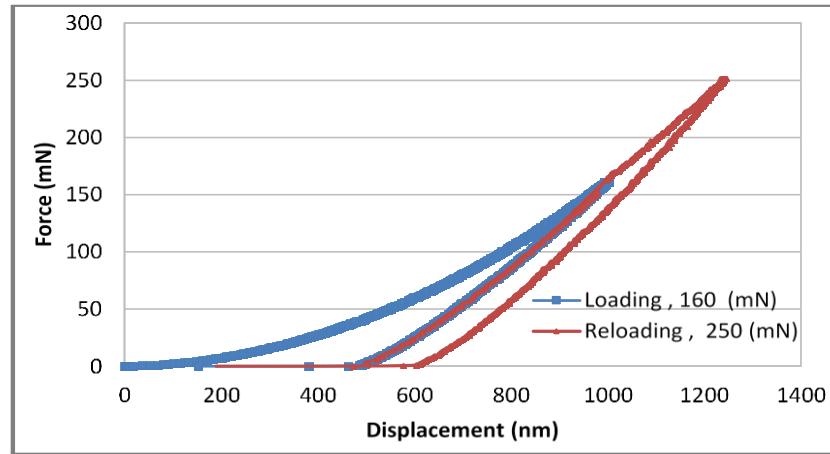
Figure 7-2 Results obtained from the nanoindentation loading and reloading experiments

The expression derived by SNEDDON (1948) to describe the elastic unloading curve obtained from the elastic load-displacement relationship for the case of an indentation by a rigid conical indenter on a linear elastic half-plane, is given as

$$P = \frac{2Etan\alpha'}{\pi(1 - v^2)} h_e{}^2 \tag{7.1}$$

$$h_e = \frac{\pi}{2} acot\alpha' \tag{7.2}$$

Differentiating Eq. (7.1)

$$\frac{dP}{dh_e} = \frac{4Etan\alpha'}{\pi(1 - v^2)} h_e = S_s \tag{7.3}$$

Substituting Eq.(7.2) into Eq. (7.3),

$$\frac{dP}{dh_e} = \frac{2\delta E}{\sqrt{\pi}(1 - v^2)} \sqrt{A_c} \tag{7.4}$$

-where P is the maximum load of the indenter, E and v are the Young's modulus and Poisson's ratio of the specimen respectively, α' is the effective half-angle of the indenter which takes into account the geometric half-angle of the indenter and the residual imprint from the previous indentation.

δ is the indenter correction factor, which approaches unity in the case of a small deformation of an elastic plastic material caused by an indenter of a rigid asymmetric smooth profile. Eq. (7.4) represents the conventional relationship to determine the elastic properties in depth sensing indentation. Bulychev, Alekhin et al. (1975) found this relationship suitable for cylindrical punch and spherical indenters, while Pharr, Oliver et al. (1992) showed that the relationship is also true for all types of pyramidal indenters.

The effective half-angle has been found from experiment and numerical analysis to be a function of E/σ_y and Poisson's ratio, v. As is shown in Figure 7-3, for typical materials, a narrow range of Poisson's ratio $0.01 < v < 0.47$, values of E/σ_y lie in the range between $100 < E/\sigma_y < 1000$, and the effective half-angle has a range between $88^o < \alpha' < 89.7^o$, (Poon, Rittel et al. 2008).
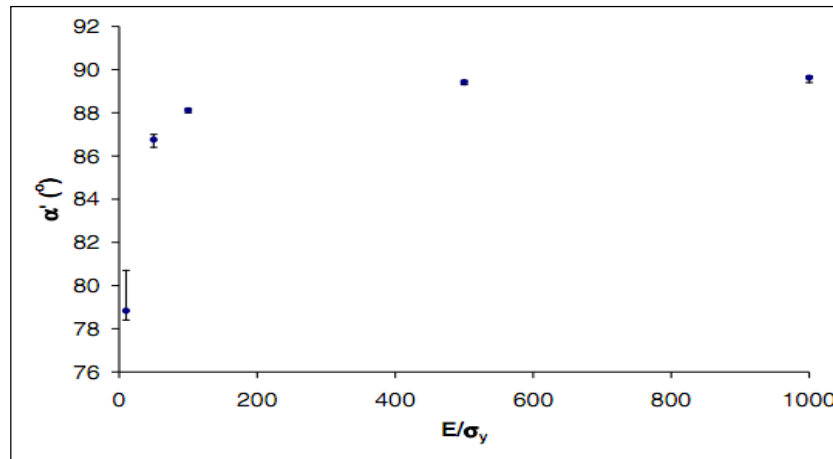
Figure 7-3 Relationship between effective half-angle and the mechanical properties, E/σ_y, and v, (Poon, Rittel et al. 2008)

A validation of the elastic unloading phase and equivalent effective angle leads to the possibility of direct use of Sneddon's elastic relation Eq. (7.1) and Pharr, Oliver et al. (1992) have shown that for a range of indenter shapes, the relation given by Eq. (7.4) is applicable.

The Vickers indenter is usually assumed to be a rigid body possessing a geometry that accords with a perfect pyramidal shape having a face angle θ, of 68°. The projected contact area A_p to depth relationship proposed by Doerner and Nix (1986) is given by:

$$A_P = 4\,h_c{}^2 tan^2\theta \qquad (7.5)$$

The actual projected area of a Vickers indenter (blunting indenter) is similar to that given for a blunting Berkovich indenter [Ref. Chapter 6] as described by Martin and Troyon (2002) and Pharr, Oliver et al. (1992), can be determined from

$$A_P = C (h_c + h_d)^2 \tag{7.6}$$

-where, h_d is the distance between the blunted edge and the cone-end. Neglecting this value will result in an underestimation of the projected area. This relation also shows that the projected area is a function of contact depth h_c. Thus, the accurate determination of contact depth and indenter tip radius is crucial for the determination of elastic properties when using Eq. (7.4). The contact depth is obtained from the expression

$$h_c = h_{max} - \varepsilon \frac{P_{max}}{dP/dh_e|h_{max}} \tag{7.7}$$

-where ε is a constant depending on Vickers indenter geometry. The value of ε may change in magnitude between $\varepsilon = 0.75$ as proposed by Oliver and Pharr (1992) and $\varepsilon = 0.785$ as proposed by Martin and Troyon (Martin and Troyon 2002, Troyon and Martin 2003), over a wide range of exponents of the unloading elastic-plastic indentation curve relationship.

It is found from numerical simulation and experimental works proposed by many researchers that the indentation material will exhibit a pile–up around the plastic imprint should the ratio of E/σ_y be large enough, typically greater than 30. This type of deformation will result in the deviation of the actual contact depth, h_c, from the value derived by Eq. (7.7). Cheng and Cheng (2004) found this deviation to be more than 30% in some cases. Oliver and Pharr (2004) reported that the values due to pile-up are only significant when *hr / hmax* > 0.7, this principle value again being relevant for the case of E/σ_y> 30. This criterion strictly limits the possibility of use of the Oliver & Pharr approach, Eq. (7.7) to accurately determine h_c for typical materials. Therefore, the accurate measurement of the projected contact area, A_p is considered as a primary challenge to reduce the errors in the determination of mechanical properties such as hardness, and reduced modulus E_r .

It is recognized that h_c is affected by the material behaviour during the indentation process, which is shown, either pile-up or sink-in. The available methods to approximate *hc* based on the material behaviour may result in overestimation or underestimation of the material property values.

Thus, the following section proposes an experimental technique to directly and most accurately determine the projected contact area, A_p without any assumptions or restrictions on material properties.

7.2 Direct measurement of Vickers indenter area function

A knowledge of indenter geometry is key to improving and validating the accuracy of the microindentation test. Moreover, the accurate representation of the indenter's geometry has a great effect on the results of area function. The area function in [Chapter 6] was determined based on the Oliver & Pharr method of continuous stiffness measurements of the Berkovich nanoindentation experimental test, which requires a continuous depth sensing technique. This requirement has limited the application of that approach in engineering conditions. However, instrumented indentation machines require the complete set of loading-unloading indentation depth curves to compute the material properties and this is not practically possible for all material systems such as those that are brittle. These materials exhibit crack initiation and propagation within the indentation process. A simpler and more effective methodology needs to be developed to characterise the material properties using a standard microindentation hardness test machine. This work seeks to provide that solution.

Although fused silica has been used widely as a reference standard for nanoindentation testing, the indentation test mechanism of most glass material systems remains difficult to interpret using general load displacement curves. There are many reasons behind these difficulties. Firstly, the lack of constitutive material laws to describe the mechanical behaviour of particular glass families which exhibit permanent changes in density under very high pressures (densification behaviour) resulting in difficulties to describe the load indentation results in terms of mechanical properties. Keryvin, Gicquel et al. (2014) proposed more reasonable constitutive models implemented in FEM software by using a material sub-routine. The results show that the pressure-induced densification (PID) constitutive law can be used to interpret the mechanical response of the load displacement curve and to describe the densified zones underneath the indenter.

Secondly, a wide range of glasses and metallic glasses can exhibit high levels of sink-in and pile-up, covering a broad range of contact behaviour compared with metallic materials, and results in a demanding challenge to determination of mechanical properties using the load indentation results. Based on results of material behaviour during indentation tests, the values of projected area calculated via direct analysis of the load displacement curve, possess high levels of error and are generally unreliable for accurate prediction of material properties due to the occurrence of pile-up and sink-in.

It has been demonstrated by previous researchers of microindentation that most materials exhibit pile-up or sink-in, around the indentation imprint, and it is increasingly recognized that the estimation of the residual indentation projected area based on the analysis of the unloading part of the load displacement curve can produce errors of up to 50% or more. Some authors (Lim, Chaudhri et al. 1999, Lim and Chaudhri 1999, Bec, and Tonck et al. 2004) suggested that the most appropriate and accurate method is to directly image the indentation using a well calibrated high-resolution atomic force microscope (AFM) and obtain the projected contact area of the indentation from the AFM image processing software. Recent developments in indenter tip scanning probe microscopy (ITSPM) based on contact mode imaging have been concerned with residual imprint image processing without any major influence on the sample or any great damage to the imprint image. However, the ITSPM technique has disadvantages when compared with AFM. The slower image scan operation, and the probe used in the scanning process usually has a higher blunting tip radius due to the use of a much wider pyramidal geometry which requires a larger force to scan the whole indentation surface and results in greater surface damage compared with AFM. Therefore, this technique is more widely used in the height image application.

(Charleux, Keryvin et al. 2014) proposed a new post-mortem ITSPM method for residual imprint observation using a height based imaging technique produced by built-in scanning probe microscopy (SPM). The SPM method was compared with three different direct methods by analysis of the load displacement curves obtained from numerical analysis and experiment, covering a wide range of material properties. It was shown that the new method systematically leads to lower error levels regardless of the type of material.

Figure 7-4 shows the experimental test results for three different materials chosen to cover a wide range of contact geometries, including fused quartz (FQ) - a sink-in material; window glass (WG) - a material having intermediate behaviour; and zirconium-based

metallic glass (BNG) - a pile-up material. The materials chosen are classified as glass materials, which exhibit negligible creep for temperatures below the glass transition temperature, are homogeneous and isotropic under the test condition and have no indentation size effect behaviour. It can be seen from the load displacement curves of the three different materials that the loading stage for each is similar, while unloading curves are different and are based on the magnitude of elastic recovery of each material. The right side shows the ITSPM images, heights below 10 nm are masked in order to highlight the shape and size of the residual pile-up. No pile-up on FQ, low peaks are marked on WG (white shadow), and high pile-up on the faces on BMG.
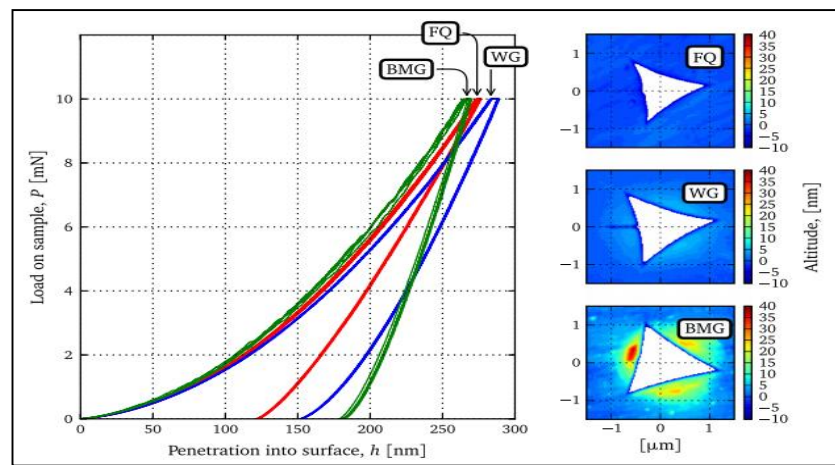
Figure 7-4 Berkovich nanoindentation work coupled with ITSPM results for three selected materials: FQ, WG and BMG,(Charleux, Keryvin et al. 2014)

(Gerberich, Nelson et al. 1996) proposed that the residual depth of penetration indicated by the line profile obtained from the AFM probe image after the nanoindentation test is about 65% of the residual depth of penetration obtained by the same nanoindentation SPM. This large discrepancy was attributed to the fact that the geometry of the AFM probe tip is much sharper than the tip used for indentation and imaging ITSPM. However, in such applications the indentation residual relaxation should be considered by assuming a delay time after the indentation process in order to achieve the final residual indentation depth. Lilleodden et. (1995) proposed that the relaxation of the residual indentation was caused by dislocations on the indentation surface, which may affect the accuracy of results for the following reasons: Firstly, the indentation depth was less than or the same as the surface roughness of the specimen. Secondly, the AFM probe tip was the same as the one with which the indentation had been made, in which case results would not be useful.

Therefore, the scanning probe geometry should be carefully considered in the case of both AFM and ITSPM based on the indentation size and material type. However, with the development of microscopic imaging processes, the systematic residual imprint imaging makes the indentation results more reliable and much faster to obtain.

The aim of this chapter is to introduce a new non-contact methodology, based on residual imprint imaging, to reduce the discrepancy in the result. It will provide increased precision in the measurement of the projected contact area and overcome issues of damage associated with the probe contact. In this study a quantitative and qualitative 3-D topography analysis of residual imprint from microindentation tests were developed using a three-dimensional optical profiler instrument Wyko NT1100 coupled with Wyko vision 64 analysis software to determine the indentation geometry and indenter area function. This new approach has been tested and validated on amorphous materials.

7.3   Experimental procedure

Fused silica samples with known mechanical properties were chosen as a test material for this work. The material was prepared to standard metallographic and microindentation test specification as described in [Chapter 6].The three-dimensional optical profiler instrument (Wyko) was used to investigate the morphology of the specimen surface after indentation. The Wyko is a first-rate tool for characterizing surface height variations and quantifying the degree of sink-in or pile-up due to plasticity, having excellent spatial resolution.

The scanned indentation imprint images from the Wyko were examined with a projected top view and in radial line mode. The new technique was employed to calculate the projected contact area of residual imprints using Wyko Vision 64 software analysis. The contact edges between the indenter and the specimen were obtained in radial line mode with reference to projected top view images, edges can be identified by a discontinuity in the slope of the cross sectional shape of the line profile. In addition, the radial line can clearly show any pile-up or sink-in around the indentation. During the maximum loading stage, the contact edge produced from a general pyramidal indenter such as that used with Vickers indentation equipment can exhibit either sink-in or pile-up and in some cases both sink-in and pile-up may occur simultaneously.

In the case of pile-up, the material appears at above the reference surface due to plastic flow around the indenter during indentation, and the phenomenon is commonly observed with low strain hardening metallic materials. In the case of sink-in, material flows to a depth below the reference surface, a phenomenon observed in high yield strength materials such as fused quartz. During the unloading stage, and in the case of the contact edge exhibiting residual pile-up behaviour, the cross-section of the contact area measurement should commence from the lowest point of the imprint to the highest point on the pile-up material. Continuous measurement of the highest points on each of the sections around the imprint form the contact zone boundary regarded as belonging to the imprint area. The inherent surface roughness of the material may make the high point positions of pile-up on the contact edge profile unclear. Therefore, in order to overcome this effect, the imprint is considered to lie inside the specified circular area and the radial line mode rotated by a small angle β_i along an axis parallel to the projected top plane and running through the lowest point of the imprint. Repeating this process from 0 to 360° leads to determination of the whole contact edge.

Figure 7-5 shows key steps of the proposed technique to calculate the contact area: (a) Represents the projected top view of the Wyko image of the Vickers indentation on fused silica with maximum load of 2.94N, (b) projected top view with different orientation of rotated angle, β_i , (c) full cross-section graph showing the radial line mode position at particular (r, β_i) , which indicates that the position of the contact edge of microindentation is above the original surface level, representing pile-up behaviour around the indentation, and (d) the process is repeated for all required values of β resulting in a full description of the contact edge boundary, specified by the black line. This describes the novelty and key differences of this new approach.
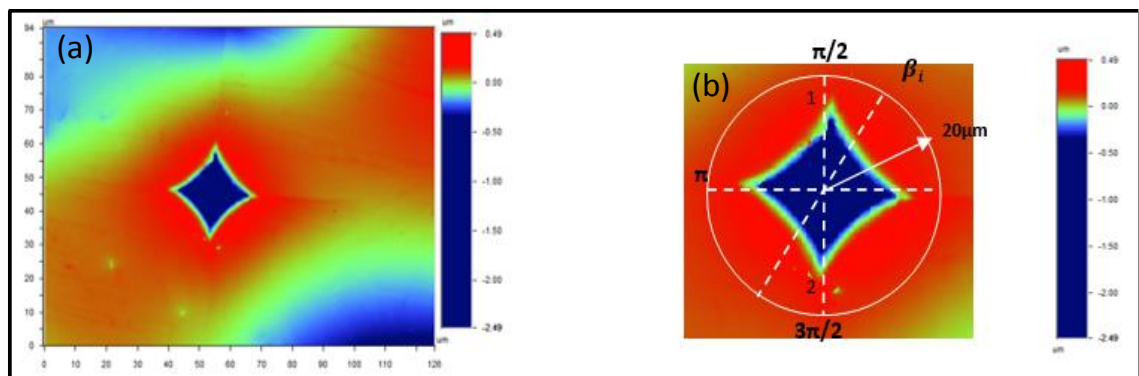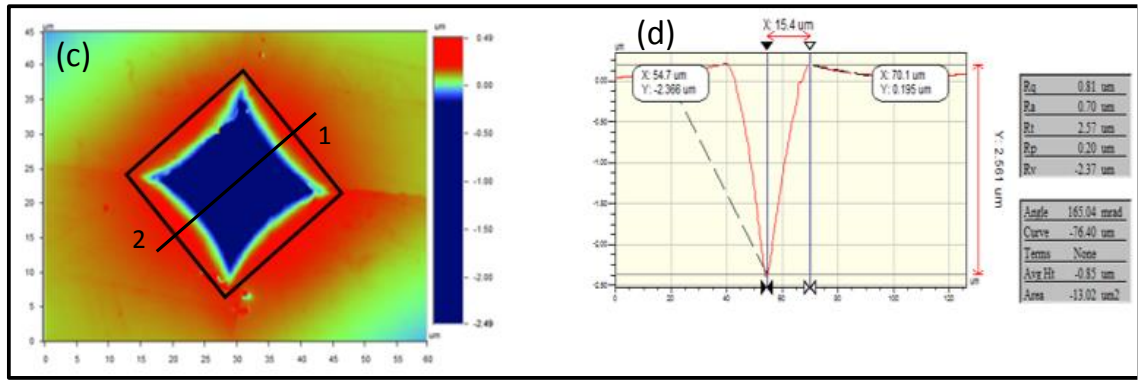
Figure 7-5 images showing the key steps of new proposed (three-dimensional optical profiler measurement) method.

7.4 Results and discussion

7.4.1 Projected area determined by new proposed method of 3-D optical profile-meter

Commercial micro-indentation testing and 3-D optical profilometry (non-contact Wyko instrument) methods have been coupled to measure the mechanical properties of fused silica and a wide range of thermally treated glass. A series of micro-indentation tests at different indentation loads were applied to the fused silica. The method to determine the area function is based on the analysis of the two-dimensional image sets obtained from micro-indentation results. The contact area, *Ac,* and indentation depth profiles corresponding to projected top view and radial line mode were extracted directly from the imprint images data analysis software as is shown in Figure 7-6. In image (*a*) a radial line position at particular (r, β_i) across the 3-D optical profile-meter image and two arrows, 1 and 2, are located on it. These arrows identify the positions of the contact edge between the specimen and the indenter along the line. Image (*b*) gives the line profile across the radial line mode on the indentation image along the direction indicated by arrows 1 and 2 shown in image (*a*). Moreover, the positions of arrows 1 and 2 in images (*a*) have identical scale and hence a one-to-one correspondence with arrows 1 and 2, respectively, in image (*b*). The distance between the two arrows in frames (*b*) is measured directly from the Wyko image. Repeating this process from around the indentation image will lead to identification of the whole contact counter (black line), and then the contact area directly determined across the counter edge, black line in image (a), that is related to the residual imprint behaviour of either the sink-in or pile-up.

However, very small discrepancies in the positioning of the arrows are unavoidable. Vickers hardness values were determined from the measurements of residual indentation size using the Wyko images Further information from the residual Vickers indentation can also be measured such as the angle at the apex and the residual depth which help to identify the elastic recovery depth and densification values.

To calculate the hardness corresponding to a given indentation, the projected contact area of the indentation was measured using the top projected mode with reference to the radial line mode of the Wyko image, and a subsequent image analysis program.

(a)   (b)
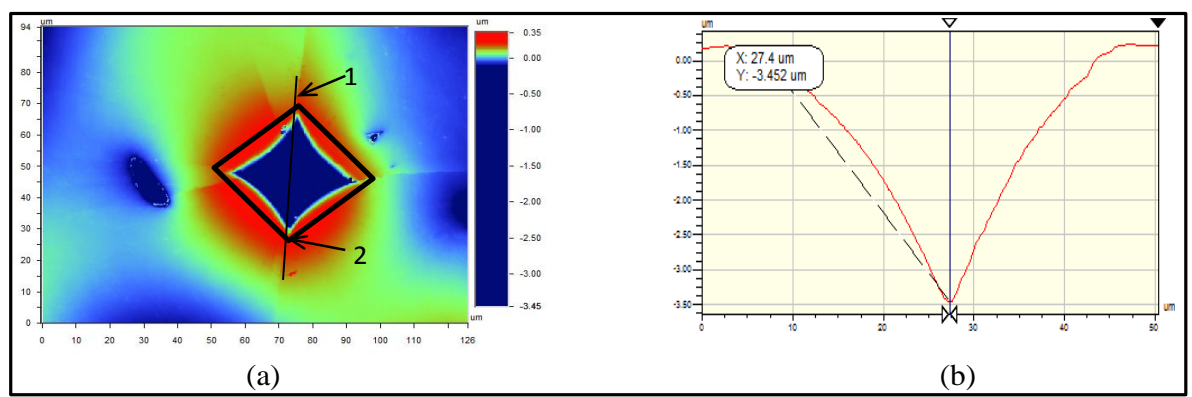
Figure 7-6 2-D optical image from Wyko profile-meter supported by Vision 64 software, a) Arrows 1, and 2 locations on residual indentation image at $\pi/2$ and specific r, radial line position, and b) Arrows 1, and 2 positions, gives at the line profile across the radial line mode on the indentation image.

7.4.2 Projected area determined by load displacement analysis

A series of Vickers indentation tests were carried out at six pre-determined maximum load values in the range of 10-1000gf (approximately 0.1-10N). Three indentations tests were performed at each peak load, and for each indentation the impression diagonals were measured three times with a resolution of 0.1µm. The average of the group results are presented in this study with thermal drift neglected. Table 7.1 shows the results of microindentation tests, and demonstrates the dependence of the measured Vickers hardness on the applied load for the fused silica material. Figure 7-7 shows Vickers indentation images at different maximum peak loads. For each loading-unloading cycle, an approach speed of 5µm/min and dwell time of 3 seconds was programmed at each interval of load. Figure 7-8 shows the typical load indentation curves obtained from this experimental work.

Table 7-1 Buehler Omnimet MHT microindentation results

Distance from Edge (mm)	Diagonal 1 (µm)	Diagonal 2 (µm)	Hardness (HV)	Load (gf)	Magnification
0.13	5.05	5.21	7.048	10	50x
0.13	17.4	15.6	6.832	100	50x
0.13	23.32	23.87	6.660	200	50x
0.13	27.54	31.88	6.341	300	50x
0.20	38.57	38.15	6.301	500	50x
0.20	51.83	57.14	6.280	1000	50x

Figure 7-7 Buheler MHT Vickers indentation images at different maximum peak load
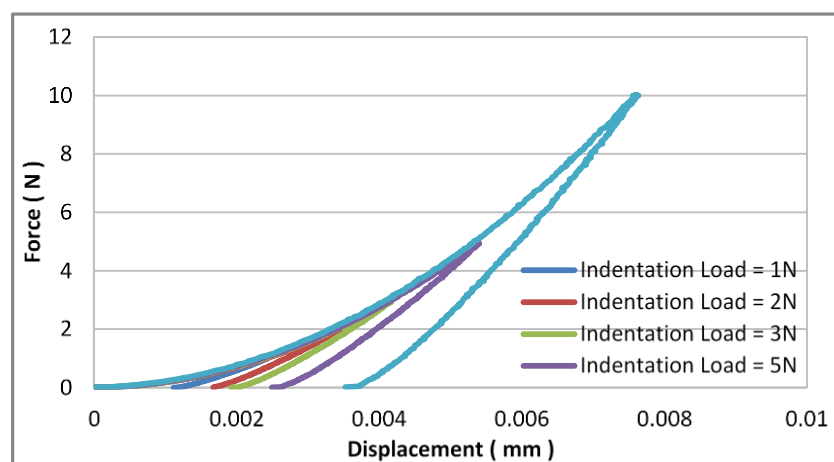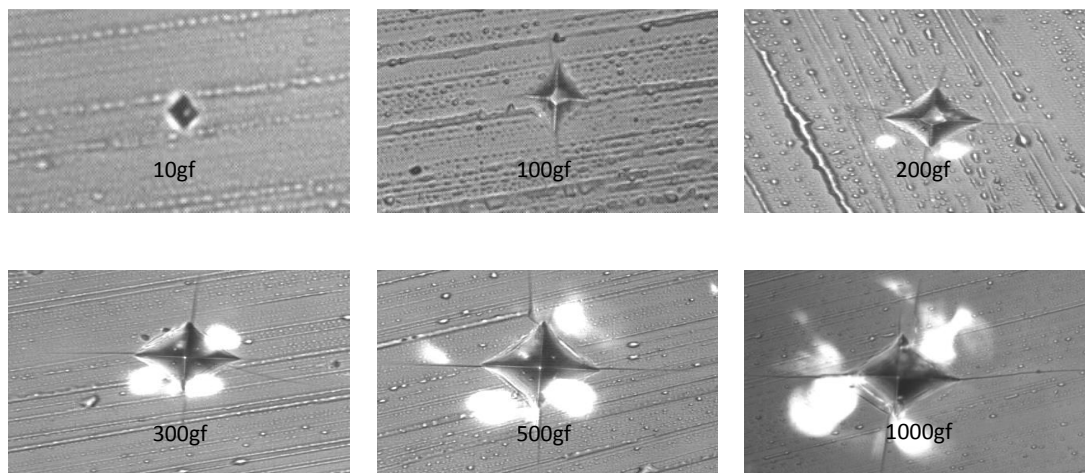
Figure 7-8 Typical microindentation loading- unloading curves for fused silica

The contact area Ac of the Vickers indentation was determined using the same methodology as that used for the Berkovich inventor as described in [Chapter 6]. However, the main disadvantage of the method is the inability to include effects of pile-up. To accommodate this constraint we have chosen fused silica as the reference material as this exhibits very little pile-up during deformation. This procedure will take into account the compliance of both the load structure and specimen. Different indentation loads were applied to the fused silica specimens and the load displacement curves were analysed using Eq. (6.10) and Eq. (6.11). Figure 7-9 shows the relation between the initial loading curve S_T and maximum applied load, P_{max}. As displayed, there exists a very good linear relationship between the inverse of the initial load curve, $1/S_T$ and the inverse of the square root of maximum load $(1/P_{max})^{0.5}$. The linear regression fitted data obtained from Eq. (6.7) gives $C_F = 0.0215$ µm/N, and $\beta = 0.7963$ µm/N
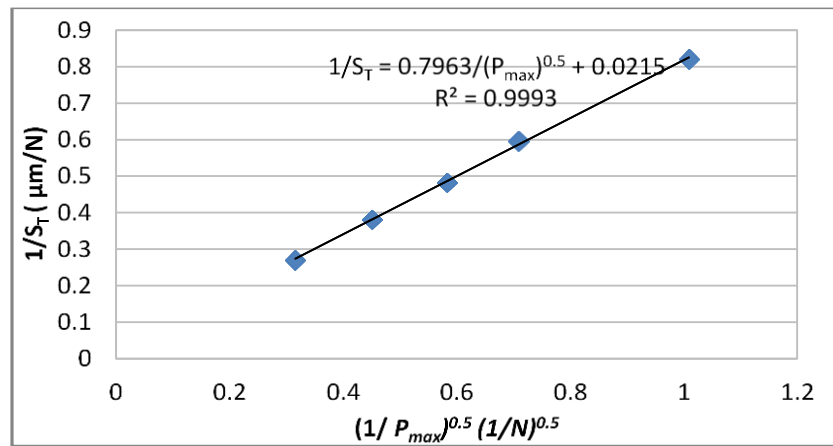
Figure 7-9 Relation between $1/S_T$ and $(1/P_{max})^{0.5}$

The Vickers indenter properties used in the experiment were Young's' modulus $E = 1147$ GPa, and Poisson's ratio $v = 0.07$ as is shown in the CSM data sheet. Based on this information the reduced modulus Er was calculated at each indentation load with known indentation elastic modulus using Eq. (6.3). The hardness values were obtained from Figure 7-9, using Eq. (6.6), then the project contact area A_p was calculated and the results plotted as a function of the contact depth, hc as is shown in Figure 7-10. The values of hc used to generate this plot were calculated using Eq. (6.13). The specimen stiffness S_S was calculated from Eq. (6.5). Using the experimentally determined S_T and the best-fit value of C_F, that is $C_F = 0.0215$. The experimental results suggested linear relationship between $\sqrt{A}$ and h_c for actual indenter regression analysis.
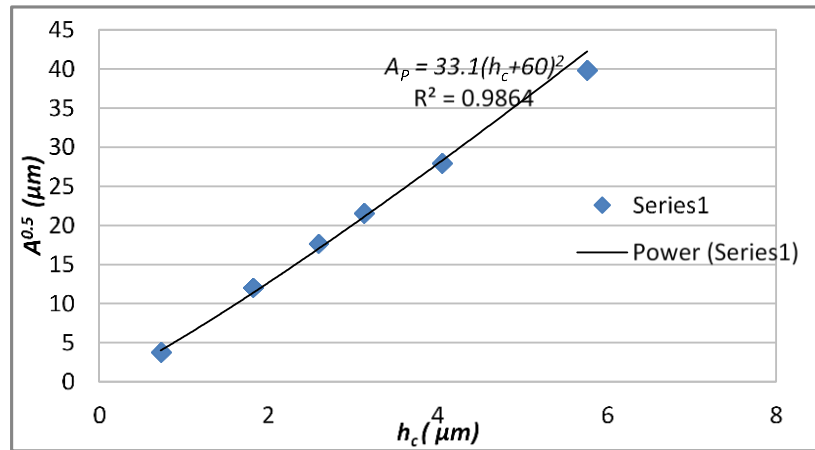
Figure 7-10 Tip area function value for a Vickers tip determined from experimental work

The regression analysis was obtained according to a non-perfect indenter approach describe by Martin and Troyon (2002), and Pharr, Oliver et al. (1992), and given by Eq. (7.6) using Sigma plot software. This analysis gives the value of C =33.1, and $h_d = 60$ nm. The experimental results shown in Figure 7-10 indicate that the deviations of the determined area function from the perfect Vickers geometry are attributed to the indenter tip blunting which affects the best-fit value of h_d and the effective half-included angle change resulting in deviation in the best-fit value of parameter C that is equal to 24.56 for the perfect indenter.

7.4.3 Measuring Vickers tip shape for instrumented microindentation using Electron Scanning Microscopy (SEM)

The expected divergence from an ideal geometry is relatively small for the Vickers indenter; such divergence is generally attributed to the manufacturing process used to fabricate these types of tips and the deformation of the indenter occurring during indentation. The highly localized contact stress field during the indentation process would make the indenter deform to a certain extent. For the perfect indenter the effective half induced angle θ = 70.32, which results in a C value of $C = 24.56$.

Figure 7-11 shows a side view magnification images (SEM) of the Vickers indenter, that is fitted to the Buehler Omnimet MHT machine at (Manufacturing Technology Centre, Coventry, UK). The Vickers indenter was examined prior to real indentation tests. As displayed the effective half-included angle, θ, is slightly different from the nominal value of 70.32 degree.

Such a discrepancy is difficult to quantify using traditional microscopy or indentation techniques. Moreover the radius of the blunting tip, *R,* and the distance between the blunted edge and the cone-end, h_d was estimated by manually fitting a circle to apex regions in the SEM images, yielding values of R = 1.25 μm and h_d = 55 nm, respectively.

Based on Eq. (6.19) Chapter 6 and the outcome from these measurements, the spherical contact becomes dominant if the contact depth is less than 600 nm, for larger contact depths, the conical angle should become dominant. The deformation of the indenter occurring during indentation causes that the effective half induced angle would increase to a certain value, thus emphasizing the non-perfect nature of the tip. The magnitude of divergence from the perfect tip geometry can provide a starting point for extracting geometric parameters from area functions. Thus, for pyramidal tip, Eq. (6.19) Chapter 6, can be used to extract the tip radius for, $h_c \leq \partial$, and Eq. (7.5) , can be used to extract an average tip angle.
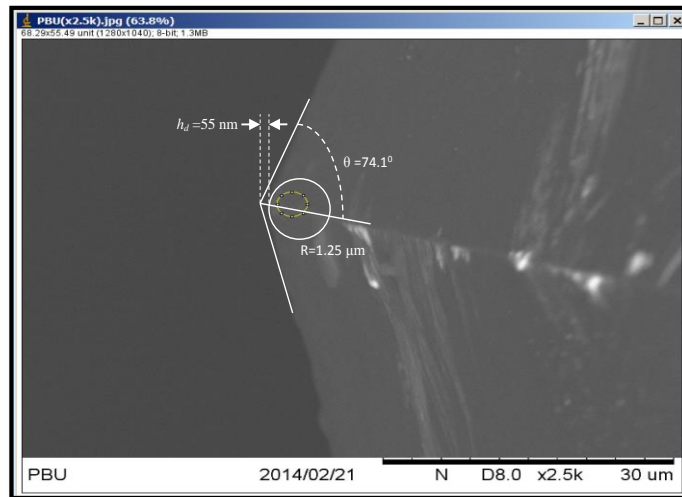
Figure 7-11 Side view magnification images of blunt Vickers indenter

7.4.4 Numerical modelling approach to determine the contact area

Numerical simulations were created using ABAQUS 6.12.1 software to determine the area function of a pyramidal Vickers indenter. An equivalent axisymmetric conical indenter approximated the pyramidal indenter represented in Figure 7-12 with a 'spherical cap' tip radius and specific inclination angle, each of the Vickers pyramid indenter and its equivalent conical indenter, having the same projected area versus the contact depth.

Lichinchi, Lenardi et al. (1998) have shown that there are no significant differences in the load–indentation curves when comparing the 3-D pyramidal indenter model with the axisymmetric conical indenter model.

The indenter is considered as a rigid cone with a spherical end exhibiting an effective half-included angle and tip radius of 1.25 μm to match the results obtained from the SEM images. The indentation displacement of the indenter h is controlled and the indentation force P recorded during the loading and unloading cycle. The specimen was modelled as isentropic elastic perfectly plastic material to match with the material constitutive law of fused silica.

All specimen sizes used in simulation were greater than 10 times the maximum indentation depth, which is acceptably large, in order to avoid any boundary effect and specimen size effect. The boundary condition and contact mechanism between the indenter and the specimen was similar to the 2-D Berkovich FEM (presented in Chapter 6 section 6.6). Specimen mesh density under the indenter tip was refined using element type CAX3: A3-node linear axisymmetric triangle supported by adaptive re-meshing rules for accuracy control and in some cases used for distortion control. The target of adaptive re-meshing is to determine a solution that satisfies mesh discretization error indicator targets ABAQUS 6.12 (Version 2013). The friction condition at the interface contact between the indenter and the workpiece is a very important factor. Therefore, a friction coefficient of 0.15 between the indenter and specimen was used in this study based on the outcomes determined in Chapter 8.
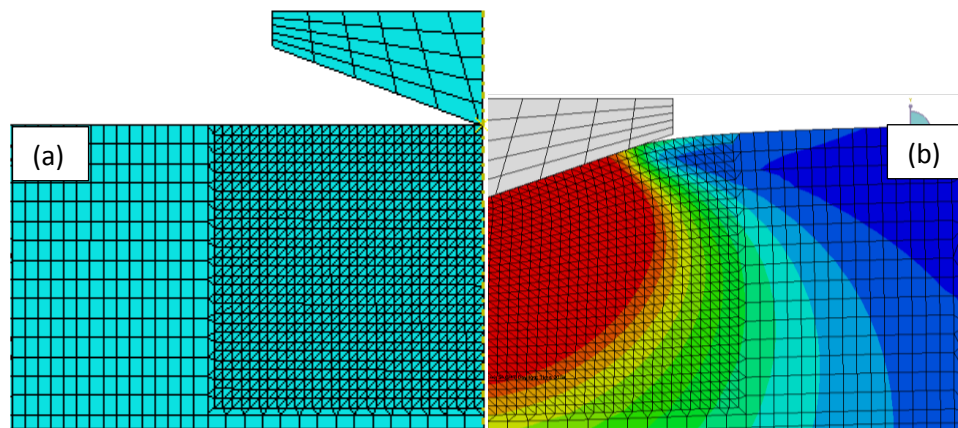
Figure 7-12 Two-dimensional axisymmetric FEM model: a) mesh shape and density for the indentation area, and b) deformable specimen under full indentation depth

7.4.4.1 Optimization method to validate the FEM results with the experimental results.

The flow chart in Figure 7-13 shows the procedure of the inverse FE modelling process based on the single indenter method. It consists of three main parts - experimental data, FE modelling using simulation space and an inverse program based on an objective function. A series of FEM simulations for a Vickers indenter were performed using a wide range of tip geometry (tip radius and inclination angle). Load displacement curves of numerical modelling were compared with experimental results at different indentation loads. The best match results were then obtained using the two stage objective function. The objective function used in this study is the root mean square error (RMSE).

This RMSE value was obtained from the difference between experimental and numerical loads for the microindentation test, defined in Eq. (6.21). The inverse FEM process was evaluated using blind tests with numerical experimental data, i.e. the numerical results were compared with known material properties, this is a commonly used approach in developing inverse programs (Delalleau, Josse et al. 2006)

In this work a parametric study was developed using simulation space to determine the tip geometry for a given set of indentation data employing a script programming language (python) interfaced with ABAQUS FEM. The proposed programme will automatically search for a range of values of tip geometries until the optimization is achieved. For the axisymmetric conical indenter under investigation, two parameters were varied within the two stages. In the first stage, tip radius was varied from 0.1 to 2.5µm using a small indentation depth of h < 1 µm with an increment of 0.01µm. The optimal tip radius from the first optimization stage is used as an input data for the second parametric study for which inclination angle was varied from 68° to 75° using an indentation depth of h > 1.25 and increment of 0.1°. The numerical results were then stored into a database to form a simulation space. The results were structured in an excel file program for interpretation.

7.4.4.2   Inverse FE modelling based on the 2-D axisymmetric Vickers indentation

In this section, the experimental load displacement for a material of known properties: Young's modulus E, 69.9 GPa, Poisson's ratio, v, of 0.22, and the yield stress, σ_y of 6.1 GPa, was used as experimental data in the blind test. The input experimental curve was divided into 40 spaced points against the indentation depth (indentation points). For each indentation depth, there is an equivalent simulation space (force and displacement) over a specific range of tip geometries.

The objective function value is then calculated at each indentation point for each set of tip properties using a predefined program in Microsoft excel. The program searched for a set of tip properties to match the experimental results. The converged results for tip radius and inclination angle with a minimum objective function (OF) of $OF < 0.01$, gave an error within 1% between the experimental and numerical load displacement curve and are plotted in Figure 7-14. As displayed, the converged results for the tip geometry of the elastic perfectly-plastic model were determined over a narrow area. This important result suggests that for a known material (fused silica) the unique tip properties can be predicted using a single indenter method based on the Vickers indentation test.

```
┌─────────────────────────────┐        ┌─────────────────────────────┐
│ Input load displacement data│        │ Input load displacement data│
└─────────────────────────────┘        └─────────────────────────────┘
              │                                        │
              ▼                                        ▼
┌─────────────────────────────┐        ┌─────────────────────────────┐
│ ABAQUS parametric study, h < 1 µm│    │ ABAQUS parametric study, h > 1.25│
│ tip radius0.1 to 2.5 µm,     │        │ inclination angle 70° to 73° │
└─────────────────────────────┘        └─────────────────────────────┘
              │                                        │
              ▼                                        ▼
┌─────────────────────────────┐        ┌─────────────────────────────┐
│ Extract load displacement data From FEM│ │ Extract load displacement data From FEM│
└─────────────────────────────┘        └─────────────────────────────┘
              │                                        │
              ▼                                        ▼
┌─────────────────────────────┐        ┌─────────────────────────────┐
│ Characterisation of the load displacement│ │ Characterisation of the load displacement│
│ curves by the indentation depth│       │ curves by the indentation depth│
└─────────────────────────────┘        └─────────────────────────────┘
              │                                        │
              ▼                                        ▼
┌─────────────────────────────┐        ┌─────────────────────────────┐
│ A series of load displacement curves│   │ A series of load displacement curves│
│ with different tip radius    │        │ with different tip inclination angle│
└─────────────────────────────┘        └─────────────────────────────┘
              │                                        │
              ▼                                        ▼
          Convergence                            Convergence
       Objective function                     Objective function
              │                                        │
              ▼                                        ▼
┌─────────────────────────────┐        ┌─────────────────────────────┐
│ Optimal parameters tip radius│       │ Optimal parameters inclination│
└─────────────────────────────┘        └─────────────────────────────┘
```

Figure 7-13 FEM programme for determining the indenter tip radius and inclination angle
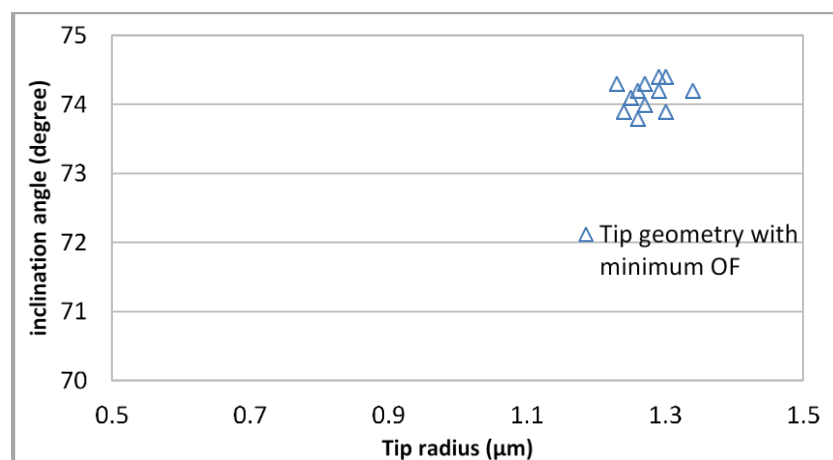
Figure 7-14 predicted tip properties with minimum objective function for elastic perfectly plastic material.

7.4.4.3 Vickers FEM supported determination of the area function

Figure 7-15 shows the comparison between the load displacement curves from theory and experiment for three different maximum loads using optimal tip radius of 1.25 µm and inclination angle of 74.1°. The two curves exhibit good correlation and only a minor deviation occurs in small loads due to the elastic-perfectly plastic material constitutive material law used in the FEM, which is not fully adequate in explaining the behaviour of fused silica material.
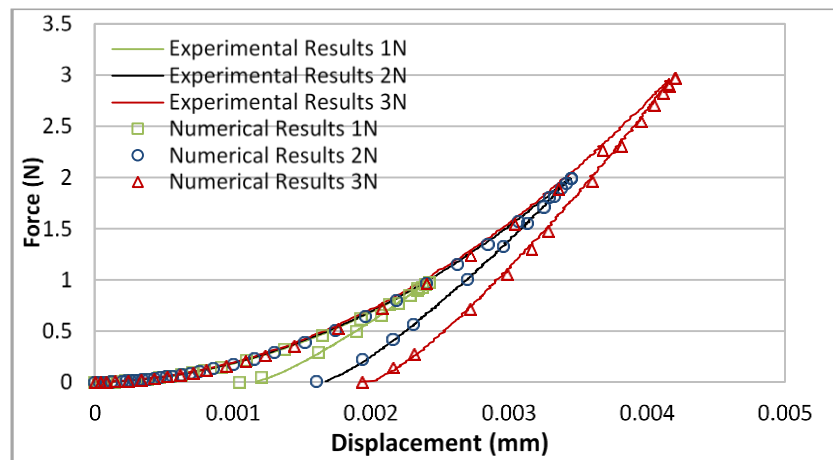
Figure 7-15 Comparison between numerical and experimental load displacement results using optimal Vickers indenter geometry

The projected area and contact depth were calculated using the same procedure as that used with the FEM Berkovich indentation Eq. (6.22) - Eq. (6.25) Chapter 6. The projected area is calculated for the best match between the loading unloading curves from theory and from experiment using the two stage optimization approach. A series of FEM simulations were carried out at various indentation loads enabling the indenter projected area A_P to be plotted against contact depth h_c (area function of Vickers indenter) for the examined fused silica reference material, Figure 7-16.
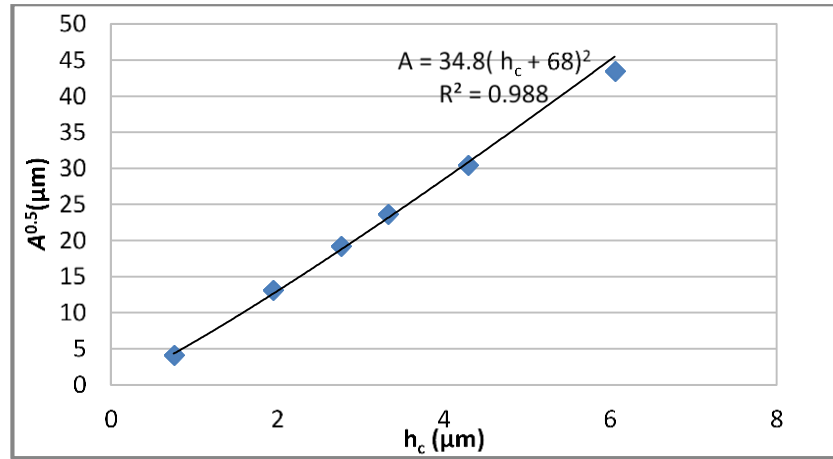
Figure 7-16 Numerical tip area function value for a Vickers tip

7.5 FEM and Experimental Results and discussion

Contact area was investigated at different indentation loads using experimental and numerical results. Three different experimental methods were employed to determine the contact area. The first method was carried out using the Martin & Oliver method to analyse the experimental load displacement curve for determination of the actual indenter geometry area function A_{MO}, as proposed in section (7.4.2). The second, newly proposed method, employed a 3-D optical Profilometer image processing technique to determine the contact area A_{PM} , as described in section(7.4.1)**.** The third method was that proposed by the Oliver & Pharr method in which the contact area for a perfect indenter geometry is obtained using, A_{OP}, Eq. (7.5). The numerical approaches were developed to determine the contact area using the actual indenter geometry derived from FEM analysis, A_{FEM} as proposed in section (7.4.4).

In this study, the analyses concentrated on the determination of the relative error, *Re*, between the true contact area *Ac* estimated through Sneddon's Eq. (7.4) and the contact area predicted by each method. Based on the Sneddon's method the relative deviation in the contact area will give roughly the same deviation in the hardness value and half of the Elastic modulus value (see Eq. (7.4))

The, *Re* is given by the expression Eq. (7.8)

$$R_e = \left(\frac{A - A_C}{A_C}\right) 100\% \tag{7.8}$$

Figure 7-17 shows a comparison of the relative error in values obtained from theory and experiment (A_{MO}, A_{PM}, A_{OP}, and A_{FEM}), at different indentation loads. The relative error Eq. (7.8) between the true projected contact area estimated from experiment data by Sneddon's Eq. (7.4) and each of the other methods is plotted. Each bar refers to one of the four methods obtained at different indentation loads. The use of such a procedure will allow for comparison between the numerical and experimental tests.
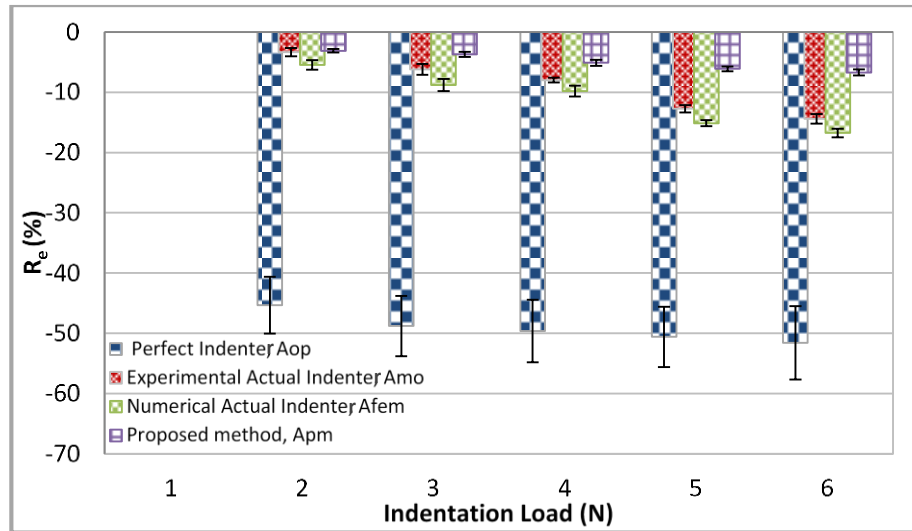
Figure 7-17 Experimental and numerical comparison the relative error at different indentation load by four methods a) Experimental actual indenter, A_{MO}, b) New proposed method, A_{PM}, and c) Numerical perfect indenter, A_{OP}, and d) Numerical actual indenter, A_{FEM}

The success rate of the method chosen was based on their capability to match the true value of Ac, within $\mp$ 10 % error, which is still realistic from a numerical and experimental point of view. As displayed, the Re values estimated from the four methods systematically underestimates the contact area.

The A_{MO}, and A_{FEM}, methods perform well only for loads less than 3N, though both methods give reasonable results for the fused silica sample. Increases in the indentation load greater than 3N leads to increase yield strain rate and results in an unexpectedly high error level. This suggests that both methods were optimized using this material as a reference for microindentation load of up to 3N. Based on observation of the results, the A_{MO}, method performs better than the A_{FEM}, method although each underestimates the contact area.

The determination of the contact area using perfect indenter geometry A_{OP}, clearly leads to a severe underestimate of the contact area due to inaccurate estimation of the contact geometry by assuming finite sharp tip radius. Poon, Rittel et al. (2008) observed that the values of the indentation load increase for a larger tip radius at the same indentation depth compared with the sharp indenter.

The overall performance of the proposed new method, using 3-D optical profilometry and image processing, for A_{PM} , is more reliable compared with the other direct methods .

The main advantages of the proposed method are firstly, that it is a non-contact measurement technique, which eliminates all effects of indenter shape and force values in comparison with other imaging techniques such as AFM, and ITSPM. Secondly, it does not necessarily require use of a highly expensive instrumented indentation machine to extract the mechanical properties from load displacement curves. Thirdly, the contact area measurement obtained from this method is not related to the load indentation, such as is the case with the Oliver & Pharr method, therefore the contact area is insensitive to the frame and specimen compliances, i.e. stiffness issues. Fourthly, this method is compatible with any tip blunting values, and does not require a tip calibration process. Finally, it is a realistic method for any indentation load and fully accounts for material sinking or pile-up behaviour.

7.6   FEM Dimensional analysis of contact area

Dimensional analyses were employed to investigate the effect of elastic and plastic parameters on the contact area. Two sets of material constitutive law were examined to cover a wide range of contact geometry and material properties. The first constitutive law, used for an isentropic elastic plastic material with power law strain hardening (EPH) driven by the tensile behaviour (stress, σ, and strain, ϵ), is given by Eq. (7.9). This is commonly used in the numerical simulation of metallic alloys, (Swaddiwudhipong, Hua et al. 2006)

$$\sigma = \begin{cases} E\varepsilon & , for : \sigma < \sigma_y \\ \sigma_y (E/\sigma_y)^n , for: \sigma > \sigma_y \end{cases} \tag{7.9}$$

The second constitutive law, is the Linear Drucker-Prager law for plasticity (LDP) of soil and granular material (Prager 1955), which is widely used to explain the influence of the hydrostatic stress component on yielding stress (Khoei 2010). Such a model can be used to describe the deformation behaviour of metallic glass and polymer materials, (Keryvin 2007). The linear plastic Drucker-Prager model is given by Eq. (7.10):

$$F = q + \beta\,\sigma_m - \sigma_{yc} = 0 \tag{7.10}$$

Where: $q = \sqrt{\frac{3}{2}S_{ij}S_{ij}}$ is the Von Mises equivalent stress, and S_{ij} is the stress deviator, $\sigma_m = \sigma_{kk}/3 = -P$, where P is the hydrostatic pressure stress, σ_{yc} is the compressive stress, and β is the friction coefficient

$$S_{ij} = \sigma_{ij} - \sigma_m \varepsilon_{ij} \tag{7.11}$$

The friction coefficient, β, is considered based on the assumption that in the case of pure shear loading $\sigma_m = 0$, β may be neglected resulting in, $q = \sigma_{yc}$. Secondly, in the case of pure hydrostatic loading the stress $q = 0$, $\beta = -\sigma_{yc}/P$. Therefore, β may be considered as the ratio between the compressive yield stress of the material and the hydrostatic pressure stress in pure hydrostatic loading.

Based on each of the above constitutive material law models, the dimensional analysis of material properties effect on the contact area is given by Eq. (17.2):

$$A_c = \begin{cases} h_m^2 \prod_{EPH}(v, \sigma_y/E\,, n) \\ h_m^2 \prod_{DPP}(v, \sigma_{yc}/E\,, \beta) \end{cases} \tag{7.12}$$

A series of FEM simulations were performed using an equivalent two-dimensional axisymmetric model developed in a previous section (7.4.4) to investigate the effect of (EPH, and LDP) constitutive models on the contact area. At each simulation, load displacement data and height indentation image were extracted and analysed. In the both models the Poisson's ratio and the Elastic modulus were fixed at values of 0.3, and 100 GPa respectively. However, it was found from the dimensional analysis of material properties that only the parameters (σ_y, n) in the case of the EPH constitutive model, and (σ_{yc}, β) in the case of the LDP constitutive model have a major influence on the contact area. Accordingly, the values of (σ_y,n), and (σ_{yc},β) are modified in the numerical simulations of EPH, and LDP respectively.

Table (2) shows the range of values for the dimensionless parameters, for both the EPH, and LDP constitutive models, used in the Numerical simulations.

Table 7-2 Numerical simulations range of dimensionless parameters for EPH, and LDP

Dimensionless Parameter	Model	Range
σ_y/E	EPH	0.01-0.1 of 0.01 interval rate
n	EPH	0.1-0.4 0f 0.1 interval rate
σ_{yc}/E	DPP	0.1-0.5 of 0.05 interval rate
β	DPP	0°-30° of 10° interval rate

Three numerical methods was developed to predict the contact area: the first method based on Oliver & Pharr determined the contact area using Eq. (7.5) for a perfect indenter geometry $A_{perfect}$. The second method based on Martin and Oliver, used the optimized value of the indenter geometry derived from FEM analysis A_{actual} section (7.4.4), for the fused silica reference material. The third method used the newly proposed approach in which the contact area was determined by analysis of the residual imprint based on indentation height image processing and indentation curves after each simulation.

7.7   FEM Dimensional analysis results and discussion

The relative error, R_e, were obtained from each of the three methods as plotted in Figures 7-18 (a1-a2), 7-19 (a1-a2) and 7-20 (a), and the absolute relative error, $|R_e|$, also plotted in Figures 7-18 (b1-b2), 7-19 (b1-b2), and 7-20 (b) for EPH, and LDP material constitutive laws respectively. The magnitude of error at particular tensile and compressive yield strain values, σ_y/E, and σ_{yc}/E were highlighted .

A parametric study was carried out on both material law equations to determine the contact area for a given set of material properties based on indentation data using a script programming language (python) interfaced with ABAQUS FEM. In this arrangement the true contact area, A_{true} is directly measured from the indentation results using Eq. (6.22) and the two methods of contact area $A_{perfect}$, and A_{actual} were estimated from load

displacement curves based on the indenter geometry. The A_{pm} was estimated from the indentation height image processing and indentation curves using Python script subroutine interfaced with ABAQUS. The output data base file from ABAQUS of the residual imprint images will then be imported into Gwyddion software as a (GSF) format in order to use this algorithm for image processing analysis.

Based on the FEM observation of the material laws (EPH, and LDP), the magnitude of, Re, given by Eq. 7.13 was found to strongly depend on the specimen mechanical properties and the indenter geometry which produced different contact behaviour, either pile-up or sinking in.

$$R_e = \left(\frac{A - A_{true}}{A_{true}}\right) 100\% \qquad (7.13)$$

In case of the EPH type material, the relative error measurements for perfect indenter geometry, $A_{perfect}$ were calculated. Figure 7-18 (a1, a2) shows an underestimation of the contact area for materials exhibiting strain hardening of $0.1 \leq n \leq 0.4$ over a wide range of tensile strain values of $0.001 \leq \sigma_y/E \leq 0.01$. This suggests an underestimation of contact area when pile-up occurs and agreement with results predicted by Cheng and Cheng (1998).

Figure 7-18 (b1, b2) shows the absolute relative error measurements $|R_e|$ for perfect indenter geometry, $A_{perfect,}$. As displayed, the $|R_e| > 10\%$ for all material properties. This suggests that the perfect indenter geometry with sharp indentation edge does not consider the piling up behaviour of the examined materials for a given yield strain values, as well as providing a lower load displacement curves compared with the actual indenter geometry.

Figure 7-18 (a1, a2) presents the relative error measurements for actual indenter geometry A_{actual} . The results demonstrated underestimation $R_e \leq 10\%$ of the contact area for all range of tensile strain values with strain hardening of, $n \leq 0.1$. It is also clearly noticed that R_e of A_c for strain hardening $n \geq 0.1$ is overestimated. The strain hardening increases with the increase in the tensile strain σ_y/E of the strain hardening range $0.1 \leq n \leq 0.3$. The overestimation of contact area at this stage is due to the sinking in behaviour. The over estimation behaviour exhibit decreasing trends with increasing σ_y/E for $n = 0.4$.

Figure 7-18 (b1, b2) shows the absolute relative error measurements $|R_e|$ for the actual indenter geometry, A_{actual}. This method performed well for all material properties with $n \leq$ 0.2, which produces a value of $|R_e| \leq 10\%$ where the materials show no or little pile-up behaviour. The results also suggest that this method is not suitable for material with high strain hardening values.

Figure 7-19 (a1,a2) shows that the $A_{perfect}$ method systematically tends to underestimate the A_c for materials with friction angle range $0^o \leq \beta \leq 30^o$, these measurements has been recorded irrespective of the magnitude of compressive yield strain, σ_{yc}/E (i:e regardless of the pile-up or sinking in material behaviour).

Figure 7-19 (b1,b2) shows the magnitude of the absolute relative error, $|R_e|$ is higher than that for the other methods. This may be attributed to the fact that the perfect indenter (sharp tip geometry) modelling will lower the resulting of force and consequently A_c. The absolute relative error of the contact area decreases with the increasing compressive yield strain for the friction angle range $0^o \leq \beta \leq 30^o$

Figure 7-19 (a1, a2) represents the relative error measurements of actual indenter geometry A_{actual} for LDP type materials, this method systematically tends to underestimate the A_c when the compressive yield strain is lower than 0.02 and friction angle range $0^o \leq \beta \leq 30^o$, and to underestimate the results within the whole range of compressive yield strain properties and $\beta = 30^o$. This suggests an inability to cope with pile-up material behaviour. Figure 7-19 (b1,b2) demonstrated that although the value of $|R_e| > 10\%$, this method performs well with materials exhibiting high compressive yield strains $(> 0.02\%)$

Figure 7-20 (a, and b) shows the numerical results of the newly proposed method to determine the contact area in the case of EPH and LDP for different combinations of (n, σ_y/E) and (β ,σ_{yc}/E) respectively. The numerical simulations demonstrate that the relative error of this method performs very well with both material constitutive laws giving a 100% success rate within a specified relative error target of less than 10%.

(a1)

(a2)

(b1)

(b2)
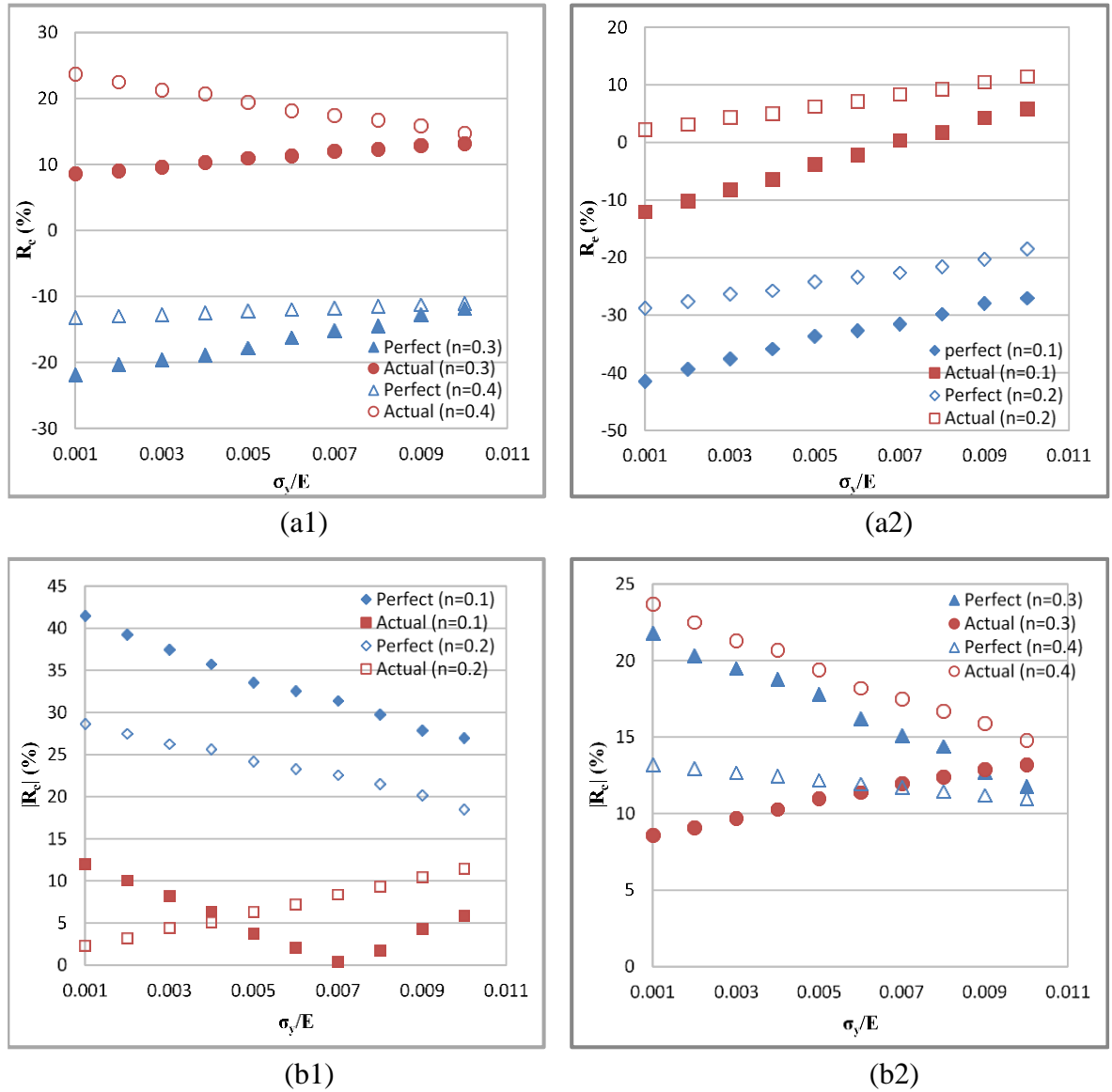
Figure 7-18 Numerical results of perfect and actual indenters geometry in the case of EPH for different combinations of the strain hardening, *n,* yield strain, σ_y/E. a -1,2) The relative error, *Re*, Between the true contact area *Ac* , and the contact area predicted by each method at different value of strain hardening. B-1,2) The absolute value of relative error , |*Re*|.
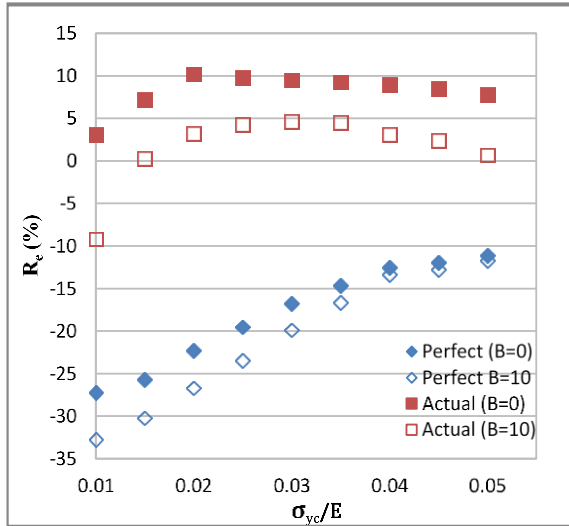
(a1)
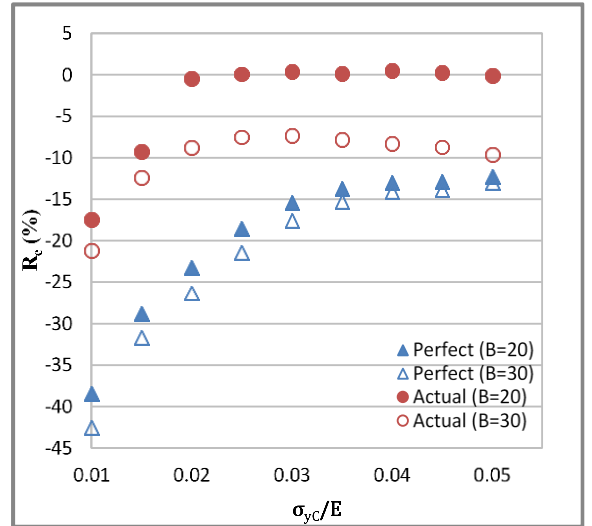
(a2)
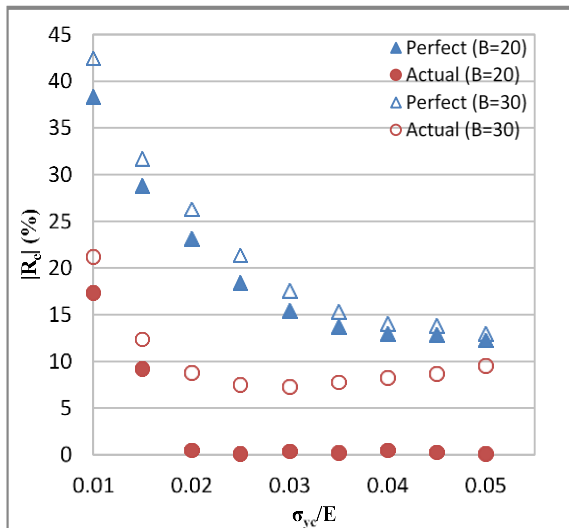
(b1)
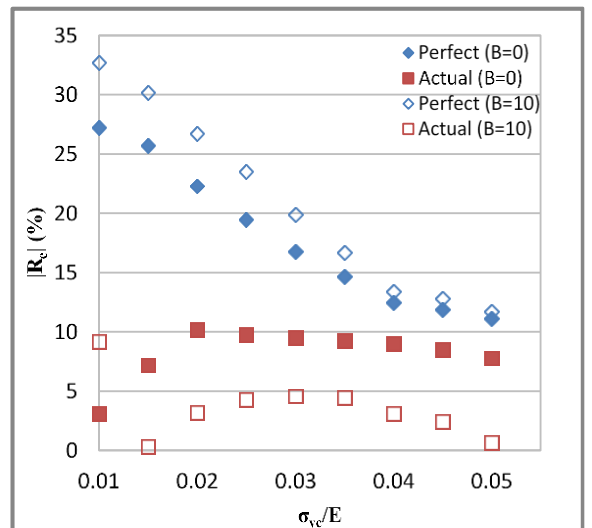
(b2)

Figure 7-19 Numerical results of perfect and actual indenters geometry in the case of LDP for different combinations of friction angle, β, and compressive yield strain, σ_{yc}/E. a - 1,2) The relative error, Re, Between the true contact area Ac, and the contact area predicted by each method at different value of strain hardening. B-1,2) The absolute value of relative error, $|R_e|$.
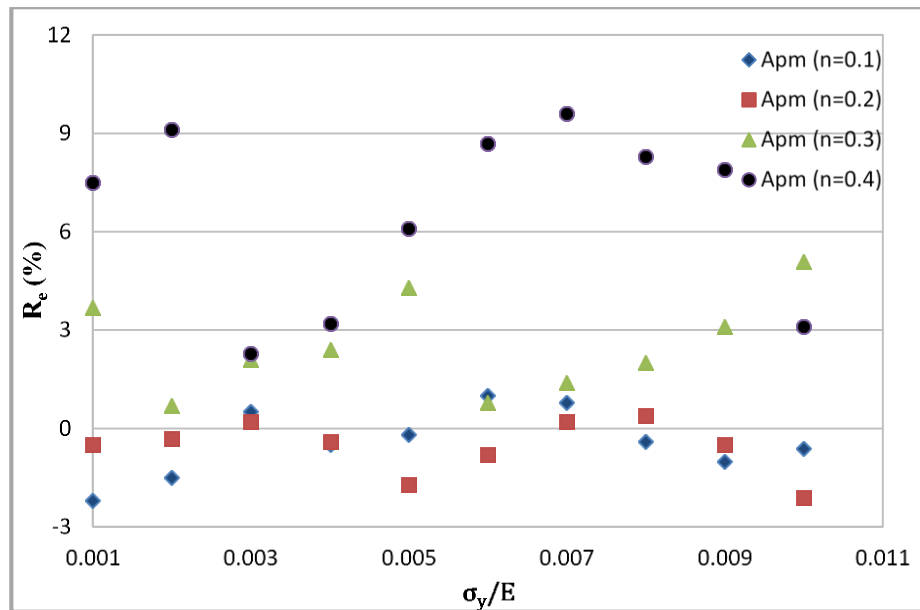
(a)
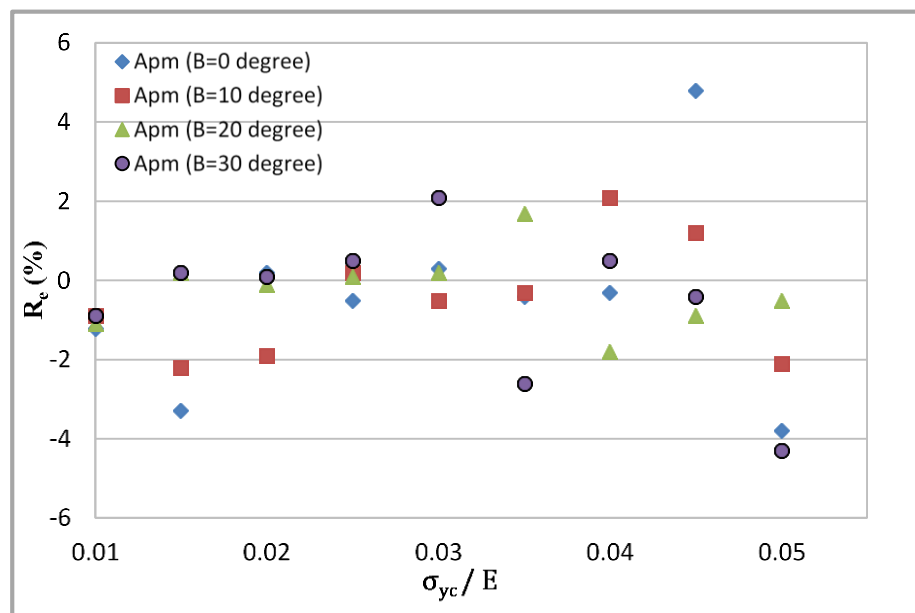
(b)

Figure 7-20   Numerical results for new proposed method, A_{PM} to determine the contact area. a) The relative error, Re, of the EPH material versus the yield strain, σ_{yc}/E at different values of strain hardening, n. b) The relative error, Re, of the LDP material versus the compressive yield strain, σ_{yc}/E at different values of friction angle, β.

7.8   Conclusion

The effect of variation in the tip geometry of the Vickers hardness stylus on the determination of contact area in instrumented microindentation tests was analysed and compared with different theories. A new method is proposed for the determination of contact area based on residual imprint measurements using 3-D optical profilometry supported by Vision 64 and Gwyddion software for image processing and analysis. For evaluation, results for contact area computed using the new method have been compared with results from three other numerical and experimental methods based on data for fused silica reference material. An assessment using dimensional analysis has permitted a wide range of contact geometry and material properties to be explored. It has been shown that the proposed method is more accurate compared with other methods regardless of the mechanical properties of the material under test. The outcomes show that measuring contact area with the new method improves the overall relative error in the obtained mechanical properties such as Hardness and Young's modulus of elasticity. We have also to emphasize the fact that the measurement of contact area using actual indenter geometry obtained from experimental load displacement analysis or FEM numerical analysis is more accurate than the contact area measurement from the assumption of perfect indenter geometry and can be used for materials with low strain hardening property.

7.9   References

Bec, S., A. Tonck, J.-M. Georges and G. W. Roper (2004). "Synergistic effects of MoDTC and ZDTP on frictional behaviour of tribofilms at the nanometer scale." <u>Tribology Letters</u> **17**(4): 797-809.

Bulychev, S., V. Alekhin, M. Shorshorov, A. Ternovskii and G. Shnyrev (1975). "Determining Young's modulus from the indentor penetration diagram." <u>Ind. Lab.</u> **41**(9): 1409-1412.

Charleux, L., V. Keryvin, M. Nivard, J.-P. Guin, J.-C. Sanglebœuf and Y. Yokoyama (2014). "A method for measuring the contact area in instrumented indentation testing by tip scanning probe microscopy imaging." <u>Acta Materialia</u> **70**: 249-258.

Cheng, Y.-T. and C.-M. Cheng (1998). "Scaling approach to conical indentation in elastic-plastic solids with work hardening." <u>Journal of Applied Physics</u> **84**(3): 1284-1291.

Cheng, Y.-T. and C.-M. Cheng (2004). "Scaling, dimensional analysis, and indentation measurements." <u>Materials Science and Engineering: R: Reports</u> **44**(4): 91-149.

Delalleau, A., G. Josse, J.-M. Lagarde, H. Zahouani and J.-M. Bergheau (2006). "Characterization of the mechanical properties of skin by inverse analysis combined with the indentation test." <u>Journal of biomechanics</u> **39**(9): 1603-1610.

Doerner, M. F. and W. D. Nix (1986). "A method for interpreting the data from depth-sensing indentation instruments." <u>Journal of Materials Research</u> **1**(04): 601-609.

Fischer-Cripps, A. C. (2011). <u>Nanoindentation</u>, Springer Science & Business Media.

Gerberich, W., J. Nelson, E. Lilleodden, P. Anderson and J. Wyrobek (1996). "Indentation induced dislocation nucleation: the initial yield point." <u>Acta Materialia</u> **44**(9): 3585-3598.

Keryvin, V. (2007). "Indentation of bulk metallic glasses: Relationships between shear bands observed around the prints and hardness." <u>Acta materialia</u> **55**(8): 2565-2578.

Keryvin, V., S. Gicquel, L. Charleux, J. P. Guin, M. Nivard and J. C. Sangleboeuf (2014). "Densification as the only mechanism at stake during indentation of silica glass?" <u>Key Engineering Materials</u> **606**: 53-60.

Khoei, A. (2010). <u>Computational plasticity in powder forming processes</u>, Elsevier.

Lichinchi, M., C. Lenardi, J. Haupt and R. Vitali (1998). "Simulation of Berkovich nanoindentation experiments on thin films using finite element method." <u>Thin solid films</u> **312**(1): 240-248.

LILLEODDEN E. T. , B. W., NELSON J. , WYROBEK J. T. (1995). "IN SITU IMAGING OF MU N LOAD INDENTS INTO GAAS." <u>Journal of materials research</u> **10**(9): 2162 - 2165.

Lim, Y., M. Chaudhri and Y. Enomoto (1999). "Accurate determination of the mechanical properties of thin aluminum films deposited on sapphire flats using nanoindentations." <u>Journal of materials research</u> **14**(06): 2314-2327.

Lim, Y. Y. and M. M. Chaudhri (1999). "The effect of the indenter load on the nanohardness of ductile metals: an experimental study on polycrystalline work-hardened and annealed oxygen-free copper." <u>Philosophical Magazine A</u> **79**(12): 2979-3000.

Martin, M. and M. Troyon (2002). "Fundamental relations used in nanoindentation: Critical examination based on experimental measurements." Journal of materials research **17**(09): 2227-2234.

Oliver, W. C. and G. M. Pharr (1992). "An improved technique for determining hardness and elastic modulus using load and displacement sensing indentation experiments." Journal of materials research **7**(06): 1564-1583.

Oliver, W. C. and G. M. Pharr (2004). "Measurement of hardness and elastic modulus by instrumented indentation: Advances in understanding and refinements to methodology." Journal of materials research **19**(01): 3-20.

Pharr, G., W. Oliver and F. Brotzen (1992). "On the generality of the relationship among contact stiffness, contact area, and elastic modulus during indentation." Journal of materials research **7**(03): 613-617.

Poon, B., D. Rittel and G. Ravichandran (2008). "An analysis of nanoindentation in elasto-plastic solids." International Journal of Solids and Structures **45**(25): 6399-6415.

Poon, B., D. Rittel and G. Ravichandran (2008). "An analysis of nanoindentation in linearly elastic solids." International Journal of Solids and Structures **45**(24): 6018-6033.

Prager, W. (1955). "The theory of plasticity: a survey of recent achievements." Proceedings of the Institution of Mechanical Engineers **169**(1): 41-57.

SNEDDON, I. (1948). "BOUSSLNESQ'S PROBLEM FOR A RIGID CONE."

Swaddiwudhipong, S., J. Hua, K. Tho and Z. Liu (2006). "Equivalency of Berkovich and conical load-indentation curves." Modelling and Simulation in Materials Science and Engineering **14**(1): 71.

Troyon, M. and M. Martin (2003). "A critical examination of the P-h2 relationship in nanoindentation." Applied physics letters **83**: 863.

Version, A. (2013). "6.12 Documentation Collection." ABAQUS/CAE User's Manual.

CHAPTER EIGHT

DEVELOPMENT AND PARAMETRIC STUDY OF 2-D AND 3-D FEM SIMULATION FOR INDENTATION ANALYSIS

8.1 Introduction

Due to the complex contact mechanics during the indentation process, there is interest and value in using numerical modelling of the indentation test with a finite element method FEM. The application of FEM to indentation processes with different indenter geometries such as Vickers, Berkovich and Spherical indenters has previously been studied and used to predict the elastic plastic material properties of various material systems. Thus, the importance of understanding the behaviour of various indenter geometries during the indentation process is a crucial requirement in material characterization. Research studies concerning the comparison between Berkovich, Vickers and Spherical indentation processes are unusual, and only a few experimental and numerical investigations regarding the correspondence in results obtained from various material systems, have been performed by (Rother, Steiner et al. 1998, Min, Wei-Min et al. 2004). (Bucaille, Felder et al. 2002) developed a reverse FEM analysis to predict the stress strain curves of polymers. The results demonstrated that the strain hardening at high strain rate of polymers has been the most affected parameter during a sharp indentation process. The results also show that the friction coefficient has a bigger influence in the case of a rounded tip compared to Berkovich or Vickers indentations and should be considered. Several research studies have been recognized and are still in progress to compare the experimental and numerical results for those of high complex material systems because the contact geometry between the indenter and specimen does not need to be known (Cheng and Cheng 1999, Suresh 1999, Venkatesh, Van Vliet et al. 2000, Futakawa, Wakui et al. 2001). One of the most important FEM numerical studies to identify the elastic plastic material properties of ductile materials using different instrumented indentation processes and to measure the sensitivity of such extracted properties to variations in the measured indentation data has been published by (Dao, Chollacoop et al. 2001).

In this chapter, 2-D and 3-D axisymmetric FEM of four commonly used indenters in nano and microindentation processes (Berkovich, Vickers, spherical, and conical) were developed. For each indenter type, the influences of a variation in sample size, tip geometry, frictional condition, mesh density sensitivity and material properties on the force displacement curves during the loading and unloading stages were investigated using a parametric study. The convergence resulting in optimum modelling parameters was established.

The effect on projected area of different indenters on the predicted material properties was investigated, and the results compared to examine the effect of using different indenter geometries.

8.2   Finite element modelling

8.2.1   ABAQUS software package

ABAQUS is FEM software developed by Hibbitt, Karlsson& Sorensen, Inc in 1992. It is a powerful engineering simulation program, which solves problems by adapting a simple linear analysis to the most difficult nonlinear simulations. There are two main analysis modules built in to the software package. The first module is the ABAQUS standard which can be used to solve the linear and non-linear problems with high accuracy and repeatability. The second module is ABAQUS explicit that is used specially for the analysis of dynamic FEM simulations such as those problems having a transient dynamic and quasi-static nature. The ABAQUS processing solution consists of three separate stages: processing, simulations and post processing. Since the indentation procedure is assumed quasi-static with no rate effect, the ABAQUS standard was used in this work. ABAQUS (CAE) is the graphical user interface of tools that includes a capability of generating CAD modelling; submit the jobs for analysis, monitoring and then review results using a Visualization module. ABAQUS standard was used for the modelling of the indentation processes which includes different stages starting from creation of the parts geometry, setting of material properties, assembly, defining the Step, defining the Interaction, boundary conditions and Load, Mesh, generating the Job, and Post-processor to extract results.

8.2.2   Types of indentation load

There are two methods that can be used to simulate the indentation process: displacement control indentation and load control indentation. When the displacement is controlled, the vertical displacement of the indenter is specified as an input value corresponding to total indentation depth.

The reaction force measured along the direction of indentation depth, which is equal to the summation of forces at a reference point on the rigid indenter. When the load is controlled, a concentrated force applied on a reference point on the analytical rigid indenter. The penetration depth is measured along the direction of indenter movement, which is equal to the total displacement of the node specified at a reference point at the indenter tip.

The indentation simulations of both methods were performed to observe the differences in the indentation load displacement curves. Elastic perfectly plastic material was selected for this test including material properties of, E = 72GPa, $\sigma_y = 6.2$, and $v = 0.25$. The 2-D axisymmetric indentation simulation with an assumption of a perfectly sharp conical indenter was employed. The indenter modelled using a R3D4 element type and considered as a rigid body with a Young's Modulus greater than 1000GPa, and Poisson's ratio of 0.07.The specimen modelled with element type of linear axi-symmetric triangle (CAX4R). The specimen size was ten times greater than the maximum indentation depth, which is satisfactorily large, in order to avoid any specimen size effect and boundary effect (Johnson and Johnson 1987). Both models were created with the same mesh density of 7692 elements, and same contact friction coefficient of 0.15. Figure 8-1 shows the comparison between displacement control indentation and load control indentation methods. As displayed, there is good agreement between the both methods, which indicates that the results are similar no matter which method of applying the load is used.
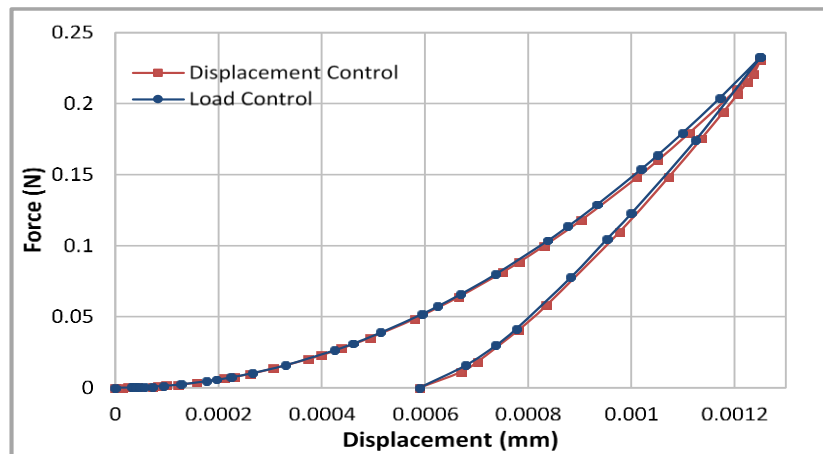
Figure 8-1 Comparison between displacement and load control for 2-D conical indentation

8.2.3   Sample size converged

The relation between the maximum indentation depth and sample size values has a significant effect on the accuracy of measured load displacement data particularly when the specimen size is less than ten times the maximum indentation depth (Johnson and Johnson 1987). Therefore, in the case of load indentation control of two specimens with different length, the resulting displacement is not unique. This is also correct for the measured load in a displacement indentation control. However, numerical simulations were carried out to investigate the effect of sample size on the indentation results using ABAQUS software. The indentation procedure was developed with the same modelling procedure used in [Chapter 6] using a 2-D model with linear axisymmetric triangular elements (CAX3) as is shown in Figure 8-2. Five different ratios of specimen depth (depth ratio) to indentation depth $hw{:}hm = 10,25,50,80,100,150$ were examined against the optimal specimen dimension ratio $rw{:}hw = 0.5, 1.0, 1.5,$ at each test the number of nodes were changed based on the dimensions of specimen geometry. A fine mesh was created below the indenter of each simulation with convergence achieved to eliminate the effect of mesh density, so not to yield significantly different results. The indenter was modelled as a conical perfect indenter using a R3D4 element type and considered as a rigid body. A displacement control indentation method was employed in all simulations with the maximum indentation depth set to 1.25 μm, which is much larger than the indenter tip radius, in order to reduce the contact area effect attributed to shape transition of the tip geometry.
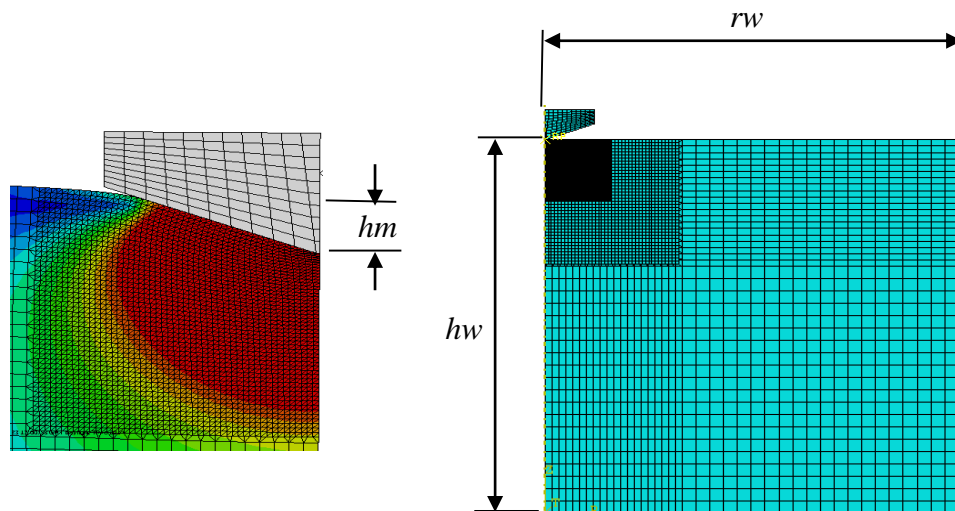
Figure 8-2 2-D linear axisymmetric model

The numerical simulations were performed using elastic perfectly plastic material properties (E = 72GPa, σ_y = 6.2GPa, and v = 0.25). Two parts of the simulation process were considered in order to achieve optimal workpiece size. The first simulation installed, changing workpiece height, *hw* for a given maximum indentation depth, *hm,* and keeping workpiece radius, *rw*, constant. Figure 8-3 shows numerical simulation of load displacement curves (loading unloading) for the same *rw*, of 25μm but different *hw, hw:hm* = 10,25,50,80,100,150. As displayed in the figure the indentation force is affected by the *hw* for a given, *rw*, higher load monitored in a small material thickness for a given displacement, and the same for a given load small displacement. The differences in the loading stage are much higher than in the unloading stage, such an observation will have an effect on the value of the reduced modulus obtained from the conventional Oliver Pharr method.
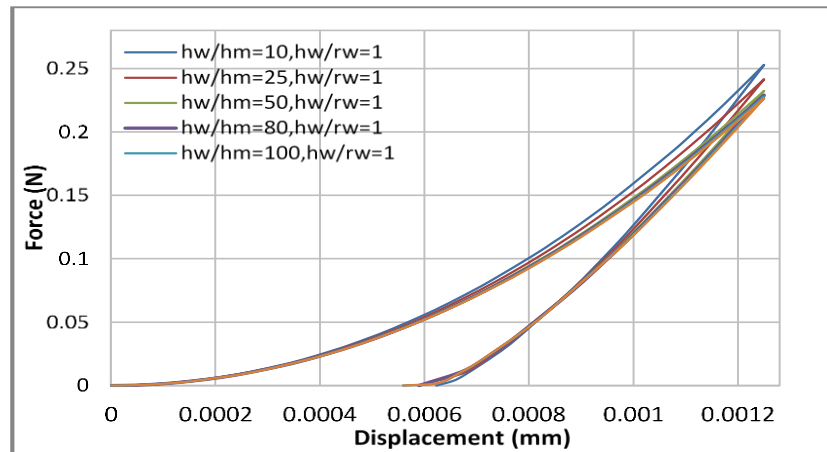
Figure 8-3 Comparison numerical simulation of load displacement curves for a given workpiece width, *rw* and different height, *hw:hm*

The next simulation installed, changing *rw,* and keeping, *hw* for a given, *hm*, is constant. Figure 8-4 shows numerical simulations of load displacement curves (loading unloading) for the same, *hw, hw=100 hm* but different *rw*, of *rw:hw* = 0.5, 1.0, 1.5. As shown *rw* change has a limited effect on the indentation force compared with *hw* change, higher load is monitored in a small workpiece radius for a given displacement. From the exploded figure it is determined that convergence is attained at the condition: specimen dimension ratio *rw:hw* ≥ unity.

Figure 8-5 shows the convergence results for a different *hw:hm*. As demonstrated, the depth ratio *hw:hm* was examined against the optimal specimen dimension ratio *rw:hw*. It is evident that at the greater indentation depths ratio the results begin to converge.

Fischer-Cripps (2000) suggested that the convergence can be achieved when *hw:hm* is larger than 10, this study implies that in practical applications (actual measurements) it is preferable to design the test with a small indentation depth and large specimen depth, i.e. *hw:hm>* 100, to achieve the highest accuracy in the shortest computational time. This finding is consistent with results obtained by Poon (2009).
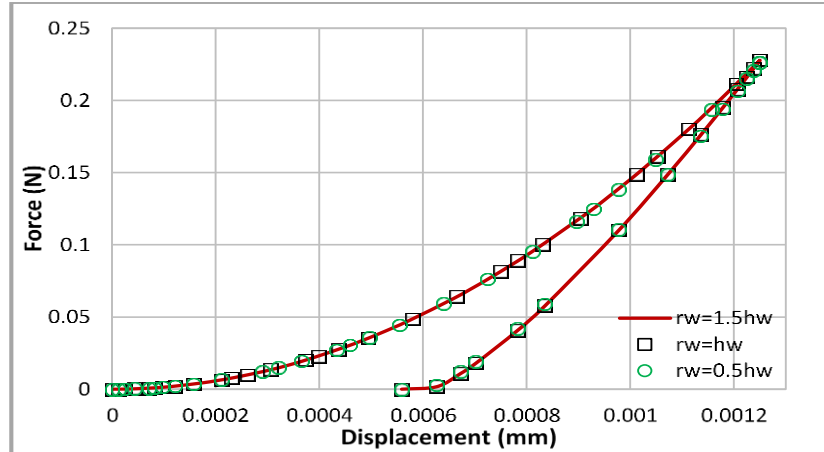
Figure 8-4 loading unloading curves for a constant specimens height *hw=100hm* and different specimen dimension ratio *rw:hw*
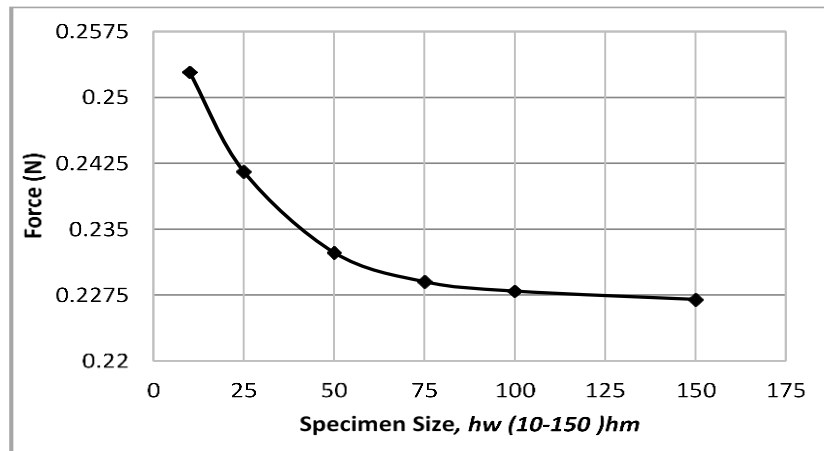
Figure 8-5 Convergence results for a different *hw:hm*

Figure 8-6 shows the convergence relationship between Force and displacement for a specimen ratio in the range 0.5< *rw:hw* <1.5, depth ratio in the range 10< *hw:hm* <150 for the case of varying indentation depth *hm*, at 100nm intervals between 750nm and maximum indentation depth of *hm* = 1250nm. From the exploded view of the previous results it is determined that convergence is attained at the condition: specimen dimension ratio *rw:hw* = unity; and depth ratio *hw/hm* = 100.
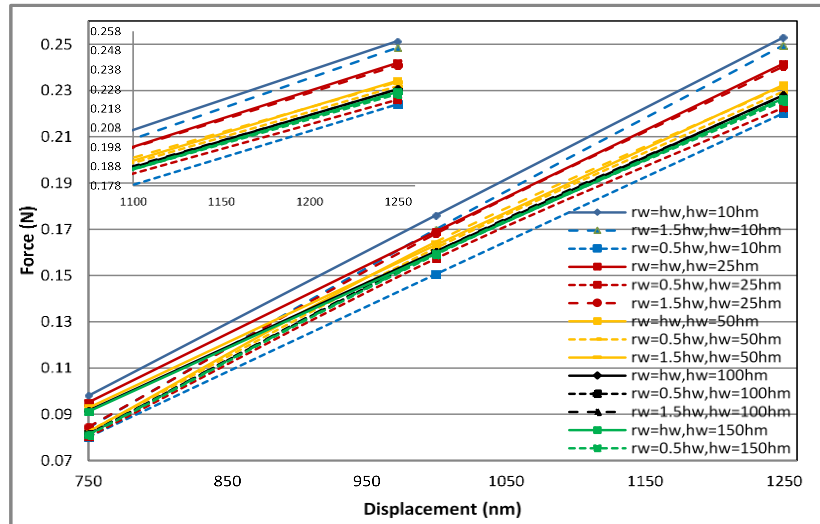
Figure 8-6 Convergence results for different specimen ratio rw:hw, and depth ratio hw:hm

8.3 Three- dimensional FEM indenter geometry

Three-dimensional numerical simulations of three different axisymmetric (Berkovich, Vickers, and Spherical) indenters were employed to investigate the influence of indenter geometry on indentation test results of various material systems. Figure 8-7 shows the Berkovich indenter as a three similar side pyramid with a semi-angle between the vertical and each face of 65.27°, only 1:6 of the specimen and indenter are modelled as a result of a plane symmetric geometry concentrated in the y and x direction. Figure 8-8 shows the Vickers indenter of square based pyramidal-shape geometry with a semi-angle between the vertical plane and each face of 68°, a quarter of the specimen and indenter are modelled, as a consequence symmetric surfaces are concentrated on both y and x sides along symmetry planes. An area of difficulty in modelling the 3-D pyramidal shape was in the process of rounding the tip. A pyramidal geometry cannot be tangentially rounded by a sphere along all sides and edges. However, the rounding tip was neglected based on the assumption of all applied loads being performed with contact depth greater than tip radius.

Consequently, only the inclination angles were taken into account in this study. The specimens and both indenters are modelled with 8-node element type reduced integration (C3D8R element), and 4-node element type rigid quadrilateral (R3D4 element) respectively, both element types are used for stress and displacement analysis. The indenters geometrical imperfections used in the present study were designed to make the numerical indenter geometry as similar as possible to the experimental case.

Therefore, the Berkovich and Vickers tip geometries were created based on the results obtained in [Chapter 6] and [Chapter 7] regarding inclination angle size. Figure 8-9 shows the spherical indenter, a quarter of the specimen and indenter are modelled; as a result symmetric surfaces are concentrated on both x and y directions along symmetry planes. The specimens and indenters are modelled with 8-node linear brick, reduced integration (C3D8R element). Similar with the previous indenters this type of element is used for the stress analysis approach.

The contact and simulation mechanism are the same in all types of indenters' geometries, which can be described by: The specimen size used in the simulations were greater or equal to 100 times the maximum indentation depth, which is satisfactorily large, in order to avoid any specimen size effect and boundary effect as proposed in the previous section. The lower surfaces of the specimens are fixed for all degrees of freedom, free surface modelled at the top and outside surface of specimen.

The contact constraint between the indenter and material was defined as the 'master surface (indenter)' and 'slave surface (material)' interaction with a normal contact, to allow the master surface to move and contact the material at all times during the simulation. The contact direction is then obtained in relation to the master surface.

The mesh density under the indenter tip was refined in order to achieve the deformation and stress gradients during indentation to a high accuracy as it shown in Figure 8-10. The indentation method was simulated in two alternating steps, during the loading step the indenter was moved along the z-direction in ramp mode and penetrated the specimen until the maximum depth of 1.25 μm was achieved. The reaction force was recorded at a reference point representing the overall load on the specimen. During the unloading step, the indenter was returned to the initial position and same reference point. The loading curve represents the resistance of material while the difference between loading and unloading represents the energy loss (Swaddiwudhipong, Tho et al. 2005). The indentation finite element modelling was performed based on the assumption of there being no exponent to the value of strain hardening of the material. Commonly, amorphous materials do not present a predictable strain hardening behaviour (Knapp, Follstaedt et al. 1999, Youn and Kang 2005). Figure 8-11 shows typical numerical load displacement curves of different indentation techniques (Berkovich, Vickers and Spherical). The design material is defined as isotropic elastic perfectly plastic with E= 72GPa, σ_y = 6.2Gpa, and v = 0.25 based on Gadelrab, Bonilla et al. (2012).

The loading stage of the load displacement curve is primarily influenced by σ_y, and n, while the unloading part correlates with E (Taljat, Zacharia et al. 1998). This work focused on the studies of elastic plastic parameters, therefore both loading and unloading stages are parts of interest.

From the load displacement curves, the slope of the first segment of the unloading curve can be obtained which leads to the determination of the elastic modulus and hardness by using the Oliver and Pharr method. The results in Figure 8-11 demonstrate that the loading unloading curves of Berkovich and Vickers indenters deviate slightly from each other when different face angles are employed. The results also show significant difference in the loading unloading curve of the Spherical indenter compared with others, the peak reaction force in the spherical indentation FEM is consistently higher than Berkovich and Vickers FEM. This may be attributed to the projected contact area and other factors such as stress distribution in the contact points. The accuracy of the FEM results is influenced by many factors such as mesh density, contact frictional coefficient and boundary condition. Bhattacharya and Nix (1988) proposed that the most relevant factors to have an effect on the simulation of indentation process are mesh density and friction coefficient.
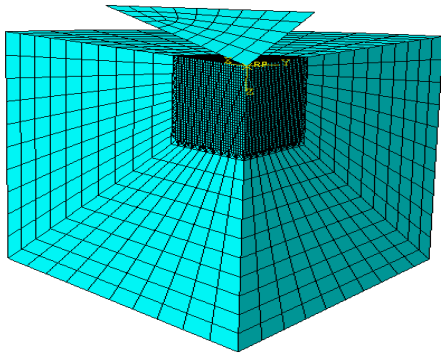
Figure 8-7 FEM of Berkovich indentation
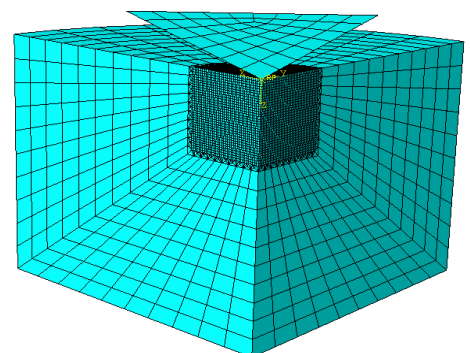
Figure 8-8 FEM of Vickers indentation
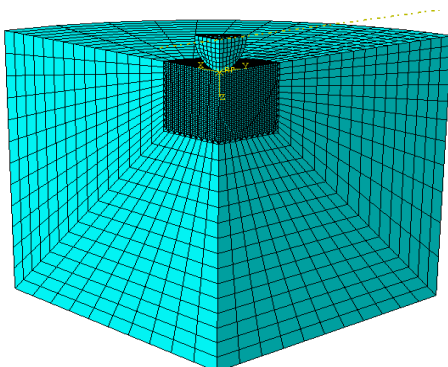
Figure 8-9 FEM of Spherical indentation indenter
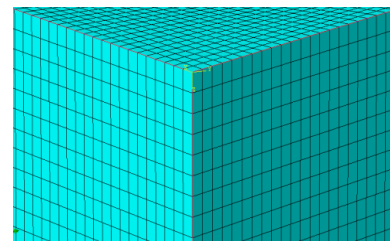
Figure 8-10 Mesh density underneath
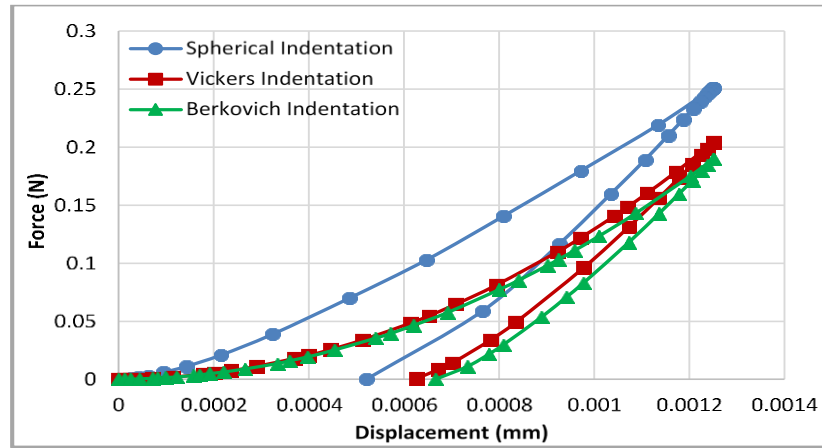
Figure 8-11 Numerical load displacement curves of elastic perfectly plastic material ($E=$ 72GPa, σ_y = 6.2Gpa, and v = 0.25) at various indentation techniques a) Spherical, b) Berkovich, and c) Vickers

8.3.1 Mesh density sensitivity effect and results

The analysis of the Mesh density of the proposed tip geometries has been systematically performed by comparing load displacement curves and maximum load results from models with different mesh sizes, after converging the results, the optimal density distribution is achieved. In order to restrict the effect of results change on the mesh sensitivity study, all simulations were generated with the same indentation depth of 1.25µm, boundary conditions and friction coefficient of 0.15 and dimension of the workpiece of (100×100) µm. Figure 8-12 shows results from a series of FEM analyses performed for each type of indentation test, each indenter simulation consisting of a seven different of elements (mesh density). The maximum indentation force from each analysis was determined as a function of mesh density. For the Berkovich indentation test, the load displacement results highlight that the indentation load increases with the increase in mesh density and convergence can be achieved after the model mesh density size increases above 7000 elements, and it is therefore assumed that analyses with 7,000 or more elements yield a converged solution. However, all simulations performed well using models containing approximately 7500 elements where the element size < 60 nm. For the Vickers indentation test, it is clearly shown that models with fine mesh (small element size) have resulted in higher indentation forces and, therefore the results became more sensitive to the mesh density. As displayed, the maximum indentation force almost converges after the model mesh density size is increased above 7,700 elements which was considered as the optimal mesh density.

The spherical indentation results suggested that, at lower mesh density level, the load displacement curves are significantly different compared with the indentation curves from coarser mesh size, thus the results become highly sensitive to the mesh density. As displayed, the numerical model consists of more than 8,300 elements, the indentation force increased and it is almost constant, and load displacement curves converged and become identical.

The result of optimal mesh density for each tip geometry indentation test, show both computational time and variation in predicted Force is minimised. It is also the value at which indentation depth correlates most accurately with the convergence value associated with higher element numbers.
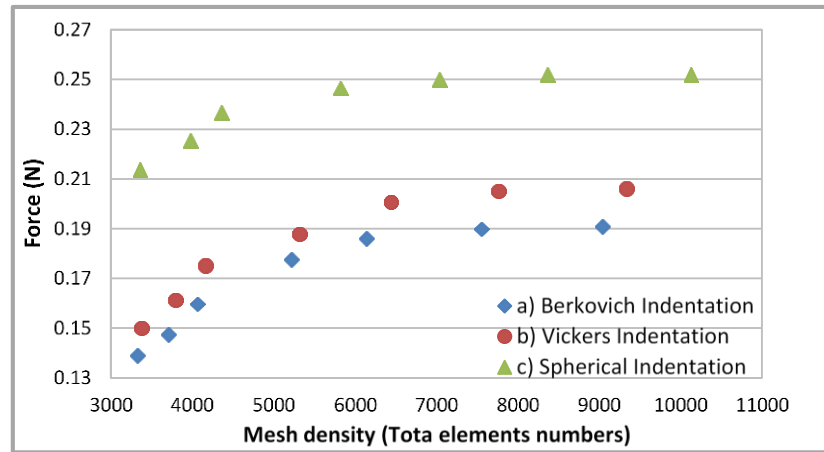
Figure 8-12 Mesh density effect on the maximum indentation force for a) Berkovich indentation, b) Vickers indentation, and c) Spherical indentation

8.3.2   Frictional coefficient effect and results

The relation between the normal force, inclination angle and friction coefficient can be defined by the analytical model proposed by Tabor (1948). The friction coefficient between the tip contact geometry and the material is modelled with a Coulomb's friction coefficient, μ. Therefore, the analytical model is given by Eq. (8.1).

$$F_n = \pi P r_c^2 \left(1 + \frac{\mu}{tan\theta}\right) \qquad (8.1)$$

Where, P is the contact pressure. However; for frictionless contact; the contact pressure is a function of projected contact area, πr_c^2 and independent of inclination angle θ .

Tabor (1948) neglected the effect of friction coefficient on the normal force in case of perfect (Berkovich and Vickers) tip geometries with high included angle of 70.3º due to the high values of θ resulting in small ratio of $\mu/\tan\theta$. Bucaille, Stauss et al. (2003) proposed that the normal force varies from 2% to 3% as friction increases from 0 to 0.3 for the 60° and the 70.3° indenters. Mata and Alcala (2004) proposed that the friction coefficient has a large influence on material exhibiting a piling up behaviour. Therefore, the actual friction coefficient has to be taken into account in the determination of mechanical properties of such materials. Figure 8-13 shows the indentation surface profile along the distance from the specimen centre, the observation suggested that for materials with low values of Yield stress and strain hardening ($\sigma_{y=}$ 500MPa, *n*=0.1), which exhibit a piling up phenomenon, the impression surface profile simulation without friction showed a significantly greater pileup height than the simulation with friction. The residual depth h_r of the simulation with friction was slightly smaller than frictionless simulation.

When the friction coefficient increases gradually from 0 to 0.3, the plastic zone size increases. In the other case for materials exhibiting a sinking in behaviour, Figure 8-14 shows that the friction coefficient increase does not provide significant changes to the plastic zone size for material with large Yield stress and strain hardening such as ($\sigma_{y=}$ 6000MPa, *n*=0.3).

In order to evaluate friction more accurately, the effect of friction coefficients variation from 0 to 0.3 on the load displacement curves were investigated for different types of contact geometries (Berkovich, Vickers, and Spherical) at the same maximum indentation depth of 1.25 micron. Figure 8-15 shows the indentation loading unloading results of the Berkovich indentation test for various coefficients of friction. As displayed, there is a small difference between the frictional and frictionless models, the increases in the friction increase the load slightly, and there is no significant difference in the indentation loading unloading curves over the range of parameters under investigation. The results also show a slight difference in the residual depth after unloading stage of frictional and frictionless conditions, due to the sliding characteristics of the frictionless surface resulting in less vertical displacement during the unloading stage.

The study state will be achieved when the coefficient of friction is equal to 0.1. This agrees with the published results suggested by a number of studies (Alcala, Barone et al. 2000, Bucaille, Stauss et al. 2003, Mata and Alcala 2004), based on the fact that the material used in numerical indentation tests (Fused Silica) does not show a high piling up behaviour.
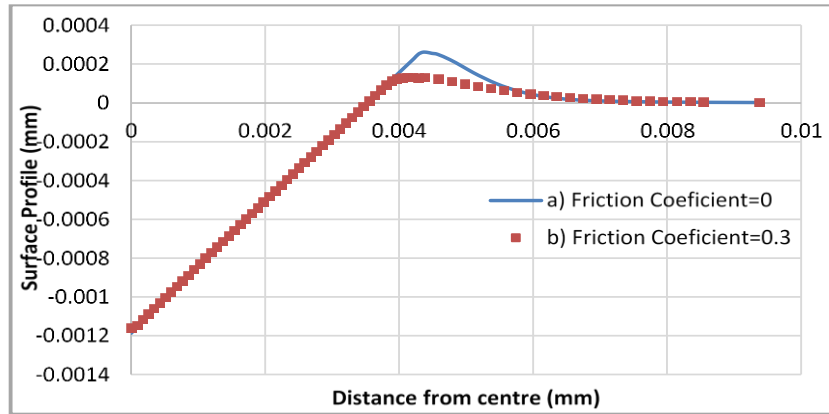
Figure 8-13 Indentation surface profile along the distance from the specimen centre for piling up material system at: a) Frictionless, and b) friction contacts
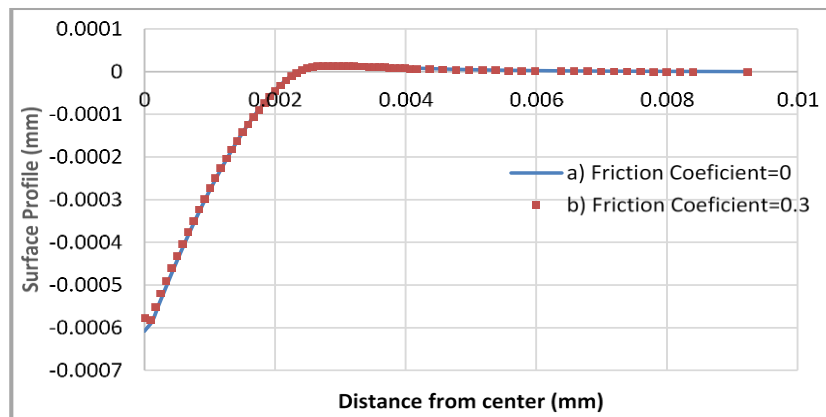
Figure 8-14 Indentation surface profile along the distance from the specimen centre for sinking in material system at: a) Frictionless contact, and b) Friction coefficient
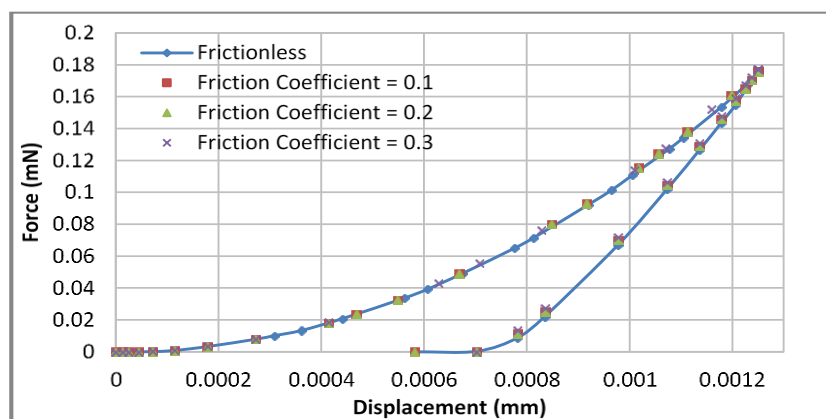
Figure 8-15 Numerical indentation loading- unloading results of Berkovich test at (0, 0.1, 0.2, and 0.3) friction coefficients

Figure 8-16 shows the Von Mises stress distribution for different indentation geometries (Berkovich, Vickers and Spherical) using two levels of friction contact (frictionless and 0.3

friction coefficient). Figure 8-16 (a) illustrates no significant differences in the Von Mises stress magnitudes and distributions during the loading phase to the maximum indentation depths of the friction and frictionless contact, except that a clear difference was observed during the unloading phase between frictionless and frictional surfaces. Figure 8-16 (b) shows that the magnitude of the maximum Von Mises stress at frictionless contact is higher than the frictional one in Berkovich, Vickers, and Spherical indentation processes, the magnitudes of the frictional simulations after unloading were about 21%, 33%, and 27% less than that of the frictionless one, respectively. These results agree with results obtained by Wang, Fang et al. (2007).

The results also showed that the smaller blunting tip radius of the Berkovich indenter geometry results in a higher residual stress concentration compared with Vickers indenter geometry. This may be attributed to the fact that the stress concentration increase with reducing tip radius, which causes displacement of a higher volume of material. The distributions of residual stress in the indentation imprint, illustrate that the maximum Von Mises stress frictional contact is concentrated at the centre of the workpiece surface while in the frictionless contact it is located at the inner region of the workpiece towards the contact edge with the indenters. The outcomes from these analyses agree with the results obtained by Fujisawa, Li et al. (2004), and Demiral, Roy et al. (2010).
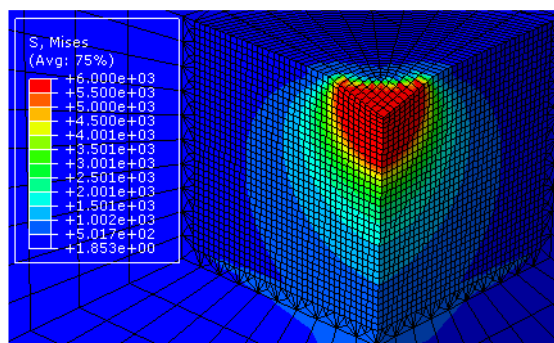
a) Vickers Loading (frictionless)   b) Vickers unloading (frictionless)
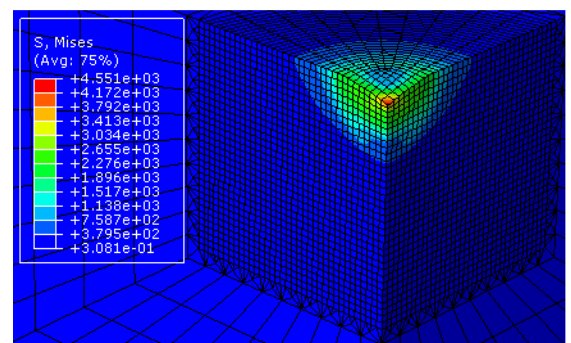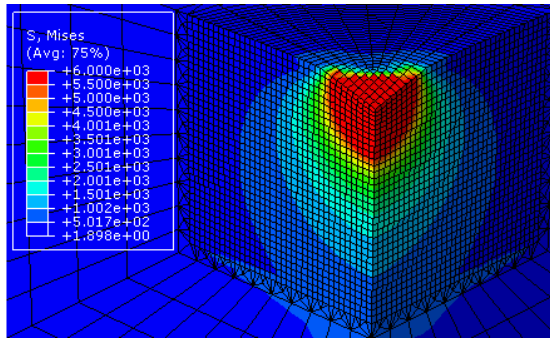
a) Vickers Loading (0.3 friction)
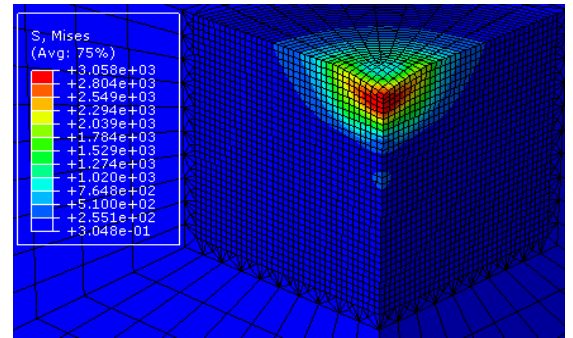
b) Vickers unloading (0.3 friction)
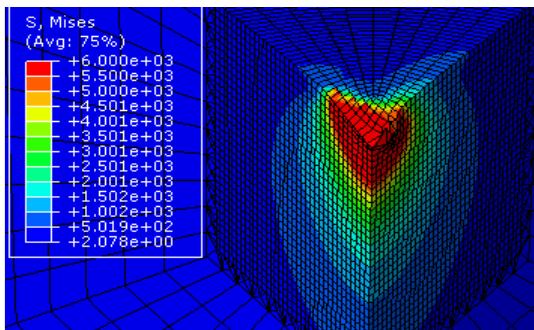
a) Berkovich Loading (frictionless)
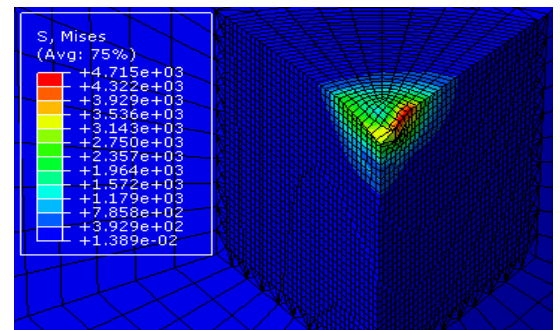
b) Berkovich unloading (frictionless)
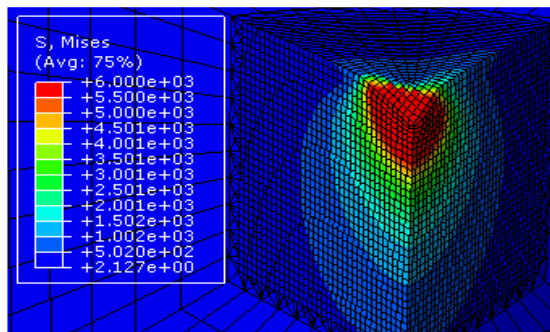
a) Berkovich Loading (0.3 friction)
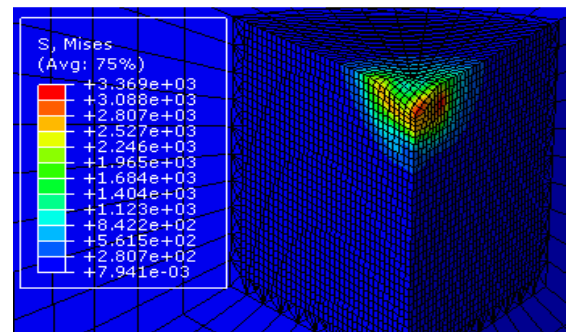
b) Berkovich unloading (0.3 friction)
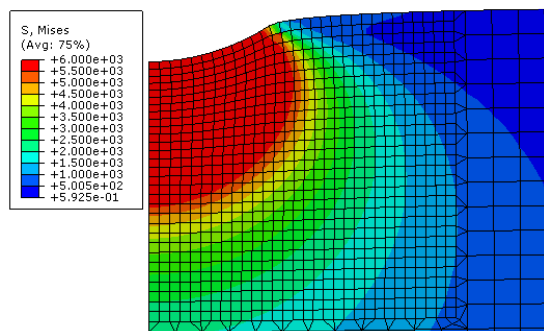
a) Spherical loading (frictionless)
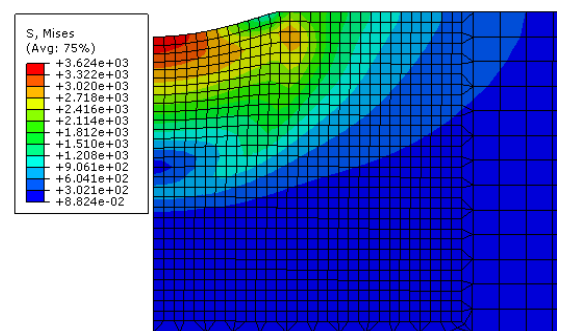
b) Spherical unloading (frictionless)

a)….Spherical Loading (0.3 friction)   b)….Spherical unloading (0.3 friction)
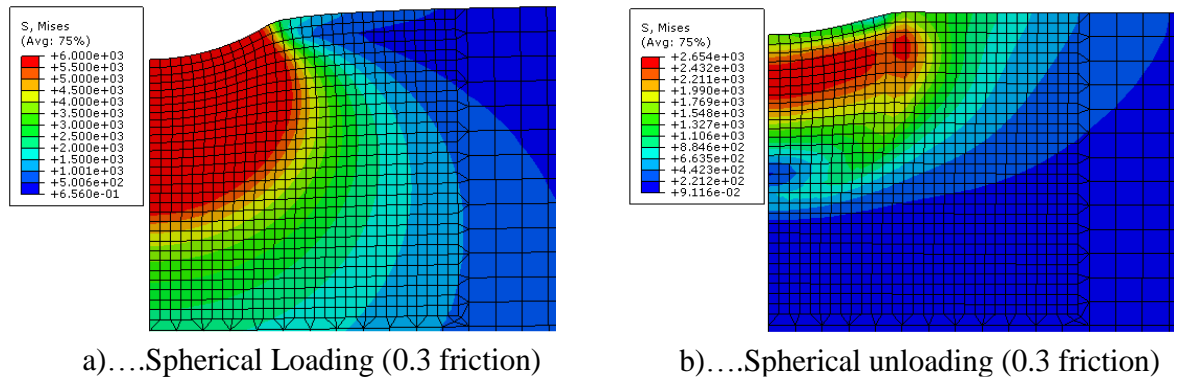
Figure 8-16 Von Mises stress concentration and distribution for different indentation geometries (Berkovich, Vickers and Spherical) using frictional and frictionless contact at: a) Loading phase, b) Unloading phase

According to the outcomes from the above analysis, a friction coefficient of 0.15 between the indenter and material surface will be used in this study to cover a wide range of material properties.

8.3.3   Effect of elastic plastic properties and sensitivity analysis

A series of FEM were performed using different contact geometries (Berkovich, Vickers, and Spherical) to investigate the effect of the material properties (E, σ_y and n) on the behaviour of the load displacement curves. The effect of material parameters on the curvature of loading unloading curves has been systematically studied using an ABAQUS parametric study, in which the Young's modules and Yield stress were varied over a wide range. Figure 8-17 shows results of the parametric study when changing elastic properties, E and keeping the plastic properties σ_y, n constant and Figure 8-18 shows results of the parametric study when changing plastic properties σ_y, n and keeping the elastic properties, E constant. The relationship between yield stress and Force, illustrates that increasing yield stress corresponds to the higher values of Force, as one would anticipate. Similarly, and logically, the intercept value of displacement (residual depth *hr),* is reduced at the higher values of yield stress. The results also show that the material exhibits elastic plastic behaviour beneath the indentation tip with similar trends and a clear stiffness effect at maximum indentation depth. According to Kick's law $F = Ch^2$, the loading curve for elastic plastic material normally follows power law equation (Swaddiwudhipong, Tho et al. 2005).

As displayed the indentation curve of materials under investigation follows the power law equation where the loading curves is a function of yield stress and strain hardening while the unloading curves is a function of Young's modulus. The parametric study confirmed the variation of curvature with respect to σ_y, and E and showed increased curvatures' coefficient values with the increasing of σ_y, and E regardless of the of contact geometry. The results also demonstrate that the indentation force and curvature profile predicted by Spherical indentation is higher compared with the forces generated from other indentation processes (Berkovich, and Vickers). This indicates that the greatest the contact surface area between the tip geometry and material surface, the greater the load response from the tip. The force and curvature profile from the Vickers indenter is higher than the Berkovich for the same reason.

However, for the same material properties and maximum indentation depth, the indenter geometry with the smaller tip radius (blunting edge), such as the Berkovich indenter , shows higher stress concentration results and induced greatest residual Von Mises stress distribution after unloading. The elastic recovery value of the design material after the unloading cycles varies according to the indentation process technique. The results of numerical load displacement curves demonstrate that the spherical indenter is associated with large elastic recovery on the design material compared with other indenters and the greatest effective angle of the Vickers indenter results in greater elastic recovery than Berkovich tip. As expected, the indenter tip with the larger diameter will result in a higher load, higher Young's modulus and higher hardness. However, the elastic recovery increases with the increasing tip radius due to the smoother surface contact of the indenter to the design material.
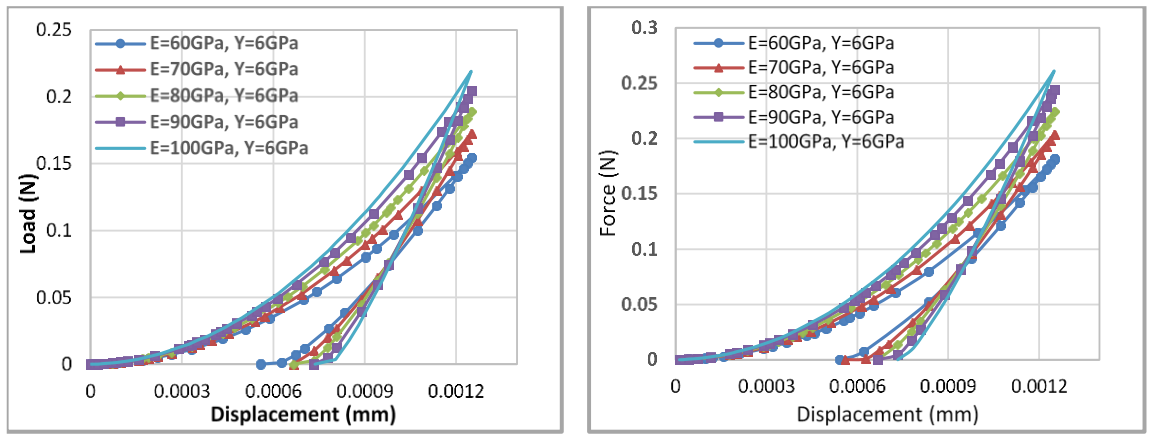
a) Berkovich Indenter
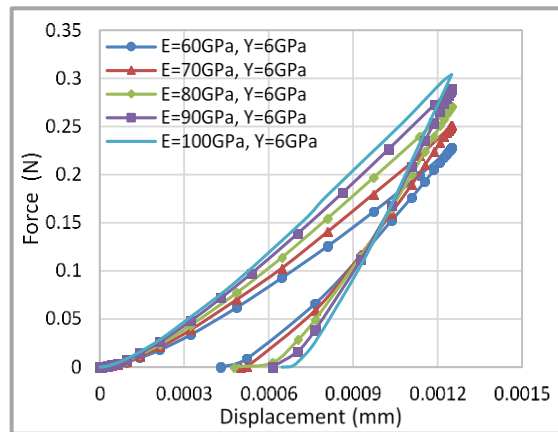
b) Vickers Indenter

c) Spherical indenter

Figure 8-17 The effect of Young modulus on the load displacement curves of: a) Berkovich, b) Vickers and c) Spherical indentation processes
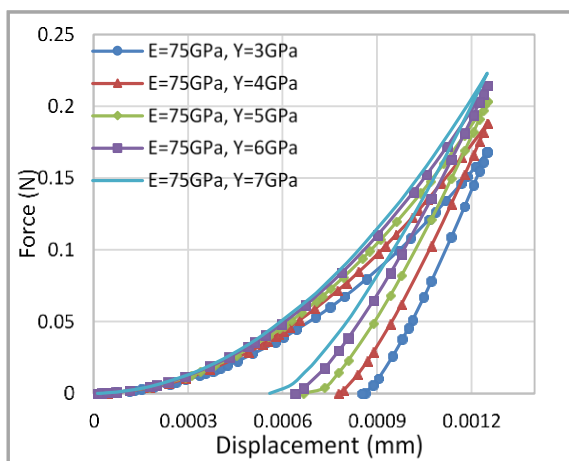
a) Vickers indenter
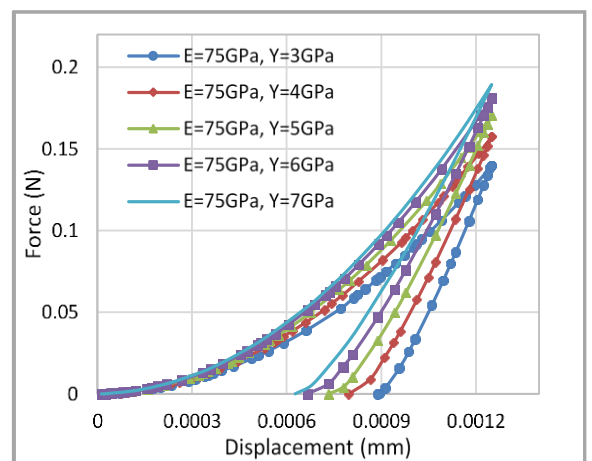
b) Berkovich indenter
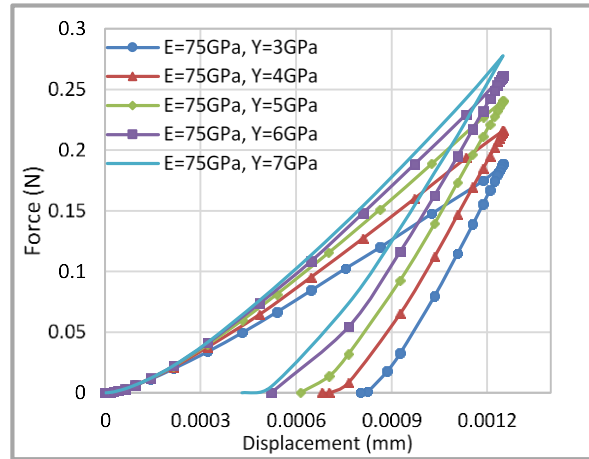
c) Spherical indenter

Figure 8-18 The Effect of Yield stress on the load displacement curves of a) Vickers, b) Berkovich and c) Spherical indentation processes

Figure 8-19 (a) and (b) shows the indentation surface profile along the distance from the centre during loading cycle at a maximum indentation depth on fused silica and the residual surface profile after unloading using different indenter geometries. The results demonstrate that the tip geometry with the large diameter will result in the greater indentation load on the specimen surface. It is clearly noticed that the spherical tip geometry incurred a deeper indentation surface profile and residual surface profile in the direction opposite to the centre resulting in greater indentation hardness compared to the Berkovich and Vickers tip geometries. The results also show, the pile-up of the design material produced by the spherical tip on the residual surface profile is the greatest while that produced by the Vickers tip is the lowest due to the fact that the Vickers indenter geometry has the greater effective angle.

(a)

(b)
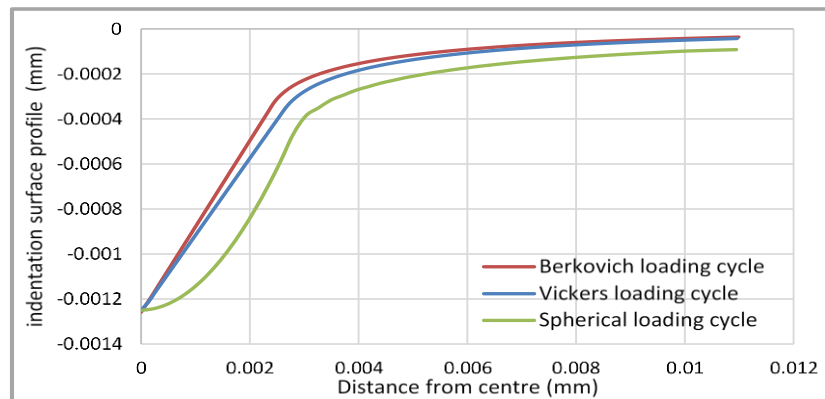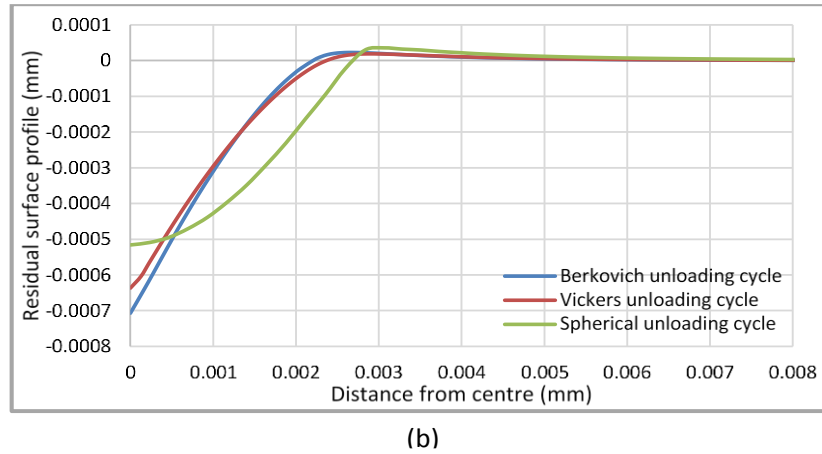
Figure 8-19 Indentation surface profile along the distance from the centre during: a) loading cycle at a maximum indentation depth on fused silica and b) the residual surface profile after unloading using different indenter geometries

8.3.4 Effect of Poisson's ratio and sensitivity analysis

A series of FEM parametric studies were performed using different contact geometries (Berkovich, Vickers and Spherical) to investigate the effect of Poisson's ratio on the behaviour of the load displacement curves for a given set of material properties. Figure 8-20 shows the results in non-dimensional form for different values of the Poisson ratio $0.1 \leq v \leq 0.5$, the indentation load is normalized by the Young modulus and square indentation depth, and the indentation depth is normalized by maximum indentation depth. The numerical simulations were performed on the basis that the indentation depth is the only representative length of the problem, and the average contact pressure is constant from dimensional considerations . The numerical results actually confirmed the curvature relation between maximum indentation load *F* and indentation depth *h*, typified by Kick's law $F = Ch^2$, where $C = F/h^2$ is a function of the Poisson ratio. The numerical parametric study demonstrates that the curvature coefficient C increases with increases of v, , the results also show that the values of coefficient, C with different indentation load by spherical indenter is higher compared with the C values of Vickers and Berkovich indenters. Figure 8-21 shows the effect of the Poisson ratio on C at different indentation techniques, the value of C is normalized by Young modulus of elasticity. The trend line fitting the numerical results with respect to the Poisson ratio, indicate that C is related to the elastic and plasic properties as:

The curve fitting the coefficient values of the Berkovich indenter is given by Eq. (8.2):

$$C(1 - v^2)/E = 1.448(1 - 0.685v^3 - 0.051v^2 + 0.141v) \quad\quad (8.2)$$

The curve fitting the coefficient values of the Vickers indenter is given by Eq. (8.3):

$$C(1 - v^2)/E = 1.711(1 - 0.305v^3 - 0.262v^2 + 0.171v) \quad\quad (8.3)$$

The curve fitting the coefficient values of the Spherical indenter is given by Eq. (4):

$$C(1 - v^2)/E = 2.161(1 - 0.108v^3 - 0.611v^2 + 0.291v) \quad\quad (8.4)$$

The analysis of numerical results showed good agreement with previous work on Vickers and Berkovich indentations by Giannakopoulos, Larsson et al. (1994) and Larsson, Giannakopoulos et al. (1996), respectively, which suggests that the Poisson ratio has a minor effect on the elastic properties because the displacements tangential to the contact surface are very small compared to the indentation depth.

a) Berkovich indenter

b) Vickers indenter

c) Spherical indenter
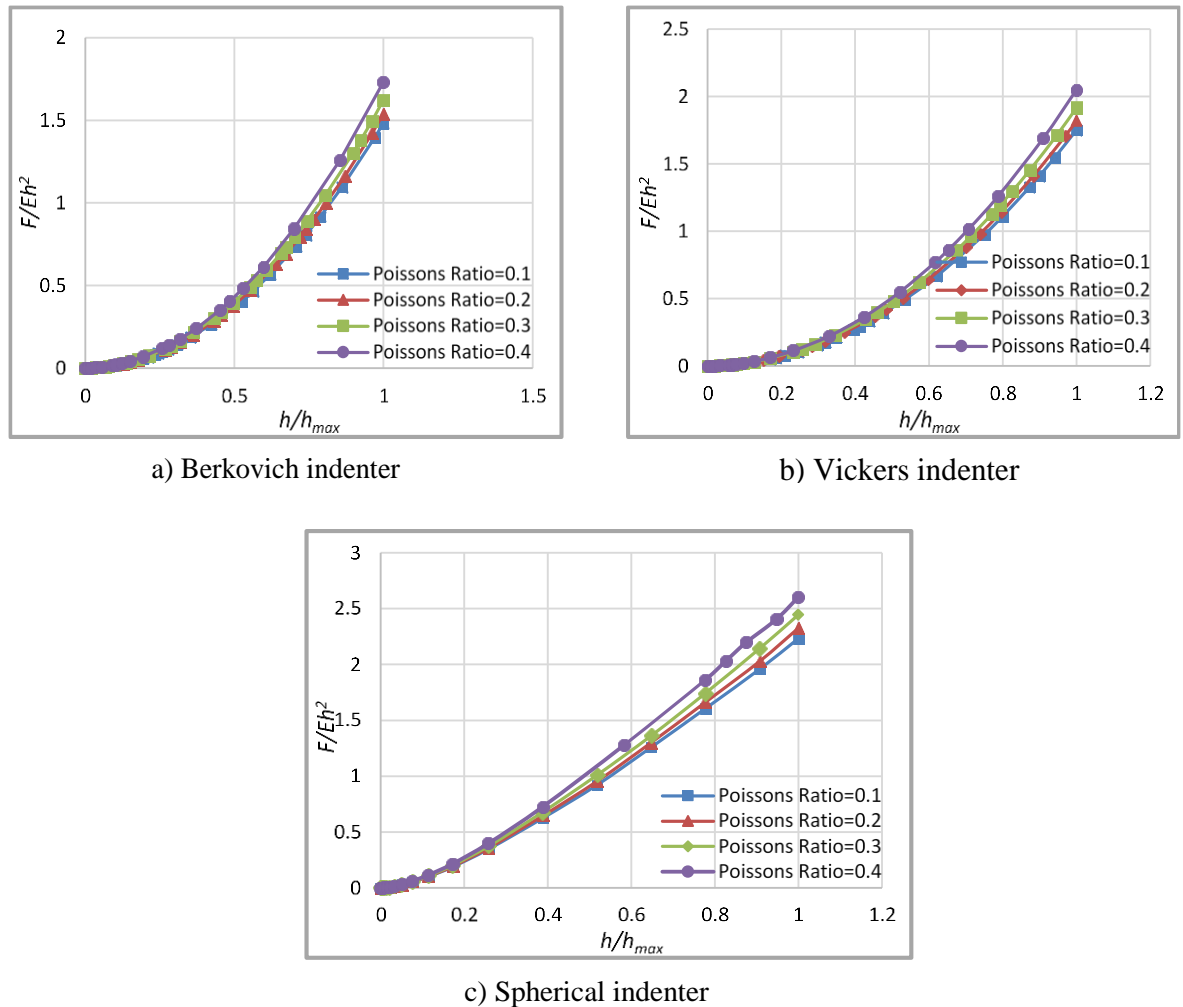
Figure 8-20 Non-dimensional analysis of F/Eh^2 vs. h/h_{max} for various values of the Poisson ratio using. a) Berkovich, b) Vickers and c) Spherical indentation processes
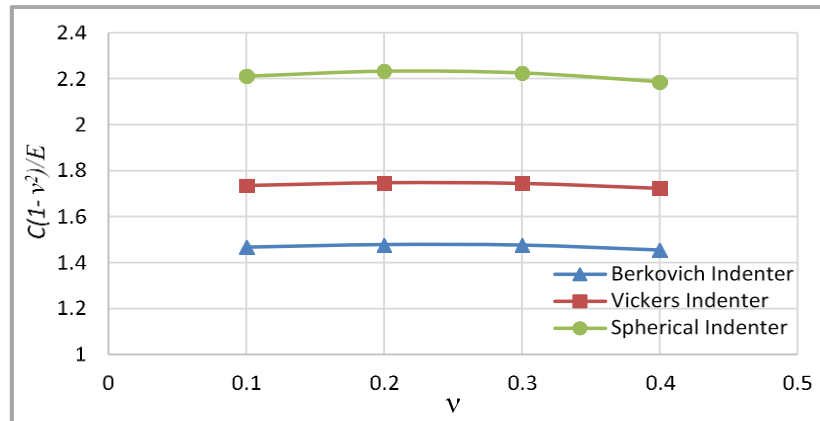
Figure 8-21 The effect of Poisson ratio on the indentation curvatures, C at different indenter geometries

8.4   Validation of the 3-D FE models against published data

The Validation of the 3-D FE models against published data was performed by comparing the predicted results with published numerical and experimental results. The   FEM of Vickers indentation test was verified by comparing the numerical results from this work with the numerical and experimental results developed by Dao, Chollacoop et al. (2001), both numerical works adapted the same elastic plastic material properties of 7075T551AL and then the predicted load displacement curves were compared with the published results. Figure 8-22 shows good agreement between the predicted loading displacement curve and the published numerical and experimental data.

| (a) | (b) |
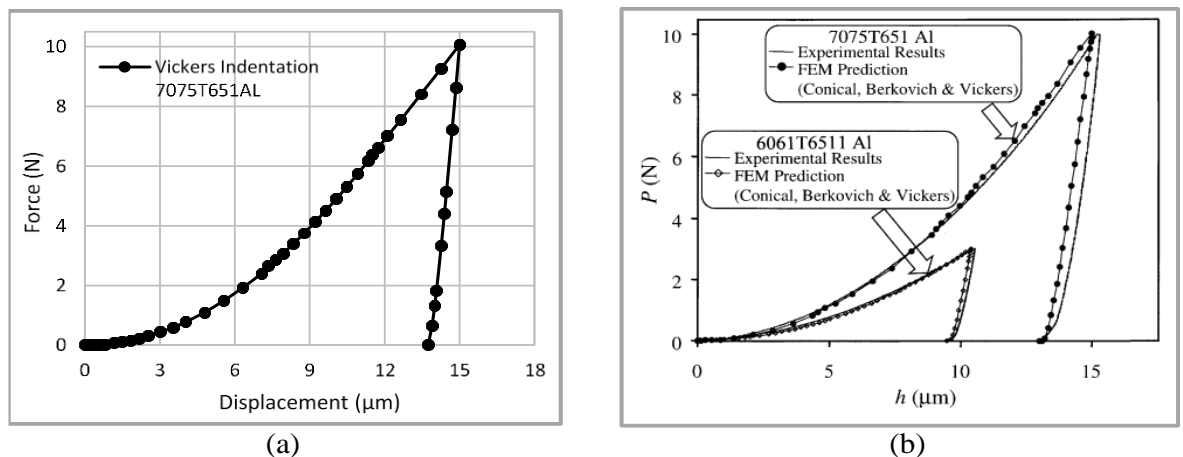
Figure 8-22 Loading unloading curves of 7075T551AL: a) FEM predicted results with Vickers indenter, and b) published numerical and experimental data (Dao, Chollacoop et al. 2001)

The numerical results of the Berkovich indentation test were verified with the numerical and experimental published data. The elastic plastic material properties of Al 2024-T351

were adapted by Khan, Hainsworth et al. (2010) to validate the FEM with the experimental results. Figure 8-23 shows the predicted load displacement curve and the published numerical and experimental results. As displayed in the figures, the predicted results from this work are a satisfactory match with the published results.

| (a) | (b) |
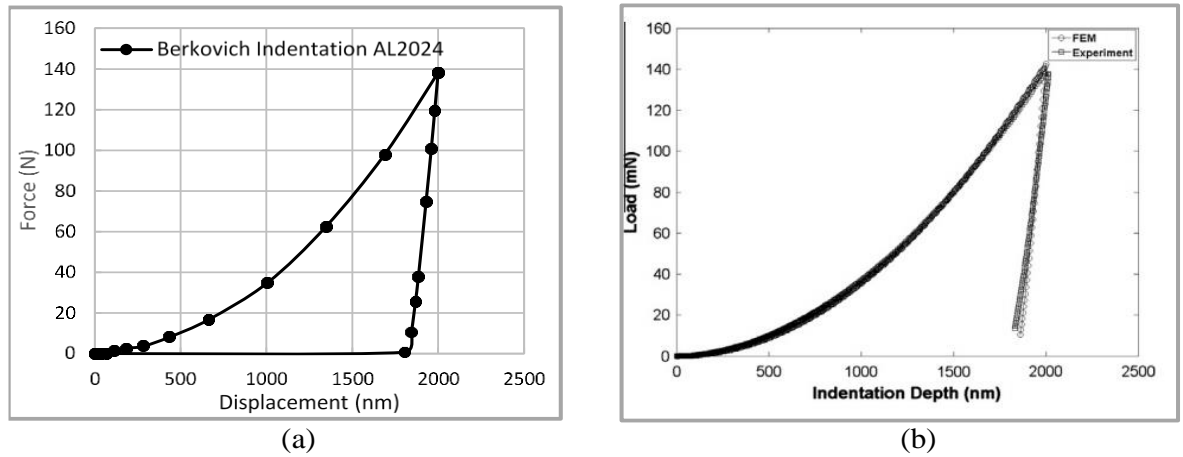
Figure 8-23 Loading unloading curves of AL2024: a) FEM predicted results with Berkovich indenter, and b) published numerical and experimental data (Khan, Hainsworth et al. 2010)

The FEM results of the Spherical indentation test were verified using published numerical and experimental data (Celentano, Guelorget et al. 2012, and Diego 2012). FEM of a spherical indenter with a radius of 0.05mm was performed with the reported material properties. As shown in Figure 8-24; the predicted results showed good agreement with the published data.

| (a) | (b) |
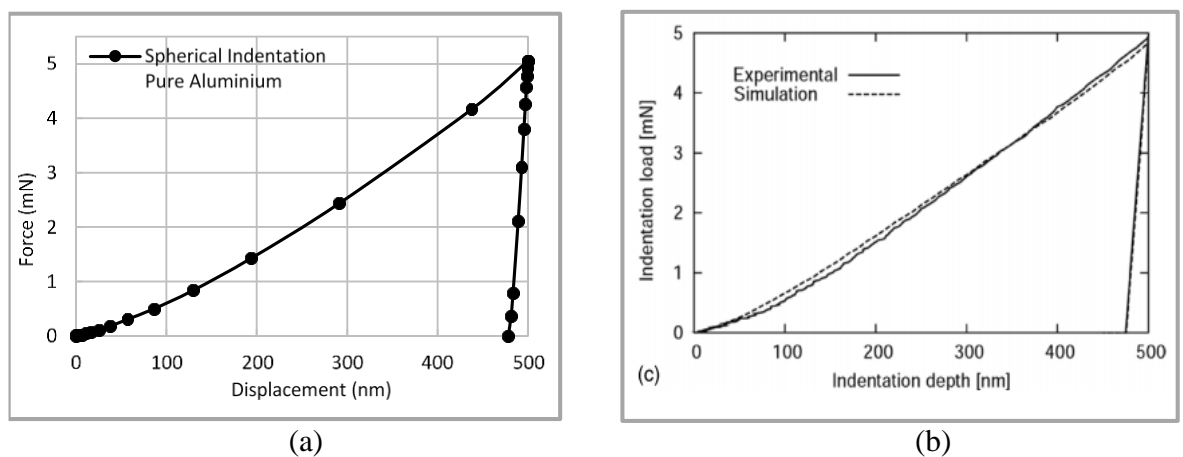
Figure 8-24 Load unloading curves with Spherical indentation (Pure Aluminium) a) predicted loading unloading results, and b) published numerical and experimental data (Celentano, Guelorget et al. 2012)

In order to validate the numerical simulations in more depth, Hardness, Young modulus, and indentation depth ratio (final indentation depth to the maximum indentation depth) were calculated from the loading unloading curves using the Oliver and Pharr method. Table 8-1 shows the comparison between the predicted and published material properties results in non- dimensional form. In this arrangement, the results of published Hardness, $^*H_P$ is normalized by the predicted hardness, $^*H_W$, the results of published reduced modulus, $^*(Er)_P$ is normalised by predicted reduced modulus, $^*(E_r)_W$ and the results of published indentation depth ratio, $^*(h_{max}/h_f)_P$ is normalised by predicted indentation depth ratio, $^*(h_{max}/h_f)_w$. The non-dimensional analyses demonstrated no significant difference in the hardness, elastic modulus, and the indentation depth ratio between the predicted and published data for the three different indenter geometries. This suggests that all models are accurate and valid.

Table 8-1 Comparison of predicted material properties with the published results using various indentation techniques (Berkovich, Vickers and Spherical)

Indenter	Material	$^*H_P$ (GPa)	$^*(Er)_P$ (GPa)	$^*(h_f/h_{max})_P$	$H_P/^*H_W$	$(Er)_P/^*(E_r)_W$	$(h_{max}/h_f)_P/^*(h_{max}/h_f)_w$
Berkovich	AL2024-T351	1.57	75.6	0.925	1.06	1.046	1.027
Vickers	7075T551 AL	1.656	83.4	0.94	1.054	1.039	1.022
Spherical	Pure-AL	1.895	85.9	0.96	1.049	1.03	1.021

8.5 Comparison between 2-D axisymmetric and 3-D FEM of different contact geometries

The main objective of this section was to investigate the differences between 2-D axisymmetric and 3-D FEM of different indenter geometries (Berkovich, Vickers, and spherical). The numerical simulations of an equivalent 2-D axisymmetric conical to Berkovich and Vickers indenter geometries were performed as presented in Chapter 6, and Chapter 7, respectively.

The vertical displacement of the indenter is specified as an input value corresponding to total indentation depth. The penetration depth is measured along the direction of indenter movement which is equal to the total displacement of the node specified by a reference point at the indenter tip. Indentation force was obtained by extracting the total reaction

force at the reference node during the analysis. Mesh element size and distribution, sample size and the boundary condition were assumed to be fixed in all FEM simulations in order to eliminate these factors influence on the output results.

Figure 8-25 shows a series of 2-D axisymmetric conical numerical simulations were performed with different inclination angles with the same tip-blunting radius obtained from previous Chapters (6, and 7) to investigate the effect of inclination angle on the loading unloading curves. Based on the results of FEM analysis, it is noted that the loading unloading curves profile deviate from each other when different inclination angles of the indenter are used, resulting in the maximum reaction force increases with the increasing inclination angles. This suggests that a parametric study is required to validate the 2-D axisymmetric models with the 3-D models for different indenter geometries over a range of elastic plastic material properties.
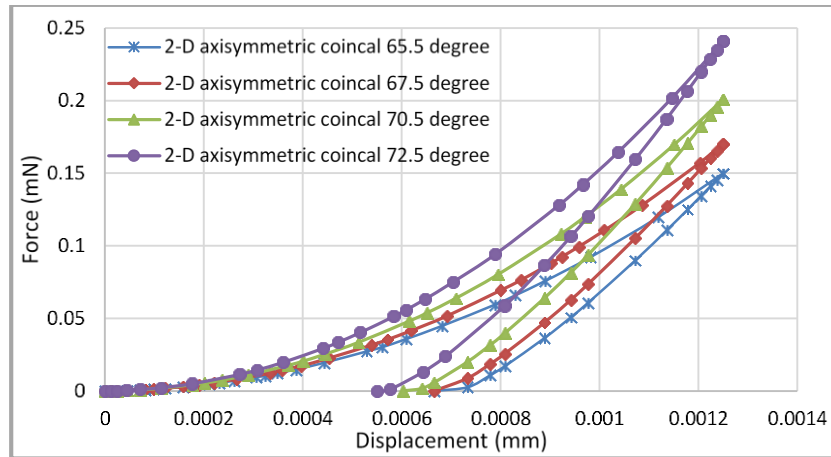
Figure 8-25 2-D axisymmetric conical indenters with different inclination angle (65.5°, 67.5°, 70.5° and 72.5°)

A parametric study was undertaken to determine the inclination angle for a given set of indentation data using script programming language (python) interfaced with ABAQUS FEM. Within this approach a series of numerical simulations were performed with different inclination angles of the 2-D axisymmetric conical shape. The results of load displacement curves were compared with the results from the 3-D Berkovich and Vickers indenters for a range of material properties using a predefined program in Microsoft Excel, until minimum convergence of load displacement curves is achieved.

Figure 8-26 shows the result of load displacement curves at optimal inclination angle, 67.5° of 2-D axisymmetric conical indenter was in a good agreement with the results of the 3-D Berkovich model over a range of material properties. The difference in the load between the two curves at each indentation depth was within 4% determined by the RMSE objective function method. In this method, the differences in indentation force are calculated at each indentation point. The final objective function was determined by the sum of objective functions at each indentation point. The discrepancy in the results may be attributed to the fact that the mesh element size of the 2-D asymmetric indenter was much finer than the 3-D Berkovich indenter in the area near the indentation zone, and other influences of the stress strain distribution beneath 3-D model as a result of perfectly sharp assumption. These results are consistent with numerical simulations reported by Moore, Manzari et al. (2010)
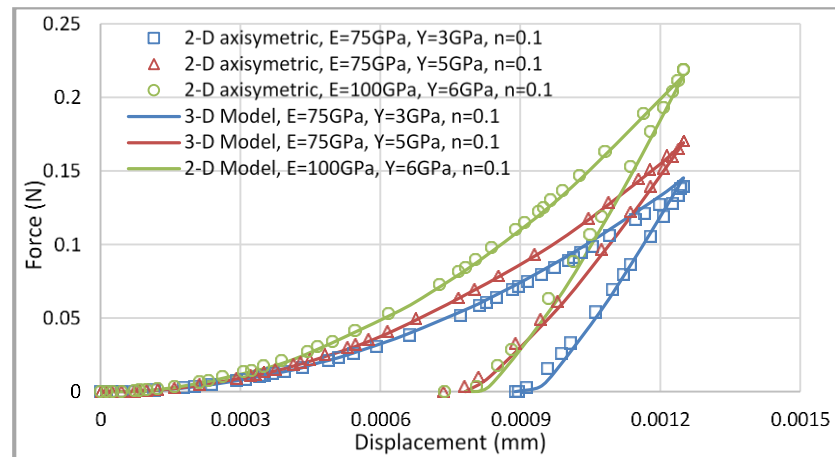
Figure 8-26 Comparison between load displacement curves of numerical 2-D and 3-D Berkovich indentation over a range of material properties

Figure 8-27 shows a comparison of load displacement curves of 2-D axisymmetric model at optimal inclination angle value of 70.3 and 3-D Vickers indentation over a range of material properties. The two curves exhibit good correlation and only a minor deviation of 3% occurs using RMSE objective function. As in the Berkovich indenter, the deviation in the results is related to the mesh density difference, the 2-D model employed finer mesh compared with 3-D model and also the tip radius geometry which is considered as perfectly sharp in the 3-D Vickers model. Increasing the mesh density in the 3-D model will lead to increasing the computational time while producing a minor improvement in the numerical results. These results agree well with numerical results obtained by Kang, Becker et al. (2012).
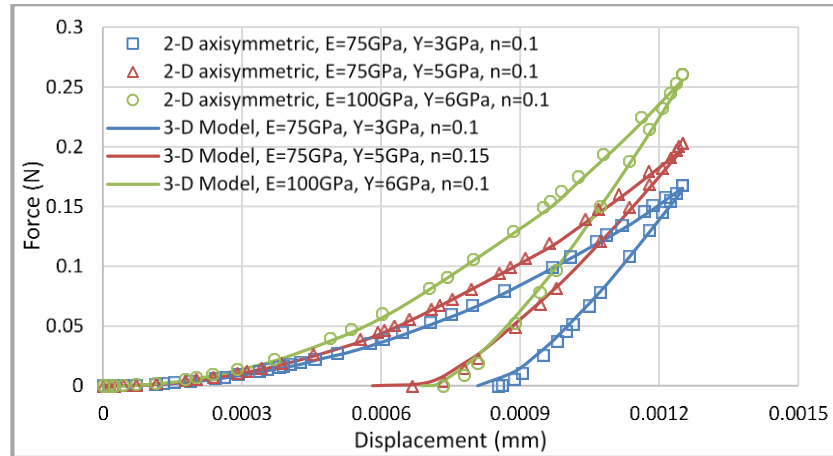
Figure 8-27 Comparison between load displacement curves of numerical 2-D and 3-D Vickers indentation over a range of material properties

Figure 8-28 shows the comparison between 3-D and 2-D spherical indentation processes. The analysis suggested a very good correlation between the 2-D and 3-D models, this may be attributed to the fact that both models used the same tip radius shape of 0.05mm.
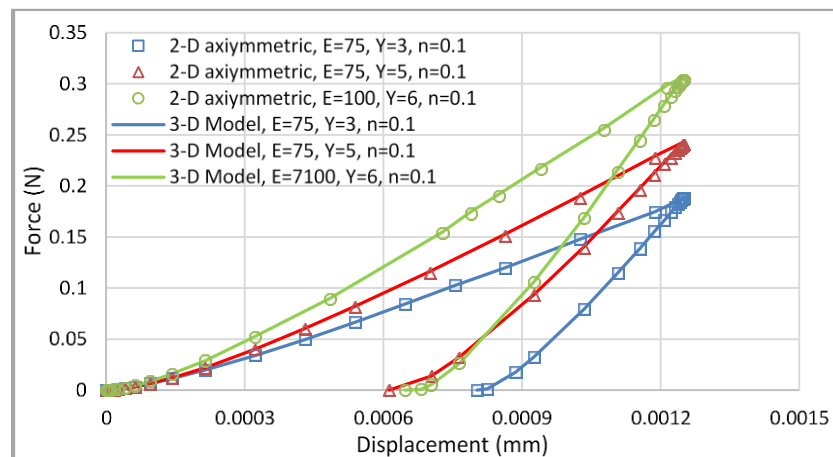
Figure 8-28 Comparison between load displacement curves of numerical 2-D and 3-D Spherical indentation over a range of material properties

The differences in the load displacement curves of different indenter geometries can be investigated in more depth by comparing the distribution of equivalent plastic strain (PEEQ), which reflects the resistance of material to a particular indentation process for a given set of elastic plastic material properties. Table 8-2 presents the mechanical properties results such as hardness, reduced modulus, PEEQ, and indentation ratio calculated from the slope of unloading curves using the Oliver and Pharr method of various 3-D indenter geometries and their equivalent 2-D asymmetric models.

The numerical simulations were performed by employing an isentropic elastic plastic material (Fused silica) with an input data of E= 72GPa, σ_y = 6.2 GPa, and v = 0.25 (Gadelrab, Bonilla et al. 2012), the maximum indentation depth was controlled as 1.25µm. Figure 8-29 shows an example of the equivalent plastic strain distribution after indentation force removal of different indenter geometries. A clear deviation was observed in the equivalent plastic strain, the Berkovich indenter exhibited a larger plastic strain compared with the Vickers and spherical indenter geometries. The proposed deviations are the main reason for the discrepancy in the load displacement curves.

Table 8-2 Comparison of mechanical properties between 3-D and their equivalent 2-D model of various indentation geometries

Indenter Geometries	F_{max} (N)	H (GPa)	Er (GPa)	h_f/h_{max}	$Er/(E_r)_{input}$	$PEEQ$ %
Berkovich	0.189	5.33	65.64	0.532	1.046	66.95
Vickers	0.203	5.67	68.73	0.501	1.039	39.29
Spherical	0.251	6.54	69.56	0.416	0.951	25.10
2-D axisymmetric eq.(Berkovich)	0.196	5.51	65.79	0.542	1.065	67.87
2-D axisymmetric eq.(Vickers)	0.211	5.92	71.82	0.511	1.055	41.12
2-D axisymmetric eq.(Spherical)	0.253	6.61	72.34	0.413	0.945	24.91

Vickers Indentation

Berkovich Indentation

Spherical Indentation
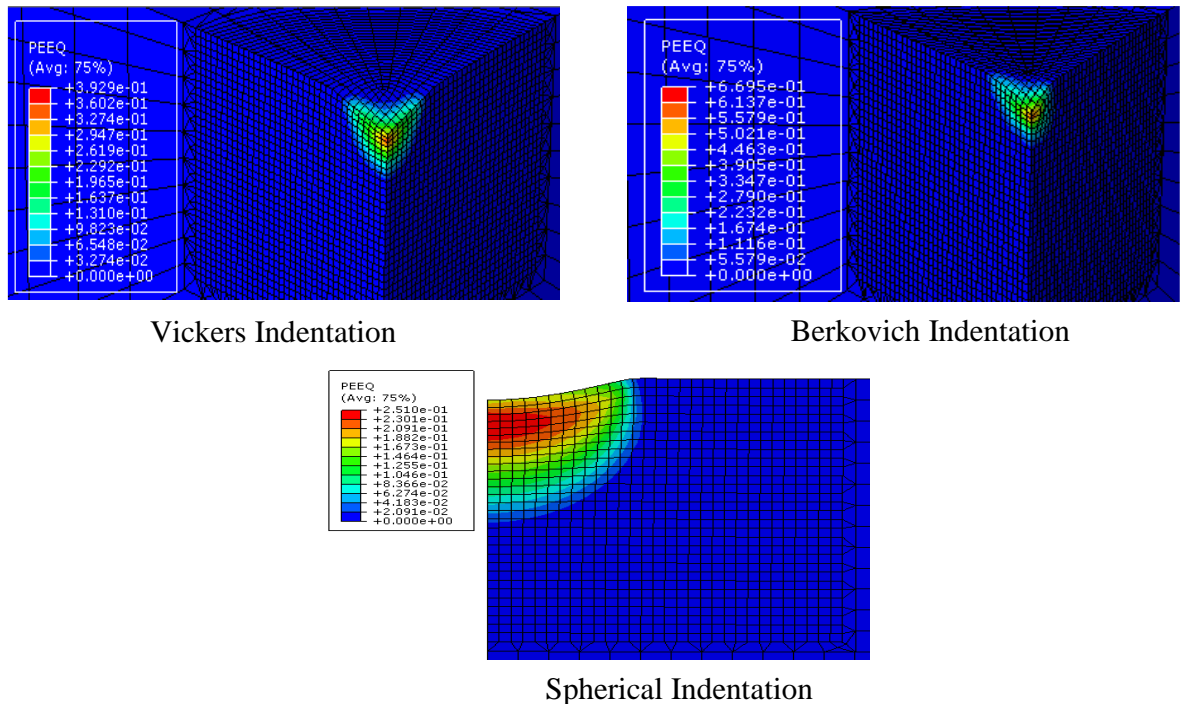
Figure 8-29 the equivalent plastic strain distribution after unloading phase of Berkovich, Vickers and Spherical indentation techniques.

8.6   Conclusion

3-D and 2-D numerical simulations of Berkovich, Vickers and Spherical indentation tests were performed in order to achieve a better understanding of the influence of indenter geometry on the materials' behaviour under indentation. The influence of a variation in sample size, tip geometry, frictional condition, mesh density and material properties on the force displacement curves during the loading and unloading stages were established using a parametric study. The following main conclusions can be drawn:

− Sample size analyses suggested that the convergence of load displacement curves can be achieved at the condition: specimen dimension ratio (workpiece radius to the workpiece height) *rw:hw* = unity; and depth ratio (workpiece height to the maximum indentation depth) *hw/hm* ≥ 100.

− No significant differences in the indentation curves at various coefficients of friction, except the Von Mises stress concentration and distribution. The results exhibited a substantial difference between frictionless and frictional surfaces. The maximum Von Misses stress at frictionless contact is higher than the frictional one in Berkovich, Vickers, and Spherical indentation processes, however the magnitude of the frictional surface after unloading was about 21%, 33%, and 27% less than that of the frictionless one, respectively.

− It is clearly noticed from various indentation techniques that the indentation load increases with the increasing tip radius due to the increased contact area with the material at a similar indentation depth. The greater tip radius such as in Spherical indentation causes a deeper indentation surface profile and residual surface profile in the direction opposite to the centre resulting in greater indentation hardness compared to the Berkovich and Vickers tip geometries. However, the residual indentation depth reduces with the increases tip radius, resulting in increasing the elastic recovery and reducing Von Misses stress after the unloading stage. In addition, the indenter tip with a larger diameter will result in a higher Young's modulus and higher hardness, while a larger plastic zone size can be formed with a sharper indenter due to the higher stress concentration employed.

− A FEM parametric study was performed using different contact geometries (Berkovich, Vickers and Spherical) to examine the effect of Poisson's ratio on the load displacement response.

The results suggested that the Poisson ratio has a minor effect on the elastic properties because the displacements tangential to the contact surface are very small compared to the indentation depth.

The parametric study confirmed the variation of loading –unloading curvature with respect to σ_y, *E,* and *n* and showed increased curvatures' coefficient values with the increasing of σ_y, and *E* regardless of the contact geometry. It is clearly noticed that the indentation force and curvature profile predicted by Spherical indentation is higher compared with the forces generated from other indentation processes (Berkovich, and Vickers).

− The ability of various 3-D FE indentation models to predict the experimental results was examined by validation of the numerical results against published data. The non-dimensional analyses demonstrated no significant difference in the hardness, elastic modulus, and the indentation depth ratio between the predicted and published data for the three different indenter geometries. The maximum differences were 6%, 5%, and 3% of hardness, elastic modulus, and the indentation depth ratio, respectively. This suggests that all models are accurate and valid.

− Parametric studies were employed to validate the 2-D axisymmetric models with respect to 3-D models with different indenter geometries over a range of elastic plastic material properties. This approach was successfully used to optimize the inclination angle of 2-D axisymmetric models to achieve the best fit load displacement curve with the 3-D model under the same indentation conditions. The comparison shows a good agreement between the two curves and only a minor deviation of 3%, 4%, and 2% of Vickers, Berkovich, and Spherical indenters, respectively were observed using the RMSE objective function. This suggests that the 2-D FEM provides valuable and qualitative information that closely describes the experimental indentation results, in particular when taking into account the effect of tip radius and inclination angle.

8.7   References

Alcala, J., A. Barone and M. Anglada (2000). "The influence of plastic hardening on surface deformation modes around Vickers and spherical indents." Acta Materialia **48**(13): 3451-3464.

Bhattacharya, A. and W. Nix (1988). "Finite element simulation of indentation experiments." International Journal of Solids and Structures **24**(9): 881-891.

Bucaille, J.-L., S. Stauss, E. Felder and J. Michler (2003). "Determination of plastic properties of metals by instrumented indentation using different sharp indenters." Acta materialia **51**(6): 1663-1678.

Bucaille, J., E. Felder and G. Hochstetter (2002). "Identification of the viscoplastic behavior of a polycarbonate based on experiments and numerical modeling of the nano-indentation test." Journal of Materials Science **37**(18): 3999-4011.

Celentano, D. J., B. Guelorget, M. François, M. A. Cruchaga and A. Slimane (2012). "Numerical simulation and experimental validation of the microindentation test applied to bulk elastoplastic materials." Modelling and Simulation in Materials Science and Engineering **20**(4): 045007.

Cheng, Y.-T. and C.-M. Cheng (1999). "Can stress–strain relationships be obtained from indentation curves using conical and pyramidal indenters?" Journal of Materials Research **14**(09): 3493-3496.

Dao, M., N. Chollacoop, K. Van Vliet, T. Venkatesh and S. Suresh (2001). "Computational modeling of the forward and reverse problems in instrumented sharp indentation." Acta materialia **49**(19): 3899-3918.

Dao, M., N. Chollacoop, K. J. Van Vliet, T. A. Venkatesh and S. Suresh (2001). "Computational modeling of the forward and reverse problems in instrumented sharp indentation." Acta Materialia **49**(19): 3899-3918.

Demiral, M., A. Roy and V. Silberschmidt (2010). Repetitive indentation of Ti-based alloys: A numerical study. IOP Conference Series: Materials Science and Engineering, IOP Publishing.

Fischer-Cripps, A. C. (2000). Factors Affecting Nanoindentation Test Data, Springer.

Fujisawa, N., W. Li and M. V. Swain (2004). "Observation and numerical simulation of an elastic-plastic solid loaded by a spherical indenter." Journal of materials research **19**(12): 3474-3483.

Futakawa, M., T. Wakui, Y. Tanabe and I. Ioka (2001). "Identification of the constitutive equation by the indentation technique using plural indenters with different apex angles." Journal of Materials Research **16**(08): 2283-2292.

Gadelrab, K., F. Bonilla and M. Chiesa (2012). "Densification modeling of fused silica under nanoindentation." Journal of Non-Crystalline Solids **358**(2): 392-398.

Giannakopoulos, A., P.-L. Larsson and R. Vestergaard (1994). "Analysis of Vickers indentation." International journal of solids and structures **31**(19): 2679-2708.

Johnson, K. L. and K. L. Johnson (1987). Contact mechanics, Cambridge university press.

Kang, J., A. Becker and W. Sun (2012). "Determining elastic–plastic properties from indentation data obtained from finite element simulations and experimental results." International Journal of Mechanical Sciences **62**(1): 34-46.

Khan, M., S. V. Hainsworth, M. Fitzpatrick and L. Edwards (2010). "A combined experimental and finite element approach for determining mechanical properties of aluminium alloys by nanoindentation." Computational Materials Science **49**(4): 751-760.

Knapp, J., D. Follstaedt, S. Myers, J. Barbour and T. Friedmann (1999). "Finite-element modeling of nanoindentation." Journal of Applied Physics **85**(3): 1460-1474.

Larsson, P.-L., A. Giannakopoulos, E. Söderlund, D. Rowcliffe and R. Vestergaard (1996). "Analysis of Berkovich indentation." International Journal of Solids and Structures **33**(2): 221-248.

Mata, M. and J. Alcala (2004). "The role of friction on sharp indentation." Journal of the Mechanics and Physics of Solids **52**(1): 145-165.

Min, L., C. Wei-Min, L. Nai-Gang and W. Ling-Dong (2004). "A numerical study of indentation using indenters of different geometry." Journal of materials research **19**(01): 73-78.

Moore, S. W., M. T. Manzari and Y.-L. Shen (2010). "Nanoindentation in elastoplastic materials: insights from numerical simulations." International Journal of Smart and Nano Materials **1**(2): 95-114.

Poon, P. C. B. (2009). A critical appraisal of nanoindentation with application to elastic-plastic solids and soft materials, California Institute of Technology.

Rother, B., A. Steiner, D. Dietrich, H. Jehn, J. Haupt and W. Gissler (1998). "Depth-sensing indentation measurements with Vickers and Berkovich indenters." Journal of materials research **13**(08): 2071-2076.

Suresh, A. E. G. a. S. (1999). "Determination of elastoplastic properties by instrumented sharp indentation." Acta Metallurgica Inc **40**(10): 1191–1198,.

Swaddiwudhipong, S., K. Tho, Z. Liu and K. Zeng (2005). "Material characterization based on dual indenters." International journal of solids and structures **42**(1): 69-83.

Tabor, D. (1948). A simple theory of static and dynamic hardness. Proceedings of the Royal Society of London A: Mathematical, Physical and Engineering Sciences, The Royal Society.

Taljat, B., T. Zacharia and F. Kosel (1998). "New analytical procedure to determine stress-strain curve from spherical indentation data." International Journal of Solids and Structures **35**(33): 4411-4426.

Venkatesh, T. A., K. J. Van Vliet, A. E. Giannakopoulos and S. Suresh (2000). "Determination of elasto-plastic properties by instrumented sharp indentation: guidelines for property extraction." Scripta Materialia **42**(9): 833-839.

Wang, T. H., T.-H. Fang and Y.-C. Lin (2007). "A numerical study of factors affecting the characterization of nanoindentation on silicon." Materials Science and Engineering: A **447**(1): 244-253.

Youn, S. and C. Kang (2005). "FEA study on nanodeformation behaviors of amorphous silicon and borosilicate considering tip geometry for pit array fabrication." Materials Science and Engineering: A **390**(1): 233-239